Flows during floods in urban areas: influence of the detailed topography and exchanges with the sewer system

Pierre Henri Bazin

N° d'ordre 241-2013 Année 2013

THESE DE L'UNIVERSITE DE LYON

Délivrée par

L'UNIVERSITE CLAUDE BERNARD - LYON 1

Ecole Doctorale Mécanique, Energétique, Génie Civil et Acoustique

Spécialité Mécanique

DIPLOME DE DOCTORAT (arrêté du 7 août 2006)

Ecoulements lors d'inondations en milieu urbain : influence de la topographie détaillée et des échanges avec le réseau d'assainissement

Préparée dans l'Unité de Recherche Hydrologie-Hydraulique, Irstea par

Pierre-Henri BAZIN

Soutenue publiquement le 05 décembre 2013 à Villeurbanne devant le jury composé de :

DJORDJEVIC Slobodan	Professeur, Université d'Exeter	Rapporteur
MOSE Robert	Professeur, ENGEES/UdS	Rapporteur
VINKOVIC Ivana	Maître de conférences, UCBL1	Examinateur
SERGENT Philippe	Directeur scientifique, CETMEF	Examinateur
PAQUIER André	ICPEF, IRSTEA	Directeur de thèse
MIGNOT Emmanuel	Maître de conférences, INSA de Lyon	Encadrant
KAWAIKE Kenji	Professeur, Université de Kyoto	Encadrant

Remerciements

En premier lieu, je tiens à remercier André Paquier pour avoir encadré mon travail tout au long de ces trois ans. Sa disponibilité et son pragmatisme m'ont évité bien des écueils et ont clairement contribué à la réussite de cette thèse.

Je remercie aussi Emmanuel Mignot pour son encadrement (hyper) actif, ainsi que pour ses relectures méticuleuses de ce manuscrit. En parallèle, je les remercie Nicolas Rivière et lui pour leur bon accueil au LMFA, leur aide sur l'installation expérimentale et pour les différentes discussions autour des résultats. Merci aussi à Anne Bessette et Gaston Dominguez pour leur contribution aux mesures expérimentales.

3 séjours au Japon auront rythmé cette thèse et constituent pour de nombreuses raisons l'expérience la plus marquante de ces dernières années, d'un point de vue professionnel, et évidemment personnel. S'il n'est pas possible d'en rendre compte dans ces lignes, je tiens au moins à en remercier les différents acteurs. D'abord, Benoît Camenen, comme initiateur de ces relations franco-japonaises, qui s'est pleinement impliqué dans ce projet et m'a de plus introduit dans le petit cercle de l'Ujigawa Open Laboratory. Ensuite, les professeurs Hajime Nakagawa et Kenji Kawaike pour m'avoir accueilli dans d'excellentes conditions de travail, investissant des moyens considérables dans la maquette expérimentale et me laissant une grande liberté dans mes recherches. Un grand merci à la secrétaire du laboratoire, Natsuyo Sugimura, pour avoir facilité le quotidien dans ce pays malheureusement peu anglophone. Enfin, je remercie la Japan Society for the Promotion of Science (JSPS[1]) et la Région Rhône-Alpes[2], qui ont financé - et par là rendu possibles - ces différents séjours.

Je remercie les deux rapporteurs de cette thèse, Slobodan Djordjevic et Robert Mosé pour avoir pris le temps de relire ce manuscrit et être venu en discuter pendant la soutenance. Je remercie au passage les autres membres du jury pour leur participation à cette dernière, qui restera une belle validation dynamique de ces travaux !

Il y a ça de génial dans « la recherche », c'est que les discussions spontanées, les échanges et l'entraide sont naturelles, et que l'altruisme n'a pas encore tout à fait fui devant le productivisme. Ainsi ces trois ans de thèse ont été l'occasion de profiter de nombreuses discussions enrichissantes, qu'elles contribuent effectivement à cette thèse, ou simplement à

[1] Bourse n°PE12501 du JSPS Postdoctoral Fellowship (Short-term)
[2] Bourse Explora Doc n° 11 015439 01

ma culture personnelle. Je rends hommage ici à cet état d'esprit fabuleux, particulièrement présent au sein de l'équipe Hydrologie-Hydraulique et plus généralement au sein du groupement Irstea de Lyon-Villeurbanne. Je remercie donc les chercheurs qui participent de cet état d'esprit (et qui j'espère se reconnaîtront), ainsi que les collègues des « fonctions support » du centre qui m'ont aidé sur d'autres aspects du travail de thèse, avec un professionnalisme et une bonne humeur toujours appréciés. Si je ne devais citer qu'un nom, je pense évidemment à Yves Confesson, qui a toujours su se montrer à l'écoute et n'a pas hésité à ouvrir la porte de son bureau lorsqu'il en avait envie…

La vie de rat de laboratoire (ou petit scarabée au Japon) peut sembler un peu ennuyeuse aux premiers abords. Ce serait sans compter les moments passés avec les autres animaux de la ménagerie : fouines, belettes, chacals, raton-laveurs, goupils, orangs-outans et autres… A ces animaux d'excellente compagnie, j'adresse de chaleureux remerciements, pour leur soutien, et simplement pour leur amitié au long de ces trois ans. Pika Pika.

Enfin, un grand merci à Cécile, qui a partagé les hauts et les bas de cette vie de thésard et m'a supporté du début jusqu'à la fin.

Résumé

ECOULEMENTS LORS D'INONDATIONS EN MILIEU URBAIN : INFLUENCE DE LA TOPOGRAPHIE DETAILLEE ET DES ECHANGES AVEC LE RESEAU D'ASSAINISSEMENT

Le but de cette thèse est d'étudier la modélisation détaillée des écoulements qui ont lieu lors des inondations urbaines.

Dans une première partie, des écoulements en bifurcation incluant des petits obstacles génériques ou des profils de canaux avec trottoirs sont étudiés sur une maquette expérimentale, puis simulés numériquement avec le modèle bidimensionnel Rubar20. Les résultats expérimentaux et numériques montrent l'avantage d'inclure des obstacles de petite taille dans un modèle d'inondation urbaine, alors qu'il n'y a qu'un intérêt limité à utiliser une topographie détaillée des rues.

Dans une deuxième partie, les interactions entre écoulements de surface et écoulements en conduites souterraines sont étudiées. Un modèle physique de système de drainage urbain permet de valider un modèle analytique prédisant les débits d'échange entre les deux couches d'écoulement. Une modélisation 1D/2D (conduite/rue) est mise en place avec les modèles Rubar3/Rubar20 et validée sur des écoulements expérimentaux observés sur le modèle physique.

Dans une troisième partie, les inondations dans la ville d'Oullins (près de Lyon, France) sont étudiées. La modélisation des écoulements de surface est validée avec des données de terrain, et nous discutons l'intérêt de plusieurs représentations du milieu urbain. L'intégration du réseau d'assainissement dans un modèle 1D/2D reste affectée par plusieurs incertitudes, mais cette étape montre l'intérêt de la modélisation couplée pour décrire les interactions complexes des écoulements lors d'inondations urbaines, ainsi que les limites de l'approche développée pour les écoulements à faible profondeur.

Mots clés: inondation urbaine, modèle physique, simulation numérique, obstacle, topographie détaillée, modélisation couplée du drainage, Oullins

La thèse a été préparée au centre de Lyon-Villeurbanne de l'Institut national de Recherche en Sciences et Technologies pour l'Environnement et l'Agriculture :

Irstea – centre de Lyon Villeurbanne

5, rue de la Doua

CS70077

69626 Villeurbanne cedex

Adresse des autres laboratoires d'accueil :

Laboratoire de Mécanique des Fluides et Acoustique:

LMFA – UMR 5509

Bâtiment Jacquard, 20 avenue A. Enstein

69621 Villeurbanne cedex

Disaster Prevention Research Unit :

DPRI, Kyoto University

Shimomisu, Yoko-oji, Fushimi-ku

612-8235 Kyoto

JAPON

Abstract

FLOWS DURING FLOODS IN URBAN AREAS: INFLUENCE OF THE DETAILED TOPOGRAPHY AND EXCHANGES WITH THE SEWER SYSTEM

Aim of this thesis is to study the detailed modelling of flows that occur during urban floods.

In a first part, bifurcation flows including small obstacles or channel profiles with sidewalks are studied on an experimental facility, and then numerically simulated with the two-dimensional model Rubar20. Experimental and numerical results show the benefits of including small obstacles in an urban flood model, whereas there is only little benefit of using a detailed representation of the streets topography.

In a second part, interactions between surface and underground pipe flows are studied. A physical model of an urban drainage system allows the validation of an analytical model predicting exchange discharges between both flow layers. A 1D/2D modelling (pipe/street) is set up with the models Rubar3/Rubar20 and validated on experimental flows observed on the physical model.

In a third part, floods in the city of Oullins (near Lyon, France) are studied. Surface flows modelling is validated with field data, and we discuss the interest of several representations of the urban area. Integration of the sewer system in a 1D/2D model remains impacted by several uncertainties, yet this step shows the interest of the coupled modelling to describe complex flows interactions during urban floods, as well as limitations of the developed approach for shallow flows.

Keywords: urban flood, physical model, numerical simulation, obstacle, detailed topography, dual drainage modelling, Oullins

Résumé étendu

Contexte

Les inondations constituent un risque naturel important. L'agence européenne de l'environnement estime que ces dernières ont engendré la mort de 1126 personnes entre 1998 et 2009, ainsi que 52 milliards d'euros de dégâts dans la même période (EEA 2010). Les inondations affectent particulièrement les zones urbaines. Premièrement, les zones urbaines concentrent la plupart des enjeux (population, activité économique, patrimoine, réseau de transport), et sont donc bien plus vulnérables aux aléas d'inondation que les zones naturelles. Ensuite, les écoulements de surface lors des inondations en milieu urbain sont bloqués par la présence de bâtiments et autres éléments imperméables, ce qui conduit à une concentration des écoulements dans les rues, avec des vitesses accrues. Enfin, l'imperméabilisation des sols génère des ruissellements plus rapides et plus importants sur les bassins versants urbanisés, engendrant un risque d'inondation supplémentaire dans le cas où le système de drainage urbain est défaillant. Pour ces raisons, l'aléa d'inondation doit être particulièrement bien connu dans les zones urbaines, et cet objectif est généralement atteint par l'utilisation de modèles numériques.

La littérature scientifique présente un nombre important de modèles numériques d'inondation urbaine, qui se distinguent notamment par leur niveau de complexité. Ainsi, les écoulements peuvent être modélisés de façon directe et détaillée en utilisant des codes de calculs hydrauliques résolvant les équations complètes de Saint-Venant en deux dimensions (voir par example Mignot et al. 2006; Gallegos et al. 2009). Cette approche aboutit à des résultats corrects mais les temps de calculs requis empêchent son utilisation pour des applications telles que l'analyse d'incertitude ou la prévision en temps réel. Une simplification classique des équations de Saint-Venant consiste à négliger les termes inertiels (Aronica et al. 2005; Yu and Lane 2006). D'autres concepts propres au milieu urbain ont été développés pour accroitre l'efficacité des modèles, comme la représentation de façon statistique des bâtiments (Guinot and Soares-Frazao 2006), l'inclusion de détails topographiques à une échelle plus fine que celle du maillage utilisé (Yu and Lane 2011), l'adaptation des mailles de calcul à des zones topographiques (Jamieson et al. 2012), ou la considération implicite de l'effet bloquant des bâtiments (Chen et al. 2012). A l'inverse, une partie de la recherche complexifie les approches, avec des validations de modèles numériques

sur des cas expérimentaux de plus en plus précis (Mignot et al. 2008; Van Emelen et al. 2012), ou la considération de plusieurs couches d'écoulements dans la zone urbaine (surface / réseau d'assainissement, voir Djordjevic et al. 2005; Vojinovic and Tutulic 2009). Ces deux approches (détaillée/simplifiée) sont complémentaires et peuvent être attribuées au nécessaire équilibre entre la complexité des écoulements et leur impact (Xia et al. 2011), et le caractère opérationnel de ce sujet de recherche (Aronica et al. 2012).

Objectifs de la thèse

La thèse s'intéresse à la modélisation détaillée des écoulements lors des inondations en milieu urbain. L'état de l'art montre que la structure primaire des villes vis-à-vis des écoulements est bien comprise (alternance de rues et de bâtiments), avec plusieurs options de modélisation validées dans la littérature. En revanche, un certain nombre de phénomènes *a priori* secondaires restent peu étudiés, notamment car la rareté des inondations et des données de terrain empêche une évaluation objective. La thèse se propose de répondre aux questions suivantes :

- Quel est l'impact d'obstacles de petite taille sur les écoulements de surface et peut-on le représenter dans un modèle d'inondation urbaine?
- Quelle précision dans la topographie des rues faut-il considérer et quelles sont les possibilités de simplification?
- Comment modéliser les échanges entre les écoulements dans les rues et dans les conduites souterraines?

La thèse s'articule autour de trois parties :

- Une étude expérimentale et numérique sur l'effet des obstacles et des trottoirs sur les écoulements dans une bifurcation à 3 branches
- Une étude expérimentale et numérique des interactions entre les écoulements de surface et ceux d'une conduite de drainage lors d'une inondation
- Une étude numérique d'un cas réel, appuyée par des données de terrain

Par la suite, on présente les résultats scientifiques de chacune de ces parties, puis une conclusion générale qui résume les différents éléments de réponse aux trois questions énoncées.

Influence d'obstacles et de trottoirs sur les écoulements dans une bifurcation à 3 branches

Les écoulements dans des modèles réduits de carrefour (i.e. écoulements en jonctions et bifurcations) ont été particulièrement bien étudiés vis-à-vis de la problématique des inondations en milieu urbain (voir par exemple Mignot et al. 2008; Ghostine et al. 2010). Ces écoulements sont de plus bien renseignés dans la littérature car ils correspondent à des cas typiques d'ingénierie hydraulique, comme les réseaux de canaux. Le but ici est de perturber ce genre d'écoulements de référence en introduisant des obstacles ou des trottoirs, et d'envisager des configurations plus complexes qui peuvent se produire lors d'une inondation en milieu urbain. Le plan expérimental vise à la fois à apporter des indicateurs globaux sur l'impact des obstacles pour un nombre important de configurations, et à affiner les mesures pour pouvoir appuyer les hypothèses sur les mécanismes en jeu.

Mesures expérimentales de l'impact des obstacles

Une maquette du Laboratoire de Mécanique des Fluides et Acoustique (LMFA, INSA de Lyon) a été utilisée pour observer expérimentalement l'impact d'obstacles sur les écoulements à travers un carrefour urbain. La maquette est constituée de trois canaux en verre (2 m de long, 30 cm de largeur, 20 cm de hauteur) horizontaux qui se joignent perpendiculairement (Figure 2.3 p.18). L'alimentation des canaux est dite en « bifurcation », avec un canal amont, un latéral et un aval. L'écoulement général consiste donc en un écoulement dans le canal amont (alimenté à débit constant) qui se divise au niveau de la jonction en deux écoulements vers les canaux latéral et aval. Un seuil mince réglable est installé dans ces deux derniers canaux pour contrôler les conditions d'écoulement à l'aval. Au final, les écoulements sont contrôlés par 3 paramètres expérimentaux : le débit dans la branche amont et la hauteur des seuils dans les branches latérale et aval. Deux débitmètres électromagnétiques sont installés dans la boucle de pompage et mesurent le débit dans les branches amont et latérale (celui dans la branche aval est alors connu par conservation de la masse). Un pied à coulisse digital est utilisé pour mesurer manuellement les hauteurs d'eau. Un système de PIV (Particle Image Velocimetry) est mis en place pour mesurer des champs de vitesses dans des plans horizontaux.

Après une analyse dimensionnelle, il ressort que l'écoulement initial (i.e. sans obstacles, dénoté avec un « 0 ») peut être défini par les 3 paramètres adimensionnels suivants :

- Le nombre de Froude dans la branche amont F_{u0}
- La répartition de débit initiale R_{q0} (part du débit de la branche amont qui rejoint la branche latérale)
- La hauteur d'eau dans le canal amont normalisée par la largeur du canal h_{u0} /b

14 écoulements initiaux sont définis et regroupés en 3 séries afin de pouvoir faire une étude paramétrique : pour chaque série, un des paramètres définis ci-dessus varie alors que les 2 autres restent fixés (valeurs de référence : F_{u0}=0.45, Rq_0=0.39, h_{u0}/b=0.15).

Les obstacles sont des parallélépipèdes à base carrée de 5 cm de côté et suffisamment haut (15 cm) pour ne jamais être submergé. Leur taille (largeur égale à 1/6 de la largeur des canaux) permet de représenter des éléments de mobilier urbains (abris bus, kiosques…). Au total, 9 configurations sont étudiées :

- 7 configurations avec un seul obstacle qui permettent de couvrir différentes zones d'intérêt autour de la bifurcation (2 emplacements d'obstacle définis dans chaque branche, et un emplacement pris comme le point central de la bifurcation)
- 2 configurations avec 2 obstacles reprenant les emplacements des configurations précédentes

Pour l'ensemble des couples écoulement/obstacles (14 écoulements, 9+1 configurations d'obstacle), on mesure une hauteur d'eau et le débit dans chaque branche. On étudie alors l'évolution de la répartition de débit dans la branche latérale entre une configuration sans obstacle (initiale) et une configuration avec obstacle, qui permet de caractériser l'effet global de l'obstacle. Les mesures de vitesse par PIV sont limitées à un écoulement et quelques configurations d'obstacle, pour servir de base à l'analyse.

Analyse de l'impact des obstacles

Pour l'ensemble couples écoulements/obstacles, la répartition de débit peut évoluer entre -12% et +8% par rapport à celle des écoulements initiaux, ce qui est significatif. L'analyse des données PIV et de résultats de simulations numériques préliminaires montre que la plupart des effets des obstacles peut être expliqué simplement (pour une vision synthétique voir l'ensemble des mesures *Exp* sur la Figure 3.9 p.56). :

- Les obstacles de la branche amont accélèrent l'écoulement dans la branche amont et à l'entrée de la jonction. Cette accélération diminue la capacité de l'écoulement à tourner vers la branche latérale et tend donc à augmenter le débit dans la branche aval.
- Les obstacles dans la branche latérale (respectivement aval) bloquent l'écoulement dans cette branche et le renvoient en partie dans la branche aval (respectivement latérale).
- L'obstacle dans la bifurcation renvoie l'écoulement amont dans l'une des deux branches aval ou latérale selon sa position vis-à-vis de la ligne de séparation initiale des écoulements
- L'effet de deux obstacles combinés sur la répartition de débit se résume assez bien à la somme des effets singuliers de chaque obstacle pris séparément

Ces processus affectent toutefois les écoulements avec des intensités très variables et sont sensibles à au moins deux des paramètres étudiés. Le paramètre d'écoulement le plus influent est le nombre de Froude dans la branche amont Plus celui-ci est important, plus l'inertie de l'écoulement est grande au droit de chaque obstacle, et plus l'effet des obstacles est marqué (l'évolution de la répartition de débit est plus forte, mais le mécanisme d'action reste le même). L'influence de la répartition de débit initiale est plus complexe. En particulier ce paramètre définit la structure générale de l'écoulement à travers la bifurcation, notamment la ligne de séparation des écoulements dans la jonction, et la forme de la zone de recirculation dans la branche latérale. Cette structure initiale de l'écoulement permet de comprendre les évolutions observées, en analysant les positions respectives des obstacles amont ou de la bifurcation par rapport à la ligne de séparation, ou la position d'un obstacle de la branche latérale vis-à-vis de la zone de recirculation. L'impact de la hauteur d'eau normalisée sur l'évolution de la répartition de débit est insignifiant pour tous les obstacles sauf un, pour lequel une légère tendance est observée. Des simulations numériques à l'aide d'un modèle 3D réalisées par la Hong Kong Polytechnic University (Mignot et al. 2013) suggèrent que la tendance observée peut venir de la modification du sillage derrière l'obstacle en question, mais une interprétation détaillée reste hasardeuse sans autres preuves expérimentales.

Simulations numériques

La simulation numérique de l'ensemble des écoulements expérimentaux (initiaux et avec obstacles) est conduite à l'aide du code de calcul Rubar20, qui résout les équations de

Saint-Venant bidimensionnelles avec un schéma explicite en volumes finis. On vise ici deux objectifs :

- Une modélisation fine des écoulements expérimentaux pour évaluer les capacités maximales du code (maillage fin avec des éléments de 0.5 cm de côté, calage d'un coefficient de diffusion)
- Une modélisation plus grossière, qui prend en compte les contraintes opérationnelles et permet de discuter de la faisabilité sur un cas réel (maillage grossier à 5 cm, pas de diffusion)

Le modèle numérique est d'abord utilisé pour simuler les écoulements initiaux. Les résultats montrent que l'incertitude liée à la modélisation des frottements est négligeable, alors que le choix du coefficient de diffusion est important pour retrouver une bonne structure d'écoulement dans la branche latérale (zone de recirculation). D'un point de vue plus global, la répartition de débit initiale - qui est une valeur clé pour cette étude - est correctement simulée et peu influencée par ces paramètres.

La simulation des écoulements avec obstacles tient compte de ces premiers résultats, avec une attention particulière portée sur le coefficient de diffusion. Vu le nombre de cas (14 écoulements x 9 obstacles = 126) on analyse d'abord de façon statistique l'influence du coefficient de diffusion et de la taille du maillage sur deux valeurs clés : l'évolution de la répartition de débit ΔRq et celle de la hauteur d'eau dans le canal amont Δh_u après introduction d'un obstacle. D'une façon générale, ces évolutions sont bien prédites, et les erreurs observées sont principalement attribuées à la modélisation des obstacles amont (Figure 3.8 p.54). Le maillage fin est sensible au coefficient de diffusion et une valeur calée permet une meilleure prédiction de la répartition de débit (calage entre les runs 2 et 4 sur la même figure), avec notamment une baisse significative de la surestimation de l'effet des obstacles par le modèle numérique. Le modèle avec un maillage grossier tend lui à sous-estimer l'impact des obstacles sur la répartition de débit, et reste peu sensible à la valeur du coefficient de diffusion (runs 8 et 9 sur la même figure). L'évolution de la hauteur d'eau dans la branche amont est bien prédite, et reste moins sensible au coefficient de diffusion ou à la densité du maillage.

Le coefficient de diffusion impacte fortement le champ de vitesse calculé autour des obstacles pour le maillage fin, notamment dans le sillage (voir les runs 1, 2 et 4 sur la Figure 3.10 p.57). La difficulté accrue de modélisation pour les obstacles amont résulte de ce fait, puisque le sillage ou le champ proche de ces obstacles peut agir sur la séparation des

écoulements dans la jonction. Le fait que l'on considère un coefficient de diffusion constant implique à la fois un calage arbitraire, et fixe aussi une limite à la qualité de prédiction du modèle une fois calé. Il est probable que certaines erreurs pourraient être corrigées par l'utilisation d'un modèle de turbulence plus complet, voire un maillage plus fin. La moindre sensibilité au coefficient de diffusion pour le maillage grossier s'explique de fait par la forte diffusion numérique associée à ce maillage, dont les mailles ont des dimensions comparables à celles des obstacles.

Au final, l'erreur caractéristique sur la répartition de débit est de 1.17% pour le modèle fin non calé (diffusion nulle) et tombe à 0.83 % après calage (Table 3.2 p.53). Le résultat le plus intéressant concerne probablement les simulations faites avec un maillage grossier et sans diffusion, ou l'erreur reste à 1.15%. Ce dernier cas montre tout l'intérêt qu'il y a à considérer les obstacles de taille équivalente (1/6 de la largeur d'une rue) dans un modèle d'inondation urbaine.

Cas des trottoirs

En plus des obstacles, une configuration de trottoirs a été étudiée, en installant des planches de bois de 2 x 6 cm au pied de toutes les parois verticales des canaux, afin de créer une section en travers de rue caractéristique. L'ajout de ces trottoirs diminue la section d'écoulement et accélère l'écoulement dans les canaux les conditions aux limites restant identiques). L'inertie accrue de l'écoulement amont limite sa capacité à tourner dans la branche latérale, de sorte qu'on observe systématiquement une déviation vers la branche aval. Cet effet est d'autant plus important que la hauteur d'eau à l'amont est faible, que le nombre de Froude amont est fort et que la répartition de débit initiale est forte. L'effet de la hauteur d'eau est intuitif puisque le trottoir modifie d'autant plus l'écoulement que la section d'écoulement initiale est faible. L'effet des deux autres paramètres reste difficile à expliquer avec certitude en l'absence de données supplémentaires.

La modélisation numérique de ces écoulements avec trottoirs est réalisée avec Rubar20. Les simulations sont notamment faites en considérant deux représentations de la topographie des canaux (Figure 3.11 p.58):

- Un modèle *Ref*, où la topographie dans le modèle numérique est la plus proche possible de celle du modèle expérimental (claire identification des rehausses du fond au niveau des trottoirs)

- Un modèle *Avg*, où la cote du fond des canaux est modélisée par une cote constante et égale à la surélévation moyenne du fond due à la présence des trottoirs

Les deux modèles prédisent des évolutions similaires de la répartition de débit. Ces évolutions prédites sont de plus en bon accord avec les mesures, sauf dans deux cas : pour une valeur critique du nombre de Froude amont qui fait apparaître un changement de régime à l'entrée de la jonction, et pour une très faible hauteur d'eau. Ces deux exceptions restent des cas « extrêmes », avec d'un côté des problèmes liés aux calculs des ressaut hydrauliques qui peuvent engendrer des erreurs importantes (Mignot et al. 2008), et de l'autre des hauteurs d'eau de quelques millimètres sur les trottoirs, hors des hypothèses d'applicabilité du modèle et avec des erreurs importantes associée à la condition aval. Dans tous les cas, il est remarquable de voir que la considération de la topographie détaillée des trottoirs n'apporte aucun bénéfice à l'échelle du carrefour (répartitions de débit identiques entre les modèles *Ref* et *Avg*), même si elle permet de simuler des hauteur d'eau et des vitesses locales plus réalistes. Ainsi, dans le cas d'un régime fluvial, la prise en compte de la vitesse moyenne dans chaque rue est suffisante pour prédire la répartition de débit au sein des carrefours. C'est aussi une condition nécessaire, qui signifie que pour de tels régimes d'écoulement il est important de ne pas avoir de biais dans la topographie.

Interactions entre les écoulements d'une rue et d'une conduite souterraine

La description fine des écoulements lors d'inondations urbaines ou l'étude des systèmes de drainage urbains nécessite de considérer les écoulements à la fois dans la rue et dans les conduites de drainage souterraines. Ceci passe par une bonne description des échanges entre les deux couches d'écoulements, ainsi que la mise en place d'un système de modélisation couplée qui permet de simuler les deux types d'écoulement simultanément. Ces deux points ont été réalisés, notamment sur la base de données expérimentales produites sur la maquette de système de drainage urbain du Disaster Prevention Research Institute (DPRI, Université de Kyoto, Japon). La modélisation couplée est basée sur un couplage de deux codes de calculs d'IRSTEA et l'application présentée ici est une première. L'étude des échanges vise particulièrement les cas où l'inondation dans les rues est significative, cas assez peu traité dans la littérature scientifique. En effet, la plupart des études sur ce sujet concernent l'efficacité des avaloirs pour des écoulements de surface peu profonds (Despotovic et al.

2005; Gomez et al. 2011), qui ne constituent qu'une partie des écoulements rencontrés lors d'une inondation urbaine. De par sa nature fortement tridimensionnelle, l'écoulement d'échange entre une rue et une conduite de drainage n'est généralement pas modélisé avec un modèle hydrodynamique, et l'interaction des écoulements entre les deux couches se résume au calcul du débit d'échange (par la suite on appelle modèle d'échange le modèle qui permet d'évaluer ce débit).

Présentation de la maquette et des mesures

La maquette utilisée (Figure 4.3 p.71) représente une rue horizontale de 10 m x 0.5 m longée en continu par deux trottoirs (2 cm x 15 cm), et drainée par une conduite située environ 25 cm en dessous (5 cm de diamètre, pente 1/900). La connexion entre les deux entités est assurée par 10 couples d'avaloirs (grille carrée de 5 cm de côté) répartis le long des trottoirs, eux même connectés à la conduite principale par l'intermédiaire d'un compartiment et d'un tuyau de drainage. On dénomme par la suite « structure d'échange » l'ensemble avaloirs-compartiment-tuyau. La rue et la conduite sont alimentées en débit par deux boucles indépendantes. La condition d'écoulement à l'aval de la rue peut être libre ou modifiée par un seuil épais. La pression dans la conduite à l'aval est fixée via l'intermédiaire d'un réservoir et d'un seuil réglable. La définition de ces 4 conditions aux limites permet de générer différents types d'interactions, allant d'un drainage complet de la rue par la conduite à un débordement de cette dernière dans la rue (surcharge).

Les mesures réalisées ont pour but de comprendre comment sont régis les échanges entre la rue et la conduite, et de fournir un jeu de données pour valider une modélisation hydrodynamique complète des écoulements. L'instrumentation utilisée comprend une sonde à ultrasons montée sur un chariot glissant pour mesurer les hauteurs d'eau, 11 piézomètres sur la conduite, deux débitmètres électromagnétiques et deux seuils en V mesurant respectivement les débits entrant et sortant dans la rue et la conduite, et finalement une caméra pour mesurer les vitesses de surface par LSPIV (Large Scale PIV). Trois grandes séries de mesures sont effectuées :

- Des drainages de la rue par un seul couple d'avaloirs en régime permanent, les autres étant volontairement bloqués
- Des cas de drainage et de débordement en régime permanent à l'échelle de la rue avec tous les avaloirs qui fonctionnent

- Des écoulements similaires à cette dernière série mais en transitoire

Afin d'éviter des problèmes liés à la capillarité ou aux rugosités de fond, les écoulements de surface ont toujours une profondeur d'au moins 1 cm. Ceci implique deux phénomènes importants qui fixent le cadre de l'étude :

- Les avaloirs sont toujours submergés, de sorte qu'ils ne contrôlent pas *a priori* les échanges, et que l'écoulement dans la structure d'échange est en charge
- Les hauteurs d'eau locales autour des avaloirs ne sont pas significativement affectées par les échanges, et par la suite la hauteur d'eau dans la rue est moyennée transversalement et on considère une ligne d'eau le long de l'axe de l'écoulement.

Développement d'un modèle d'échange

Nous partons de l'hypothèse que le débit d'échange entre la rue et la conduite est contrôlé par la différence de charge entre les deux couches d'écoulements (rue/conduite). En appliquant le principe de Bernouilli, la différence de charge entre les deux écoulements de part et d'autre de la structure d'échange est exprimée comme la somme des pertes de charge locales subies par l'écoulement à travers la structure d'échange. La simplicité de la géométrie de cette structure permet d'exprimer ces termes de perte de charge de façon précise à l'aide d'ouvrages de référence (Miller 1978; Idelchik and Steinberg 1996), en prenant en compte les paramètres géométriques, la rugosité ou bien l'effet du nombre de Reynolds. Au final, le modèle d'échange analytique ainsi construit permet de relier une différence de charge totale à un débit d'échange.

Le modèle est testé sur deux jeux de données expérimentaux, en considérant les écoulements limités à un couple d'avaloir ou fonctionnant avec tous les couples d'avaloir. Le principe de la validation consiste à appliquer le modèle d'échange aux différences de charge mesurées expérimentalement pour prédire les débits d'échange et les comparer à ceux mesurés. La prédiction de ces débits d'échange est tout à fait correcte pour les cas de drainage, mais il y a des erreurs plus importantes pour les débits de débordements (Figure 4.8 p.84). Les écoulements d'échange en drainage et en débordement ne sont pas équivalents, de sorte qu'un terme de perte de charge en cas de débordement est probablement mal évalué. Des mesures plus précises seraient requises pour confirmer cette hypothèse (ce qui nécessiterait de travailler à une échelle plus grande). Cela dit, la capacité de prédiction du modèle d'échange reste correcte, ce qui montre l'intérêt de la démarche et valide l'utilisation de ce modèle au

sein d'une modélisation hydrodynamique complète. Une tentative de ramener le modèle d'échange à une équation simple du type orifice (largement utilisée pour les études de cas réels) est proposée, en calculant un coefficient de débit équivalent. L'analyse conjointe des mesures expérimentales et des résultats détaillés du modèle d'échange montre que ce coefficient varie d'un écoulement à l'autre, d'où une difficulté de suivre cette démarche de simplification pour la maquette expérimentale. Ceci est expliqué par la dépendance de certains termes de perte de charge aux nombres de Reynolds locaux dans la structure d'échange ou au débit dans la conduite principale.

Ce modèle d'échange est ensuite extrapolé pour pouvoir être utilisé dans un cas réel. En plus du cas où le drainage se fait à travers un écoulement contrôlé par l'ensemble de la structure d'échange (cas expérimental), nous ajoutons deux sections de contrôle, d'après l'idée de Leandro et al. (2007). La première consiste en un écoulement de seuil sur le périmètre de l'avaloir, la deuxième en un écoulement de type orifice appliqué à l'embouchure supérieure de la conduite raccordant l'avaloir à la conduite principale (ou à un trou d'homme selon le cas réel considéré). Les débordements sont calculés de la même façon que pour la maquette expérimentale. Il apparaît que la mise à l'échelle augmente significativement les nombres de Reynolds dans la structure d'échange « réelle », ce qui permet de ramener une partie du modèle d'échange à l'utilisation d'une loi d'orifice, pourvu que le coefficient de débit soit correctement estimé (d'après la méthode validée sur l'expérience). Ceci permet une estimation plus rigoureuse des débits d'échange, sans trop alourdir son calcul au sein d'un modèle hydrodynamique couplé rue/conduite. Enfin, l'ajout de section de contrôle influe sur le débit d'échange principalement lorsque les hauteurs d'eau dans la rue sont faibles, typiquement plus petites que 10 cm pour un cas réel. La justesse du modèle d'échange ainsi extrapolé et complété ne peut pas être étudiée, mais au vu de la littérature et de la validation de la méthode sur le cas expérimental le modèle d'échange doit pouvoir rendre compte des principaux phénomènes pour un cas réel.

Validation d'un modèle couplé 1D/2D

Les simulations hydrodynamiques des écoulements expérimentaux de la maquette du système de drainage urbain sont réalisées à l'aide d'un couplage des codes de calcul hydrauliques Rubar3 (1D, conduite) et Rubar20 (2D, rue), avec une intégration du modèle d'échange développé spécifiquement pour la maquette. La validation préliminaire du modèle d'échange et le paramétrage optimal du modèle numérique (loi de frottement empirique pour

la conduite) permet d'atteindre une très bonne adéquation entre les résultats de simulations et les mesures expérimentales. Pour les écoulements permanents, les niveaux d'eau dans la rue et les pressions dans la conduite convergent correctement vers les mesures, ainsi que les débits d'échange qui en découlent. Les erreurs sont de l'ordre de quelques %, et sont attribuées en partie à de légers biais du modèle d'échange. Pour les écoulements en transitoire, l'adéquation reste globalement satisfaisante, avec cependant quelques erreurs provenant de l'existence de très faibles hauteurs d'eau pour des cas où l'écoulement consiste en une vague d'inondation se propageant sur une rue initialement vide (Figure 5.5 p.109). Hormis ce cas, la dynamique des écoulements en transitoire est bien simulée, avec notamment des passages de situation de drainage à débordement de la conduite, qui valide l'utilisation du modèle 1D/2D pour un cas de terrain.

D'un point de vue plus détaillé, une limite de ce modèle couplé vient de con incapacité à rendre compte de l'effet du processus d'échange sur l'écoulement de surface, caractérisé expérimentalement par une déformation locale du champ de vitesse (Figure 5.3 p.105). Ce processus est par nature fortement tridimensionnel, et aucun jeu de paramètre testé n'aboutit à une meilleure représentation par le modèle numérique. Cette erreur dans le calcul du champ de vitesse n'a aucun impact global dans la simulation des écoulements expérimentaux, mais illustre bien la limite de l'approche utilisée.

L'ensemble des écoulements ont été simulés à nouveau en utilisant une représentation simplifiée de la topographie de la rue, en spécifiant la cote moyenne du fond de la rue sur tout le domaine (modèle *Avg*, voir Figure 5.6 p.111), plutôt qu'une représentation détaillée des trottoirs. Cette représentation simplifiée conduit à une surestimation systématique du niveau d'eau dans la rue. Cette erreur est évidemment d'autant plus importante que le niveau d'eau dans la rue est bas, est devient particulièrement grande dans le cas des vagues d'inondation sur la rue initialement vide. Cependant, l'impact sur les échanges est modéré, voire imperceptible selon les cas. En effet, les échanges pour les écoulements expérimentaux sont contrôlés par la différence de charge entre la rue et la conduite au niveau des structures d'échange. Cette différence de charge est dans la grande majorité des cas plus importante (un ordre de grandeur) que les erreurs de calcul sur la hauteur d'eau dans la rue engendrées par des simplifications de la topographie. Dans le cas où les débits d'échange sont contrôlés par les caractéristiques des écoulements dans la rue uniquement (non étudié expérimentalement), les possibilités de simplification de la topographie doivent être plus réduites.

Modélisation des inondations à Oullins

Problématique et présentation du site

Oullins est une ville située en bordure de l'Yzeron, une rivière qui draine un bassin versant péri-urbain de 130 km^2 près de Lyon, avant de rejoindre le Rhône. Pendant la dernière décennie, les crues de l'Yzeron ont engendré à 4 reprises des inondations à l'aval du bassin versant, notamment dans une partie du centre-ville d'Oullins (en 2003, 2005, 2008 et 2009). La récurrence de ce type d'évènement est attribuée en partie à l'urbanisation croissante qu'a connue le bassin versant dans la seconde moitié du $20^{ème}$ siècle (Breil et al. 2010). Les données historiques montrent que les zones inondées se situent principalement en rive droite d'une boucle de la rivière, et que l'extension spatiale des inondations pour ces événements est contrôlée par la topographie du lit majeur.

En plus de ces inondations d'origine fluviale, la ville d'Oullins est régulièrement affectée par des débordements du réseau d'assainissement, majoritairement unitaire sur la zone. Etant donné la position d'Oullins sur le bassin versant, le réseau d'assainissement dans la ville a une structure particulière :

- Deux collecteurs sont installés de part et d'autre de la rivière, dans des zones de faibles pentes. Un collecteur principal draine une grande partie des zones urbaines du bassin versant de l'Yzeron, et traverse Oullins en rive gauche de la rivière. Un collecteur secondaire draine un bassin versant urbain plus petit à l'amont de la zone et traverse Oullins en rive droite, au-dessous des zones inondées par la rivière. Une connexion entre les deux collecteurs est installée sous le lit mineur de la rivière pour permettre au collecteur secondaire de se décharger dans le collecteur principal au-delà d'un débit critique.
- Des conduites de plus faible capacité drainent les zones urbaines au sud de la zone inondée ainsi que le centre-ville ; elles sont connectées au collecteur secondaire.

Enfin il faut noter la présence de plusieurs déversoirs d'orage sur la zone (5 dans la zone étudiée), qui permettent au réseau de déborder dans la rivière en cas de surcharge. La particularité de ce réseau vient d'une part de sa forte hétérogénéité, et d'autre part des écoulements complexes qu'il peut engendrer : drainage des zones inondées par la rivière, débordement du réseau dans les rues ou dans la rivière, échanges entre les deux collecteurs.

La modélisation de ces écoulements est effectuée en 3 étapes. D'abord seuls les écoulements de surface sont modélisés (modèle 2D), en négligeant totalement les interactions avec le réseau. Ensuite, le processus de drainage est représenté dans le modèle de surface, mais sans considération du réseau d'assainissement. Enfin, le réseau d'assainissement est ajouté pour aboutir à une modélisation du type 1D/2D. Le but de cette démarche est de pouvoir identifier à chaque étape les éléments importants de la modélisation, et éventuellement recourir à des simplifications pour alléger le traitement de l'étape suivante.

Ecoulements de surface

L'ensemble des écoulements de surface (lit mineur de la rivière et lit majeur urbanisé) est modélisé avec le modèle 2D Rubar20. Un soin particulier est apporté à la représentation du milieu urbain, et plusieurs simulations sont réalisées, en faisant intervenir les différents niveaux de complexité ou paramètres suivants :

- Représentation ou non des éléments structurels comme les bâtiments (emplacement donnés par le Grand Lyon), murs et barrières (relevés sur le terrain), voire considération du réseau de rues uniquement
- Représentation détaillée de la topographie des rues (d'après des levés topographiques des profils en travers) ou simplifiée (cote moyenne sur les profils)
- Valeurs du frottement pour la rivière, les rues ou les zones bâties
- Finesse du maillage

La simulation de la crue de 2008 avec le modèle le plus fin prédit avec une précision de l'ordre de 10-15 cm les niveaux d'eau maximaux mesurés dans les zones inondées. L'analyse attentive de ces résultats révèle cependant un biais dans le modèle. Notamment, la confrontation avec des cotes enregistrées en 3 points dans la rivière (Figure 6.15 p.138) montre que le modèle sous-estime les niveaux d'eau dans la partie centrale des inondations, alors qu'ils sont raisonnablement bien modélisés ailleurs (i.e. zones à l'amont et à l'aval). Ce biais est confirmé par les laisses de crue, ainsi que par la modélisation de la crue de 2009. Cette dernière étant faiblement débordante, l'erreur est associée à la modélisation des écoulements dans la rivière, et non pas de ceux dans la zone urbaine. Plusieurs tentatives d'amélioration du modèle en calant les frottements de la rivière ont été effectuées, mais aucune ne permet de corriger le biais constaté. L'hypothèse avancée est que la géométrie du lit mineur est mal représentée, du fait des variations importantes des sections du lit mineur sur

la zone : présence de deux ponts, de deux passerelles et d'un méandre, qui apportent de l'incertitude sur l'interpolation des profils mesurés sur le terrain.

Les résultats de simulation de référence pour la crue de 2008 (modèle calé au mieux et comprenant un niveau de détail maximum) permettent une description des écoulements dans la zone urbaine (Figure 6.11 p.134). Les débordements de la rivière sont rapidement canalisés dans le réseau de rues, avec une diffusion au final assez peu importante dans les zones bâties (principalement des maisons individuelles avec jardin, séparées par des murs, murets et barrières). Ceci s'explique d'une part par les modestes hauteurs d'eau dans les rues (quelques dizaines de centimètres), et d'autre part par la présence de nombreux murs qui viennent nettement séparer les rues des zones bâties. Au pic de crue, la majeur partie de l'écoulement dans le lit majeur s'effectue le long du *Boulevard de l'Yzeron*, qui longe la rivière en rive droite. Le reste des écoulements dans le lit majeur est rapidement contraint par la topographie marquée en rive droite, de sorte que l'on note des débits importants surtout dans les rues qui suivent la direction ouest-est de la rivière (voire la répartition des débits sur le carrefour central sur la Figure 6.21 p.144). Les inondations résultant des autres crues sont similaires.

En termes de niveaux d'eau maximaux, la représentation de la zone urbaine a une influence limitée, de sorte que les données de terrain ne permettent pas de discriminer les différents niveaux de détail considérés dans les simulations numériques. Le niveau d'eau maximal dans la zone urbaine suit de près celui dans la rivière, notamment dans la zone centrale étudiée (Figure 6.12 p.135). Ceci vient de la longue durée de submersion pour les crues considérée (plusieurs heures), de l'importance du débit dans le lit mineur par rapport à celui dans la zone urbaine (typiquement quelques $m^3.s^{-1}$ dans les rues pour des débits totaux au pic de l'ordre de 70 $m^3.s^{-1}$), et de la forme générale de la plaine d'inondation (cuvette assez étroite). Il en résulte que l'extension globale de l'inondation varie peu d'un jeu de paramètre à un autre. Pour autant, les différentes simulations pour un évènement engendrent des variations locales ou à l'échelle des rues des écoulements.

L'effet le plus marquant vient du fait d'intégrer les murs (*run1*) ou non (*run2*), avec des erreurs sur la prédiction des zones inondées dépassant facilement les 100% (Figure 6.17 p.141). Ceci montre la prédominance de l'effet des murs pour ce genre de zone urbaine devant celle des bâtiments, ces derniers étant en fait majoritairement compris dans un réseau de parcelles bien délimitées physiquement. Une autre conséquence est que l'inclusion des murs empêche les écoulements à travers les zones bâties, ce qui influe sur la structure globale de l'écoulement à l'échelle de la zone inondée. En ce sens, une représentation du réseau de rues

uniquement (*run4* sur la Figure 6.17 p.141) est probablement plus juste qu'une représentation de la plaine d'inondation entière sans les murs (*run2*) voire sans murs ni bâtiments (*run3*).

La topographie détaillée des rues a un impact moins important. A cause des contraintes sur la finesse du maillage utilisable, deux adaptations de la topographie des rues sont proposées (Figure 6.5 et Figure 6.6 p.126):

- Un modèle de référence (*Ref*) où on reprend au mieux la topographie détaillée des rues, ce qui tend toutefois à augmenter la section d'écoulement à cause de la discrétisation spatiale autour de l'interface caniveaux/trottoirs.
- Un modèle simplifié (*Avg*) suivant l'approche précédemment utilisée sur les écoulements expérimentaux et représentant chaque section de rue par une cote unique et égale à la cote moyenne sur la section. Ceci revient en pratique à ne pas représenter les caniveaux (points bas), mais a l'avantage de minimiser les erreurs globales pour des hauteurs d'eau importantes (typiquement supérieures à 20 cm).

L'inondation est majoritairement contrôlée par la topographie générale de la plaine d'inondation, de sorte que la simplification de la description des rues (modèle *Avg*) a un impact limité à l'échelle de la zone étudiée (pas d'effets de la suppression des caniveaux par exemple). D'un point de vue global, le modèle simplifié *Avg* conduit à une élévation moyenne du fond des rues de + 3.0 cm par rapport au modèle *Ref*, ce qui se traduit par des niveaux d'eau maximum simulés supérieurs de 2.4 cm en moyenne par rapport à la représentation détaillée (modèle *Ref*). Ce biais dans la cote moyenne du terrain (a priori dans le modèle *Ref*) ne peut pas être critiqué par des données de validation, mais il est intéressant de noter que son impact est significatif par rapport aux autres paramètres étudiés dans l'analyse de sensibilité (Table 6.4 p.140).

Localement, les champs de hauteurs d'eau et de vitesses sont plus homogènes avec la topographie simplifiée, et les écoulements s'étendent systématiquement sur toute la largeur des rues. Comme pour la maquette expérimentale de carrefour urbain, on retrouve une répartition de débit au sein du carrefour central inondé similaire pour les deux représentations de la topographie des rues. Enfin, un modèle avec maillage grossier et topographie simplifiée est testé, et les observations suivent en partie les précédentes, à savoir une modification importante des caractéristiques locales de l'écoulement et un impact modéré à l'échelle de la zone inondée.

Drainage des écoulements de surface par les avaloirs

Le modèle 2D est utilisé pour simuler les écoulements de surface de la crue de 2008, en prenant en compte le drainage par les avaloirs, avec un débit drainé défini par une des deux sections de contrôle suivantes du modèle d'échange précédemment développé :

- Débit sur l'avaloir, déterminé par une loi de seuil sur le contour de l'avaloir
- Débit à l'entrée de la conduite reliant le compartiment sous l'avaloir à la conduite de drainage principale, déterminé par une loi d'orifice appliquée à l'entrée de la conduite de connexion

Une étude de sensibilité sur la topographie de la surface utilisée et la finesse du maillage montre une difficulté importante liée à ce genre de modélisation. Pour des hauteurs d'eau faibles, les débits drainés sont contrôlés par la capacité de l'avaloir et sont très sensibles à la hauteur d'eau locale dans la rue. Pour des hauteurs d'eau plus importantes (supérieures à 10 cm), le débit drainé est contrôlé par la capacité de la conduite de connexion et deviennent beaucoup moins sensibles à la hauteur d'eau dans la rue. Le test de sensibilité montre que dans le premier cas la modélisation nécessite une description fine de la rue (maillage fin et topographie détaillée), alors que dans le deuxième cas un artifice de modélisation permet de retrouver des débits drainés corrects quel que soit le niveau de détail dans le modèle de surface.

A l'échelle de la zone inondée, les hauteurs d'eau sont assez fortes pour souvent dépasser la capacité des avaloirs. De fait, les débits d'échange sont majoritairement contrôlés par la structure d'échange au-dessous de l'avaloir, et le débit total drainé sur la zone est peu sensible à la représentation détaillée de la rue (Figure 7.6 p.162). Au pic de la crue de 2008, le débit total drainé estimé est de l'ordre de 2 $m^3.s^{-1}$, ce qui diminue les hauteurs d'eau jusqu'à 5 cm dans les rues ou dans la rivière à l'aval. L'impact du drainage sur les écoulements de surface est donc limité (le drainage ne change pas les conclusions sur la modélisation des écoulements de surface), et ces dernières valeurs sont une limite haute puisque l'éventuelle limitation due au réseau n'est pas prise en compte.

Interactions entre les écoulements dans la rivière, les rues et le réseau d'assainissement

Un modèle du réseau d'assainissement est construit à l'aide du code 1D Rubar3, et couplé à un modèle 2D simplifié de la surface, suivant la méthodologie utilisée pour la maquette expérimentale du système de drainage urbain. Les incertitudes liées à la modélisation du réseau d'assainissement sont nombreuses et les données de terrain non suffisantes pour permettre une réelle validation. L'analyse des résultats est donc faite de manière prudente.

L'intégration du réseau d'assainissement a pour principale conséquence de limiter le débit drainé dans les rues. Les résultats suggèrent l'existence de trois zones avec des interactions rues/réseau d'assainissement différentes :

- La rue longeant l'Yzeron en rive gauche est inondée mais l'écoulement n'est pas drainé vers le réseau, car seul le collecteur principal passe dans cette zone et il n'est pas connecté à des avaloirs dans la zone inondée
- Dans le méandre en rive droite de la ville, le drainage des rues est limité par la capacité du réseau d'assainissement, avec des conduites qui sont mises en charge par le processus de drainage
- Dans la partie sud de la zone inondée, le drainage des rues est limité par la capacité des structures d'échange (avaloirs et conduite de connexion) et non pas par le réseau lui-même. En effet les débits drainés rejoignent directement le collecteur secondaire dont la capacité n'est jamais atteinte.

La totalité du débit drainé dans la zone inondée rejoint le collecteur secondaire en rive droite, dont une des fonctions est d'évacuer les eaux arrivant des zones urbaines au sud. Quelle que soit la crue considérée ce collecteur n'est jamais saturé, et le drainage des eaux pluviales devance toujours de quelques heures l'inondation d'origine fluviale et le parasitage du réseau d'assainissement qu'elle engendre. Ceci est dû aux types d'évènements hydrologiques initiaux considérés (pluies assez longues et peu intenses), et au temps de réaction plus long du bassin versant de l'Yzeron que celui des bassins versants urbains autour d'Oullins. Par conséquent, les crues de la rivière étudiées n'empêchent pas la bonne évacuation des eaux provenant du ruissellement urbain.

Enfin, les résultats de simulation montrent des interactions intéressantes entre la rivière et le réseau. Pour la crue de 2008, le collecteur principal en rive gauche est saturé pendant un laps de temps important, étant en fait nettement sous-dimensionné vis-à-vis des zones urbaines qu'il draine. Ceci engendre des débordements dans l'Yzeron à travers un déversoir d'orage à l'amont de la zone étudiée. Pendant la montée de la crue, le niveau d'eau dans la rivière devient à un moment suffisamment important pour bloquer le fonctionnement de ce déversoir d'orage, surchargeant un peu plus le collecteur dans cette zone. Ce dernier se déverse alors en partie vers le collecteur en rive droite à travers la conduite d'échange normalement conçue pour fonctionner dans le sens opposé. Ce genre d'interactions complexes montre le potentiel qu'il y a à utiliser des modèles couplant les écoulements de surface à ceux du réseau. Toutefois, au vu du nombre de paramètres nécessaires pour une telle modélisation est conséquent, et des données de terrain pour le calage ou la validation devraient être produites pour asseoir l'interprétation des résultats.

Conclusions générales et perspectives

L'étude expérimentale et numérique sur l'impact de petits obstacles sur les écoulements de surface lors d'inondation en ville montre qu'il y a tout avantage à représenter ces derniers dans les modèles d'écoulements de surface. En effet, une modélisation explicite permet de prendre en compte l'effet potentiel d'un obstacle sur la répartition des débits à un carrefour voisin, la perte d'énergie associée à la résistance de l'obstacle à l'écoulement, ainsi que les modifications locales de l'écoulement dues au contournement de l'obstacle. Dans le cas réel étudié, l'effet de tels obstacles n'a pas pu être étudié, à cause du manque d'information d'une part, et de l'autre de la difficulté d'adapter le maillage à de tels éléments. En revanche, des éléments structurels de taille plus importantes ont été inclus : les bâtiments d'un côté, et les murs/murets/barrières de l'autre. La structure de la ville étudiée fait que les bâtiments seuls ont peu d'effet et que la structure de l'écoulement à l'échelle de la zone étudiée est beaucoup plus contrainte par la présence des murs. L'ensemble de ces résultats montre qu'il y a un intérêt à construire des modèles d'inondation urbaine considérant plus de détails que la topographie du sol et les bâtiments. En revanche, pour être opérationnel, de tels modèles nécessitent de développer des moyens d'acquisition et de traitement des données spécifiques. Les progrès en modélisation topographique des zones urbaines (Sampson et al. 2012; Heo et al. 2013), ou les capacités de certains mailleurs (Geuzaine and Remacle 2009) ouvrent la voie à l'utilisation d'un tel niveau de détail. L'utilisation de ces données et de ces outils reste

toutefois peu répandue, et un effort de développement est à réaliser pour les rendre opérationnels, l'efficacité d'un modèle dépendant aussi de sa facilité de mise en œuvre. Enfin, l'effet des très petits obstacles (poteaux, arbres) n'a pas été considéré, et il est probable que ces derniers puissent être correctement représentés en augmentant les frottements. Une telle hypothèse demanderait une étude expérimentale, qui pourrait être conduite comme celle présentée ici sur les écoulements en bifurcation.

La gestion de la topographie des rues reste un problème plus délicat à la lumière des résultats de la thèse. Les résultats de simulation sur les écoulements en carrefours montrent que pour des écoulements en régime fluvial, il n'est pas nécessaire de prendre en compte une topographie détaillée des rues mais en revanche il ne doit pas y avoir de biais dans la topographie moyenne (i.e. sur une largeur de rue) si l'on veut prédire correctement la répartition des débits dans les rues. De ce point de vue, la simplification de la topographie proposée constitue un bon compromis entre un calcul correct des écoulements à l'échelle du réseau de rues, et peu de contrainte sur la finesse du maillage à utiliser. Les simulations sur Oullins tendent à confirmer ce résultat, pour des profils de rue réels. En revanche, la simplification de la topographie homogénéise l'écoulement sur une rue et peut avoir des conséquences importantes sur l'estimation des débits drainés par les avaloirs, si la hauteur d'eau dans les caniveaux est mal évaluée. Dès lors, le traitement optimal de la topographie va dépendre de l'intensité de l'inondation et de la nécessité de prendre en compte les échanges avec le réseau d'assainissement.

La définition des débits drainés des rues vers le réseau d'assainissement fait apparaître deux grands cas de figure. Pour des hauteurs d'eau assez importantes dans les rues, le débit drainé est contrôlé par l'ensemble de la structure d'échange. Dans ce cas, l'approche développée ici (étude des pertes de charge dans la structure) permet une évaluation objective des échanges, au sens où un coefficient de débit peut être calculé sur la base de la géométrie de la structure d'échange. Les simulations à la fois des écoulements expérimentaux mesurés au DPRI ou sur Oullins montrent que cette formulation est relativement peu sensible aux hauteurs d'eau dans la rue, et donc peu affectée par des modèles simplifiés d'écoulements de surface. Cette conclusion est aussi valable pour les débordements, quelle que soit la hauteur d'eau dans la rue. En revanche, pour des hauteurs d'eau faibles dans la rue, le contrôle des débits drainés se fait au niveau des avaloirs, avec une forte sensibilité des formules d'échange à la hauteur d'eau sur l'avaloir. L'incertitude sur la topographie dans les modèles usuels peut alors engendrer des erreurs très importantes. Une validation (*a priori* expérimentale) d'une

modélisation si fine du drainage par un modèle d'inondation urbaine serait intéressante, éventuellement en passant par l'utilisation de lois d'échange globales (en calculant par exemple le débit drainé en fonction du débit total approchant l'avaloir).

En plus des perspectives évoquées ci-dessus (étude des très petits obstacles et des frottements dans les rues, méthodes d'acquisition et de traitement de données, modélisation du drainage pour les écoulements peu profonds), la confrontation de modèles simplifiés sur les données expérimentales ou de terrain utilisées dans cette thèse serait intéressante. En effet, certains résultats de cette thèse sont conditionnés par les modèles numériques utilisés, et l'utilisation d'autres modèles pourrait par exemple aider à la généralisation de certains résultats.

Contents

List of figures

List of Tables

Notations

A	flow area	m^2
A_p	pipe area	m^2
A_t	drainage tube area	m^2
At	connecting pipe/tube area	m^2
b	channel width	m
C_b	branch channel weir crest height	m
C_d	downstream channel weir crest height	m
D_p	pipe diameter	m
D_t	connecting pipe/tube diameter	m
F	Froude number	-
F	friction factor	-
f_p	pipe friction factor	-
f_{SI}	opening ratio of a street inlet	-
f_t	drainage tube friction factor	-
g	acceleration due to gravity	$m.s^{-2}$
h	water depth	m
H	hydraulic head	m
h_b	branch channel water depht	m
h_d	downstream channel water depht	m
H_{pipe}	pipe height	m
h_s	water depth over a street drain channel	m
h_{sw}	sidewalk height	m
h_u	upstream channel water depht	m
K	diffusion coefficient	$m^2.s^{-1}$
k	non-dimensionnal parameter to compute the diffusion coefficient	-
K_{i-j}	local head loss coefficient between points i and j	-
k_s	roughness height	m
Ks	Strickler coefficient	$m^{1/3}.s^{-1}$
L_b	branch channel length	m
L_d	downstream channel length	m
L_t	drainage tube length	m
L_u	upstream channel length	m
m	mesh resolution	m
n	Manning coefficient	$s.m^{-1/3}$
Q	flow discharge	$m^3.s^{-1}$
q_{ex}	exchange discharge at one street inlet of the DPRI model	$m^3.s^{-1}$
Q_{ex}	exchange discharge	$m^3.s^{-1}$

$q_{ex,1D}$	local exchange discharge divided by the mesh length in the 1D model	$m^2.s^{-1}$
$q_{ex,2D}$	ponctual exchange discharge divided by the mesh area in the 2D model	$m.s^{-1}$
$Q_{ex,total}$	total exchange discharge	$m^3.s^{-1}$
Q_p	pipe discharge	$m^3.s^{-1}$
Q_{pi}	pipe inlet discharge	$m^3.s^{-1}$
Q_{po}	pipe outet discharge	$m^3.s^{-1}$
Q_{si}	street inlet discharge	$m^3.s^{-1}$
Q_{so}	street outlet discharge	$m^3.s^{-1}$
R_0	curvature radius	m
Re	Reynolds number	-
R_h	hydraulic radius	m
Rq	discharge distribution	-
t	time	s
u	velocity along x axis	$m.s^{-1}$
$u*$	friction velocity	$m.s^{-1}$
v	velocity along y axis	$m.s^{-1}$
V	velocity magnitude	$m.s^{-1}$
w_o	obstacle width	m
w_p	Preissman slot width	m
W_{street}	street width	m
z	pipe bottom elevation	m
Z_b	bottom elevation	m
Z_p	pipe water level	m
$Z_{p,dn}$	downstream pipe water level	m
Z_s	surface water level	m
α_{Vi-j}	velocity correction factor	-
ΔH_{i-j}	head loss between points i and j	m
Δh_u	evolution of upstream channel water depth	m
ΔRq	evolution of discharge distribution	-
Δt	time step	s
μ	discharge coefficient	-
μ_o	orifice discharge coefficient	-
μ_w	weir discharge coefficient	-

Chapter 1.
Introduction

1.1 Flood risk and urban areas

According to the recent report from the European Environment Agency (EEA 2010), floods have caused 1126 deaths in the period 1998-2009. Besides, they remain the most costly natural hazard, with cumulated damages evaluated to EUR 52 billion in the same period. Most of these human losses and economic damages actually happen in urban areas, as the latter concentrate a large part of the stakes: population, economical activities and industries, historical centres, road networks…etc.). Similarly, this link between flood risk and urban areas is also explained by the fact that the latter are often located in flood-prone areas such as river floodplains, coastal areas or valleys downstream of water dams.

Besides this increased vulnerability to flood risk, two characteristics of urban areas exacerbate flood hazards. First, soils imperviousness associated to the urbanization increases volumes of surface runoff and shortens reaction times of urban catchments. Evacuation of this runoff in urban areas depends mostly on the efficiency of the urban drainage system, and the latter does not always grow as fast as the urbanization or may not be well-designed. Secondly, once flooding occurs in urban areas, surface flows are usually more violent than in natural floodplains, as many impervious elements such as buildings or walls block the flows and concentrate them in the smooth and straight street network. Therefore, evaluating impact of floods in urban areas is of paramount importance for flood risk management.

Most of the time, inundations in urban areas are due to phenomena that have a much larger scale than the impacted areas, so that modelling of the initial event and its propagation

in urban areas can be independently carried out. Exceptions exist, such as cases of intense rainfall that lead to local discrepancies of the urban drainage system and for which an integrated modelling may be preferred (Djordjevic et al. 1999; Schmitt et al. 2004). In other cases, the first part of the modelling consists in determining characteristics of the initial flood event away from the urbanized area. This part of the modelling involves many fields of environmental research and still defines a significant part of the final modelling accuracy (see for instance Brown et al. 2007): hydrology, ocean engineering, seismology (tsunamis) and soil/solid mechanics (dams, levees), as well as climatology or weather forecast. In a second step, results from these calculations can be used as boundary conditions in a hydrodynamic model to simulate the flood propagation in the studied urban area itself.

On the one hand, modelling of flows during urban floods uses similar techniques as the ones used for other free surface flow modelling (e.g. river, channel, or floodplain flows), mainly the numerical simulation of the full or simplified shallow water equations (see Eqs. 3.1 - 3.3). On the other hand, some features of urban areas require a careful adaptation of these approaches, which have been often used for simpler configurations (e.g. natural floodplains or laboratory experiments). Specificity of urban areas towards hydraulic modelling is described in the next section, synthesizing general principles and approaches proposed in the literature, and highlighting some key points on which additional research is required.

1.2 Modelling floods in urban areas

1.2.1 Aim of modelling and consequences on the choice of models

Modelling floods in urban areas is compulsory for any sound flood risk management planning, yet the required accuracy strongly depends on the type of risk estimation that is carried out afterwards. Simulation results from a depth averaged two-dimensional model (2D) solving the full shallow water equations can provide global flood extents and spatial distributions of maximum water levels, but also detailed time series of local flow depths and velocities. However this method is not always well-fitted for applications such as real time forecasting, uncertainty analysis or modelling at large scale (Golding 2009). Therefore a significant number of simplified urban flood models have been presented in the literature, by solving simplified forms of the shallow water equations

(Aronica and Lanza 2005; Yu and Lane 2006), adding porosity while removing building representation (Guinot and Soares-Frazao 2006; Soares-Frazao et al. 2008; Cea and Vazquez-Cendon 2010) or specific sub grid treatments (Inoue et al. 2000; Chen et al. 2012) to increase computational efficiency. Obviously, these simplifications cannot achieve similar accuracy as explicit modelling based on full shallow water equations, as they tend to neglect some flows patterns or average them in space, or simplify flow dynamics.

This question on models accuracy has been directly discussed when the modelling aims at some economical flood damages modelling or cost-benefit assessment (Apel et al. 2009; Freni et al. 2010), usually carried out by applying depth damages curves on computed flow depth fields. One of the conclusions of these studies is that the uncertainty associated to the depth-damage curves is much greater than the uncertainties on the hazard assessment (that is, the flows characteristics). For such applications, the flood dynamics (e.g. arrival time or flow velocities) is not really considered and this pushes towards the use of simple flood models, reporting modelling efforts on economic aspects.

Now, other applications require a better description of the surface flows dynamics. Evaluating human losses or the capacity of pedestrians to walk in a flooded street requires empirical relationships based on both flow depths and velocities (Jonkman et al. 2008; Ishigaki et al. 2010; Gomez et al. 2011). Similarly, vehicles in the streets can be moved by flood waves, leading to increased damages and potentially flow blockages if a car dam is created in the street network (Cemagref 2009). Role of the flow velocity on cars motion has been proved to be of paramount importance (Xia et al. 2011). At a larger scale, for violent flows, collapse of buildings is obviously associated to high momentum flows. By coupling an adequate hydrodynamic model with different damage functions, (Gallegos et al. 2012) managed to predict buildings washout or structural failures during a real dam break. Similarly, (Xia et al. 2011) use detailed simulation results to assess detailed vulnerability maps for cars and people during flash floods. In the end, numerous urban flood models have been presented in the literature, including more or less physics and having different initial potential. Two recurrent questions remain for all modellers, namely how to adapt models to particularities of urban areas, and what accuracy can be expected.

1.2.2 General principles of urban flood modelling

1.2.2.1 Integration of urban areas impervious elements

Buildings are probably the features that distinguish most urban areas from natural areas when studying floods, as these impervious macro-elements represent a large part of the surface area. When studying dense urban areas or urban drainage systems, flows can be assumed to occur mainly in the street network so that surface flow models can be restrained to this network (e.g. Lhomme et al. 2006; Mignot et al. 2006; Leandro et al. 2009). In other cases (significant flooding in moderately urbanized areas), flows can occur outside the streets and reach built-up areas. A common approach consists in considering buildings as totally impervious and excluding them from the computational domain (Schubert et al. 2008; Tsubaki and Fujita 2010). A quite similar method consists in including directly buildings elevation in the digital elevation model (Yu and Lane 2006; Vojinovic and Tutulic 2009). Both methods explicitly account for the effects of buildings, with slight differences arising from the buildings footprint delineation and different sensitivity to the mesh resolution. An implicit modelling well fitted to structured grids consists in assigning occupying and conveyance ratios to each cell partly at least partly occupied by buildings (Inoue et al. 2000), to account for the decrease of surface storage capacity and flow conveyance. A complementary approach to the latter consists in analysing *a priori* the possible flow pathways (Chen et al. 2012), and integrating them to more precisely account for flow blockages. Finally, for large scale flooding, impact of buildings on surface flows can be computed in a statistical and macroscopic manner. The most precise method includes addition of porosity and specific head losses to account for the non-explicit consideration of the flow contractions and expansions through the urban areas (Guinot and Soares-Frazao 2006). A less detailed method consists in increasing friction in built-up areas (Gallegos et al. 2009), the main problem being that the adequate friction is difficult to define.

Clearly, integration of buildings in urban flood models has been well studied and there are several approaches to represent their effects. Now, consider a typical urban area and its representation by a quite accurate model (Figure 1.1). It can be easily seen that buildings alone cannot depict all surface elements that can affect floods: cars, trees, urban furniture, walls, fences…etc. Somehow, effect of small size obstacles is acknowledged but it is often considered as an uncertainty source, or included in friction parameterization, which is quite arbitrary. Effects of singular walls (when not part of a building) have been seldom

investigated (Yu and Lane 2011), perhaps because of the difficulty to gather relevant data (Mason et al. 2007). In a detailed modelling perspective, effects of these elements remain to be assessed.

Figure 1.1: Aerial photograph of the city centre of Oullins (top) and 3D visualization of a digital elevation model with buildings in white (right)

1.2.2.2 Consideration of the topography in urban areas

Accuracy of urban flood models relies also deeply on the topographical data used and its integration in the different models. Digital elevation model (DEM) can be derived from urban data base (Aronica and Lanza 2005), direct measurements of street profiles (Mignot et al. 2006), or from remote sensing technologies such as aerial (Mason et al. 2007) and terrestrial LiDAR (Sampson et al. 2012).

For conventional flood models, integration of this data remains constrained by the mesh resolution. Coarse resolutions (10-50 m) accelerate the calculations but tend to smooth the topography, which can bias model results (ponds, small flow pathways). Some sub-grid scale treatments have been proposed to overcome this difficulty in the case of raster storage cell models (Yu and Lane 2006; McMillan and Brasington 2007) or “impact zones” model (Jamieson et al. 2012). This allows a decoupling of the considered topographical resolution from the computational grid resolution, enhancing models accuracy at low computational costs.

Well-established data acquisition techniques (such as aerial LiDAR) can provide DEM with vertical accuracy typically of +/-0.1 m. Even such accuracy cannot capture all elements impacting the flood propagation, given the complexity of a typical street profile. For urban drainage application, the streets topography can be enhanced by burning their footprints into DEM (Vojinovic and Tutulic 2009) or by using more accurate algorithms (Ettrich et al. 2005). These techniques permit to enhance small flow pathways and improve global representation of the surface drainage network. Errors subside, as many topographical details cannot be retrieved. Now, **running models with more accurate topographical data may be limited by the data acquisition process and computational times, so that benefits of using detailed topography should be assessed as precisely as possible.** Whereas consequences of large topographical errors is relatively intuitive (e.g. removal of a pond), influence of local topography is less evident (drain channels, sidewalks).

1.2.3 Friction Parameterization

All flood models account for energy losses due to bottom friction (i.e. friction on the ground). In most cases, the friction term includes the use of a Manning (n) or Strickler (K_s=1/n) coefficient. Adequacy of this formulation for highly unsteady flows may be questioned (El Kadi Abderrezzak et al. 2009), yet it is generally assumed to be correct for slower flows. This modelling point has initially a deep physical meaning (Yen 2002), so that in principle the range of values to use can be derived from ground types and eventually some macro roughness (Schubert et al. 2008). Now, there are two strong limitations to this approach. First, several typical elements of floods or urban areas increase the effective roughness if they are not explicitly considered: flood debris, topographical details, cars and urban furniture, etc. As this effective roughness cannot be directly measured on field and may vary from one case to another, this parameter remains quite uncertain. Secondly, the friction can be artificially increased to account for momentum losses that are not considered by the hydrodynamic model such as turbulence stresses (generally assumed to be negligible compared to bottom friction) or inertial terms (i.e. diffusive wave models). The model benchmark and sensitivity analysis (notably on friction) carried out by (Hunter et al. 2008) gives a particularly interesting insight on this aspect. The study reveals that the range of assumable friction for urban areas covers the differences amongst the different model formulations. **However, we can assume that the more physical processes are explicitly represented, the less uncertainty remains on the friction modelling.** This is clearly shown

in the simulations carried out by (Yu and Lane 2006), where an excessively simplified simulation (diffusive wave on a coarse mesh) requires non-physical values of Manning coefficients (up to n=10, against typical values of 0.04 for their reference simulations) to achieve good performance. Besides, compensating all models approximations (topography, governing equations, numerical scheme) by the bottom friction may allow calibrations on a few characteristics (flood extent, local water levels), yet it cannot improve all computed flow characteristics at the same time and may lead to misjudgements on actual models performance.

1.2.4 Coupling of several flow types

Most of urban areas include a drainage system made of major system (streets) and a minor one (underground drainage pipes). Whether flooding occurs from local intense rainfall or direct overland flow, it will lead to flows in both systems, as a result of the streets drainage into the underground pipes, and/or of pipes overflow into the streets. Because of these bi-directional interactions, it is more adequate to simultaneously simulate both flow layers, and this method is referred to *dual drainage modelling* (Djordjevic et al. 1999; Smith 2006). Pipe flows are usually modelled with 1D models. For such urban drainage-oriented applications, both 1D and 2D models show benefits to model surface flows (Mark et al. 2004; Leandro et al. 2009; Vojinovic and Tutulic 2009). Actually, coupling models is a common practice for flood inundation analysis. For instance, surface flows can be coupled to large underground spaces (Toda et al. 2001; Chen et al. 2005) or be themselves represented as combinations of 1D flows (drain, river, channels) and 2D overland flows (Kawaike et al. 2004; Vojinovic and Tutulic 2009).

Particularity of dual drainage modelling is that there are two distinct flow layers that are almost always separated but can interact at some specific points (street inlets, sewer overflow devices, manholes), in both directions (drainage and overflow). Drainage processes in normal conditions have been a focus point for decades, with considerable research on street inlets efficiencies (e.g. Despotovic et al. 2005). These results are perfectly fitted to design urban drainage systems. Yet **interactions between surface and subsurface flows are actually poorly assessed for flooding conditions** (as recalled by Leandro et al. 2007), where surface flows are usually out of the urban drainage systems design assumptions. Moreover, **increasing model complexity (i.e. consideration of two flow layers) should be supported by more accurate validation data** (Mark et al. 2004). Despite the growing interest on dual

drainage modelling, few of the proposed models have been accurately validated, and though relevance of this approach is evident, detailed validation should help assess its potential.

1.2.5 Model validation

Direct validation of urban flood models against field data remains limited, considering both the small amount of validation data usually available and what the latter can validate (typically local water levels). This limitation, along with the uncertainties inherent to real case modelling, implies that it is difficult to assess the true benefits of using detailed models over simplified ones, or whether all simulation results can be relied on (e.g. rate of water level rise or velocity field in the streets). Use of remote sensing techniques (Schumann et al. 2011), of data from flood warning system (gauges, cameras) or other techniques may help achieving detailed validation in the future. Yet these data are not widely available, and also they are determined by floods occurrence, which – fortunately – do not happen as often as we need to model.

A complementary approach is to validate numerical models against experimental measurements. Flows through crossroads (Mignot et al. 2008; El Kadi Abderrezzak et al. 2011) or groups of buildings (Mignot et al. 2006; Soares-Frazão and Zech 2008; Van Emelen et al. 2012) have been investigated with experiments and numerical simulations. These configurations remain simplified, so that experimental and simulations results are easier to understand. On the other hand, some processes are ignored or biased (typically the friction) and conclusions may not stand when shifting to field cases. This last issue can be addressed by gradually increasing physical models complexity and improving measurements, so that this validation approach remains clearly promising.

A widespread practice consists in carrying sensitivity analysis on models parameters (e.g. building representation, mesh density) or in benchmarking different flow models. These approaches have given interesting insights on each model abilities (Hunter et al. 2008; Schubert et al. 2008; Fewtrell et al. 2011). Though this approach is pragmatic, it cannot totally replace a validation with reliable measurements. Note that most of the model validations based on experimental observations concern quite complete numerical models, often designed to simulate other types of environmental flows and not especially dedicated to urban flood modelling. Exceptions exist (e.g. Dottori and Todini 2013) but remain scarce. Research on urban flood modelling would gain from a more systematic model validation with experimental data, whatever the numerical model.

1.3 Thesis objectives and manuscript outline

Floods in urban areas can lead to complex flows due to the artificial topography, the presence of impervious elements of different size, or the interaction between different flow layers. Prediction of these flows is essential for flood risk management, and is mainly achieved using numerical models. The latter can be designed either to account for local physical phenomena or represent global flooding processes, both these general directions being justified by the different levels of complexity that can be required when studying urban floods.

This thesis aims at studying the detailed modelling of flows during urban floods, especially considering the impact of topographical details on the surface flows and the modelling of exchange flows between streets and underground pipes. In particular, the following questions are asked:

- What is the impact of small-scale obstacles on the surface flows and can it be represented in an urban flood model?
- What accuracy on the streets topography should be considered?
- How to model exchanges between street flows and pipe flows?

As recalled earlier, many types of surface flows can occur during urban floods. The thesis mainly deals with subcritical flow regimes in relatively flat areas. An important part of this thesis work is carried out using experimental models dedicated to the previous questions, feeding the discussion with accurate and reliable measurements. Besides, two types of numerical models previously developed by IRSTEA are used through the thesis. A 2D model solving the shallow water equations (Rubar20) is used to simulate surface flows, and a 1D model (Rubar3) for the pipe flows. A coupling of this model with a 1D shallow water equation model is used to achieve 1D (pipe) / 2D (surface) numerical simulations. These numerical models are used to extend their validation and to derive operational conclusions on the way of setting-up urban flood models. A well-documented field case is also studied to complete this validation and address some additional questions inherent to field case modelling.

The structure of the manuscript is as follows. In the **first part**, effects of small scale obstacles and street topography on the flow discharge distribution through a 3 branch junction

are studied. Chapter 2 presents experimental observations carried out at the LMFA (Laboratory of Fluid Mechanics and Acoustics, INSA de Lyon, France) on flows through a 3 branch bifurcation model impacted by the presence of small obstacles or sidewalks. In Chapter 3, modelling of these flows with the 2D code Rubar20 is performed and these results are used to discuss the need and the feasibility of considering such details in an urban flood model.

In the **second part**, interactions between street and pipe flows are studied. In Chapter 4, measurements carried out on a DPRI (Disaster Prevention Research Institute, Kyoto University, Japan) experimental model are presented. The model permits to generate vertical exchanges between a flooded street and its underground drainage system, which allows us to study and model these exchanges. The complete numerical modelling of these bi-layer flows is presented in Chapter 5, using a 1D/2D coupled model.

Finally, the **third part** aims at studying past flood events in the city of Oullins. At first, a modelling of the surface flows alone is performed (Chapter 6), then their interaction with the underground drainage system is included (Chapter 7).

Adequacy of these 3 parts towards the questions mentioned earlier is summed up in Table 1.1, along with the use of the 2D and 1D/2D models. Results of these different parts will be notably analysed considering these three questions in a general conclusion.

	Obstacles	Street Topography	Street/Pipe Exchanges	2D modelling	1D/2D Modelling
Part I	•	•		•	
Part II		•	•		•
Part III		•	•	•	•

Table 1.1: Thesis objectives distribution amongst the 3 parts

Part I.

Influence of obstacles and sidewalks on 3 branch bifurcation flows

We have seen in the introduction the ability of standard numerical models to represent the global surface flow pattern during urban floods. This ability has been assessed by comparing numerical simulations and laboratory experiments for schematic urban areas (Mignot et al. 2006; Soares-Frazão and Zech 2008; Van Emelen et al. 2012) or idealized urban crossroads (Mignot et al. 2008; Ghostine et al. 2010; El Kadi Abderrezzak et al. 2011). However, (Mignot et al. 2006) pointed out that when modelling real field cases, uncertainty will arise from the accuracy of the street topography, as well as the presence of small scale obstacles in the street. These elements can have a significant impact, even when compared to the numerical model ability to predict the complex combining and dividing flows through a crossroad.

In this part, the effects of detailed topography and small obstacles on the flow at one crossroad scale are assessed. The chosen approach follows two steps. First, measurements are carried out on an idealized experimental crossroad to study the influence of such elements on a series of dividing flows (Chapter 2). The main focus point lies in the study of the flow distribution through the experimental crossroad, which reflects the global effects that the studied singularities could have at a city scale. Besides flow distribution measurements, finer measurements of velocity fields are carried out to understand the physical processes affected by obstacles or topographical details. Then, in Chapter 3, the ability of a numerical model to

predict the effects of these obstacles and topographical details is studied, in order to assess whether such fine elements could be included in urban flood models.

Preliminary work has been done to study the ability of the numerical model used in Chapter 3 to simulate velocity fields for combining flows in a 3 branch junction, and to assess (only with numerical simulations) the influence of introducing obstacles and sidewalks on such flows (Bazin et al. 2012). Results show that the constant eddy viscosity has to be carefully calibrated in the numerical model for the latter to be able to predict accurate velocity fields for flows without obstacles or sidewalks. With such calibration, the numerical model appears to fairly predict the general flow pattern (acceleration zone and recirculation area in the downstream branch), which proves the relevance of using such model to study at least global effects of local obstacles or variations of the channel geometry (bottom topography). However for combining flows, effects of obstacles or sidewalks have only local effects, as the flow discharge in each channel is fixed by the inflow discharges and the mass conservation (the downstream channel discharge being equal to the sum of both incoming discharges). Therefore, as local flow perturbations are out of this thesis framework, further investigation of combining flows has not been carried out. The corresponding preliminary results can be found in the mentioned article.

Chapter 2.
Experimental study on the LMFA urban crossroad model

2.1 Preliminary description of the physical processes expected in the experiments

The problem of combing and dividing flows in channel junctions has been extensively studied, as it is linked to many engineering applications. Studies have covered a wide range of junction configurations and hydraulic conditions, to provide practical ways of determining flow distribution and energy losses (e.g. Taylor 1944; Law and Reynolds 1966; Hsu et al. 2002), or to accurately describe the flow patterns (e.g. Neary and Odgaard 1993; Mignot et al. 2008).

In order to reduce the number of flow parameters and junction geometrical parameters, one type of dividing flow is studied. It consists in a subcritical dividing flow through a 3 branch junction, the 3 branches being horizontal and having the same width, and joining with a 90° angle. The choice of subcritical flows is justified first by the general framework of this thesis, and also because the ability of 2D numerical models to simulate such flows has been demonstrated (Shettar and Murthy 1996), whereas supercritical (Mignot et al. 2008) or transcritical (El Kadi Abderrezzak et al. 2011) flows can lead to discrepancies when using 2D numerical models. As one aim of this study is to assess the ability of a 2D model to predict influence of obstacles and detailed topography on the dividing flows, a prior requirement is the ability of such model to accurately simulate dividing flows without obstacles. Then, the

chosen junction configuration is the most studied configuration, for which flow patterns have been described and relationships linking global flow characteristics have been derived. Results of previous studies on such configuration are summed up in the following.

2.1.1 Dividing flow in a 3 branch junction

2.1.1.1 Flow pattern

It should be noted that dividing flows that remain subcritical everywhere form only one fraction of what is usually considered as "subcritical dividing flows". Indeed, as stated in Riviere et al. (2007), three regimes can be identified:

- Subcritical flow everywhere
- Subcritical everywhere except in the contracted region of the branch channel (occurrence of a choked flow)
- Transition from sub to supercritical flow in the main channel

Choked flow in the branch channel is reported to occur for a branch channel Froude number larger than 0.35 (Ramamurthy et al. 1990), despite this should be considered as a fuzzy transition (Riviere et al. 2007).

The flow pattern for a full subcritical dividing flow in a 3 branch junction has been studied with laboratory measurements and 3D simulations by Neary et al. (1999), and a scheme is shown on Figure 2.1. The flow in the main (upstream) branch is divided through a dividing stream surface, starting upstream of the junction and reaching the downstream corner of the junction. The location of the corresponding dividing streamlines varies over depth, because the velocities are larger near the surface than near the bed, and the capacity of the flow to rotate towards the branch is then higher near the bed than near the surface. This was observed experimentally by Neary and Odgaard (1993), with larger variations occurring for larger bed roughness or upstream to branch velocity ratios. The flow entering the branch channel separates at the upstream corner of the junction, leading to a separation zone along the upstream wall of the branch channel (zone A in Figure 2.1). This separation zone reduces the effective width and capacity of the branch channel, and corresponding contraction coefficient has been studied to develop flow distribution models (Law and Reynolds 1966; Hsu et al. 2002). A stagnation region is located at the downstream corner of the junction, where downflow occurs and secondary flows are generated in both downstream and branch channels. The secondary circulation interacts with the recirculating flow in the branch

channel, which leads to very complex 3D flow patterns (Neary et al. 1999). Finally, for large branch to main channel flow discharges ratios, another separation zone can form downstream of the junction, along the channel wall opposite to the branch (zone B in Figure 2.1).

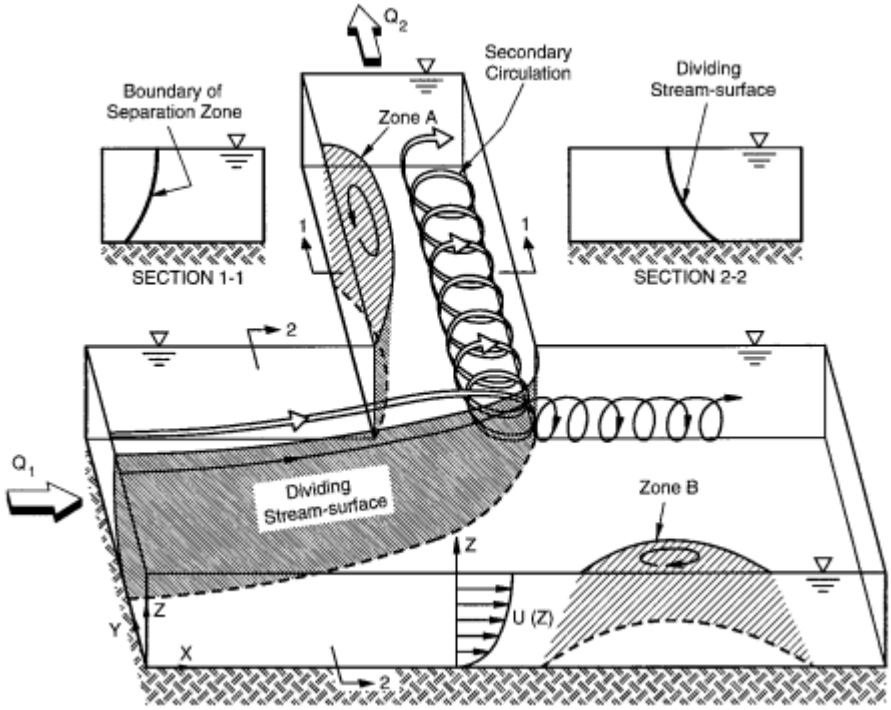

Figure 2.1 : Flow pattern in a subcritical dividing flow (from Neary et al. 1999)

Because of the flow expansion in the junction and its contraction in the branch channel, local Froude number can rise and exceed 1, leading to supercritical flows in the junction or in its vicinity. In such cases, besides the flow patterns described for subcritical flows, additional flow structure can form (e.g. hydraulic jumps, standing waves or bow waves). Law and Reynolds (1966) shows that occurrence of these flow structures can be related to both the main branch Froude number and the discharge ratio. The whole flow in the junction can become supercritical for high main branch Froude numbers and/or extreme values of the discharge distribution, but no threshold values are reported in the literature.

2.1.1.2 Distribution models and numerical modelling

Presence of waves and hydraulic jumps can affect the control of the flow distribution, therefore the proposed analytical distribution models are usually restrained to a range of flow conditions (e.g. Froude number in one branch) (Ramamurthy and Satish 1988; Hsu et al. 2002; Riviere et al. 2007). For urban flood modelling, integrating such models for 1D modelling of the flows through a street network is compulsory. However, attempts previously

carried out (Lhomme et al. 2006; Kouyi et al. 2010; Ghostine et al. 2012) showed that these distribution models may not be appropriate, and in all cases lead to higher errors than when using an explicit modelling with two-dimensional models. Complexity of street cross sections and of urban flood flows in a street network do not actually allow for a generalization and extensive use of these analytical distribution models, the latter being more adapted for standard geometries (open channels, pipe networks…etc.).

2.1.2 Flow around obstacles

Graf and Yulistiyanto (1998) reported laboratory measurements of a fully turbulent subcritical open-channel flow around a non-submerged cylinder. Extensive 3D velocity fields allowed them to describe the flow pattern in the vicinity of the cylinder (Figure 2.2). Presence of the obstacle forces the flow to pile up upstream, creating an adverse pressure gradient upstream and a separation of the incoming flow from the bottom. This results in a three-dimensional *horseshoe-vortex system*, with a vortex which starts in front of the cylinder bottom, and stretches downstream, remaining close to the cylinder. As the flow is deviated around the cylinder, local accelerations are observed on the sides of the cylinder. Moreover, a wake is observed downstream of the cylinder, with a reverse flow and high turbulent intensities.

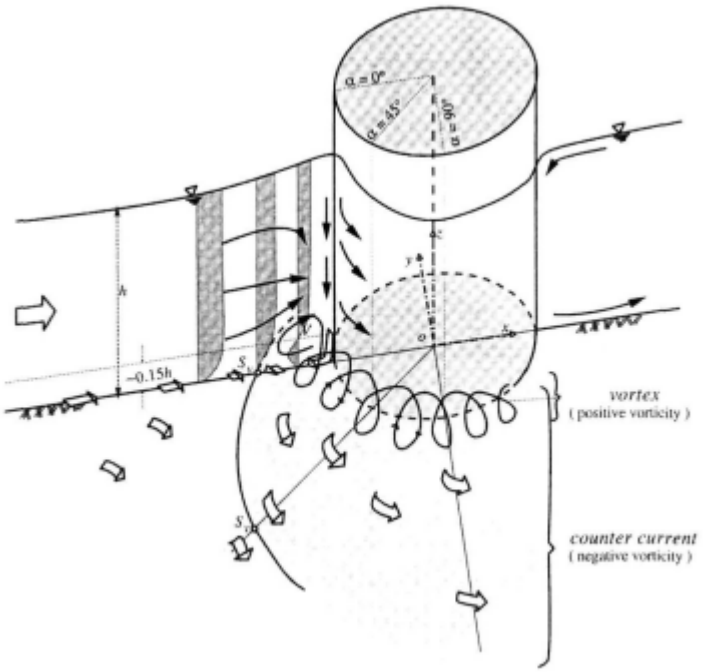

Figure 2.2 : Flow pattern around a cylinder (from Graf and Yulistiyanto (1998))

Chen and Jirka (1995) studied the structure of the wake for **turbulent shallow flows**. At high Reynolds number, the structure of the wake downstream of the obstacle does not depend on the Reynolds number (in contrast with low Reynolds number flow) and is governed by a wake parameter $S=fD/4H$, with D the obstacle width, H the water depth upstream and f the channel Darcy-Weisbach friction factor. For a cylinder, for S<0.2, vortex shedding occurs and leads to a vortex street in the wake, differing from the low Reynolds Von Karman vortex street because of the two-dimensionality of the coherent structures in shallow flows. For 0.2<S<0.5, the wake consists in an unsteady bubble reaching a length between 1.5 and 2.5 times the obstacle width. For higher wake parameters (S>0.5), a steady bubble wake appears, with the same length as the unsteady ones.

Applications of flow around obstacles in hydraulics mainly concern evaluation of scour around bridge piers (e.g., Breusers et al. 1977) and flow resistance of vegetated channels (e.g., Wilkerson 2007; Aberle and Järvelä 2013), and corresponding studies are carried out with uniform approaching flow. One example of study of emerged obstacles in the vicinity of a dividing flow is reported by Nougaro et al. (1975). The authors place an emerged cylinder at the entrance of a branch channel to stabilize the flow in this channel. The study does not report precise measurements of the effects of the obstacle, but visual observations indicate that the latter can stop oscillations in the branch channel. No other studies coupling dividing flows and obstacles could be found.

2.2 Experimental facility and measuring devices

Experiments were carried out at the LMFA (Laboratoire de Mécanique des Fluides et Acoustique), on the urban crossroad model (see Figure 2.3). The facility consists in 3 horizontal glass channels with the same width (b=0.3 m) joining perpendicularly. A flow is generated in the upstream channel (length L_u = 2.0 m) and divides into the branch and the downstream channel (of respective lengths L_b = 2.6 m and L_d = 2.6 m). The upstream flow discharge Q_u is generated using a pump and a valve, and is stabilized through the use of a feeding tank and a honeycomb placed at the entrance of the channel. Branch and downstream channel flows are controlled at the outlets by sharp crested weirs of adjustable height (respectively C_b and C_d), and outflows are collected in tanks located downstream. The branch flow is redirected to the downstream channel collecting tank, and the whole collected flow returns into the pumping loop, so that the whole set-up operates in a closed loop.

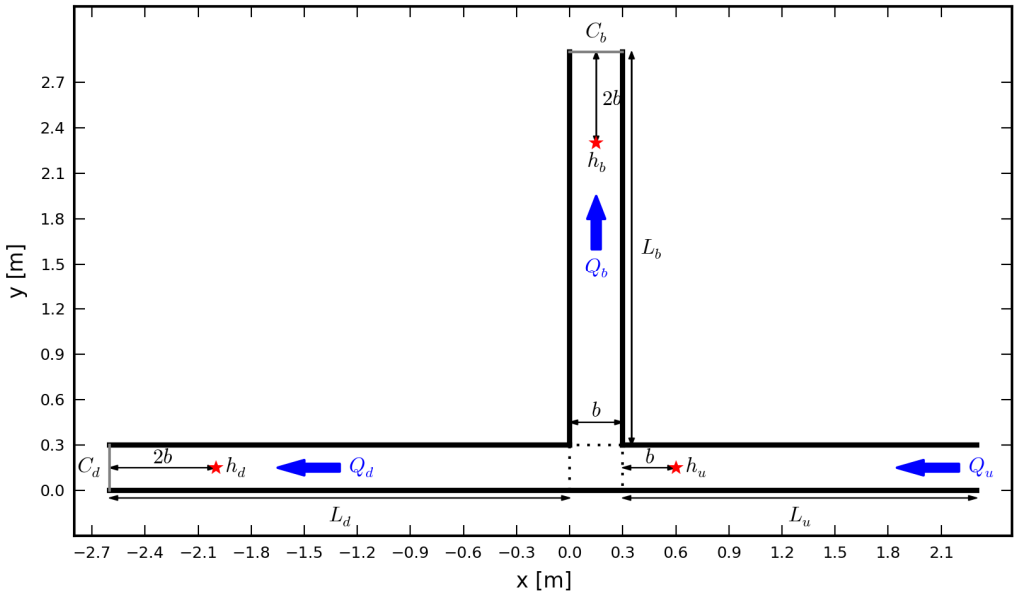

Figure 2.3 : Scheme of the LMFA crossroad model in a 3branch dividing flow configuration and main notations

Upstream and branch channel flow discharges Q_u and Q_b are measured with electromagnetic flow meters (accuracy being the maximum of 0.02 L.s-1 or 0.5% of the flow discharge) located in the pumping loop. A movable point gauge is used to measure the water depths and the weir crest height, with an estimated accuracy of 0.25 mm. The controlled boundary conditions are thus Q_u, h_b and h_d, and the main measurements are Q_u and Q_b.

Particle Image Velocimetry (PIV) measurements are carried out in the junction and in the branch channel to measure horizontal velocity fields for a few flow configurations. Polyamide particles (50 µm diameter) are used as tracers. Black tissues are used to put recorded flow regions in the dark, and a white light generator is used to create a horizontal light sheet with a thickness of around 5mm. To record particle motions within this light sheet, we use a 1280x1920 pixels CCD camera, located above the free surface at an elevation of about 1.1 m. This set up leads to a horizontal resolution of 0.5mm per pixel, with an effective 350 x 500 mm measurement area. For each horizontal plane, a series of 4000 images are recorded with a time step of 1/30 s (30 Hz). PIV computations are carried out on a 15 x 15 mm regular grid with the commercial software Davis from Lavision, and time averaged velocities are computed to use in this thesis.

Experimental conditions could not ensure accurate PIV computations for fast flows (typically velocities larger than 0.25 $m.s^{-1}$). Large-Scale PIV (LSPIV) is carried out for faster flows. However this technique cannot capture flow velocities in all areas, as seeded particles

may be ejected by vertical flows reaching the free surface. LSPIV data provide only limited information and are only considered as a global validation data for numerical simulations.

2.3 Choice of flows, obstacles and sidewalks configurations

2.3.1 Dimensional analysis

Dimensional analysis follows the approach presented by Riviere et al. (2007). For a reference dividing flow without obstacles/sidewalks, there are 10 variables that rule the discharge distribution: the acceleration due to gravity g, the channel width b, the flow discharges and water depths in each branch (Q_u, h_u, Q_b, h_b, Q_d and h_d), and the two weir crest heights C_b and C_d. The available equations are:

- The mass conservation $Q_u=Q_b+Q_d$
- The stage discharge relationships for each sharp crested weir (Q_b, C_b, h_b) and (Q_d, C_d, h_d)
- The relationship proposed by Ramamurthy et al. (1990) linking the depth in the upstream channel h_u to the depth h_b and flow rate Q_b in the branch channel.
- The empirical discharge distribution law (Q_b, Q_d, C_b, C_d, Q_u, g) provided by Riviere et al. (2007)

The 5 remaining variables are then b, g, Q_u, h_u and Q_b, including a length scale b and a time scale b^3/Q_u. The 3 final parameters that rule the flow distribution in the bifurcation are then:

- The Froude number in the upstream channel $F_u = Q_u/[b.h_u(g.h_u)^{0.5}]$
- The discharge distribution $R_q=Q_b/Q_u$
- The normalized upstream water depth h_u/b

In order to investigate the effects of the three parameters defined above, 3 series of flows are defined (Table 2.1). From a reference flow (flow 3), boundary conditions (Q_u, C_b, C_d) are adjusted to vary one of the studied parameter (F_{u0}, R_{q0}, h_{u0}/b) while the two others are kept constant. Preliminary tests allowed us to assess the range of flow conditions that can be simulated experimentally, and the final chosen flows are selected to fairly represent this

available range. These 14 flows are referred as **initial flows** in the following (that is, flows without obstacles or sidewalks), and the subscript "0" is used when referring to them.

Series	Flow number	Q_{u0} L.s^{-1}	C_b mm	C_d Mm	F_{u0} -	R_{q0} -	h_{u0}/b -
S1	1	6.01	11.2	16.2	0.79	0.39	0.13
	2	4.99	20.8	19.0	0.60	0.39	0.14
	3	**4.01**	**26.5**	**22.3**	**0.45**	**0.39**	**0.15**
	4	3.00	30.2	25.6	0.33	0.39	0.15
	5	2.51	31.7	27.6	0.28	0.40	0.15
	6	2.00	31.7	27.6	0.23	0.38	0.14
S2	7	4.00	32.7	18.4	0.44	0.23	0.15
	3	**4.01**	**26.5**	**22.3**	**0.45**	**0.39**	**0.15**
	8	4.00	22.2	25.8	0.45	0.51	0.15
	9	4.00	22.2	25.8	0.44	0.65	0.15
	10	3.99	22.2	25.8	0.45	0.80	0.15
S3	11	1.66	15.2	12.7	0.44	0.40	0.08
	12	2.77	21.0	17.1	0.45	0.38	0.12
	3	**4.01**	**26.5**	**22.3**	**0.45**	**0.39**	**0.15**
	13	5.38	33.0	27.6	0.45	0.39	0.18
	14	7.00	33.0	27.6	0.45	0.39	0.22

Table 2.1 : Experimental parameters and non-dimensional parameters for the bifurcation flows grouped in 3 series (with varying F_{u0}, R_{q0} and h_{u0}/b). The reference flow is indicated in bold (common to each series). Flow 6 is the flow measured with PIV.

2.3.2 Obstacles and sidewalks configurations

A total of 9 obstacles configurations are studied: 7 single obstacle configurations, and 2 double obstacles configurations. Each obstacle is a square cylinder with a width w_o = 5 cm, that is 1/6 of the channel width b. This size has been chosen considering preliminary numerical simulations (to ensure that the impact of these obstacles would be detected experimentally) and in agreement with typical sizes of obstacles located in streets. Assuming a model scale between 1:15 and 1:30 (which corresponds to a street width of 4.5-9.0 m), this leads to a real-scale obstacle typical size of 0.75-1.5 m, which can represent pieces of urban furniture. Moreover, this obstacle dimension remains compatible with typical mesh elements size used in 2D urban flood models. Obstacles height (15 cm) and material (aluminium) ensure that in all experiments, obstacles remain non-submerged and immobile. 6 obstacle locations among the single obstacle configurations permit to cover areas just near the junction, with two obstacle locations in each channel (Figure 2.4). The seventh location consists in the centre of the junction (obstacle 7). The 8th and 9th configurations consist in coupling the obstacle 2 with respectively the obstacle 4 and the obstacle 6. Obstacle 2 has been chosen as the base obstacle for these double-obstacle configurations as it was the most influent obstacle.

One single configuration of sidewalks is studied (Figure 2.4). The sidewalks are all 2 cm high and 6 cm wide, and are located all along the channels lateral walls. They are made of wood, ballasted with steel bars to prevent floating and painted in black for PIV measurements. As for obstacles, sidewalks dimensions were defined according to preliminary numerical simulations and scaling considerations. However, note the chosen sidewalks are relatively high, a 1:15 scaling leads to 30 cm high and 0.9 m wide sidewalks (and 60 cm x 1.8 m for a 1:30 scale).

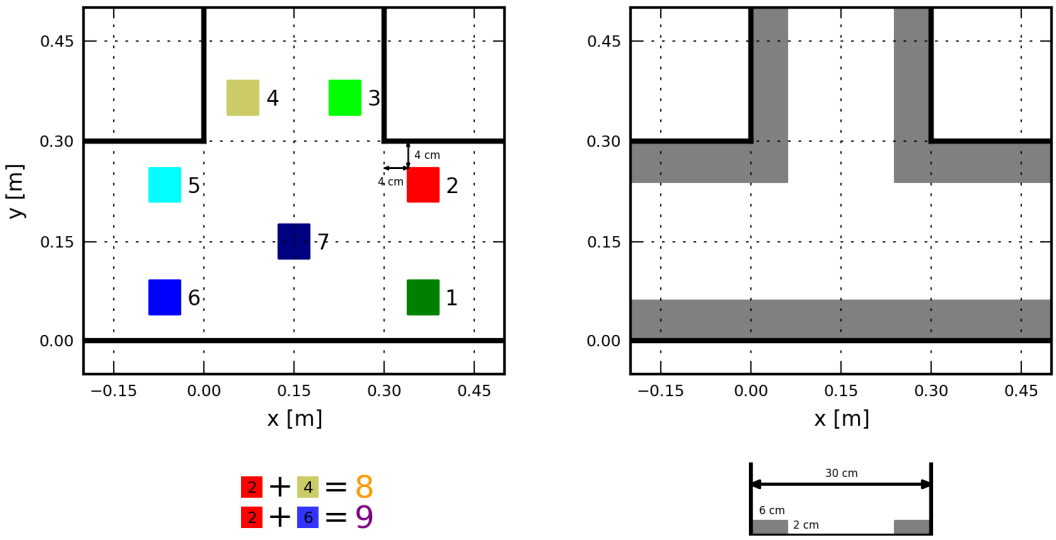

Figure 2.4 : Obstacles and sidewalks configurations

2.3.3 Methodology and measurements

The aim of the experiments is to assess the effects of several singularities on the series of 14 initial flows listed in Table 2.1. Therefore the experimental protocol aims at accurately generating the initial flows (without singularities) and minimizing errors when assessing effects of singularities on flow characteristics. For each flow (initial, and with singularities), measurements are carried out to obtain the flow discharge in the upstream and branch channels (Q_u and Q_b), the water depths two channel width upstream of both sharp crested weirs in the branch and downstream channels (h_b and h_d), and the water depth in the upstream channel h_u, at one channel width upstream of the junction (Figure 2.3). For obstacles, the protocol follows the following steps:

- The flow boundary conditions are set up to generate the initial flow (Q_u, C_b, C_d) according to Table 2.1

- Once the initial flow is stabilized, measurements mentioned above are carried out (Q_{u0}, Q_{b0}, h_{u0}, h_{b0} and h_{d0})
- Keeping the same boundary conditions, obstacle *i* is introduced
- Once the flow with obstacle *i* is stabilized, measurements are carried out (Q_{ui}, Q_{bi}, h_{ui}, h_{bi} and h_{di}), and the obstacle is replaced by another one

Due to the difficulty of positioning sidewalks, the corresponding protocol slightly differs. Sidewalks are set up in the experimental model and measurements of each flow with sidewalks are carried out in a row, by adjusting the boundary conditions again for each flow. Therefore, this method is slightly less accurate, as the boundary conditions are set up twice for a flow (initial flow, and flow with sidewalks). To ensure continuity in the variable notations, the sidewalks configurations are noted with the subscript "10".

For each flow and each obstacle *i* (*i* in [0, 10]), the branch to upstream discharge ratio R_{qi} is calculated:

$$R_{qi} = \frac{Q_{bi}}{Q_{ui}} \tag{2.1}$$

The evolution of this discharge ratio ΔR_{qi} is then computed for each obstacle or sidewalk configuration *i* (*i* in [1, 10]):

$$\Delta R_{qi} = R_{qi} - R_{q0} \tag{2.2}$$

Besides this reference value, maximum and minimum values are computed considering flow discharge measurement uncertainties:

$$\Delta R_{qi,max} = \frac{Q_{bi} + Q_{bi,err}}{Q_{ui} - Q_{ui,err}} - \frac{Q_{b0} - Q_{b0,err}}{Q_{u0} + Q_{u0,err}} \tag{2.3}$$

$$\Delta R_{qi,min} = \frac{Q_{bi} - Q_{bi,err}}{Q_{ui} + Q_{ui,err}} - \frac{Q_{b0} + Q_{b0,err}}{Q_{u0} - Q_{u0,err}} \tag{2.4}$$

With the error in discharge estimation $Q_{xi,err}$ = max(0.02 L.s-1, $0.005 \cdot Q_{xi}$), "*x*" being either "*b*" or "*u*". This method is severely conservative for obstacles, as the subtraction operated in Eq.2.2 should compensate most of the errors on the measurement discharges, considering the experimental protocol.

One water depths line is measured in the main channel (15 points) and in the branch channel (3 points) for each flow, except for flows 5 and 6, as their characteristics are very close to the ones of flow 4. For each measured flow, the water depths are measured for the

initial flow and for the same flow with one obstacle configuration, chosen as the one which impacts the most the water depths (based on visual observations). Additionally, for a few flows, these water depths are also measured for flows with sidewalks. These data are not used in the experimental analysis but will be used as validation data for numerical modelling (Chapter 3). Figures of these water depths lines can be found in Appendix A.2.1.

Besides these discharges and water depths measurements, velocity fields were measured for two flows to help analysing the measured discharge ratio evolutions. For the reference flow (flow 3 in Table 2.1), all flow cases (initial, obstacles, sidewalks) are measured with LSPIV in the junction and in the branch and downstream channels. Nevertheless, this technique suffers from inaccuracy in highly 3-dimensionnal flow areas and recirculating areas. Thus, horizontal PIV measurements are carried out for the slowest flow (flow 6 in Table 2.1) at the elevation z=3 cm. For the latter, measurements include the initial flow, obstacle configurations (1, 2, 4, 5, 6) and the sidewalks configuration. Obstacle 3 has no significant effect for this flow (except a perturbation of the branch channel recirculation area, which is the main concern of this study) so it is not measured with PIV. Flow with obstacle 7 is not measured as the latter generates large shadow areas for which PIV measurements cannot be carried out. Finally, obstacles 8 and 9 are found to have very similar effects than obstacle 2 for this flow, so that their corresponding velocity fields are not measured.

Influence of the singularities on the initial dividing flow is analysed through the measured values of ΔR_{qi}. Water depths measurements in the downstream and branch channels are not considered in the experimental analysis but are useful for numerical simulations, as they permit to derive the stage-discharge relationships of the sharp crested weirs. Measured water depths upstream of the junction evolve as a result of the energy losses due both to the obstacles and to the evolution of the discharge distribution. Therefore, these evolutions are *a priori* complex and are not considered in the experimental analysis. However they can be used as a second validation parameter for numerical simulations.

2.4 Results

Experimental results have been presented in Mignot et al. (2013), with additional data obtained by numerical simulations with a three-dimensional model. Some of the experimental observations are not trivial to explain with the available measurements alone, and numerical simulations have proved to be useful to complete the analysis. References to this article or to

the two-dimensional simulations presented in Chapter 3 will be done in the following sub sections each time experimental data cannot explain alone the evolutions of the discharge distribution.

2.4.1 Influence of single obstacles

2.4.1.1 Qualitative description

Figure 2.5 shows the measured velocity fields for the flow 6, for the initial flow and several obstacles and sidewalks configurations. For the initial flow, the velocity field shows that as the flow expands in the junction, it divides between the downstream and the branch channels along a dividing stream line and its velocity along x axis decreases. In the branch channel, the flow is accelerated on the left bank, while a separation area appears on the right bank, with very low velocities. This structure is consistent with what was described by Neary et al. (1999) (see also Figure 2.1). Considering the velocity fields for flows with obstacles and evolutions of the discharge distribution (Figure 2.6 to Figure 2.8), effect of each single obstacle can be interpreted as follows:

- Velocity field around obstacle 1 (Figure 2.5) reveals that the latter accelerates the right part of the upstream flow in the junction. This acceleration increases the flow inertia, which limits its capacity to rotate towards the branch channel. As a result, the discharge distribution decreases ($\Delta R_q<0$ on Figure 2.6 to Figure 2.8).
- Obstacle 2 accelerates the left part of the upstream flow and deflects it towards the left wall of the upstream channel and the junction. Both phenomena tend to limit the flow capacity to enter the branch channel, so that Q_b decreases (thus $\Delta R_q<0$), and effects are larger than for obstacle 1.
- Obstacle 3 is located in the slow separation area in the branch channel; therefore its effect is almost negligible.
- Obstacle 4 is located in the acceleration zone of the branch channel, where the branch flow is contracted because of the separation zone, and the presence of the obstacle further decreases the flow area in the branch, finally preventing the incoming flow to enter this branch ($\Delta R_q<0$)
- Obstacles 5 and 6 decreases the flow area at the entrance of the downstream channel, which redirects the junction flow towards the branch channel ($\Delta R_q>0$)

- Effects of obstacle 7 are related to the initial location of the dividing streamline, as discussed in section 2.4.1.3. As in most of initial flows, the location of obstacle 7 is on the left side of the dividing streamline, introducing obstacle 7 mainly affects the left part of the upstream flow, redirecting part of it to the branch channel ($\Delta R_q>0$).

Globally, for the range of parameters tested, evolution of the discharge distribution varies between -14% to +8% but appears to vary significantly with the flow parameters, so that impact of the latter has to be assessed.

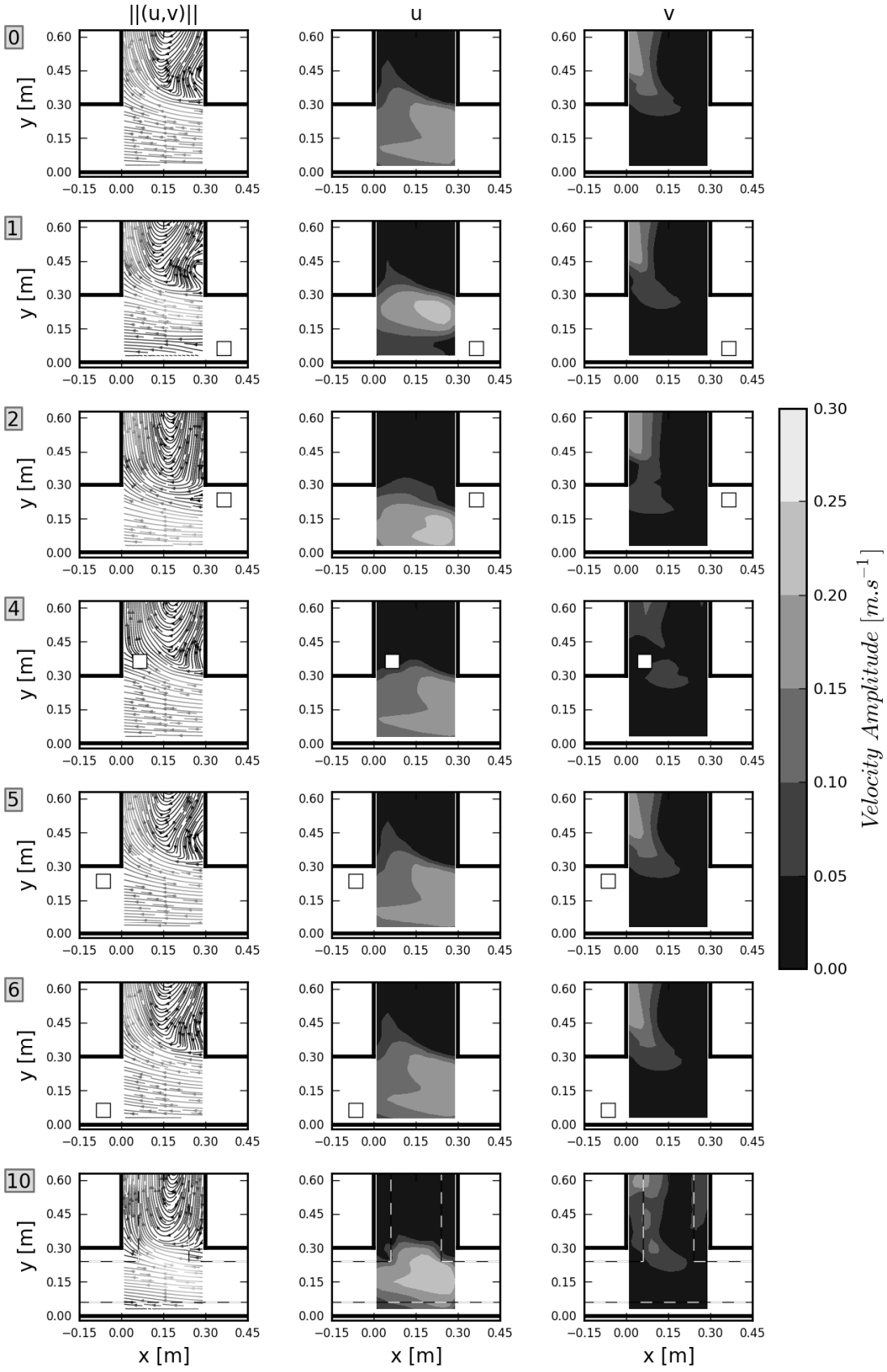

Figure 2.5 : Streamlines (left), amplitude of the x-axis (u, centre) and y-axis (v, right) components of the time-averaged velocity measured with PIV for flow6, without obstacles (0), with obstacles (1, 2, 4, 5 and 6) and with sidewalks (10).

2.4.1.2 *Influence of the initial upstream Froude number F_{u0}*

For a fixed initial upstream water depth h_{u0} and discharge distribution R_{q0}, increasing the upstream channel Froude number F_{u0} increases the effect of all obstacles (Figure 2.6): ΔR_q increases in absolute value as F_{u0} increases, without any change of sign. First, note that larger upstream channel Froude number implies larger Froude number also in the junction and in the downstream channels (and so at each obstacle location). Then, the Froude number represents the square root of the ratio of the inertia force over gravity force, and obstacles have larger effects on flow with larger inertia. From another point of view, as the upstream water depth is constant in this series, the upstream channel flow velocity directly rises with F_{u0}. Drag force (or resistance force) on an obstacle is proportional to the square of the approaching flow velocity, so that in this series effects of obstacles are enhanced for larger F_{u0}. Finally, visual observations show the presence of supercritical flow with an oblique hydraulic jump for flow 1 (F_{u0}=0.79), but this flow pattern does not lead to abrupt changes or trend inversion for the curves ΔR_q=f(F_{u0}).

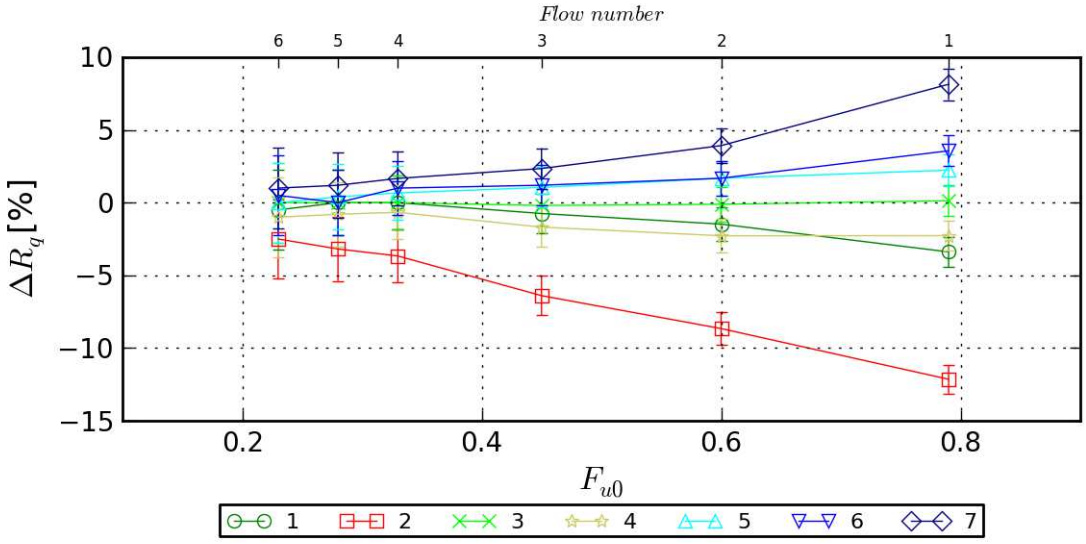

Figure 2.6 : Influence of the upstream Froude number Fu0 on the discharge distribution evolution for obstacles 1 to 7

2.4.1.3 *Influence of the initial discharge distribution R_{q0}*

The 2 other flow parameters (F_{u0} and h_{u0}/b) being fixed, the initial discharge ratioR_{q0} defines the flow pattern in the junction and in both outlet channels without obstacles. This flow pattern is essential in the understanding of the effects of obstacles for this series, which evolution is somehow complex (see Figure 2.7); however it was not measured in the experiments. Therefore, we introduce results from some numerical simulation here.

Simulations are presented in details in the next chapter, and in the present chapter we only refer to the series of figures shown in Appendix A.1, where the simulated two-dimensional flow pattern in the vicinity of the junction is sketched for each initial flow. As the initial discharge distribution R_{q0} increases, it appears that i) the dividing streamline in the junction moves towards the left bank wall and ii) the branch channel recirculation area narrows (that is its frontier with the lateral flow approaches the right bank). Considering both these physical lines, evolution of the discharge ratio ΔR_{qi} when introducing obstacles can be interpreted as follows:

- Obstacle 1 accelerates the upstream flow and deflects a part of it on the right side of the upstream channel (see section 2.4.1.1). This acceleration limits the upstream flow capacity to rotate in the branch channel. However, as the initial discharge distribution R_{q0} increases, the dividing streamline moves towards the obstacle 1, and part of the deflected flow crosses this line and reaches the branch channel. Therefore effects of the obstacle decrease with increasing R_{q0} and ΔR_{q1} can become non-significant (flows 9 and 10).
- Oppositely, for obstacle 2, as R_{q0} increases, the dividing streamline moves away from the obstacle and effects of the latter are reduced (the flow accelerated and deflected toward the left bank remains in the part of the upstream flow that finally reaches the branch channel). However, for very low initial discharge distribution (flow7), the dividing streamline is very close to the obstacle, and an important proportion of the upstream flow is deflected to the right side of the obstacle (between the obstacle and the right bank wall), so that the effect of the obstacle is reduced when compared to higher values of R_{q0}.
- As R_{q0} increases, the flow discharge in the branch channel increases, and effects of obstacles 3 and 4 thus increase. Obstacle 3 has significant effects only as R_{q0} exceeds a threshold value (around 0.6 according to Figure 2.7). Indeed, as R_{q0} increases, the width of the branch channel recirculating area decreases, and obstacle 3 passes from the slow recirculating flow region to the accelerated flow region and then affects the branch channel main flow.
- Oppositely, obstacles 5 and 6 being at the entrance of the downstream channel, their effect is enhanced as the downstream channel flow discharge increases, that is for decreasing values of R_{q0}.

- Due to its central position in the junction, obstacle 7 can be located either on the right or left side of the dividing streamline and redirect the upstream flow accordingly. For low values of R_{q0}, part of the left portion of the upstream flow is deflected by obstacle 7 to the branch channel and $\Delta R_q>0$. This effect is enhanced as R_{q0} increases and as the dividing streamline approaches the obstacle, until a value of 0.5, and then effects are reduced. For large values of R_{q0}, obstacle 7 deflects towards the left bank wall a part of the upstream flow that was initially reaching the branch channel, so that $\Delta R_q<0$.

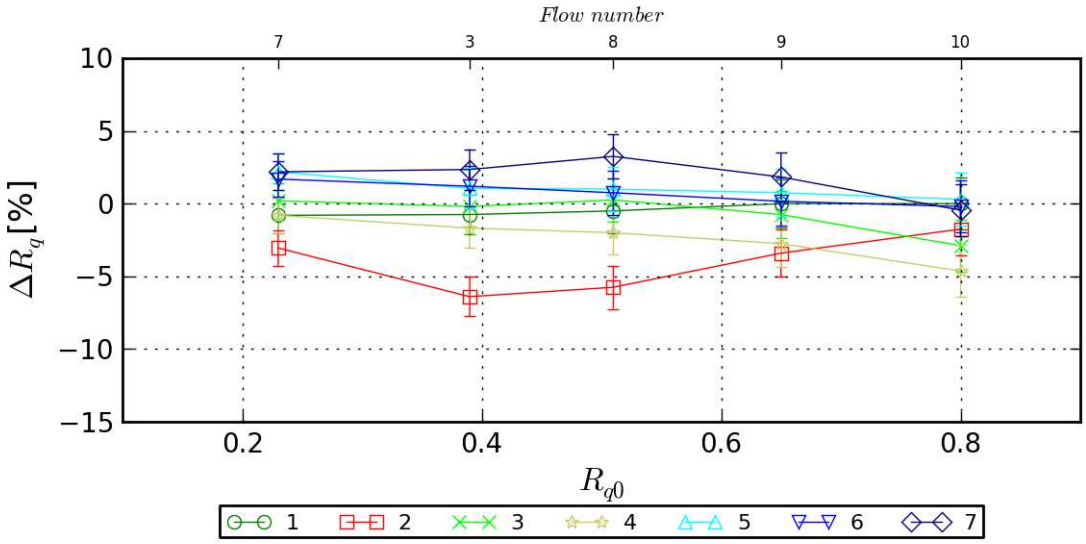

Figure 2.7 : Influence of the initial discharge ratio R_{q0} on the discharge distribution evolution for obstacles 1 to 7

2.4.1.4 *Influence of the initial normalized upstream water depth h_{u0}/b*

The normalized water depth does not have a significant influence on the impact of obstacles on the discharge distribution, especially when considering measurement uncertainties for low water depths (flow 11 and 12 on Figure 2.8). The only remarkable trend lies in the evolution of ΔR_q for obstacle 2. Higher water depths may increase three-dimensional flow patterns in the obstacles wake and in the whole flow in the vicinity of the junction. Modification of the wake for obstacle 2 and interaction of the latter with the highly three-dimensional flow entering the branch channel may explain the observed evolution of ΔR_q. This is suggested by the numerical simulations carried out by the Hong Kong Polytechnic University (Mignot et al. 2013), but an advanced interpretation of these interactions remain difficult considering the available data.

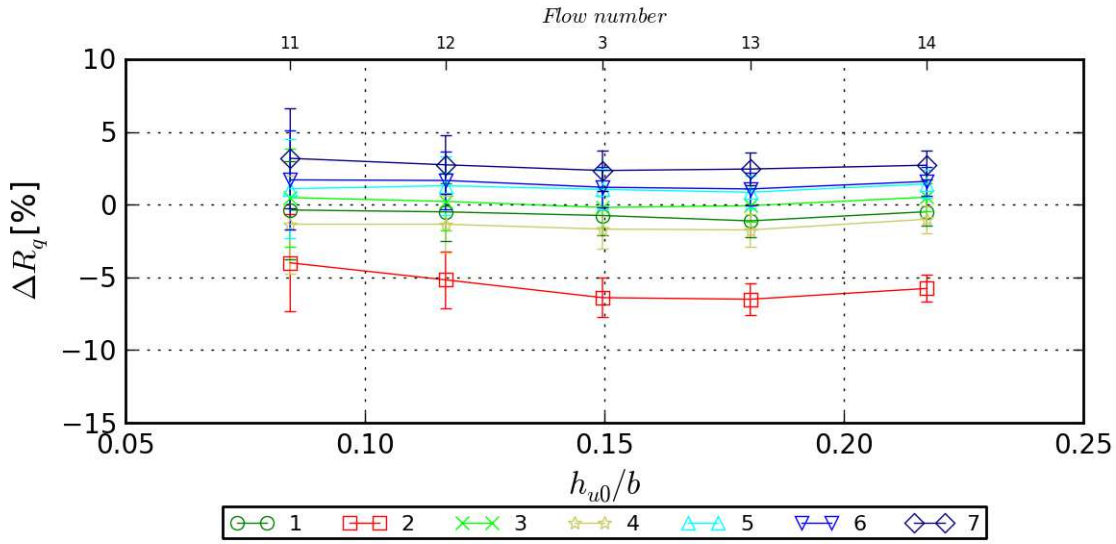

Figure 2.8 : Influence of the normalized upstream water depth h_{u0} on the discharge distribution evolution for obstacles 1 to 7

2.4.2 Influence of double obstacles

Effects of the double obstacles configuration 8 (respectively 9) can be explained by the effects of the corresponding single obstacles 2 and 4 (respectively 2 and 6). Figure 2.9 shows the measured effect of these double obstacle configurations, along with the arithmetic sum of the measured effects of the two corresponding single obstacles:

- Effect of obstacle 8 is very close to the cumulated effects of obstacles 2 and 4, except for the flow with the lowest initial discharge distribution (flow 7, R_{q0}=0.23). For this flow, assuming that the upstream single obstacle 2 keeps the same effect on ΔR_q when combined with obstacle 4, the observed discrepancy should arise from a change of flow characteristics in the surroundings of obstacle 4. For other flows, this discrepancy is not observed, which means the flow characteristics in the branch channel are not significantly modified by obstacle 2.
- The sum of obstacles 2 and 6 effects lead to lower values of $|\Delta R_q|$ than with obstacle 9 for every flow. As obstacle 2 accelerates the flow in the junction near the left bank wall, the flow approaches obstacle 6 with larger velocities and effect of this obstacle are enhanced. Therefore, a larger part of the junction flow is diverted into the branch channel and this explains the observed discrepancies.

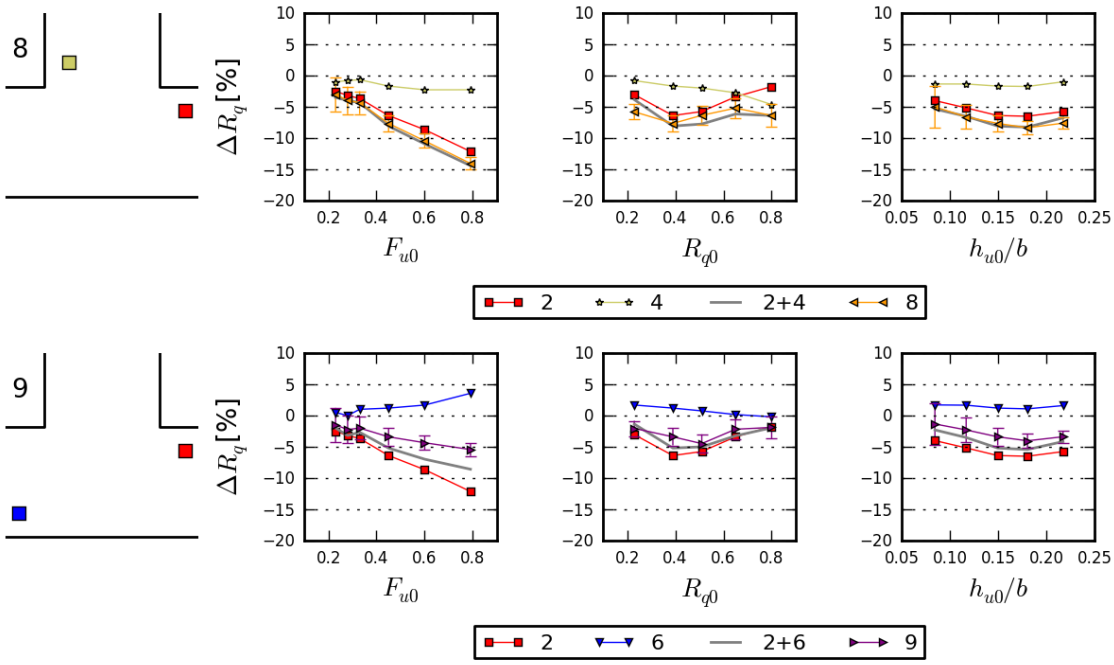

Figure 2.9 : Effects of the double obstacles configurations, and comparison to the sum of the effects of the corresponding single obstacles

2.4.3 Influence of sidewalks

As seen on the bottom of Figure 2.5, the sidewalks accelerate the flow in the centre part of the channels. As for obstacles 1 and 2, the larger inertia of the upstream flow limits its capacity to rotate in the branch channel. Neary et al. (1999) show that a larger portion of the near bed flow compared to near surface flow is deviated in the branch channel (hence the shape of the three-dimensional dividing surface shown on Figure 2.1), as a consequence of the vertical velocity profiles. Sidewalks partially block the near bed flow, so that their effects may be impacted by this 3-dimensional flow structure (yet this was not measured in the experiments).

For each flow, introduction of sidewalks leads to a decrease of the branch channel discharge (Figure 2.10). As for obstacles, the effect is enhanced for larger upstream Froude numbers F_{u0}. What may differ by nature is the fact that this evolution is not as continuous as for the obstacles, and there is an abrupt variation between flow 2 (F_{u0}=0.60) and flow 1 (F_{u0}=0.79), with occurrence of a hydraulic jump for the latter (as mentioned in section 2.4.1.2). Numerical simulations show that introducing the sidewalks increases the portion of supercritical flow in the junction for flow 1, with an important modification of the initial hydraulic jump location and extent (see Figure 3.14). Such a clear modification of the flow

pattern does not appear for flow 2, so that the abrupt change in the discharge distribution evolution ΔR_{q10} is attributed to this phenomenon.

For the series with varying R_{q0}, the upstream flow acceleration due to the sidewalks remains the same (F_{u0} and h_{u0}/b are kept constant), and effects are to be explained by the branch channel or the junction flow characteristics. The presence of sidewalks may limit the flow acceleration along the left bank wall of the branch channel, where the local water depth is reduced. This limitation would be larger for larger approaching discharge, and so larger values of the initial discharge distribution R_{q0}, hence the trend observed. Such explanation yet lacks support of more precise experimental or numerical data, especially if there are three-dimensional effects.

Effect of the sidewalks also increases with smaller normalized upstream water depth $h_{u0}/_{\mathrm{b}}$. For the latter, the trend comes from the fact that smaller water depths imply larger flow acceleration when introducing the sidewalks and finally larger difficulties for the upstream flow to rotate in the branch.

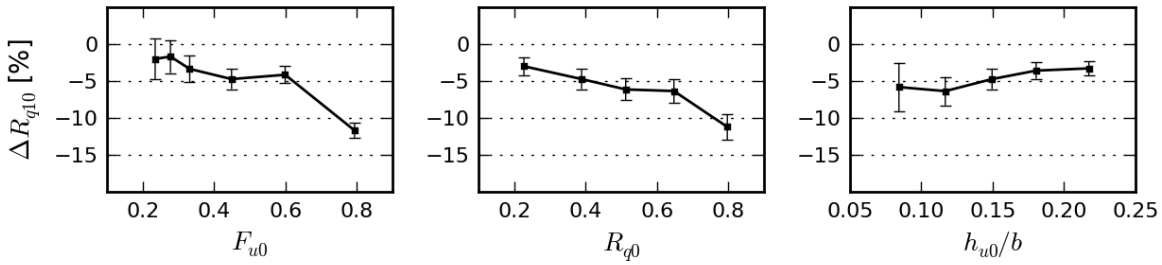

Figure 2.10 : Influence of the sidewalks on the discharge distribution

Conclusion

Experiments have been carried out at the LMFA to investigate effects of obstacles and sidewalks on the flow distribution through a 3 branch right-angle bifurcation. 9 obstacles and 1 sidewalks configurations have been studied for 14 flows, which allowed to detail the influence of 3 hydraulics parameters: the initial upstream branch Froude number F_{u0} and water depth h_{u0} and the initial discharge distribution R_{q0}. Measured evolutions of the discharge distribution can be significant (up to 12%), and especially show large variations depending on obstacles location and initial flow characteristics (i.e. flow without obstacle).

Analysis of these discharge distribution evolutions is carried out using experimental velocity fields available for one flow and several obstacles, along with preliminary numerical simulation results used to describe other initial flows characteristics and understand the corresponding impact. Even though the flows studied are highly three-dimensional, use of depth averaged two-dimensional flow pattern (obtained with numerical simulations) such as the dividing streamline in the junction and the recirculation area in the branch channel permits to explain most of experimental observations. Only effects due to the evolution of the wake downstream of a specific obstacle (obstacle 2, series with varying h_{u0}/b, Figure 2.8) remain difficult to explain without additional experimental data or more advanced CFD. For other flows and obstacles configurations, effects of obstacles remain relatively simple: flow acceleration (enhanced by the channel confinement), flow deflection around obstacles, and flow blockage upstream of the obstacles. However, combinations of these mechanisms and of the different initial flow characteristics lead to discharge distribution evolutions ranging from -12% to +8%, with a paramount importance of the obstacles location, then of the initial flow parameters F_{u0} and R_{q0}. Finally, introduction of sidewalks in the initial flows always redirect a part of the junction flow towards the downstream channel, as a result of the global flow acceleration. Effects of the upstream branch flow parameters (F_{u0}, h_{u0}/b) are intuitive, but the initial flow discharge R_{q0} may require additional data to be more clearly explained.

The observed discharge distribution evolutions are substantial and push towards an integration of such singularities in urban flood modelling. It is obvious that analytical models used for bifurcation models in 1D numerical modelling cannot be adapted to account for any kind of obstacles, so that such attempt should be carried out with 2D or 3D numerical models. Moreover, given the very local mechanisms observed, a simplified modelling based on porosity (Guinot and Soares-Frazao 2006) or explicit drag forces (Struve et al. 2003) may not be adequate. Therefore modelling of obstacles should be explicit, the remaining questions being the ability of the chosen numerical model to simulate the flow around the obstacle and its implication at the scale of the bifurcation flow. Considering the present experimental analysis, the key points in the numerical modelling should be an adequate simulation of the initial flows (discharge distribution, general flow pattern, including modelling of hydraulic jumps for high F_{u0} configurations), and of the deflections, accelerations and wakes generated by obstacles. Such modelling is presented in the next chapter with the use of a two-dimensional model, which is the typical tool used to simulate urban floods.

Chapter 3.

Numerical simulations of experimental crossroad flows

In this chapter, the depth-averaged two-dimensional (2D) code Rubar20 is presented and used for the simulation of the experimental flows described in the previous chapter. Simulations of the initial bifurcation flows (without obstacles or sidewalks) are studied in details, as the latter flows form the base of the experimental dataset. Simulations are then carried out for flows including obstacles or sidewalks. The different sets of numerical parameters follow two objectives:

- A calibration of a fine mesh model to achieve the best accuracy and discuss such model abilities and limitations
- An assessment of the model accuracy when used as in real case modelling conditions, that is with a coarse mesh and simpler parameterization

Expected results concern the possibility of integrating small-scale obstacles in urban flood models, and the necessity of considering detailed topography (i.e. sidewalks on a typical street profile).

3.1 Review of numerical simulations on dividing flows and flows around obstacle

3.1.1 Dividing flows

Finest modelling of subcritical dividing flows has been carried out with 3D models (e.g. Neary et al. 1999; Ramamurthy et al. 2007). Neary et al. (1999) showed the interest of using 3D models when the modelling objectives concern sediment transport and deposition. They found their model could accurately predict the averaged velocity field, which helps them explaining the deposition process in the surroundings of a bifurcation (1 inlet, 2 outlets). Other 3D models report fair agreement with experimental observations, and they have been used to derive more general results on dividing flows that may be fastidious to obtain through experimental measurements (Ramamurthy et al. 2007; Li and Zeng 2010). Discrepancies usually concern the velocity field for zones where the flow is highly three-dimensional, such as in the separation zone (Neary et al. 1999). According to these authors, a better agreement could be achieved by the use of a more advanced turbulence model (the various mentioned articles use a k-ε turbulence model).

2D modelling of subcritical dividing flows in a three branch junction has been carried out by Khan et al. (2000) and Shettar and Murthy (1996). Both models proved an excellent ability to compute the discharge ratio. Besides, Shettar and Murthy (1996) performed an extensive validation of the numerical model, using vertically-averaged velocity fields, water surface profiles at the junction, as well as more global flow characteristics such as the size of the branch separation zone and the energy loss in the junction. Note that the presence of supercritical flows and hydraulic jumps did not lead to particular errors in the simulations. Also, El Kadi Abderrezzak and Paquier (2009) showed the interest of using a two-dimensional model for subcritical flows, if expected modelling results concern the discharge distribution and the water depths.

Additional 2D modelling has focused on supercritical flows through 3 or 4 branch junctions. (Ghostine et al. 2009; Ghostine et al. 2010) used a 2D finite element method to predict these types of supercritical flows, and concluded to a fair agreement when comparing simulations with previously gathered experimental data. Mignot et al. (2008) proved the ability of the 2D numerical model used in the present thesis to reproduce the general flow patterns for supercritical flows in a cross junction. However, the difficulty linked to some

specific flow regimes and to the computation of the size and positioning of the hydraulic jumps may lead to considerable errors when estimating the discharge distributions to the downstream branches. For transcritical flows in a 3 branch junction and using the same numerical model, El Kadi Abderrezzak et al. (2011) reported similar difficulties, with errors in the discharge distribution up to 25 or 40 % depending on numerical parameters.

3.1.2 Flows around obstacles

In the literature, simulations of flows around obstacles mainly include detailed simulations of flows around bridge piers and other vertical hydraulic structures such as groynes. Obtaining detailed flow velocities is crucial to estimate bed deformation, so that 3D numerical models are used with elaborate turbulence and deposition/erosion models (e.g., Richardson and Panchang 1998). Numerical simulations of the depth-averaged flow around obstacles can be carried out by solving the shallow water equations, if adequate turbulence models are used. Yulistiyanto et al. (1998) simulated flow around a cylinder with a model solving such equations and considering a detailed modelling of the dispersion stresses due to vertical velocity profiles. Simulations predict well the velocities and water depths around the cylinder, without any calibration. Jiang et al. (2009) performed 2D modelling of flow past a vertical plate, and found an eddy viscosity model (computed via the friction velocity) can achieve reasonable prediction of the velocity field, yet with slightly higher discrepancies than a k-ε turbulence model. Stansby (2006) compared simulations of flow past a conical island with a 3D and a 2D model, including respectively a two-mixing-length and a horizontal mixing-length turbulence eddy viscosity model. Prediction ability of the 2D model was found to depend on the wake type, with discrepancies arising when predicting occurrence and length of stable wakes.

Operational numerical models used for urban flood modelling rarely consider turbulence effects, or use simple turbulence models (as recalled in the thesis introduction), as accurate modelling of turbulence would require computational efforts that are not affordable for such types of large-scale studies. Modelling of obstacles has then been mainly studied at large scale to account for buildings. Most accurate technique used consists in an explicit consideration of the corresponding impervious areas, with solid boundaries (e.g., Mignot et al. 2006), yet without detailed modelling of turbulence. Simplified modelling of obstacles includes the use of porosity models, for which modelling efforts are reported on estimation of

the global head losses, considering flow contractions and expansions (Guinot and Soares-Frazao 2006; Soares-Frazão and Zech 2008) or drag forces (Struve et al. 2003).

These latter models cannot simulate local changes of the velocity fields, which are of paramount importance for the prediction of discharge distribution in the experiments presented in Chapter 2. Therefore we will consider here only an explicit modelling of obstacles. From past results on this kind of simulations, it appears that the choice of a turbulence model strongly influences the modelling quality of the flow velocity downstream of obstacles. However this is not clear whether such fine modelling is required to model the evolutions of discharge distribution observed in our experiments. Therefore, this chapter aims at assessing possibility and limitations of a surface flow model typically used for urban flood modelling (i.e. without advanced turbulence modelling) to simulate previously described experimental flows.

3.2 Numerical model

3.2.1 Equations

The Rubar20 code (Paquier 1995) solves the 2D shallow water equations. The three governing equations consist in the continuity equation (Eq. 3.1) and the conservation of momentum along orthogonal axis x and y (Eqs. 3.2 and 3.3):

$$\frac{\partial h}{\partial t}+\frac{\partial (hu)}{\partial x}+\frac{\partial (hv)}{\partial y}=0 \qquad 3.1$$

$$\frac{\partial (hu)}{\partial t}+\frac{\partial (hu^2)}{\partial x}+\frac{\partial (huv)}{\partial y}+gh\frac{\partial h}{\partial x} = -gh\frac{\partial Z_b}{\partial x}-g\frac{u\sqrt{u^2+v^2}}{{K_s}^2 h^{1/3}}+K\left[\frac{\partial}{\partial x}\left(h\frac{\partial u}{\partial x}\right)+\frac{\partial}{\partial y}\left(h\frac{\partial u}{\partial y}\right)\right] \qquad 3.2$$

$$\frac{\partial (hv)}{\partial t}+\frac{\partial (hv^2)}{\partial y}+\frac{\partial (huv)}{\partial x}+gh\frac{\partial h}{\partial y} = -gh\frac{\partial Z_b}{\partial y}-g\frac{v\sqrt{u^2+v^2}}{{K_s}^2 h^{1/3}}+K\left[\frac{\partial}{\partial x}\left(h\frac{\partial v}{\partial x}\right)+\frac{\partial}{\partial y}\left(h\frac{\partial v}{\partial y}\right)\right] \qquad 3.3$$

with h the water depth, u and v depth averaged velocities along respectively x and y axis, Z_b the bottom elevation, g the gravity acceleration, K_s the Manning-Strickler roughness coefficient (K_s=1/n), and K the eddy viscosity.

The simplest formulation for the eddy viscosity *K* assumes a constant value in time and space. Two other formulations can be used with Rubar20, by linking *K* to the local water depth *h*, the friction velocity u^* and a dimensionless coefficient *k*:

$$K = khu^* \tag{3.4}$$

The friction velocity u^* can be expressed either by considering the usual equation with the bottom friction (Eq. 3.5), and alternatively by considering the slope of the free surface (Eq. 3.6):

$$u^* = \sqrt{g\frac{u^2+v^2}{h^{1/3}{K_s}^2}} \tag{3.5}$$

$$u^* = \sqrt{gh\sqrt{\left(\frac{\partial(Z_b+h)}{\partial x}\right)^2+\left(\frac{\partial(Z_b+h)}{\partial y}\right)^2}} \tag{3.6}$$

The eddy viscosity *K* represents effects of diffusion, depth-averaging of the velocities as well as turbulent stresses. This does not form an elaborate turbulence model, as the eddy viscosity is assumed constant or calculated directly from the flow variables (without considering additional transport equations). However this offers a way to calibrate simulations in the case where turbulence effects have to be considered. Use of such simple eddy viscosity model can lead to acceptable results once *K* (or *k*) is calibrated, as it was shown for flows including strong two-dimensional patterns such as separations zones (Bravo and Holly 1996; Papanicolaou et al. 2011).

3.2.2 Numerical scheme

Equations 3.1-3.3 are written in conservative and vector form as (Paquier 2013):

$$\frac{\partial W}{\partial t} + div(f(W)) = S \tag{3.7}$$

Where *W* is the vector of conservative variables, $f(W)=[f_1(W), f_2(W)]$ the flux vector and *S* the source terms vector. *W*, f_1, f_2 are defined as:

$$W = [h, hu, hv]^T, \quad f_1 = \left[hu, hu^2 + g\frac{h^2}{2}, huv\right]^T, \quad f_2 = \left[hv, huv, hv^2 + g\frac{h^2}{2}\right]^T \tag{3.8}$$

S represents all terms of the second members of equations 3.1-3.3:

- Slope terms, treated as fluxes so that an horizontal water level remains horizontal if no additional volume is introduced
- Friction terms, assessed at the centre of the cells using a semi-implicitation in time in order to avoid numerical instabilities when rapid change of flow velocity or depth occurs
- Diffusion terms, computed as fluxes from the gradient of velocities

The code solves the above equations using an explicit second-order finite-volume scheme, adapted from MUSCL approach (Vanleer 1979). The computational mesh is made of quadrilaterals and triangles (Figure 3.1).

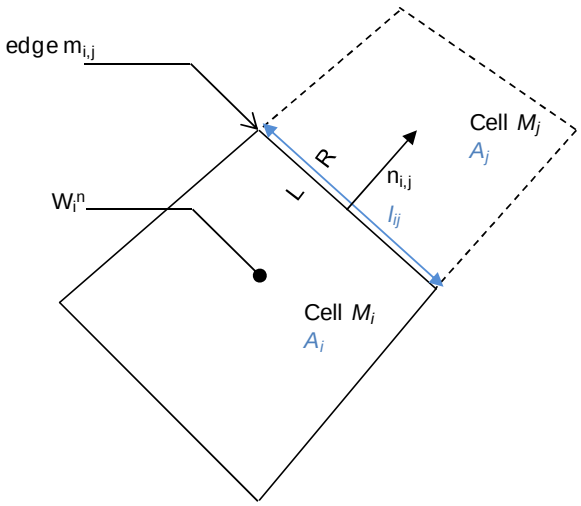

Figure 3.1 : Sketch illustrating the finite volume discretization

The numerical scheme includes 4 steps:

1. Computing at each time step n of the slope of each variable h (or water level $z=Z_b+h$), hu and hv in every cell M_i in x and y direction, using the least-squares method, and applying limitation of slopes.
2. Computing values of $W=(h,hu,hv)$ at intermediate time $t_{n+1/2}=t_n+0.5*\Delta t$ at the middle of the edge m_{ij} of cell M_i:

$$W_{m_{ij}^L}^{n+1/2} = W_{m_{ij}^L}^{n} - 0.5\Delta t\left[\frac{\partial f_1}{\partial W}(W_i^n)\cdot W_{xi}^n + \frac{\partial f_2}{\partial W}(W_i^n)\cdot W_{yi}^n\right] + 0.5\Delta t\cdot S_i^n \qquad 3.9$$

in which f_1 (respectively f_2) are the fluxes on x (respectively y) axis, S_i^n the second member, W_{xi}^n and W_{yi}^n the slopes of W along respectively x and y axis, Δt the time step. Index L (respectively R) means left (respectively right) side of the edge.

3. Solving a 1-D Riemann problem at $t_{n+1/2}$ in the direction perpendicular to the edge (Eq. 3.10 similar to Eqs. 3.1 - 3.3 without second member as these last equations do not vary through rotation) in order to estimate the fluxes through edges for the conservative part of the equations. One can use a Roe type linearization which directly provides an estimate of the fluxes :

$$\begin{cases} \dfrac{\partial W}{\partial t} + \dfrac{\partial}{\partial x}\left(f_1(W)\right) = 0 \\ W\left(x, t_{n+1/2}\right) = W_{m_{ij}^L}^{n+1/2} \; if \; x < 0 \\ W\left(x, t_{n+1/2}\right) = W_{m_{ij}^R}^{n+1/2} \; if \; x > 0 \end{cases} \qquad 3.10$$

4. Integrating the second member S of Eqs. 3.1 - 3.3 on the surface of the cell M_i, and adding the second member at intermediate time $S_i^{n+1/2}$ in order to obtain the final value of the solution at time t_{n+1}:

$$W_i^{n+1} = W_i^n + \sum_j \frac{\varepsilon_{ij} l_{ij}}{A_i} \Delta t f_1\left(W_{m_{ij}}^{n+1/2}\right) + S_i^{n+1/2} \Delta t \qquad 3.11$$

summing on the j cells that have a common edge with cell M_i (of area A_i) with ε_{ij} being -1 or 1 according to the orientation of the edge m_{ij} (length l_{ij}) common to cells M_i and M_j.

The numerical scheme can run with a fixed time step, or with an adaptive time step respecting the Courant criterion so that the scheme remains stable. Originally developed for simulations of dam-break waves, the code is well suited for simulations of shallow flows, particularly when considering changes in the flow regime (transitions from subcritical to supercritical flows). Treatment of the drying/wetting processes is by setting null water depths whenever the computed ones are lower than a threshold. The mass conservation is achieved with typical errors less than 0.01 % of the total mass.

Code validation against experimental and field data includes simulations of dividing supercritical and transcritical flows (Mignot et al. 2008; El Kadi Abderrezzak et al. 2011), floods in dense urban areas (Mignot et al. 2006) and dam-break type flows around obstacles (El Kadi Abderrezzak et al. 2009). The main discrepancies observed in previous comparisons with laboratory measurements concern the exact prediction of the location and size of hydraulic jumps. Overall, all these studies have shown the ability of the code Rubar20 to model highly unsteady flows, over steep topographies or in the presence of buildings, with dividing and combining flows.

3.2.3 Parameters

3.2.3.1 Mesh

The reference mesh consists of a square grid with a resolution m = 0.5 cm in the junction and in areas located within 20 cm of the junction boundaries, and a 2 cm square grid elsewhere (i.e. in the 3 channels) (Figure 3.2). This fine mesh in the junction permits to have 10 cells across an obstacle, which is fine enough to capture the time-averaged flow around each obstacle, but may not represent finer phenomenon such as vortex shedding (Lloyd and Stansby (1997) and Yulistiyanto et al. (1998) use around 30 cells across obstacles). A finer resolution is not adapted here, given the size of the experiments. As such a fine resolution is not required in the channels, a coarser resolution (2 cm) is chosen to reduce computational efforts. A second mesh with a coarse resolution in the junction is tested (m=5 cm), as it is more representative of an urban inundation model. Note that, in this case, 5 cm is the maximum cell dimension allowed, but due to the need of respecting obstacle locations, actual dimensions vary between 3.5 and 5 cm (leading to 7 cells across the channels).

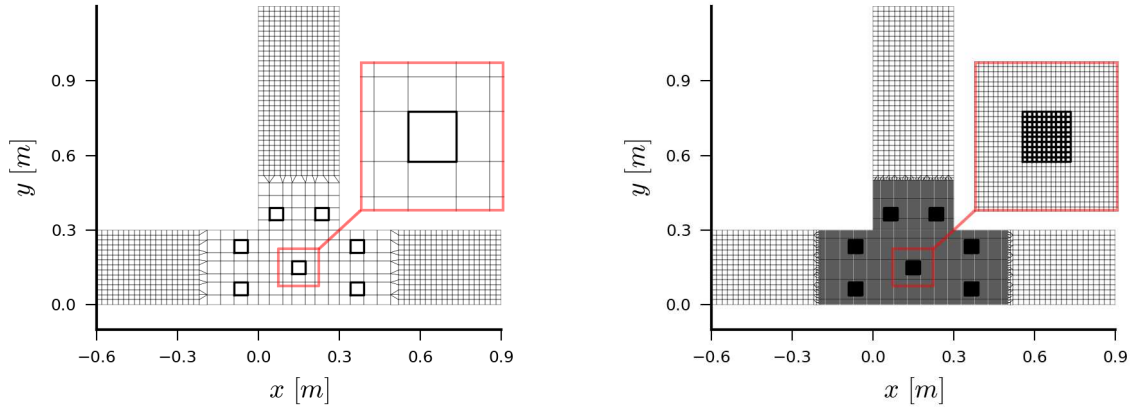

Figure 3.2: Coarse (left) and fine (right) meshes around the junction used for the numerical simulations. Cells potentially blocked to represent obstacles are indicated in bold.

3.2.3.2 Boundary conditions

The measured inlet flow discharge is imposed on the total width of the upstream channel, with a uniform velocity distribution across the boundary. Downstream and branch channel boundary conditions are set up by imposing a stage-discharge relationship derived from a preliminary experimental calibration of a weir equation, which is for the branch channel :

$$Q_b = \mu_b b\sqrt{2g}(H_b - C_b)^{3/2} \qquad 3.12$$

where Q_b, μ_b, H_b and C_b are respectively the branch channel outflow discharge, weir discharge coefficient, hydraulic head and weir crest height. Calibration lies in fitting the weir discharge coefficient μ_b with the measured values of Q_b, C_b and H_b (estimated with the branch channel bulk velocity). Standard values[1] can be found for different ratios H_b/C_b, but a direct calibration is more accurate, especially because the flow approaching the sharp crested weir in our experiments may not be uniform. One value of the discharge coefficient is fitted for each weir crest height C_b, considering all the measured flows corresponding to this condition (that is the initial flow, plus the flows with obstacles/sidewalks). A similar relationship is used and calibrated for the downstream branch weir.

Figure 3.3 gives the best fit values of these coefficients ($\mu_{b,ref}$ and $\mu_{d,ref}$), along with estimated maximum ($\mu_{b,max}$ and $\mu_{d,max}$) and minimum ($\mu_{b,min}$ and $\mu_{d,min}$) values. Maximum values (respectively minimum values) are computed as the reference values plus (respectively minus) half the standard deviation on the series of the 10 individual values computed for each configuration of the same flow. Results show that $\mu_{b,ref}$ and $\mu_{d,ref}$ are significantly different, which may arise from the different flow conditions in both channels. Moreover, variations of the discharge coefficient are lower for the downstream channel, which comes from the fact that the downstream channel flow has more limited three-dimensional patterns and is likely to approach the weir in uniform condition. Coefficients variations for the branch weir may exceed 5%, which is significant when compared to typical obstacle effects. Therefore a sensitivity analysis will be carried out on the downstream condition.

[1] For example, the ones provided by Bazin, H. E. (1898). *Expériences nouvelles sur l'écoulement en déversoir exécutées a Dijon de 1886-1895*. Paris, V. C. Dunod. For example.

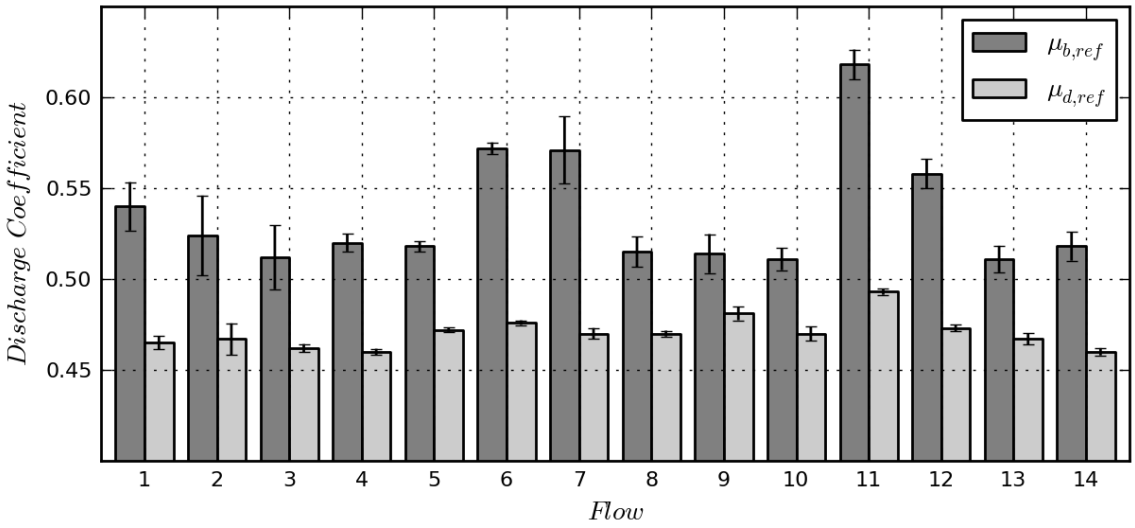

Figure 3.3 : Sharp-crested weirs discharge coefficients computed with experimental measurements. Reference values are indicated with grey bars, extreme values with dark vertical error bars. Flow numbers are defined in Table 2.1.

3.2.3.3 Bottom friction

The average Reynolds number Re in the different branches is between 10^4 and $5x10^4$,and the roughness height to hydraulic radius ratio is around 0.002, (typical water depths of 5 cm, and a roughness height k_s of 0.1 mm, see 3.3.2). In such flow condition, the flow regime can be considered either as hydraulically smooth or in the transition zone toward fully rough flow, and the channel friction factor depends on both R_e and k_s. Therefore, instead of using a Manning-Strickler coefficient (valid for full rough turbulent flows), we use the following approximation of the Colebrook-White formula given in (Yen 2002), which allows an explicit calculation of the friction factor f depending on local Reynolds number and roughness height :

$$f = \frac{1}{4}\left[-log_{10}\left(\frac{k_s}{12R_h} + \frac{6.79}{{R_e}^{0.9}}\right)\right]^{-2} \qquad 3.13$$

Where R_h is the hydraulic radius, taken as the local water depth h when used in the present 2D model. The computed friction factor is then transformed in an equivalent Strickler coefficient to use in Eqs. 3.2 and 3.3 :

$$K_s = \sqrt{\frac{8g}{h^{1/3}f}} \qquad 3.14$$

Preliminary simulations suggested that linear head losses were rather high for a glass channel (see 3.3.2) so a high value is chosen for the channels roughness height (k_s=0.1 mm) as

a reference. The range of equivalent Strickler coefficients is 85-105 $m^{1/3}.s^{-1}$. Smoother walls are considered in a sensitivity test, using a smaller roughness height k_s=0.01 mm.

Moreover, wall friction is added, considering a formulation similar to the bottom friction, but calculating the friction of the water column for cells located along solid boundaries (including obstacles).

3.2.3.4 Eddy viscosity

The constant eddy viscosity model (K=constant) is the simplest formulation, when compared to the ones using a friction velocity-dependent eddy viscosity (Eqs. 3.4, and 3.5 - 3.6). Now, the present flows involve combinations of straight uniform flows, shear layers, recirculation zones and wakes. For such configurations, there is no recommended value for the constant eddy viscosity K or the non-dimensional parameter k, and all eddy velocity formulations are likely to fail in representing fine turbulent phenomena. Therefore, for simplicity, the simulations are carried out assuming a constant eddy viscosity K all over the model domain, and effects of the latter are carefully analysed through a sensitivity analysis.

3.3 Modelling of initial flows

3.3.1 Validation on branch flow discharge

10 runs are carried out to validate the numerical model ability to simulate the initial flow discharge distribution R_{q0} (i.e. without obstacle) and predict the general flow patterns. The different runs (detailed in Table 3.1) allows us to analyse effects of the eddy viscosity K (runs 1 to 4), the bottom friction (run 5), the boundary conditions (runs 6 and 7) and the mesh resolution (runs 8 to 10). The simulations capacity to predict the branch channel discharge is assessed by calculating the average δ and the root mean square deviation σ of the relative error Q_{b0}^{*}:

$$Q_{b0}^{*} = \frac{Q_{b0,SIM} - Q_{b0,MES}}{Q_{b0,MES}} \qquad 3.15$$

$$\delta(Q_{b0}^{*}) = \frac{1}{n_{flow}} \sum_{k=1}^{n_{flow}} Q_{b0}^{*} \qquad 3.16$$

$$\sigma(Q_{b0}{}^{*}) = \sqrt{\frac{\sum_{k=1}^{n_{flow}} (Q_{b0}{}^{*})^2}{n_{flow}}} \qquad 3.17$$

Where $Q_{b0,SIM}$ and $Q_{b0,MES}$ are respectively the simulated and measured values of the branch channel flow discharge, and n_{flow} is the number of initial flows (14). These indicators values are given in Table 3.1 for the 10 runs. All runs show a very good agreement when looking at the computed branch channel flow discharge, with typical errors about 2%, and a bias generally negative ($\delta(Q_{b0}{}^{*})$). These results do not support a particular value for the eddy viscosity K (runs 1 to 4), and do not show a significant influence of the bottom roughness k_s. Using a coarse mesh (run 8) leads to slightly higher errors, but even then, adequacy with experimental data remains very good. The extreme values tested for the downstream and branch channels weirs discharge coefficients (runs 6 and 7) lead to slightly larger typical errors ($\sigma(Q_{b0}{}^{*})$) and significantly impact the bias ($\delta(Q_{b0}{}^{*})$), being either positive or negative. This shows that both typical errors and bias observed in other runs may actually be due to slight discrepancies on the downstream boundary condition modelling.

Run	m	K	μ_b	μ_d	k_s	$\delta(Q_{b0}^*)$	$\sigma(Q_{b0}^*)$
	cm	$m^2.s^{-1}$	-	-	m	%	%
1	0.5	0	$\mu_{b,ref}$	$\mu_{d,ref}$	$1.0x10^{-4}$	-0.98	1.75
2	0.5	$2.0x10^{-4}$	$\mu_{b,ref}$	$\mu_{d,ref}$	$1.0x10^{-4}$	-1.19	2.14
3	0.5	$5.0x10^{-4}$	$\mu_{b,ref}$	$\mu_{d,ref}$	$1.0x10^{-4}$	-0.99	1.99
4	0.5	$1.0x10^{-3}$	$\mu_{b,ref}$	$\mu_{d,ref}$	$1.0x10^{-4}$	-1.11	1.97
5	0.5	0	$\mu_{b,ref}$	$\mu_{d,ref}$	$1.0x10^{-5}$	-0.98	1.79
6	0.5	0	$\mu_{b,max}$	$\mu_{d,min}$	$1.0x10^{-4}$	0.19	1.98
7	0.5	0	$\mu_{b,min}$	$\mu_{d,max}$	$1.0x10^{-4}$	-2.23	2.58
8	5	0	$\mu_{b,ref}$	$\mu_{d,ref}$	$1.0x10^{-4}$	-1.92	2.53
9	5	$5.0x10^{-4}$	$\mu_{b,ref}$	$\mu_{d,ref}$	$1.0x10^{-4}$	-1.73	2.34
10	5	$1.0x10^{-3}$	$\mu_{b,ref}$	$\mu_{d,ref}$	$1.0x10^{-4}$	-1.71	2.36

Table 3.1 : Numerical parameters for the 10 runs used for initial flow modelling and indicators on the computed branch flow discharges for the 14 initial flows

3.3.2 Validation on water depths

The simulated water depths profiles for runs 1 to 5 in the main and branch channels are shown for the reference flow 3 on Figure 3.4. Discussion is carried out here for this flow only as other flows yield to the same conclusions (comparison of experimental measurements and simulations results for run 4 is shown in AppendixA.2.1). First, in the upstream channel (x>0.3 m), all simulations fail in accurately predicting the evolution of the water depths and underestimate the linear head losses. The very simple flow pattern in this channel (straight flow in a rectangular horizontal channel) suggests there is a systematic bias.

Upstream channel water depths are used to compute the slope of the free surface and derive an experimental friction factor for each flow, using average upstream flow characteristics (bulk velocity and averaged hydraulic radius). Experimental friction factor lie in the range 0.07 and 0.1, which is extremely high for the present flows. Indeed, using Eq. 4.5, this suggests that the relative roughness height k_s/R_h should then be around 0.2, i.e. a roughness height k_s of around 7 mm. This value is not realistic, and the discrepancies observed can be attributed to an experimental error. The most plausible explanation is an actual upstream channel slope of around 0.15%, which can explain the discrepancies. Therefore the measured water depths cannot be used for a quantitative validation, especially in the upstream channel.

Simulated water depths in the downstream channel are close to the measurements at both ends of the channel (that is at x=-2 m and x = 0 m), but show discrepancies in the channel central part. Using a non-null eddy viscosity K (runs 2, 3 and 4) lead to an

overestimation of the water depths, while using K=0 (runs 1 and 5) rather leads to underestimated water depths. None of the simulations can be considered as better to predict water depths.

Comparison of measured and simulated water depths in the branch channel clearly shows the importance of calibrating the eddy viscosity (see runs 1 to run 4), while the roughness height influence is limited (runs 1 and 5). Higher eddy viscosities imply higher energy losses in the branch channel (because of the important velocity gradients in the recirculation area) and increase the channel water depths. The constant eddy viscosity of K=1.10^{-3} m^2.s^{-1} used in the run 4 leads to the best prediction of the water depths in the branch channel.

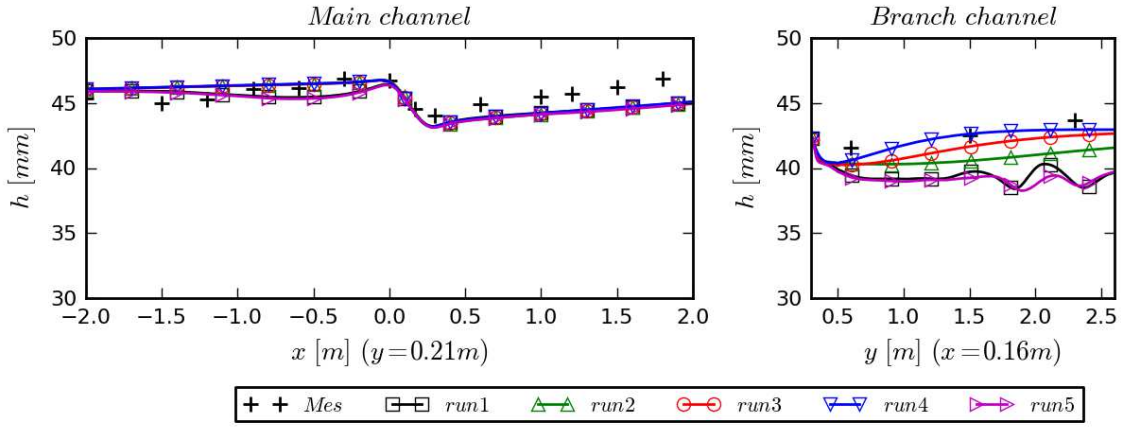

Figure 3.4 : Measured (+) and simulated (lines with symbols) water depths along the main channel and the branch channel for runs 1 to 5

3.3.3 Validation on velocity field

Figure 3.5 shows measured and simulated flow velocity fields for the flow 6 for several runs. Quantitative comparison cannot be carried out, as experimental velocities are only measured at the elevation z=3 cm, whereas the computed velocities represent depth averaged velocities. Within this comparison framework, the different runs results are in fair agreement with experimental measurements. We can notice the eddy viscosity K has an impact mainly on the velocity distribution in the branch channel for the fine mesh (bottom, runs 1, 2 and 4). The coarse mesh (runs 8 and 10) leads to a coarse representation of the velocity field, but global flow pattern remains well predicted.

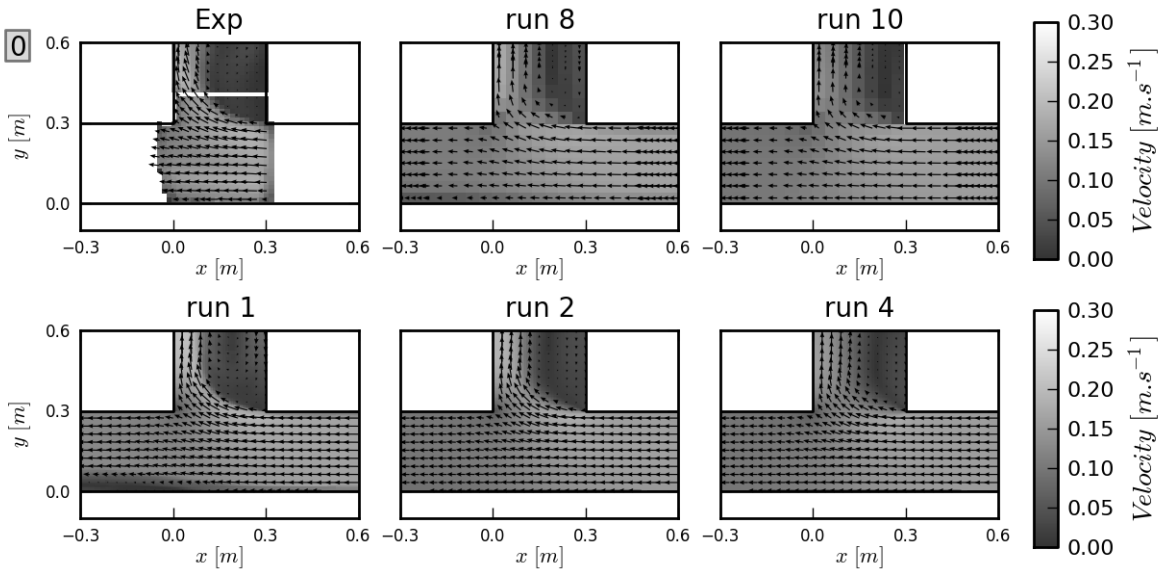

Figure 3.5 : Measured velocities at elevation z = 3 cm (Exp) and simulated depth averaged velocities (runs 1, 2, 4, 8 and 10) around the junction for initial flow 6. For fine mesh runs, only a selection of the computed velocities is shown.

3.3.4 Prediction of the different flow structures

The main flow structures in the studied dividing flows are the recirculation area located along the upstream wall of the branch channel, the dividing streamline in the junction, and potential hydraulic jumps in the junction and in the contracted zone of the branch channel. From numerical simulation results, the contour of the depth-averaged recirculation zone is computed, assuming it can be taken as the "zero-discharge area" (the width of the recirculation area W is chosen so that the integration of the streamwise unit discharge over this width yields to 0). Figure 3.6 shows the contour of this recirculation area along with the dividing streamline for 3 flows with different discharge distribution (flows 7, 8 and 10), for runs 1 and 4 (that is, with respectively K=0 and K=10^{-3} $m^2.s^{-1}$). For K=0, the recirculation area almost reaches the downstream weir of the branch channel, whereas its length (along y axis) is strongly reduced for K=10^{-3} $m^2.s^{-1}$. The maximum width of the recirculation also decreases with larger values of K, although the variations are smaller.

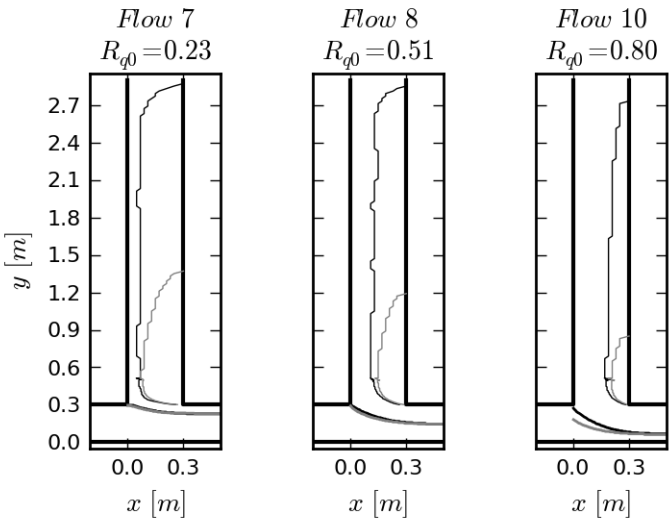

Figure 3.6 : Recirculation zones (thin line) and dividing streamlines (thick line) computed for K=0 (black) and K=10^{-3} $m^2.s^{-1}$(grey), for different discharge distributions

The dimensions of the computed recirculation areas (i.e., its normalized maximal width *W*/*b* and length *L*/*b*) are compared to the ones measured by Kasthuri and Pundarikanthan (1987) and simulated with a 2D model with a k-ε turbulence model by Shettar and Murthy (1996) on Figure 3.7. Both sets of data are limited to upstream channel Froude number ranging between 0.1 and 0.4, so that the present flows 1 and 2 are excluded of the comparison (see Table 2.1). Best agreement with the literature values is found for K=10^{-3} $m^2.s^{-1}$ (run 4), especially for the length of the recirculation area. This value is the one which also gives the best branch channel water depths (3.3.2).

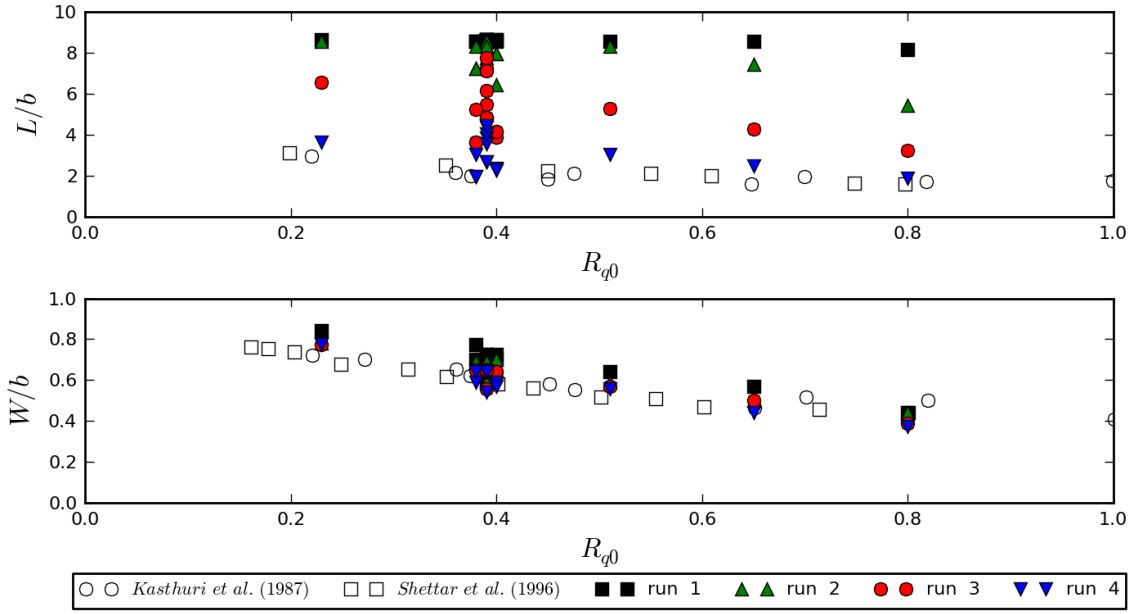

Figure 3.7 : Computed normalized branch channel recirculation length and width, and comparison with past studies

The dividing stream line shows small variations with the eddy viscosity coefficient K (Figure 3.6). This is due to the fact that the discharge ratios are poorly affected by the latter (see Table 3.1). Note that for a large discharge ratio (flow 10), the best value of K for the branch channel flow (10^{-3} $m^2.s^{-1}$) leads to a dividing streamline that is strongly deflected toward the left bank in the downstream part of the junction. This pattern does not seem realistic (there is no experimental measurements of the latter though), which means K=10^{-3} $m^2.s^{-1}$ may be a too large value for the junction flow.

Considering these different validation points, the numerical model appears to predict with enough accuracy the experimental initial flows (without obstacle) to allow the introduction of obstacles and sidewalks in the simulations. Given the results of this sub-section, simulations of these other flow configurations should be carried out with at least a sensitivity analysis on the downstream conditions (i.e. values of μ_b and μ_d) and on the eddy viscosity K, whereas the channel bottom friction has not shown significant influence on the flow in the junction (k_s=0.1 mm is adopted for the following simulations). Finally, the model being validated on initial flows, results of run 4 (K=10^{-3} $m^2.s^{-1}$) are used to plot flow characteristics near the junction (Appendix A.1), to help understanding experimentally measured effects of obstacles and sidewalks (presented in Chapter 2). Besides flow patterns described above, simulations show that flow 1 is the only case where supercritical regime occurs (in the junction and branch channel). This was not measured in details but could be visually observed during experiments.

3.4 Modelling of flows with obstacles

3.4.1 Global validation on branch flow discharge and upstream water depth evolutions

Simulations of the 14 flows with 9 obstacles are carried out for 10 runs (Table 3.2), that is 14x10x9 = 1260 simulations. These runs are globally the same as the ones used for initial flows modelling, except that the sensitivity to the downstream conditions is studied with an eddy viscosity coefficient K=5x10^{-4} $m^2.s^{-1}$ (runs 6a and 7a). This latter choice comes from the fact that simulations of flows with obstacles are more stable and achieve quicker convergence when using a non-null eddy viscosity. Sensitivity to the roughness height is not studied here, as its impact is negligible on initial flows and is assumed to remain negligible for flows

including obstacles (this is justified by the very low friction-generated head losses computed for initial flows).

9 obstacles configurations for each of the 14 flows are simulated, which leads to a total of 126 simulations for each run. Each run prediction capacity is first assessed by statistically comparing simulation results with experimental measurements. We have seen in the last sub section that the chosen downstream conditions may lead to a bias in the comparison. In order to reduce this bias, simulations quality is assessed by computing errors between measured and simulated evolutions of:

- the discharge distribution :

$$\Delta R_{qi}{}^{*} = \Delta R_{qi,SIM} - \Delta R_{qi,MES} \qquad 3.18$$

- the upstream channel water depth:

$$\begin{aligned} \Delta h_{ui}{}^{*} &= \Delta h_{ui,SIM} - \Delta h_{ui,MES} \\ &= \left(h_{ui,SIM} - h_{u0,SIM}\right) - \left(h_{ui,MES} - h_{u0,MES}\right) \end{aligned} \qquad 3.19$$

As for the experiments protocol, study of an evolution (of a given variable between a flow with obstacle *i* and without obstacle) permits a compensation (at least partially) of the errors presently due to the downstream boundary condition modelling. Note that $\Delta R_{qi}{}^{*}$ and $\Delta h_{ui}{}^{*}$ are not normalized by respectively $\Delta R_{qi,MES}$ and $\Delta h_{ui,MES}$, as these values can be small and within the measurement uncertainties, which could lead to large and non-representative relative errors. Following initial flow modelling analysis, average δ and root mean square deviation of these errors (Eqs. 3.16 and 3.17) are computed for the whole 126 flows (14 flows, obstacles 1 to 9) and are given in Table 3.2. Subscript "1-9"is used ($\Delta R_{q1\text{-}9}{}^{*}$and $\Delta h_{u1\text{-}9}{}^{*}$), as simulation results are analysed on the whole set of obstacles 1 to 9. Every run shows an overall fair ability to predict ΔR_q and Δh_u (Table 3.2). A comparison of the different runs is carried out in the following to discuss the role and importance of the tested numerical parameters.

First, runs 6a and 7a show very similar results than run 3, which shows that effects of the downstream conditions are strongly reduced and almost negligible. Therefore analysis based on $\Delta R_{qi}{}^{*}$ and $\Delta h_{ui}{}^{*}$ can be carried out without bias generated by systematic errors on the downstream conditions.

Then, results for the fine mesh indicate that increasing the eddy viscosity until K=5x10^{-4} m^2.s^{-1} (run 1 to 3) leads to a global improvement of the simulations (both $\sigma(\Delta R_{q1\text{-}9}{}^{*})$ and

$\sigma(\Delta R_{q1\text{-}9}^{*})$ decrease). A larger value of the eddy viscosity lead to similar typical errors (run 4), but with an increase of the branch channel distribution (see $\delta(\Delta R_{q1\text{-}9}^{*})$) and of the upstream water depth (yet limited, see $\delta(\Delta h_{u1\text{-}9}^{*})$). Simulations results with the coarse mesh (runs 8 to10) remain in fair agreement with experimental measurements, and the eddy viscosity has significantly less impact than for the fine mesh.

Run	m	K	μ_b	μ_d	k_s	$\delta(\Delta h_{u1\text{-}9}^{*})$	$\sigma(\Delta h_{u1\text{-}9}^{*})$	$\delta(\Delta R_{q1\text{-}9}^{*})$	$\sigma(\Delta R_{q1\text{-}9}^{*})$
	cm	$m^2.s^{-1}$	-	-	m	mm	mm	%	%
1	0.5	0	$\mu_{b,ref}$	$\mu_{d,ref}$	$1.0x10^{-4}$	-0.43	1.26	-0.07	1.17
2	0.5	$2.0x10^{-4}$	$\mu_{b,ref}$	$\mu_{d,ref}$	$1.0x10^{-4}$	0.22	0.71	-0.52	1.31
3	0.5	$5.0x10^{-4}$	$\mu_{b,ref}$	$\mu_{d,ref}$	$1.0x10^{-4}$	0.08	0.62	-0.15	0.83
4	0.5	$1.0x10^{-3}$	$\mu_{b,ref}$	$\mu_{d,ref}$	$1.0x10^{-4}$	0.14	0.63	0.23	0.84
6a	0.5	$5.0x10^{-4}$	$\mu_{b,max}$	$\mu_{d,min}$	$1.0x10^{-4}$	0.21	0.54	-0.17	0.85
7a	0.5	$5.0x10^{-4}$	$\mu_{b,min}$	$\mu_{d,max}$	$1.0x10^{-4}$	0.07	0.61	-0.13	0.80
8	5	0	$\mu_{b,ref}$	$\mu_{d,ref}$	$1.0x10^{-4}$	-0.06	0.62	-0.08	1.15
9	5	$5.0x10^{-4}$	$\mu_{b,ref}$	$\mu_{d,ref}$	$1.0x10^{-4}$	0.07	0.55	0.31	1.09
10	5	$1.0x10^{-3}$	$\mu_{b,ref}$	$\mu_{d,ref}$	$1.0x10^{-4}$	0.17	0.63	0.47	1.18

Table 3.2 : Numerical parameters for the 10 runs used for flows with obstacles modelling, and simulation quality indicators computed on the whole set of obstacle configurations (1 to 9)

Scatter plots comparing measured and simulated evolutions of the upstream channel water depths and of the discharge distribution are shown on Figure 3.8. A linear regression using a least-square method is carried out and the slope s is indicated for each run, for both ΔR_{qi} and Δh_{ui}. A large part of the flows are only slightly impacted by introduction of obstacles, and the dispersion of numerical simulations results is relatively important for the low values (i.e. typically for $|\Delta R_{qi}|<5\%$ and $\Delta h_{ui}<5$ mm). Therefore defining a meaningful relative error is delicate (especially when considering experimental uncertainties). Comparing evolutions of ΔR_{qi} for runs 2, 3 and 4 shows that increasing the eddy viscosity mainly improves modelling of upstream obstacles (1, 2, 8 and 9), whereas it increases the dispersion for other obstacles (which effects are generally low). The same behaviour is observed for the upstream water depth evolution, although effects of the eddy viscosity are less important. Linear regressions show that the fine mesh tends to overestimate effects of obstacles on the discharge distribution (though discrepancy is reduced with increasing K), whereas the coarse mesh tends to underestimate these effects. Therefore, simulated discharge distribution evolutions for each obstacle depend on both the chosen eddy viscosity and the mesh resolution. Oppositely, simulated upstream channel water depth evolutions are not significantly impacted by these two parameters.

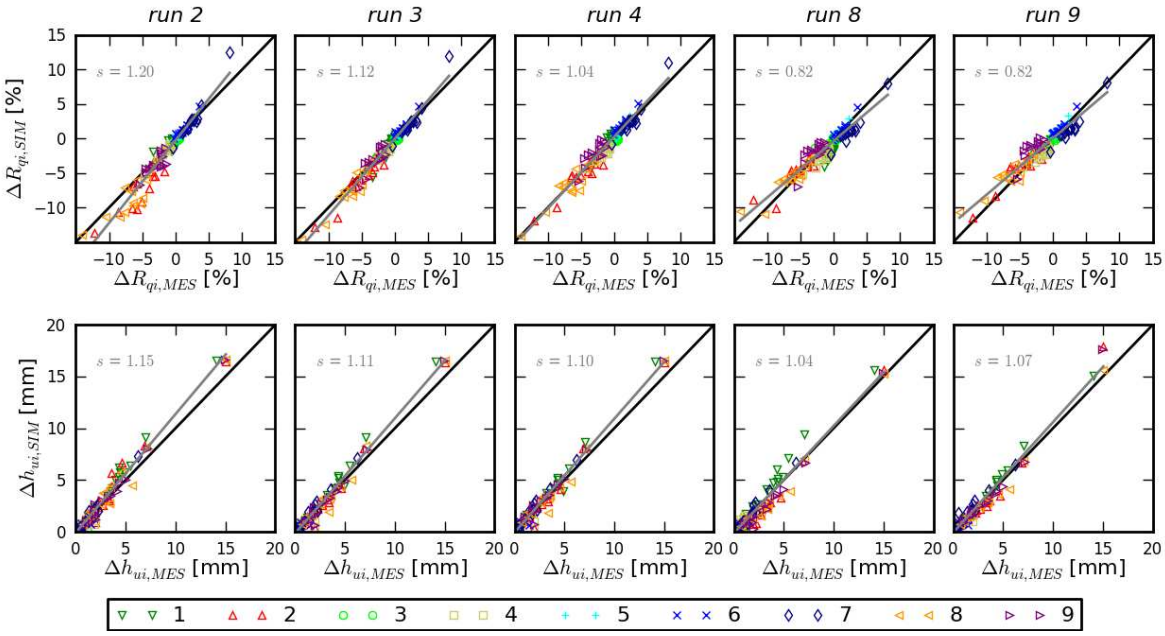

Figure 3.8 : Comparison of simulated (SIM) and measured (MES) evolutions of discharge distribution and upstream channel water depth, obstacles by obstacles. Results of the linear regression is indicated with the grey line, along with its slope s. *Upstream obstacles (1, 2, 8 and 9) are plotted with triangles.*

3.4.2 Detailed analysis of simulation results

The previous statistical analysis shows on the one hand the importance of some numerical parameters (eddy viscosity *K* and mesh resolution *m*) and on the other hand the differences in simulations quality depending on the obstacle configuration (this clearly appears on Figure 3.8). Moreover, effects of obstacles have been proved to be related to both their location and the initial flow characteristics (previous chapter). Figure 3.9 details for each obstacle and each initial flow (grouped in series as in the previous chapter, Table 2.1) the measured and simulated evolutions of the discharge distribution.

Discrepancies between experiments and simulations mainly occur for the upstream single obstacle 2, and the associated double obstacles 8 and 9. For these obstacles, it appears that increasing the eddy viscosity for the fine mesh (from K=2x10^{-4} m^2.s^{-1} for run 2 to K=5x10^{-4} m^2.s^{-1}for run 3) reduces the size of the wake downstream of the obstacle 2 (Figure 3.10). For a low value of K, the wake extends until the downstream corner of the junction, which limits the junction flow capacity to rotate into the branch channel. This leads to an increased effect of obstacle 2, hence an overestimation of $|\Delta R_{q2}|$ on Figure 3.9. This overestimation persists for obstacles 8 and 9 simulations. The computed obstacle 2 wake with the coarse mesh (runs 8 and 10 on Figure 3.10) is less sensitive to the eddy viscosity, so that even a null eddy viscosity (run 8) can predict reasonably well the flow around this obstacle.

However, the coarse mesh also smoothes the flow around obstacle 2, so that its effect is underestimated (Figure 3.9). For this obstacle, additional simulations were carried out with the fine mesh and using the friction velocity-dependent eddy viscosity formulations (Eqs. 3.4+3.5 and 3.4+3.6, both applied with k=0.1 and k=1.0, so 4 series of simulations). None of these additional runs achieved a better agreement with the measured evolution of the discharge distribution (not shown here for the sake of scarcity).

The second series of discrepancy comes from the flow 1 (with F_{u0}=0.79), for which initial flow includes a significant part of supercritical regime in the junction (detailed pattern shown in Appendix A.1). Interaction of this supercritical flow with obstacles 1, 5, 6 and 7 is not simulated with the same accuracy than other flow. Other combinations of flow/obstacle are well simulated. Particularly, simulated evolutions of $|\Delta R_{q7}|$ and $|\Delta R_{q3}|$ with R_{q0} are in fair agreement with experimental measurements, which proves the model ability to accurately compute respectively the dividing streamline line in the junction and the width of the separation area in the branch channel.

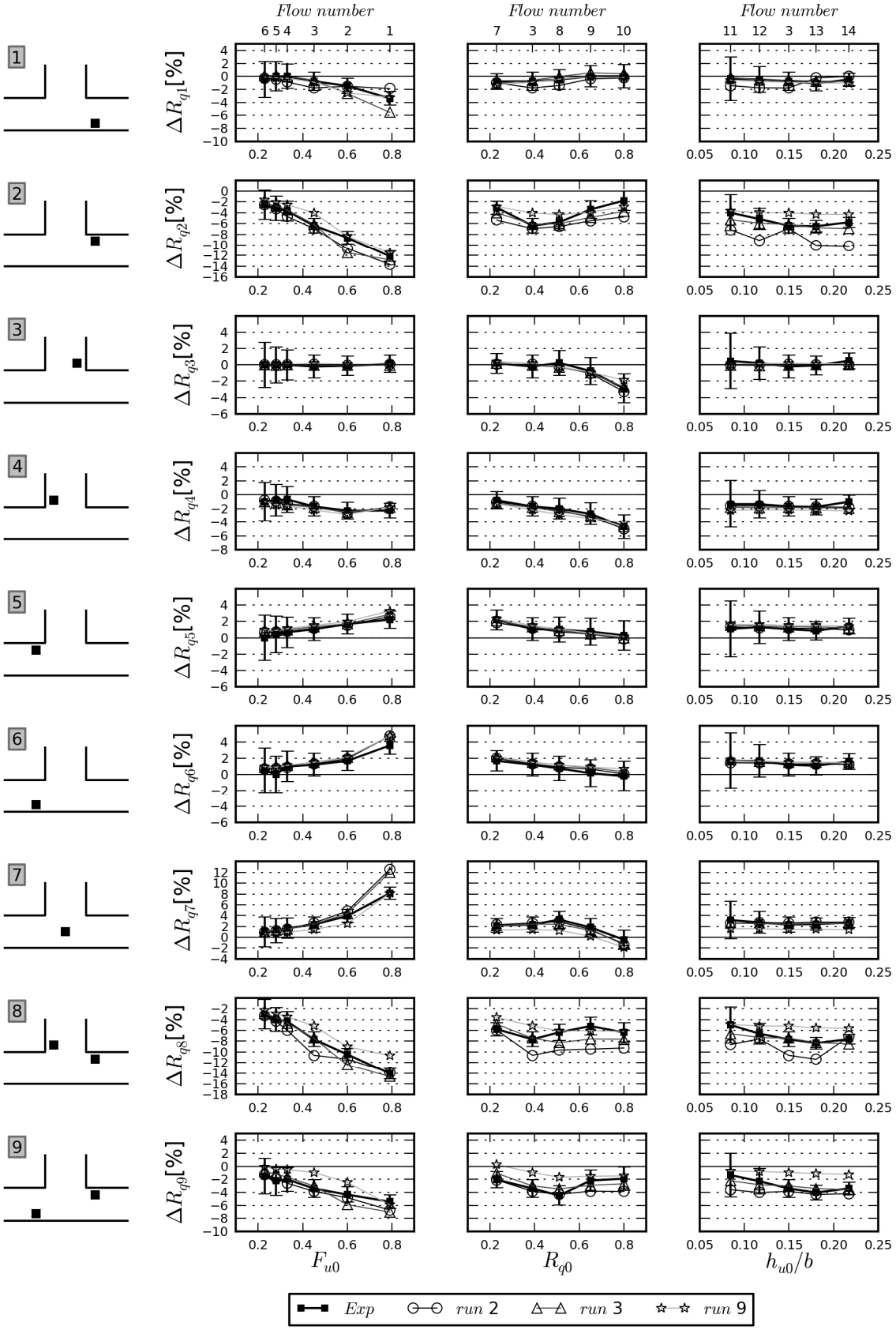

Figure 3.9 : Measured (Exp) and simulated (runs 2, 3 and 9) evolutions of the discharge distribution for each obstacle configuration

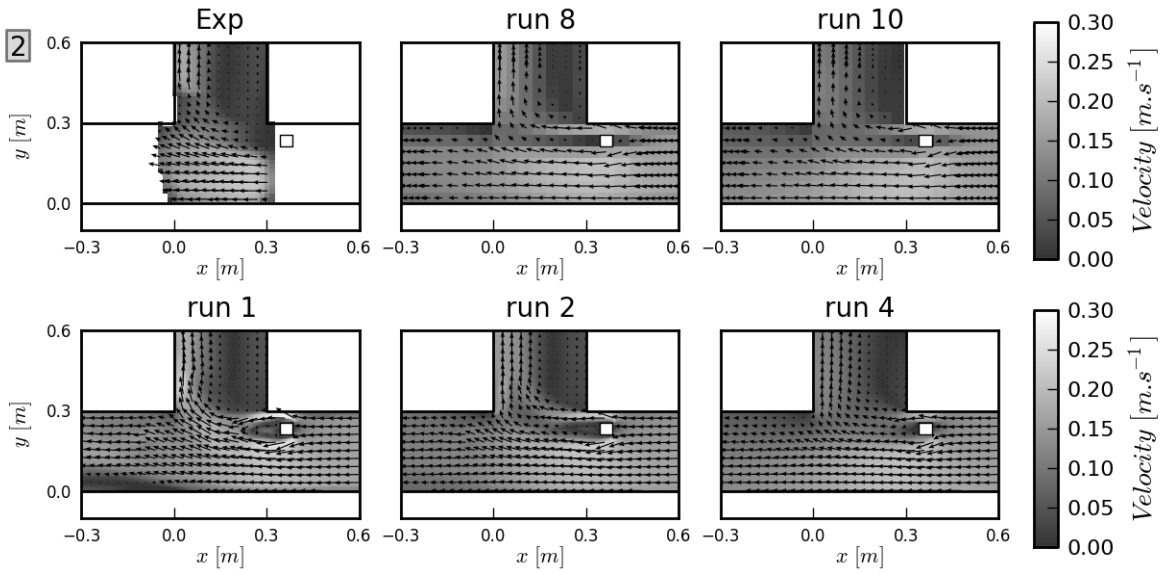

Figure 3.10 : Measured velocities at elevation z = 3 cm (Exp) and simulated depth averaged velocities (runs 1, 2, 4, 8 and 10) around the junction for flow 6

3.5 Modelling of flows with sidewalks

3.5.1 Parameters of the different numerical simulations

Accurate modelling of the obstacles was possible by adapting the mesh to the obstacles, and specifying solid boundaries. As the sidewalks are submerged, the challenge lies in an adequate representation of the topography. 2D models do not allow to use vertical cells (as in 3D models), and cells slope is limited by their dimensions for practical reasons (computation times), so simplifications have to be done. We consider here one mesh with regular 2 cm width square elements everywhere except on the sidewalks edges, where finer elements with dimensions of 0.5 cm or 1 cm are used (Figure 3.11). From this mesh, two different topographical representations are used:

- In the *Ref* model, height of the channel bottom elevation follows the actual height in the experiments (0 cm for the main channel and 2 cm for the sidewalks).
- In the *Avg* model, the channel bottom elevation is constant and equal to the average elevation on a channel cross section, i.e. (2x6 cm x2 cm)/(30 cm) = 0.8 cm.

Use of the same mesh for both models permits to study effects of topography representation without influence of the mesh structure.

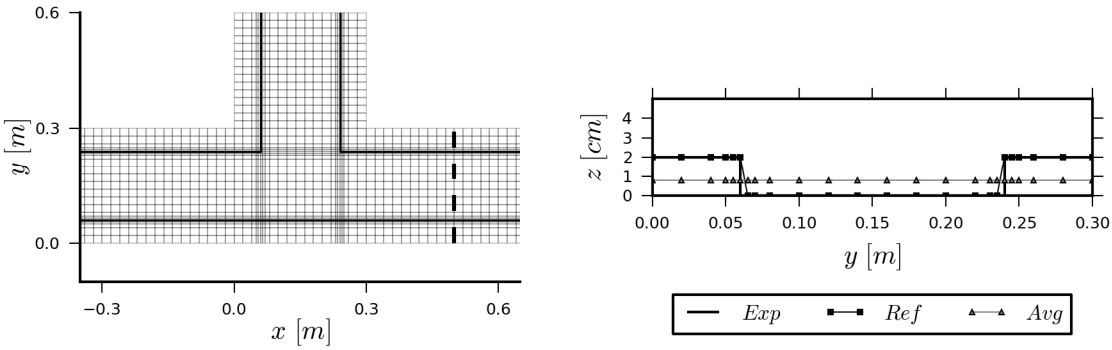

Figure 3.11 : Top view (left) of the mesh and cross section (right, shown along the dotted line on the left plot) with the channel bottom elevation used in models Ref *and* Avg *for flows with sidewalks simulations.*

Based on these two models, a series of runs are carried out to assess influence of the eddy viscosity *K*, the sidewalks roughness length $k_{s,sw}$ (increased to 10^{-3} m, while the channel roughness remains set to 10^{-4} m) and the downstream boundary conditions (via μ_b and μ_d) (Table 3.3). It is recalled here that subscript "10" refers to sidewalks configurations (as in Chapter 2).

Run	Model	K	μ_b	μ_d	$k_{s,sw}$	$\delta(\Delta h_{u10}^*)$	$\sigma(\Delta h_{u10}^*)$	$\delta(\Delta R_{q10}^*)$	$\sigma(\Delta R_{q10}^*)$
		$m^2.s^{-1}$	-	-	m	mm	mm	%	%
1	*Ref*	$5.0x10^{-4}$	$\mu_{b,ref}$	$\mu_{d,ref}$	$1.0x10^{-4}$	-0.54	0.8	-0.21	2.08
2	*Ref*	$1.0x10^{-3}$	$\mu_{b,ref}$	$\mu_{d,ref}$	$1.0x10^{-4}$	-0.48	0.75	0.01	1.88
3	*Ref*	$5.0x10^{-4}$	$\mu_{b,ref}$	$\mu_{d,ref}$	$1.0x10^{-3}$	-0.18	0.58	-0.12	1.92
4	*Ref*	$5.0x10^{-4}$	$\mu_{b,max}$	$\mu_{d,min}$	$1.0x10^{-4}$	-0.51	0.78	-0.41	2.20
5	*Ref*	$5.0x10^{-4}$	$\mu_{b,min}$	$\mu_{d,max}$	$1.0x10^{-4}$	-0.57	0.82	-0.20	2.08
6	*Avg*	$5.0x10^{-4}$	$\mu_{b,ref}$	$\mu_{d,ref}$	$1.0x10^{-4}$	-0.35	0.71	-0.48	2.05
7	*Avg*	$1.0x10^{-3}$	$\mu_{b,ref}$	$\mu_{d,ref}$	$1.0x10^{-4}$	-0.40	0.75	-0.37	1.99

Table 3.3 : Numerical parameters and indicators on the discharge distribution and upstream channel water depth evolution for the simulations of flows with sidewalks

3.5.2 Results

Figure 3.12 shows measured and simulated velocities for the flow 6, for several runs carried out with the *Ref* model. Acceleration of the flow and its concentration in the channels central area is well simulated. Expansion of the branch recirculation area towards the branch channel centre is also predicted. Increasing the eddy viscosity (run 2) tends to smooth the velocity distribution across the channels, and slightly changes the branch channel recirculation shape. Higher friction on the sidewalks (run 3) barely affects the flow pattern.

As for obstacles, average error δ and root mean square error σ on the predicted evolution of the discharge distribution and the upstream channel water depth are given in

Table 3.3. Influence of the downstream condition remains negligible (runs 4 and 5). Other runs show very similar results, with a slightly better simulation of ΔRq_{10} for the run 2 (K=10^{-3} $m^2.s^{-1}$). Increasing friction on the sidewalks is consistent as it significantly improves the modelling of Δh_{u10}. Finally the model *Avg* gives very close results to the model *Ref*, without any deterioration of the results.

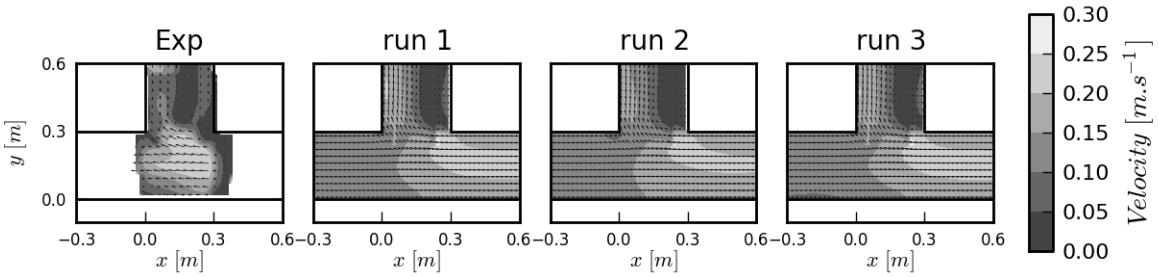

Figure 3.12 : Measured and simulated (runs 1, 2 and 3*) flow velocity magnitude around the junction for the flow 6 with sidewalks*

Measured and simulated (runs 1, 2 and 6) evolution of the discharge distribution is shown for the three flow series on Figure 3.13 to further detail the model ability and limits. All runs results are very close, and lie well within the range of experimental uncertainties, except for the flow 2, which has a large upstream channel Froude number. The discontinuity observed in the experiments around F_{u0}=0.6 (Figure 3.13) is rather predicted for F_{u0}=0.5 in the numerical simulations. Figure 3.14 shows that this discontinuity can be explained by the occurrence of an oblique hydraulic jump attached to the upstream corner of the junction, which strongly directs the flow toward the branch channel. Simulations seem to predict occurrence of this hydraulic jump for smaller F_{u0} (see flow 2 on Figure 3.14), so that discrepancies are encountered around the critical value.

Another discrepancy can be noticed for the flow 11 (h_{u0}/b=0.08), although the measurement uncertainty remains high. For this flow, water depths on the sidewalks can be locally only a few millimetres, so that flow conditions are out of the shallow water equations hypothesis. Moreover, the weir crest height is lower than the sidewalks height, so that the weir equation used to model the downstream condition may lead to larger errors than for other flow configurations.

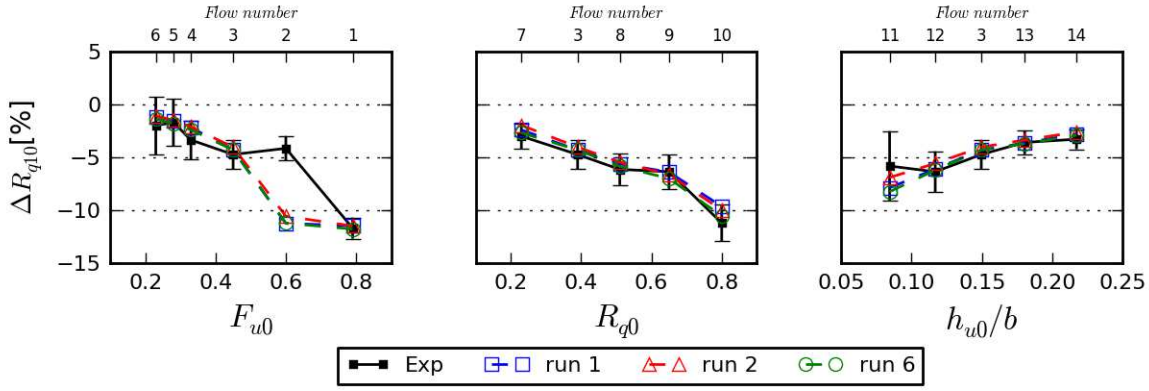

Figure 3.13: Measured (Exp) and simulated (runs 1, 2 and 6) evolution of the flow discharge distribution for the flows with sidewalks

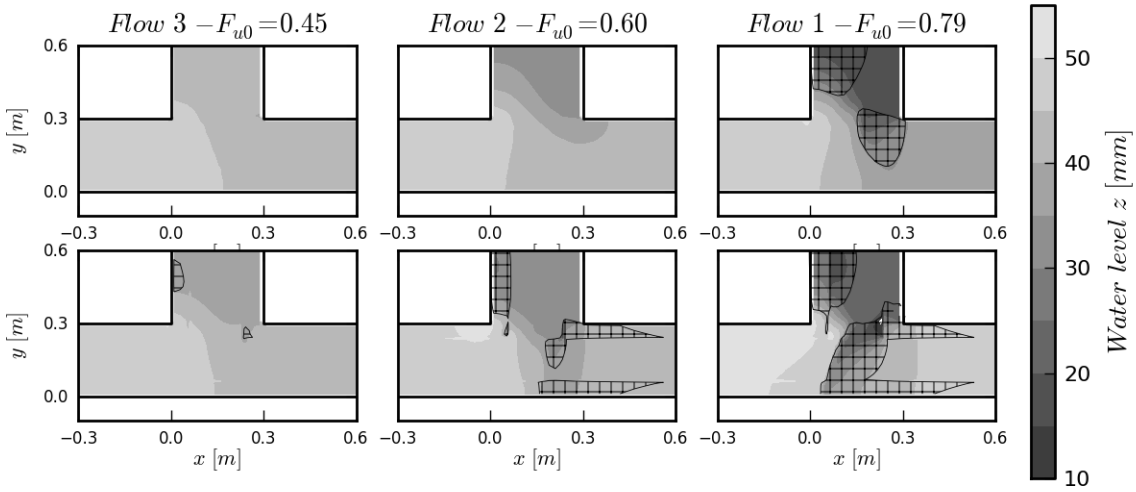

Figure 3.14 : Computed with run 1 water depths around the junction for flows 1, 2 and 3 without sidewalks (top) and with sidewalks. Supercritical flow areas (F>1) are shown as hashed.

Conclusion

Numerical simulations of experimental bifurcation flows presented in Chapter 2 have been carried out with the Rubar20 code that solves the two-dimensional shallow water equations. Comparison of simulation results with experimental measurements allowed us to assess the code ability to model a series of standard 3 branch dividing flows (initial flows), along with more complex configurations, introducing obstacles or sidewalks near the junction.

Computation of the discharge distribution for the initial flows without obstacles/sidewalks can be achieved with a fair accuracy (error typically less than 2%, see Table 3.1), without specific calibration of the numerical model. Remaining errors lie in the range of uncertainties of experimental measurements or of the modelling of the downstream boundary conditions. Therefore, prediction of the discharge distribution for subcritical dividing flows with the code Rubar20 appears to be more accurate than for supercritical (Mignot et al. 2008) or transcritical flows (El Kadi Abderrezzak et al. 2011).

Simulation of more local flow characteristics (water depths, shape of the branch recirculation area) requires a calibration of the constant eddy viscosity used to model turbulent effects. An independent (i.e., without calibration) prediction of these detailed flow characteristics would require a more accurate modelling of turbulence, as in (Shettar and Murthy 1996; Khan et al. 2000). However, the different runs used for calibration lead to very close estimations of discharge distribution and flow patterns near the junction. This preliminary result then justifies the modelling of flows through more complex configurations, with obstacles or sidewalks.

Simulations of flows with obstacles have been carried out with different sets of numerical parameters, particularly to assess the effects of the eddy viscosity and of the mesh resolution. Globally, all runs are able to predict effects of obstacles on the flow (deflections, contractions and accelerations) and consequences on global flow characteristics (evolutions of the discharge distribution and upstream channel water depths, summed-up on Figure 3.8). Deeper analysis shows that errors mainly arise from the modelling of the upstream obstacles, which greatly modify the flows in the area where the latter divide (i.e. the junction). For these obstacles, an optimum value of the eddy viscosity must be calibrated when using the fine mesh model to improve the simulated discharge distribution. Dealing with the remaining discrepancies may require the use of an even finer mesh and a real turbulence model, but both these aspects are beyond the scope of this thesis.

The coarse mesh model simulates simplified water depths and velocities around the obstacles and in the junction, which leads to globally larger errors, but also to less significant impact of the eddy viscosity. Although less accurate than a calibrated model with a fine mesh, the use of a model representative of urban flood models (coarse mesh, no eddy viscosity) then appears to lead to a correct representation of obstacles. Considering the discharge distribution, such model (*run8* on Figure 3.8) leads to average and maximum absolute errors respectively

0.9% and 3.5 %, which are smaller than the ones due to a non-integration of these obstacles (respectively 2.5% and 14%).

Modelling of flows with sidewalks has been carried out with a model representing as close as possible the sidewalks geometry and a second model that includes only an average channel bottom elevation. Both types of models fairly predict the impact of sidewalks on the discharge distribution, yet with a few discrepancies related to occurrence of supercritical flows in the junction. Results of the model with simplified geometry show that the simulation of the average flow acceleration in a channel section is sufficient to predict impact of sidewalks. This suggests that effects of the latter are mainly related to the upstream flow acceleration, and there is no significant impact on the mechanism of flow division (except when the flow in the junction becomes supercritical).

As a conclusion, it seems interesting for modellers to integrate small obstacles into urban flood models. This integration is likely to improve the simulations of i) the flood spreading with more accurate discharge distribution through crossroads, ii) an explicit modelling of the head losses due to the obstacles (which then reduces uncertainties related to the choice of a bottom friction) and iii) local flow characteristics (at least accelerations due to the flow contractions in the street). However, such integration requires an accurate knowledge of the obstacle locations and the use of a mesh that can be easily adapted, as effects of obstacles are strongly linked to their size and location.

Following flows with sidewalks simulations results, no specific treatment of topographical data can be recommended to enhance the sharp topography changes, as it can be done for urban drainage models (Ettrich et al. 2005). As long as the street is significantly flooded, an average street bottom elevation should lead to similar results as a detailed representation of the street topography. This result also points out that an unbiased street topography has to be used, that is with a correct average street bottom elevation. This may not always be the case, depending on how Digital Elevation Model (DEM) and meshes are generated. Therefore, integration of the detailed topography into the numerical models will be carefully studied for the real case modelling presented in Chapter 6.

Part II.
Interactions between street flows and underground pipe flows

Floods in urban areas imply the existence and interactions of several types of flows including surface flows, which are actually equivalent to flooding, and sewer flows, which will occur if the flooded urban area has an underground drainage system (which is most often the case). The simultaneous modelling of these two flow layers is referred to as *dual drainage* modelling (Djordjevic et al. 1999), and requires at least a coupling of two hydrodynamic flow models (for the surface and the pipe flows), as well as a model to calculate the exchange flow discharges between both layers. The two next chapters are dedicated to dual drainage modelling. Chapter 4 focuses on the modelling of exchanges between both layers, whereas Chapter 5 deals with the validation of a complete hydrodynamic model coupling surface and subsurface flows. Validation data have been produced on the experimental urban drainage model at the Disaster Research Prevention Institute of Kyoto University and form the base of the analysis and modelling of the next two chapters. The coupled numerical model is based on the use of the 2D code presented in last chapter (3.2) and a similar 1D code that will be introduced in Chapter 5.

Chapter 4.

Experimental study on the DPRI urban drainage model

4.1 Introduction

Flow exchanges between street flows and buried pipe flows are allowed through a variety of exchange structures, that can be originally designed to allow drainage of the surface towards the sewer, or that becomes an exchange structure during floods because of the hydraulic conditions (e.g. a flooded manhole). When designed for drainage, an exchange structure typically consists of a surface receptor (generally a curb opening inlet or a grated inlet) that is connected through a series of intermediary pipes to a main underground drainage pipe. On the one hand, design of urban drainage system from a flood risk perspective consists in choosing the appropriate spacing of such inlets, in order to intercept a project surface flow discharge. On the other hand, the underground pipes are designed to convey these intercepted flows, without generating overflow in the drainage network. These design steps are carried out respectively with laboratory measurements or advanced CFD methods for inlets efficiency (e.g. Despotovic et al. 2005; Fang et al. 2010) and hydraulic calculations in pipe networks, which is a common and well established practice.

However, when flooding occurs, with large amount of water in the street and pressurized flows in the pipe network, the hydraulic behaviour of these exchange structures change, as the flow conditions exceed the design hypotheses. As noted by Leandro et al. (2007), modelling of the flow exchanges through these exchange structures during flood has

actually received little attention and requires more specific studies. This chapter is dedicated to the modelling of these exchanges. Use of an experimental model of a typical urban drainage system is required to provide data which cannot be gathered on the field. However this method cannot be exhaustive and extrapolation to field cases must be carefully done. The structure of this chapter follows these remarks.

A literature review detailing exchange modelling techniques is proposed in the next sub-section. Then the experimental facility and measurements are presented, and a preliminary analysis allows us to set the type of flow exchanges that can be studied on this set-up. This framework being set, an exchange model adapted to the experimental set-up is developed and validated against experimental data. Finally an extrapolation of this model to a field case is proposed.

4.2 Literature review of exchange flows studies

4.2.1 General considerations

Exchange flows between surface and subsurface flows in an urban drainage system are imposed by both the geometry of the exchange structure and the hydraulics parameters of the surface and subsurface flows. Although exchange structures might have different possible designs, they can be schematically summed up to the combination of a surface inlet and a connecting structure to a main underground drainage pipe. Then, for a given exchange structure, one can define 3 typical hydraulic configurations that will determine the exchange process:

- Free drainage: the pipe hydraulic head is lower than the street ground elevation and the exchange flow is controlled by the capacity of the upper part of the exchange structure (Figure 4.1a), without influence of the rest of the exchange structure underneath.
- Influenced drainage: the exchange flow is controlled by the whole exchange structure, as a result of the pipe hydraulic head reaching the ground elevation (Figure 4.1b), or because the lower part of the exchange structure itself limits the exchanges.
- Overflow: the pipe hydraulic head exceeds the water elevation at the surface, which forces the water out of the underground drainage system (Figure 4.1c).

This representation is schematic but is consistent with the hydraulic configurations encountered in usual exchange structures. Modelling of each of these types of exchanges is reviewed below.

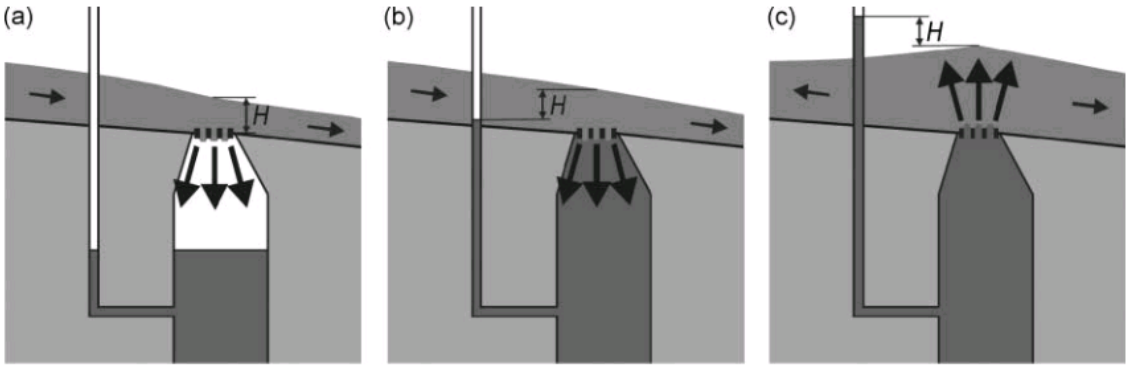

Figure 4.1: Types of exchange flows depending on hydraulic configurations through a schematic exchange structure: free drainage (a), influenced drainage (b) and overflow (c). From (Djordjevic et al. 2005)

4.2.2 Exchanges characterization

The wide range of exchange structures that can be implemented in urban areas prevents from doing extensive characterization of the flow processes in all possible structures. Therefore, detailed studies have focused on sub elements of these structures, such as street inlets or manholes. Laboratory measurements have allowed efficiency of street inlets to be characterized, notably showing the significant dependence on the street topography and the street flow characteristics (Despotovic et al. 2005; Gomez and Russo 2009). The testing of different inlets have led to well established guidelines to design the shape or spacing of these elements (e.g. MacKenzie and Guo 2011) in order to catch a design discharge or avoid lateral spreading of street gutter flows. These studies usually aim at providing practical results, without deep understanding of the physical processes involved. More recently, Djordjevic et al. (2013) used both experiments and a CFD model to study the flow pattern around a typical inlet receiving flows from a street. Results suggest that the behaviour of the inlet passes from a weir type flow to an orifice type flow depending on the street slope and flow discharge. Authors conclude that, as a result, no unique equivalent weir discharge coefficient can be assessed. These studies show the difficulty of estimating discharges through street inlets with simple exchange laws when street flows are shallow or fast. However, it is worth noticing that the street flow characteristics considered in these studies are related to usual drainage flows and do not cover all street flow conditions typical of urban flooding, such as slower and deeper street flows (which is the general framework of this thesis).

Characterization of other exchange structure elements or physical processes due to overflow have received little or even no attention. In (Djordjevic et al. 2013) and (Hilden 2005), overflow from a manhole is also considered, and the analysis focuses respectively on the water depth and velocity field around the manhole. Lopes et al. (2013) studied overflow from a gully, detailing with CFD the structure of the jet and of eddies in the gully box, and linking the pressure in the gully with the overflow discharges. Use of large-scale experiments in combination with CFD looks promising when studying complex flows involved by manhole or gully surcharges, yet no practical considerations are given for now concerning the evaluation of the exchange discharge.

Other studies on manholes exists, but essentially focuses on the head losses generated on pipe flows (Marsalek 1984; Pedersen and Mark 1990), without consideration of the possible interactions with the street flow. Finally, note that this lack of data regarding the exchange processes for extreme hydraulic conditions (i.e. flooded streets and underground drainage systems) can be attributed to the overall low probability of urban floods.

4.2.3 Implementation of the exchange discharge calculation in urban drainage models

To account for the street inlet efficiency, Gomez et al. (2011) directly implemented empirical laws into a numerical model of a street drainage system, with the use of a 2D flow model to accurately compute local characteristics of the street flow and the related local exchange discharges. Alternatively, when such information on the inlet efficiency is not available, a weir equation is commonly applied on the contour of the inlet:

$$Q_{ex} = \mu_w L_{SI} \sqrt{2g} (Z_s - Z_w)^{1.5} \qquad 4.1$$

Where Q_{ex} is the exchange discharge, μ_w is a weir discharge coefficient, L_{SI} is the perimeter of the street inlet, Z_s is the surface flow water elevation and Z_w the weir crest elevation. As mentioned earlier, this law remains a simplification and should be used only for low inertia street flows.

This equation is completed by an orifice equation when the water level in the pipe connected to the inlet reaches a threshold, to model an influenced drainage process:

$$Q_{ex} = \mu_o A_p \sqrt{2g} \left(Z_s - Z_p\right)^{0.5} \qquad 4.2$$

Where μ_o is an orifice discharge coefficient, A_p is the area of the pipe connecting the inlet to the main drainage pipe, and Z_p the water level in this main drainage pipe. If the pipe water level exceeds the street water level, there is overflow from the pipe to the street, and the latter equation becomes:

$$Q_{ex} = -\mu_o A_p \sqrt{2g}\left(Z_p - Z_s\right)^{0.5} \qquad 4.3$$

These simple equations are consistent with the general structure of the exchange flow, but they were developed for hydraulic structures much simpler than urban drainage elements, so that there are no existing guidelines to choose the appropriate discharge coefficients μ to be included in the weir or orifice equations. The latter coefficients can be selected on the basis of standard geometry coefficients (Nasello and Tucciarelli 2005; Leandro et al. 2009) or calibrated whenever it is possible (Lipeme Kouyi et al. 2009), but remains a major source of uncertainty in any field study.

(Leandro et al. 2007) extended this approach by splitting their exchange structure (or single linking element, see Figure 4.2) into three parts, each one being able to limit the exchange discharge, and by selecting the lowest exchange discharge. They developed their model for a generic exchange structure made of a surface inlet, an inlet box, a connecting pipe and a manhole. This modelling technique is less subjective, as it comprises detailed geometrical information, physical parameters such as Manning roughness coefficients and hypotheses on governing physical process (e.g. to switch from one control section to another), but a limitation is that there is no consideration of the flow through the whole exchange structure.

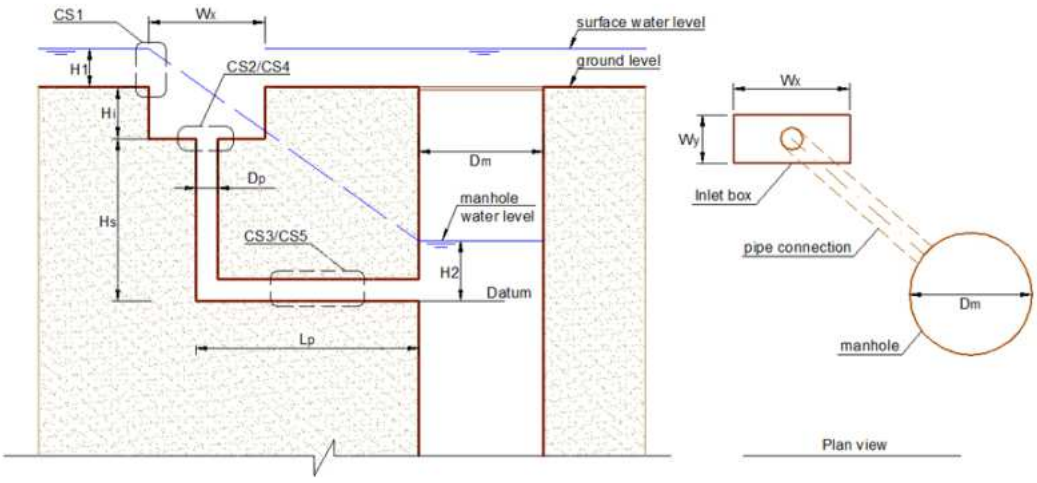

Figure 4.2 : Representation of an exchange structure through the use of a generic single linking element (Leandro et al. 2007). The control sections CS_i are indicated in dashed lines.

Finally, exchange discharges between both layers can be computed in an indirect manner, by limiting drainage when a pipe reaches its full capacity and by adjusting overflow so that the pipe pressure does not continuously exceed the ground level (Schmitt et al. 2004; Fang and Su 2006). This is equivalent to neglecting the potentially limiting capacity of the exchange structure itself. This hypothesis is rather difficult to justify without any preliminary simulations and knowledge of surface and subsurface flows characteristics.

4.3 Experimental measurements on the urban drainage model

4.3.1 Presentation of the experimental facility

The experimental facility used to study flow interactions represents an urban drainage system with two layers: a street and an underground pipe underneath, both connected by drainage tubes. The surface of the physical model consists of a zero slope 10 m long and 0.5 m wide street, lined on its sides with sidewalks and a series of street inlets (Figure 4.3). The sidewalks are 15cm wide by 2 cm high and are set along the whole length of the street. Walls are included along the sidewalks, which means a total channel width of 80 cm. The street inlets are located every 1 m, leading to a total number of 20 street inlets (10 on each side of the street). Each of these street inlets comprises a 5 by 5 cm *grid* placed at the street level, under which a *drainage box* and a *drainage tube* are set to connect the street to the side of the 5 cm diameter and 10 m long *pipe* that runs about 25cm below the street level. The pipe slope is 1/900.

Two independent loops permit to adjust the upstream street and pipe inflows. Each loop includes a pump, a valve, a downstream collecting tank, and an upstream feeding tank that allows the flows to stabilize (a scheme of these loops is shown on Figure C.2 in Appendix C). The pressure head at the downstream limit of the pipe is controlled through the water elevation of an intermediary tank equipped with a movable weir. The downstream flow in the street is usually critical, but a weir at the downstream end of the street can be raised in order to increase the water elevation. By adjusting these four upstream and downstream boundary conditions, one can simulate various flows with different exchange processes, from an efficient street drainage towards the pipe to a full overflow from the pipe to the street. A

modified version of this experimental facility was used with additional drain channels and a rainfall generator; results can be found in (Kawaike et al. 2011).

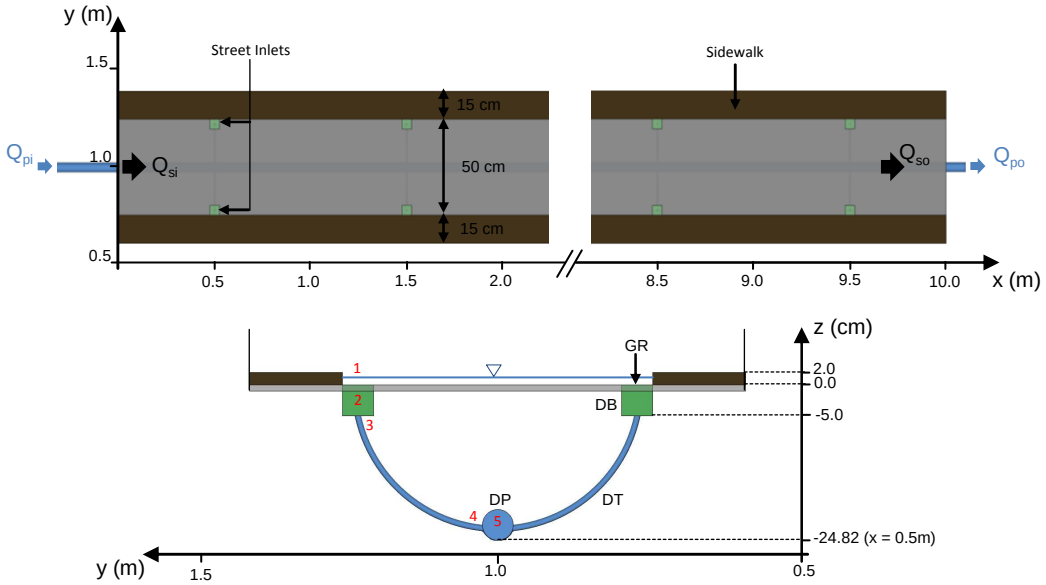

Figure 4.3 : Top view and cross section view (at x = 0.5m) of the experimental facility with its main dimensions. The drainage structure elements are indicated in upper case: street inlet grid (GR), drainage box (DB), drainage tube (DT) and drainage pipe (DP). The street level is at z=0.

4.3.2 Measurement devices

The street and pipe inflow discharges (respectively Q_{si} and Q_{pi}) are measured with electromagnetic flow meters (Admag AXF GS 01E20D01-02E-A from Yokogama, accuracy +/- 0.01L.s^{-1}) within each pumping loop. The outflow discharges from the street and the pipe (respectively Q_{so} and Q_{po}) are measured with a point gauge and a V-notch weir (accuracy +/- 0.01L.s^{-1}) set up on each downstream collecting tank. These values can be used to compute the total exchange discharge Q_{ex} and an associated error $Q_{ex,err}$:

$$Q_{ex} = 0.5 \times \left(Q_{si} - Q_{so} + Q_{po} - Q_{pi}\right) \quad 4.4$$

$$Q_{ex,err} = 0.5 \times \left(Q_{si} + Q_{pi} - Q_{so} - Q_{po}\right) \quad 4.5$$

The water elevation in the street Z_s is measured with an ultra sound sensor (UNDK 20U6914/S35A from Baumer) mounted on a sliding chariot with a horizontal positioning accuracy of +/-5mm and a vertical measurement accuracy of +/- 0.5 mm. The pressure in the pipe is measured through 10 piezometers (accuracy +/- 0.5 mm) located 10 cm upstream of each tube/pipe junction, plus one at the pipe outlet. The street bottom elevation is used as the

reference to express both the street water elevation Z_s (which then equals the street water depth) and the pipe piezometric head Z_p (so that this latter is positive only when exceeding the street bottom elevation).

Additionally, for unsteady flow measurements, time evolution of the water elevation upstream of the V-notch weirs is measured with resisting probes, and video cameras are used to record the other measurement devices or their display (flow meters and ultra sound sensor display, water column in the piezometers). Finally, surface flow velocities are measured using Large Scale Particle Image Velocimetry (LSPIV), with a commercial video camera (Sony Handycam HDR-CX520, 30Hz progressive, 1920x1080 pixels) located above the street and fine PVC powder inserted upstream as floating tracers. Details of the LSPIV computation and of the unsteady measurements post-processing can be found in Appendix C.

4.3.3 Flow measurements

The experimental facility is used with different flow configurations, in order to be able to describe the flow characteristics, to study the exchanges between the street and the pipe, and to validate full hydrodynamic simulations. Experiments are grouped in 5 categories that are described in the next sub sections.

There are two main limitations when defining an experimental flow:

- In order to avoid too large capillarity effects that would affect the street flow and its interaction with the exchange structures, the water depth in the street is maintained higher than 1 cm.
- As air bubbles entering the drainage structure and the pipe could complicate the measurements and the analysis, flows through the drainage structures and through the drainage pipe are always pressurized.

Within these conditions, the flow exchange is assumed to be mainly influenced by the head difference between the street and the pipe flows, and *a priori* not significantly influenced by the flow inertia around the street inlets. Thus, experimental observations do not cover the effects of a transient or free surface flow in the pipe, neither a limitation of the drainage capacity by the street flow velocity or the street inlet characteristics.

4.3.3.1 Street flow only

Preliminary measurements consist of studying street flows without interaction with the pipe or the exchanges structures. The street inlets are all blocked (filled with plastic and tap) so that the street flow cannot be drained into the pipe. 3flows including different flow discharge and average water depth in the street are studied (listed in AppendixB.4), to cover major flow configurations encountered in more complete experiments. For each flow, water depths are measured on a series of cross sections, LSPIV measurements are carried out on all the street, and street inflow and outflow discharges are recorded.

4.3.3.2 Pipe flow only

A series of pipe flows without interaction with the street are studied, for different flow discharges and downstream pipe piezometric heads (listed in Appendix B.4). The widest range of possible flow conditions is measured, the only limit being that the pipe piezometric head does not reach the street level (to avoid overflow). The measurements consist of piezometric heads at each piezometer location, and of the pipe inflow and outflow discharges.

4.3.3.3 Street and pipe flows interacting through one couple of street inlets

The experimental model is used with only one couple of street inlets operating (those at x=3.5 m) in drainage configuration, under various street flow conditions grouped in series (see Table 4.1). The nine other couples of street inlets are blocked with plastic and tap, as for the surface flows (4.3.3.1). For each series, the upstream discharges in the street and in the pipe are kept similar, only the downstream pressure in the pipe is modified, leading to a series of couple exchange discharge / head difference between the street flow and the pipe flow. Water depth in the street is measured on a 3 points cross section located 20 cm upstream of the operating couple of street inlets. The pipe piezometer head is measured at the piezometer located just 10 cm upstream of the exchange point. Inlet and outlet discharges in the street and the pipe permit to compute the exchange discharge and a corresponding measurement error (Eqs4.4 and 4.5).

Series	Number of flows	Q_{pi} L.s^{-1}	Q_{si} L.s^{-1}	Z_s cm	U_s m.s^{-1}	F -
SI1	17	0.20	0.22	1.8	0.02	0.06
SI2	17	0.20	1.08	1.9	0.12	0.27
SI3	17	0.20	1.76	2.1	0.17	0.37
SI4	14	1.00	0.22	1.8	0.02	0.06

Table 4.1 : Flow characteristics for experiments with one couple of street inlets operating. Street flow characteristics (water elevation Z_s, average velocity U_s and Froude number F) are measured or derived 20 cm upstream of the couple of street inlets.

4.3.3.4 Steady street and pipe flows interacting through all the couples of street inlets

In this series of experiments, the facility is used with a full operation of the drainage system (10 couples of street inlets operating), to study drainage and overflow cases at the street scale. These flows form the main part of this experimental study and will be referred as *complete steady flows*. 12 drainage and 4 overflow cases are measured, with different upstream and downstream boundary conditions (listed in Appendix B.4). The measurement grid for the street water depths consists in a series of 10 cross sections with 3 points (5 points when the sidewalks are flooded), located 20 cm upstream of each street inlet couple. The piezometric head is measured at each piezometer. For 8 flows, LSPIV measurements are carried out on the whole street with a 5cm resolution, to be able to compute the evolution of the street flow discharge. Finally, for two reference flows detailed in Table 4.2, 2 intermediary cross sections are added between each couple of street inlets, and LSPIV measurements are carried out on a regular grid of 2.5 cm around the 4th and 5th couples of street inlets.

Flow	Type	$Q_{s,5}$ L.s^{-1}	$Q_{ex,5}$ L.s^{-1}	$Q_{ex,5}/Q_{s,5}$ -	$Z_{s\ (x=4m)}$ cm	$F_{(x=4m)}$ -	$Re_{(x=4m)}$ -	Flow on sidewalks -
D6	Drainage	1.62	0.09	5.7 %	2.0	0.37	1.10^4	No
O4	Overflow	2.74	-0.05	-1.9 %	3.0	0.28	2.10^4	Yes

Table 4.2 : Characteristics of two selected steady flows including LSPIV measurements. Results of the exchange model (see 4.5) give an estimation of the following flow discharges : $Q_{s,5}$ is the street flow discharge between the 4th and 5th couple of street inlets , $Q_{ex,5}$ is the exchange flow discharge for the 5th couple of street inlets.

4.3.3.5 Unsteady street and pipe flows interacting through all couples of street inlets

In this last series of experiments, the configuration of the experimental facility is the same as in the previous series (4.3.3.4), but flows are unsteady. Four experimental flows are measured (see Table 4.3). For cases US1 and US2, the inlet discharges in the pipe Q_{pi} and the street Q_{si} are kept constant, but the downstream pipe piezometric head $Z_{p,dn}$ is raised to a maximum of around +2.5 cm and then returns to its initial value, which creates a temporary overflow of the drainage system. For cases US3 and US4, the inlet discharge in the pipe and the downstream pipe piezometric head $Z_{p,dn}$ are kept constant; the street is initially dry, and a flow hydrograph is generated upstream of the street. The flow at the downstream end of the street remains critical for all unsteady flows. In each couple of unsteady flows, the amplitude of the variations is approximately the same, but the typical duration of the boundary condition evolution changes.

For these unsteady flows, experimental measurements consists first of a recording of the three boundary conditions (pipe and street inlet discharges Q_{pi} and Q_{si}, downstream pipe piezometric head $Z_{p,dn}$), along with the street outflow discharge Q_{so}, which is used as a global validation data. Values of the piezometric heads are also measured at the piezometers P2, P5 and P8 (located respectively just upstream of the 2nd, 5th and 8th couple of street inlets). The water elevation of the street surface flow is measured at a unique central point at (x=5m, y =1m).

Flow	Q_{si} $L.s^{-1}$	Q_{pi} $L.s^{-1}$	$Z_{p,dn}$ cm	t_{us} s
US1	1.5	0.5	**-16/+2.5**	70
US2	1.5	0.5	**-16/+2.5**	200
US3	**0/1.8**	0.5	-16.0	110
US4	**0/2.0**	0.5	-16.0	260

Table 4.3 : Flow description in unsteady state (t_{us} is the typical length of unsteady conditions). The range of values for the time varying boundary condition is indicated in bold.

4.3.4 Street topography measurements

Four bottom elevation measurements of the street have been carried out. Detailed results are presented in Appendix B.3, and a summary is provided below. The mean bottom elevation shows that a small pond exists in the centre of the street, whereas the upstream and

downstream ends are slightly higher than the average bottom elevation (Figure 4.4). In the same way, the street is globally slightly curved with higher elevations along the sidewalks than in the centre part. Moreover, analysis of the detailed measurements shows that the street bottom elevation can locally vary depending on whether or not a street flow has been previously generated. Measurements of the sidewalks elevation were also performed and showed local variations due to the different material junctions (shown in Appendix B.3).

The street is made of several layers of plastics sheets that are joined together. Due to the ambient conditions (temperature, humidity) and the need of working directly on the street channel to carry out some modifications (such as blocking street inlets to generate a street flow without drainage), the bottom topography may change from its original design. This fact does not influence the operation of the experimental device, but may limit the accuracy of the analyses related to the street flow and should therefore be kept in mind.

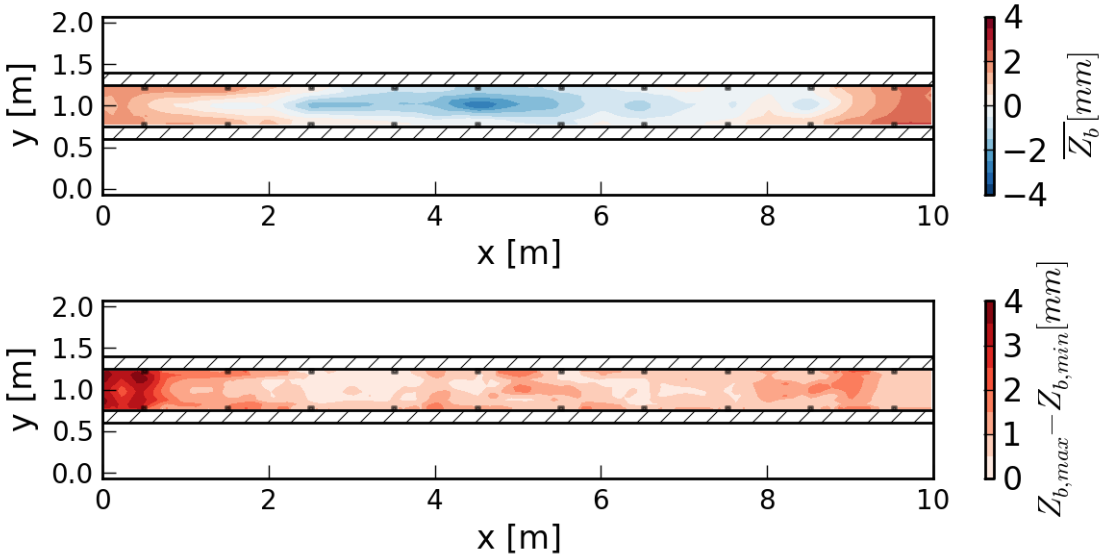

Figure 4.4: Average street bottom elevation (top) and maximum difference observed (bottom) between the 4 series of measurements. Street inlets location are indicated in gray squares and sidewalks with hashed rectangles

4.3.5 Use of the experimental data

Use of the previously described experimental data for the analysis follows four steps. First, in the following sub section a general description of the experimental flows is provided, to set the framework of analysis and applicability of this study. Then in section 4.5 an exchange model is developed and validated using both kinds of steady flows with street/pipe exchanges (flows with respectively one or ten couples of street inlets operating). Finally, in Chapter 5, results of numerical simulations are compared to measurements carried out for complete flows (full operation of the experimental model, with steady or unsteady flows).

4.4 Description of experimental flows

4.4.1 Street flows

The street flows are always subcritical, with typical Froude number between 0.2 and 0.4. The Reynolds numbers in the street are around $5x10^3$-$1.5x10^4$, and drop to $3x10^3$ when considering local flows on the sidewalks. Except right above the street inlets, the water depths are not significantly affected by the flow exchange process, and the variations inside one section are found to be within the range of measurement uncertainties. Therefore for the following sections and next chapter, cross section averaged values of the water elevation in the street will be used. Moreover, due to the smooth materials and limited Froude numbers, the longitudinal evolutions of the street water elevation remain limited in the experimental flows (typically several millimetres on the 10 m long street), so no detailed characterization is carried out.

Figure 4.5 shows the surface velocities for the flows D6 and O4 (defined in Table 4.2) around the 4th and 5th couples of street inlets. Surface velocities show that both flows tend to concentrate in the centre of the street, as a result of the friction on the sidewalks and of the exchange process. This effect is more pronounced for the overflow case (O4), as the exchange flows are similar to vertical jets and block the incoming street flow around the street inlet. When the sidewalks are flooded (O4), there is a significant difference in velocity magnitudes between the sidewalks and the street (as for a compound channel).

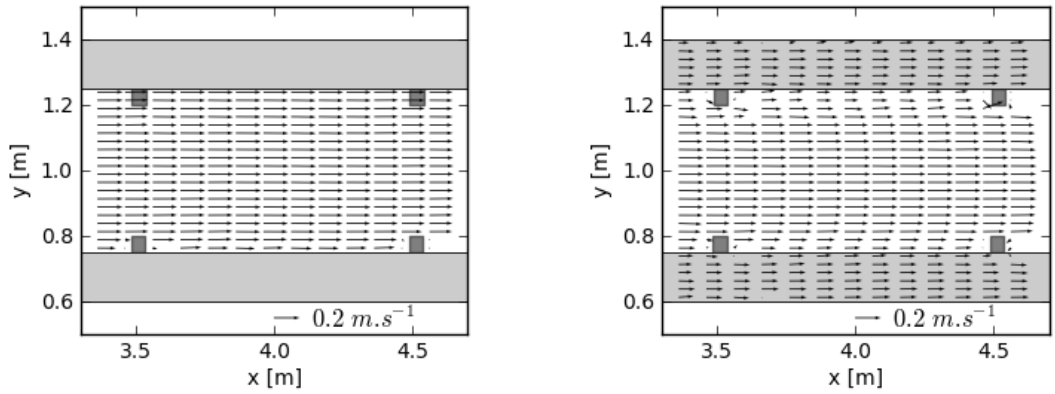

Figure 4.5 : Surface velocities around the 4th and 5th couples of street inlets for the flows D6 (left) and O4 (right)

4.4.2 Pipe flows

The pipe flows Reynolds number typically varies between $2.5x10^3$ and $4.0x10^4$. For this range, the pipe friction factor should depend on both the Reynolds number and the typical roughness height (Yen 2002). The series of pipe flow measurements provides 14 couples of pipe piezometric head evolution and pipe discharge. These data are used to calculate an empirical friction factor (Darcy-Weisbach type) for the pipe, using the following equation:

$$f_p = \frac{dZ_p}{dx}\frac{D_p \cdot 2g}{V_p^2} \qquad 4.6$$

Where f_p and D_p are respectively the pipe friction factor and diameter, V_p and Z_p are respectively the pipe flow average velocity and piezometric head. For each flow, an uncertainty range is derived considering both the flow discharge and the piezometer head measurement error. The following empirical law is fitted (considering the uncertainty range) on the 14 values :

$$f_{p,emp} = 0.363 \cdot R_e^{-0.254} \qquad 4.7$$

Friction factors are plotted on a Moody's diagram (Figure 4.6), along with the ones computed with the Blasius equation (valid for $2.8 \cdot 10^3 < Re < 10^5$, (Yen 2002)):

$$f_{p,Blasius} = 0.3164 \cdot R_e^{-0.25} \qquad 4.8$$

The empirical relationship (4.7) provides higher friction factors than the ones computed with Blasius equation (4.8), because it accounts for the various local head losses generated into the experimental pipe (piezometers, drainage tubes, pipe fittings). Measurement uncertainty for low pipe flow Reynolds number is important but the associated linear head losses are very low (a few millimetres on the whole pipe length) so that using the equation 4.7 should lead to acceptable errors considering the model dimensions and the typical pipe piezometric head evolutions. The equivalent Manning-Strickler coefficients lie between 80 and 115 $m^{1/3}.s^{-1}$, which clearly shows the benefits of using this empirical relationship for numerical simulations over a calibrated Manning-Strickler coefficient.

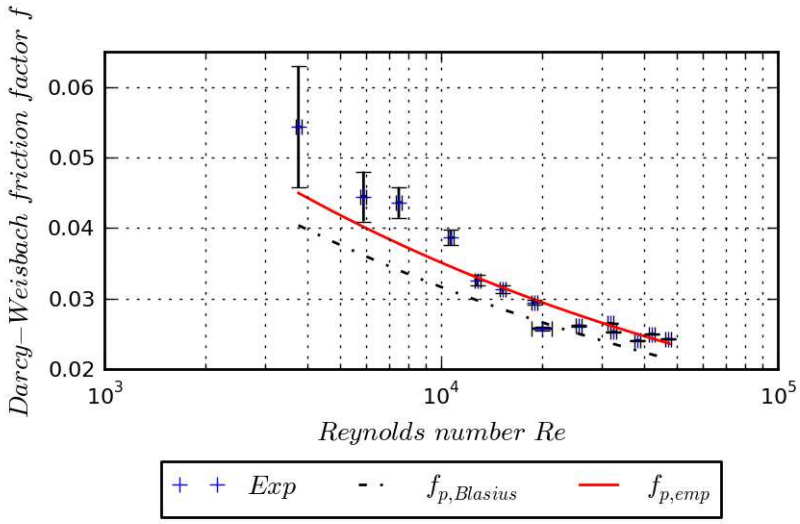

Figure 4.6 : Moody's diagram with experimental friction factor (crosses), fitted law (plain line) and Blasius equation (dotted line)

4.4.3 Exchange flows

Exchange flows are not directly instrumented but visual observations and analysis of the total exchange discharges at the street scale provide an insight of the exchange flow characteristics. When drainage occurs, the street inlets remain fully submerged and the drainage tubes remain pressurized. This is of particular importance, as it proves that in our configuration, the drainage capacity is related to the available head difference between the street flow and the pipe flow. When overflow occurs, the vertical jets flowing out of the drainage tubes create a local rise of the street water elevation, which reveals that the jet is not dissipated before reaching the surface, and that the street flow in this area becomes highly three dimensional (see Figure 4.5). For steady state flows, the drainage tubes flows Reynolds number vary between 5.0×10^2 and 1.5×10^4, which imply both laminar and turbulent flows.

4.5 Exchanges analysis

4.5.1 Development of an exchange model

Previous observations on the exchange flows set the framework for the exchange model. Assuming the exchange flow is pressurized through the entire exchange structure, one can link the exchange discharge to the total head losses in the exchange structure. The latter can be expressed as follows:

$$\Delta H_{1-5} = \Delta H_{1-2} + \Delta H_{2-3} + \Delta H_{3-4} + \Delta H_{4-5} \quad 4.9$$

with $\Delta H_{i\text{-}j}$ the head loss between the sections i and j of the drainage structure, as mentioned on Figure D.2 (Appendix D). Each of these head loss terms corresponds to a relatively standard hydraulics configuration, for which empirical and theoretical formulations have been developed in the past. Choice of the appropriate formulations and parameters are explained in details in Appendix C, and the main assumptions and results are presented below.

$\Delta H_{1\text{-}2}$ is the head loss through the street inlet grid, which can be considered as a diaphragm of an equivalent flow section area (Idelchik and Steinberg 1996). $\Delta H_{2\text{-}3}$ is the head loss at the drainage tube entrance (for the drainage case, modelled as an abrupt contraction of the drainage box flow to the tube flow) or exit (for the overflow case, modelled as a submerged pipe exit). $\Delta H_{3\text{-}4}$ is the linear head loss through the drainage tube, modelled using a Darcy-Weisbach friction coefficient f_t. Finally, $\Delta H_{4\text{-}5}$ is the head loss at the junction between the main drainage pipe and the drainage tube, for combining flows (drainage case) or dividing flows (overflow case). Based on the data and formulations compiled by Miller (1978) and Idelchik and Steinberg (1996), these terms can be expressed as a function of the exchange discharge q_{ex} in the drainage tube :

Drainage case (qex>0):

$$\Delta H_{1-5} = \left(K_{1-2} \cdot \alpha_{V1-2+}^2 K_{2-3} + f_t \cdot \frac{L_t}{D_t} + K_{4-5}\right) \cdot \frac{q_{ex}^2}{A_t^2 \cdot 2g} \quad 4.10$$

Overflow case (qex<0):

$$\Delta H_{1-5} = -\left(K_{2-1} \cdot \alpha_{V2-1+}^2 K_{3-2} + f_t \cdot \frac{L_t}{D_t} + K_{5-4}\right) \cdot \frac{q_{ex}^2}{A_t^2 \cdot 2g} \quad 4.11$$

where $K_{i\text{-}j}$ is the head loss coefficient associated to the local head loss $\Delta H_{i\text{-}j}$, $\alpha_{V1\text{-}2}$ and $\alpha_{V2\text{-}1}$ are coefficients to pass from the tube flow velocity to the flow velocity approaching the street inlet grid, f_t the friction factor of the drainage tube, L_t, D_t and A_t respectively the length, the diameter and the area of the drainage tube and g the acceleration due to the gravity. The coefficients $K_{i\text{-}j}$ are taken from the two hydraulics books previously cited, except for $K_{4\text{-}5}$ for which a more adapted formulation for our exchange structure geometry is proposed by Serre

et al. (1994). The coefficients are calculated in respect of the present exchange structure geometry, and vary with the flow exchange discharge (through the associated Reynolds number), and also with the flow discharge in the main pipe for $K_{4\text{-}5}$ and $K_{5\text{-}4}$. The typical roughness height k_s of the plastic drainage tube used to compute the friction factor f_t equals 0.01 mm. For a drainage case, it is assumed that the velocity approaching the grid is equal to the average flow velocity in the drainage box, so that $\alpha_{V1\text{-}2}=A_t/A_{db}$ with A_{db} the flow area of the drainage box. For overflow configurations, $\alpha_{V1\text{-}2}$ is related to the structure of the jet flowing out of the drainage tube. Using formulas for a submerged round jet (Idelchik and Steinberg 1996), a value of 0.6 is calculated for $\alpha_{V2\text{-}1}$.

These equations are implicit, as the head loss coefficients depend on the drainage tube flow discharge, so they are solved with a dichotomy method. **The set of equations 4.10 and 4.11 allows a computation of the local exchange flow discharges in the experimental facility, and is named exchange model in the following sub sections**.

4.5.2 Validation of the exchange model

4.5.2.1 Flows with one couple of street inlet operating

Experimental measurements of the exchange discharge through one inlet (half the measured exchange discharge performed through one couple of inlets) and the head difference for all flow configurations from the 4 series defined in Table 4.1 are plotted on Figure 4.7, along with the model results for drainage (Eq.4.10). Measurement uncertainties remain important because the exchange discharges for one street inlet are only an order of magnitude larger than the measurement errors. However, within this uncertainty range, it can be seen that the street flow Froude number does not affect the exchanges for the range tested (between 0.06 and 0.37), which confirms that the exchange flows are not limited by the street inlet grid. Oppositely, the flow discharge in the pipe upstream of the junction with the drainage tubes does have an impact on the exchanges, with higher values leading to higher exchange discharges. The model results are in fair agreement with the measurements given the uncertainty range, especially when considering the effect of the pipe flow discharge. However measurement uncertainties inherent to this restricted experimental configuration do not allow either a detailed validation of the exchange model, or a study of the overflow configurations.

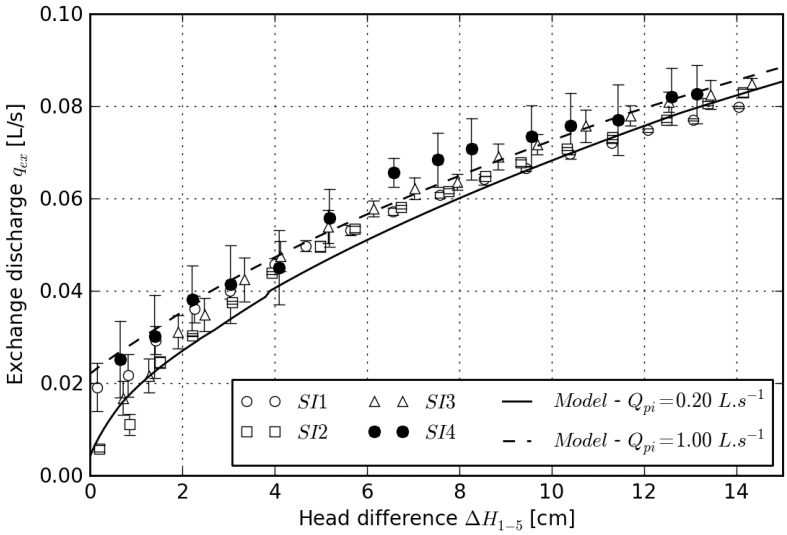

Figure 4.7 : Measurements of exchange discharges and head differences for the series SI1 to SI4 (symbols). The upstream pipe discharge is of 0.2L.s^{-1} for series SI1 to SI3, and 1.0 L.s^{-1} for SI4. Results of the exchange model (lines) are plotted for both of these upstream pipe discharges.

4.5.2.2 Flows with ten couples of street inlet operating

The exchange model is applied to the series of complete steady flows (16 runs), which includes a large range of flow conditions (12 drainage and 4 overflow cases, with various water depths in the street, pipe flow pressures and pipe flow discharges - see Appendix B.4 for a detailed listing). Street water depths and pipe pressures are measured with enough accuracy at the vicinity of the exchange points, but the street and the pipe flow discharges are only measured at the upstream and downstream ends of the experimental model. An attempt of computing local street flow discharges using water depths and surface velocities measurements has been carried out, but the resulting accuracy was found to be not sufficient to derive local exchange flow discharges (see Appendix C.1). Therefore, results of this computation cannot be used for the present exchange model validation and local street and pipe flow discharges remain unknown.

Lack of measured local exchange flow discharges means i) that the validation can only be performed considering the measured total exchange discharge $Q_{ex,mes}$ (sum of all exchanges for the 10 couples of street inlets) and ii) that the local head differences cannot be directly computed from the experimental data, as local street and pipe discharges are not known. To solve this issue, the exchange model is applied iteratively from the downstream to the upstream exchange points, and the estimated street and pipe flow discharges are updated considering the computed exchange flow discharges. The error associated to this process remains limited because i) the resulting total exchange discharges computed with the

exchange model are globally very close to the measured ones, ii) the head difference mainly consists of the hydrostatic pressure difference, and iii) variations of $K_{4\text{-}5}$ and $K_{5\text{-}4}$ with the pipe discharge remain small when compared to the variations of the head differences. This error as well as the ones associated with the other measurements is estimated by considering that:

- the street water depths are measured with a +/- 0.5 mm accuracy
- the pipe piezometric heads are measured with a +/- 0.5 mm accuracy
- the street and pipe flow discharges are locally evaluated with a +/- 10% accuracy

The two first assumptions are derived from the measurement devices, whereas the last one is arbitrarily fixed to a conservative value. Calculated total exchange discharges with the exchange model $Q_{ex,model}$ are compared with experimental measurements $Q_{ex,mes}$ on Figure 4.8, including the uncertainties presented above. Results from the exchange model are very close to the measurements, and the uncertainties associated to the experimental measurements remain low, so that the methodology used here is assumed to be fairly validated. The exchange model shows a small bias, with a trend to compute too large exchange discharges in absolute values (average error of +0.029 $L.s^{-1}$ and +0.05 $L.s^{-1}$ for respectively drainage and overflow cases, or +3.6% and +11% of the measured exchange discharge). For drainage cases, the error is higher for the flow with the lowest total exchange discharge and can be related to the corresponding low exchange flow Reynolds numbers (around $1x10^3$-$3x10^3$), for which uncertainty on head loss coefficients increases. The global bias may come from a more systematic underestimation of one or several head loss term in equations 4.10 and 4.11. For overflow cases, considering the assumptions made on the head losses through the grid and at the tube outlet (detailed in Appendix D.3.2.2), an overestimation of the corresponding head losses was expected. The present comparison with experimental data yet tends to invalidate the hypothesis of such an overestimation. Then, effects of non-uniform velocity across the sections are neglected (the Coriolis coefficient is set to unity), as such information is not available and would be complicated to estimate. Yet, the kinetic energy is usually low when compared to the total head loss, so that related uncertainties are considered as small.

There is no experimental evidence that can point out a particular inadequacy among the different head loss formulations, so no attempt of improving the model accuracy is carried out. Finally, the exchange model is considered as validated, which permits both its use in full numerical simulations (next chapter) and a more detailed analysis of its results.

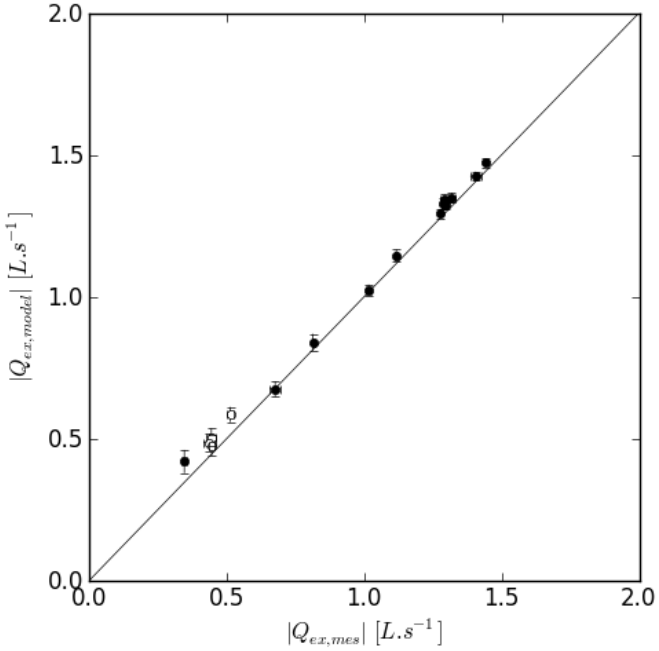

Figure 4.8 : Comparison of the total exchange discharges (in absolute values) measured and calculated with the exchange model based on experimental measurements for drainage cases (filled circles) and overflow cases (empty circles). Error bars accounts for the experimental uncertainties when applying the exchange model.

4.5.3 Analysis of the exchange model results

Equations forming the exchange model (Eqs. 4.10 and 4.11) can be easily transformed in an equivalent orifice equation (Eqs. 4.2 and 4.3 for respectively drainage and overflow cases), with the corresponding discharge coefficient:

Drainage case :

$$\mu = \left(K_{1-2} \cdot \alpha_{V1-2+}^2 K_{2-3} + f_t \cdot \frac{L_t}{D_t} + K_{4-5}\right)^{-1/2} \qquad 4.12$$

Overflow case:

$$\mu = \left(K_{2-1} \cdot \alpha_{V2-1+}^2 K_{3-2} + f_t \cdot \frac{L_t}{D_t} + K_{5-4}\right)^{-1/2} \qquad 4.13$$

Note that the coefficients $K_{i\text{-}j}$ and f_t depend on the exchange flow Reynolds number and potentially on the pipe flow discharge. Therefore the discharge coefficient μ should vary from one experimental flow to another, and even from one exchange structure to another. In order to assess the benefits of using our exchange model over a simplified orifice equation, equivalent discharge coefficients for the latter are computed for the steady flows, to assess their variations.

For a given complete steady flow, an experimental discharge coefficient is fitted, assuming a constant value for the 20 exchange structures (no experimental data can support an individual fit for each exchange structure):

$$\mu_{EXP} = \frac{Q_{ex}}{2 \cdot A_t \sqrt{2g} \sum_{k=1}^{10} \left(H_{s,k} - H_{p,k}\right)^{1/2}} \qquad 4.14$$

With Q_{ex} the total exchange discharge, $H_{s,k}$ and $H_{p,k}$ respectively the street and pipe flow hydraulic heads at the k^{th} exchange point. As previously, Q_{ex} is directly measured, but $H_{s,k}$ and $H_{p,k}$ have to be approximated. Results of the exchange model are used to estimate local street and pipe flow discharges and then the local street and pipe hydraulic heads.

Then, results of the exchange model for a given flow can be directly used to compute a discharge coefficient for each couple of exchange structures (with Eq. 4.12 and 4.13), as the local head loss coefficients are computed by the exchange model. Considering the accuracy of the exchange model, the discharge coefficients computed with this method should be very close **in average** to the ones computed with the experimental data, but this method provides every local coefficient and permits to assess their variations for a given flow.

Figure 4.9 shows the results of these computations. Fitted experimental coefficients are indicated with symbols. Range of variation of the coefficients computed by the exchange model is indicated with bars and the average value is indicated with a horizontal black line. First, fitted experimental coefficients for drainage cases tend to decrease as the total exchange flow decreases, as a result of higher head loss coefficients for low exchange flow discharges (and associated low Reynolds numbers, as explained in Appendix C). This trend is more important for very low exchange discharges, as shown by the flow for which Q_{ex}<0.4 L.s^{-1}. Experimental discharge coefficients for overflow cases are found to be around 50% smaller than the ones for drainage cases, which clearly shows that significant differences exist between both types of exchange flows. The 4 fitted values do not vary much, which is likely to come from the very similar total exchange discharges.

As expected, average discharge coefficients computed with the exchange model results (horizontal black line within each bar) are close to the ones fitted on experimental data. Remaining discrepancies reflect discrepancies observed in 4.3.3.4, with a global overestimation of the exchange flow discharges, which is more pronounced when the latter are low and for overflow cases. The variation ranges are typically of +/- 5% of the average value, which remains significant when compared to the global variations of the average coefficients.

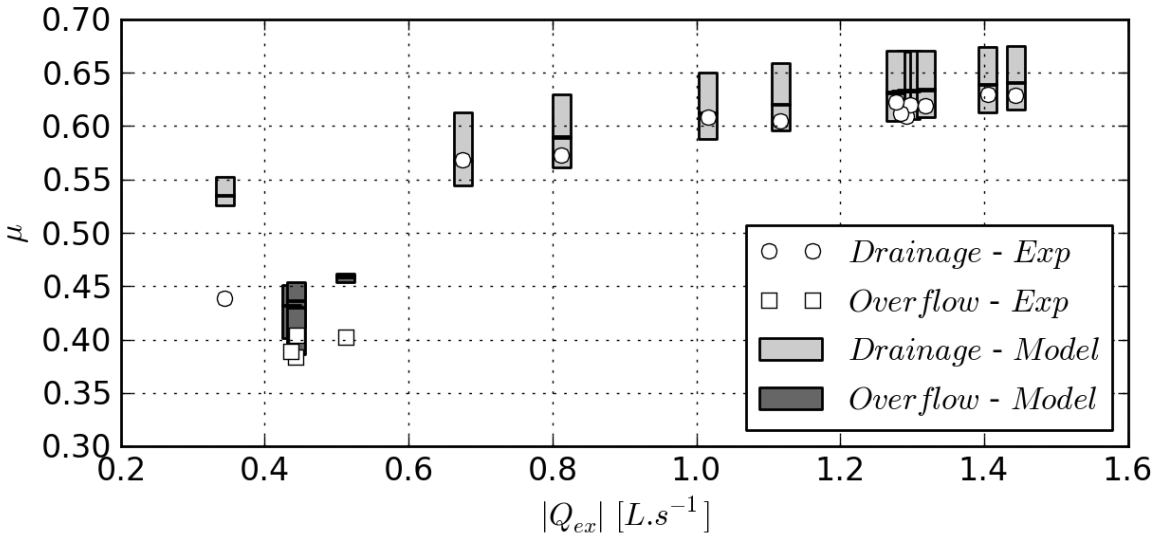

Figure 4.9 : Equivalent discharge coefficients computed for the 16 steady flows against the measured total exchange discharges (in absolute values)

Besides dependencies of the head loss coefficients on the exchange flows Reynolds numbers, disparity of the discharge coefficients also comes from the different nature of the exchange flow for drainage and overflow cases. Figure 4.10 shows the distribution of the 4 different head loss terms $\Delta H_{i\text{-}j}$ computed with the exchange model, for several hypothetical combinations of exchange flow and pipe flow discharges representative of the experimental flows. First, the important difference observed between drainage and overflow cases appears to come from the head losses associated to the grid ($\Delta H_{1\text{-}2}$). This comes from the different velocity of the flow approaching the grid for drainage and overflow cases. In the first case, the flow velocity near the grid is nearly equal to the average flow velocity in the drainage box, which is actually very low and leads to negligible head losses. In the second case, the jet flowing out of the drainage tube is not dissipated when approaching the grid and thus its velocity and the associated head losses are significant. The major difference in this head loss term values explains itself the significant differences between drainage and overflow discharge coefficients.

The three other head losses terms ($\Delta H_{2\text{-}3}$, $\Delta H_{3\text{-}4}$ and $\Delta H_{4\text{-}5}$) are of the same order of magnitude, but with relative contributions varying with the flow conditions. Head losses at the tube/pipe junctions for drainage cases are relatively smaller for low exchange discharges q_{ex}, and can even be negative (though there is always an energy loss at the tube/pipe junction, as explained in Appendix D). This happens for low ratios of tube flow discharge over pipe flow discharge (for q_{ex} = 0.01 L.s^{-1} and Q_p=1.0 L.s^{-1} on Figure 4.10). The opposite is observed for overflow, denoting the different nature of the local head losses at the junction for both types of exchange flow.

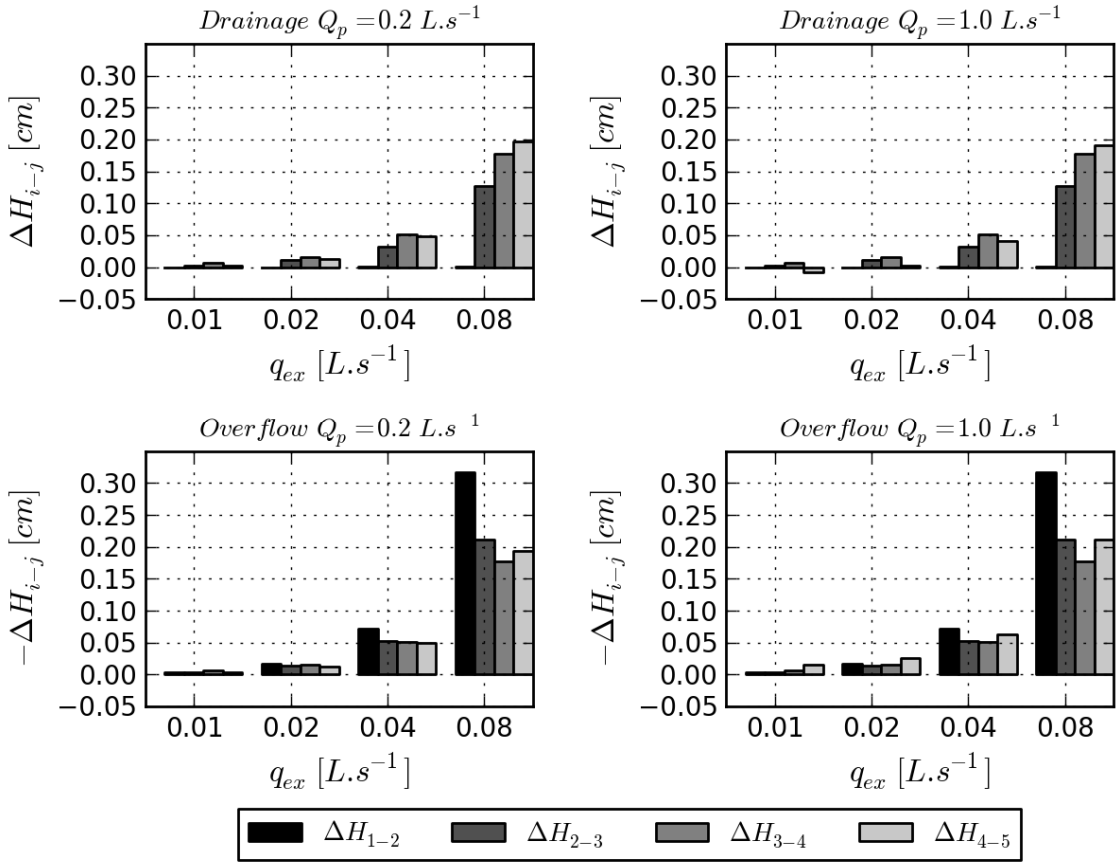

Figure 4.10: Head losses distribution for drainage (top) and overflow (bottom) configurations provided by the exchange model for typical exchange flow discharges q_{ex} and pipe flow discharges downstream of the exchange point (Q_p)

4.6 Extrapolation to real-scale urban drainage systems

Analysis of the experimental data has allowed to validate an exchange model for pressurized exchange flows and to describe its behaviour for the specific experimental exchange structure. The relevance and the main characteristics of the developed exchange model have to be studied when the latter is applied to a field case. In particular, it is interesting to assess for a real scale exchange structure) the values of equivalent orifice discharge coefficients for a simplified modelling (and their potential dependencies), and ii) the occurrence of the flow conditions required to apply the developed exchange model (exchanges controlled by a pressurized flow through the whole exchange structure). To do so, we study in the next sub sections the flow exchanges for two exchange structures: 1) a scaling of the present experimental exchange structure and 2) a simplified version, considered as more representative of the exchange structures encountered in our field case (Chapter 7) and in the scientific literature.

4.6.1 Studied exchange structures

The urban drainage model scale is assumed to be 1:10. As there are several geometrical parameters defining the exchange structure (Figure 4.11), a direct scaling may not be representative of an actual exchange structure, in particular considering the connecting pipe (equivalent of the experimental drainage tube) for which a direct scaling leads to a 10 cm diameter pipe, which seems too small for areal exchange structure. As a result, a first study is done considering a direct scaling; then a sensitivity analysis is carried out on the exchange structures geometry and materials.

The first exchange structure (STR1) consists in scaling the experimental exchange structure, replacing only the drainage tube by a connecting pipe with an elbow. The second exchange structure (STR2) is the same except that the connecting pipe is not directly connected to the underground drainage pipe but to a manhole. This implies that i) the head losses are not of the same nature at the junction between the connecting pipe and the main pipe (or manhole), and ii) hydraulic heads in the manhole and the main pipe slightly differ, assuming the manhole flow velocity is null. This last assumption may not always be true, but

it creates a reference configuration different than in STR1 and allows us to assess the influence of the main pipe flow velocity on the exchanges.

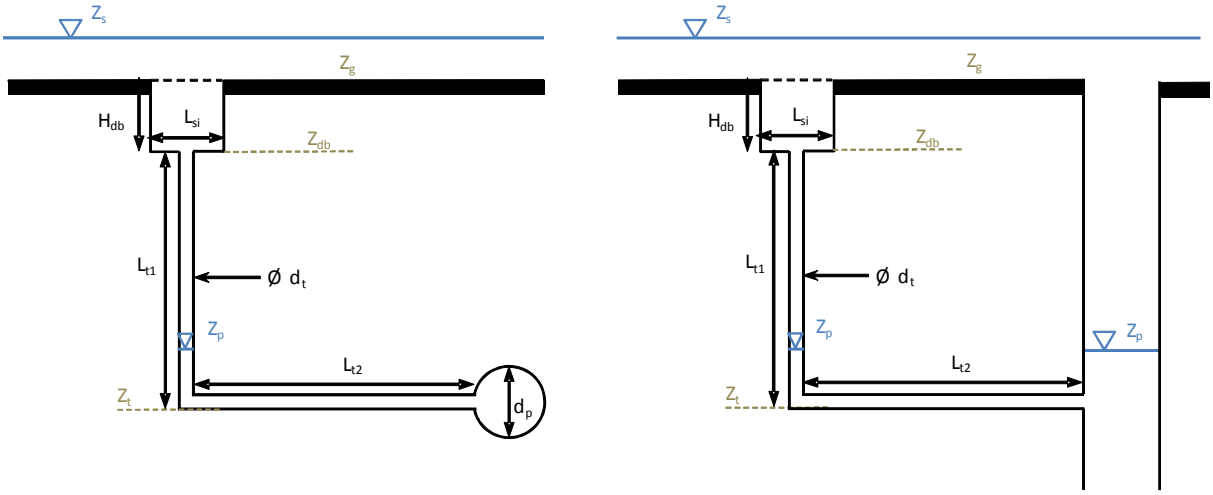

Figure 4.11: Definition of the 2 schematic exchange structures connecting a street to its underground drainage system (left: STR1, right: STR2) along with the geometrical parameters notation

4.6.2 Exchange model

The exchange model is set up by coupling the methodology of Leandro et al. (2007) and the one developed for our experimental exchange structure. For drainage cases, the exchange discharge can be either controlled by the following controlling elements:

- the flow from the street to the drainage box (C1),
- the flow from the drainage box to the connecting pipe (C2),
- or the pressurized flow through the whole exchange structure from the street to the main drainage pipe (C3)

For overflow cases, the exchange discharge is controlled uniquely by the flow through the whole exchange structure, from the main drainage pipe to the street (C4). C1 and C2 are situations where the exchange flow is controlled at a specific section of the exchange structure, whereas in C3 and C4 the flow within the whole exchange structure controls the exchange discharge, as in the experimental urban drainage model.

The discharge for C1 is modelled using a weir equation (Eq.4.1) applied to the whole perimeter of the street inlet, with a discharge coefficient μ_w. The discharge for C2 is modelled with an orifice equation applied to the connecting pipe area, with a discharge coefficient μ_o.

For C3 and C4, the methodology proposed for the experimental model is applied. The head loss formulation remains essentially the same, yet with the following additional elements:

- the elbow in the connecting pipe creates additional head losses
- head losses at the junction of the connecting pipe and the manhole for the exchange structure STR2 are modelled as a free pipe outlet. Manhole dimensions are therefore not considered.

Besides the geometrical parameters of the model (see Figure 4.11), it is necessary to choose the discharge coefficients μ_w and μ_o, and a material roughness k_s. For all these parameters, a reference value is chosen (Table 4.4) with a variation range for the sensitivity analysis. μ_w and μ_o are taken from Lencastre (1986) for standard weir and orifice configurations. Though the actual values will depend on several geometrical parameters not considered here, the chosen values remain consistent. For instance, Guo et al. (2009) derived experimental values of μ_w between 0.3 and 0.45, the variations coming from the different street inlets geometries. k_s is also taken from Lencastre (1986), considering pipes in concrete with different qualities. f_{SI} is the opening ratio of the street inlet grid.

	L_{si}	H_{db}	f_{SI}	L_{t1}	L_{t2}	D_t	D_p	k_s	μ_w	μ_o
	m	m	-	m	m	m	m	mm	-	-
Reference	0.5	0.5	0.4	1.75	2.0	0.1	0.5	0.5	0.4	0.6
Min	0.3	0.3	0.4	0.5	1.0	0.1	0.3	0.1	0.3	0.55
Max	0.6	1.0	0.8	5.0	10.0	0.25	1.0	2.0	0.45	0.65

Table 4.4 : Reference, minimum and maximal values of the parameters for the real-scale exchange structures STR1 and STR2

As in the experiments, the ground elevation is used as the reference elevation to express the street water elevation and the pipe piezometric head. The exchange model is run for the following hydraulic conditions:

- The street velocity is set to zero (V_s=0 m.s^{-1}). This parameter is only considered when computing the street flow hydraulic head so its effect can be included in the street water elevation
- The street water elevation Z_s varies between 0.02 and 0.5 m
- The main pipe piezometric head Z_p takes one of the 4 following values : -2.0 m, -1.0 m, -0.5 m, 0.5 m
- The main pipe flow velocity V_p can be either 0.2 or 2.0 m.s^{-1}

The two last hydraulic parameters form 8 fixed underground pipe flow conditions (8 combinations of Z_p and V_p), for which the exchange discharge is computed in respect of the remaining hydraulic parameter (Z_s).

4.6.3 Reference results

Figure 4.12 shows the exchange discharge computed for each controlling element with the exchange structure reference parameters, for the series of flow conditions presented above. Note C4 exchange discharge can be only computed for Z_p=0.5m, whereas exchange discharge for C1, C2 and C3 can be only computed for Z_p<0.5m. First, there is no significant differences between the structures STR1 and STR2 for C3 and C4 (C1 and C2 being strictly the same). This means that the effects of considering the pipe flow velocity in the pipe hydraulic head and of computing with different formulations the head losses at the junction with the connecting pipe are low or compensate each other. Similarly, the main pipe flow velocity considered in STR1 barely affects the exchange discharges (comparison of top and bottom series on Figure 4.12). Larger effects have been noted in the experimental model, but this was for very specific flow conditions that may not appear here (for instance the velocity in the experimental pipe could be almost zero, whereas a minimum value of 0.2 $m.s^{-1}$ is considered here).

Then, the flow from the street to the drainage box (C1) controls the exchanges only for very shallow street flow and its influence is globally negligible. For larger street water depths, the control can be assured either by C2 or C3, and the transition from C2 to C3 is mainly imposed by the pipe (or manhole) piezometric head Z_p. This transition occurs when Z_p approaches the drainage box elevation (-0.5m). This shows the relevance of the developed exchange model, as there is a significant range of hydraulic conditions for which the exchanges are controlled by the head losses affecting a pressurized exchange flow through the whole exchange structure.

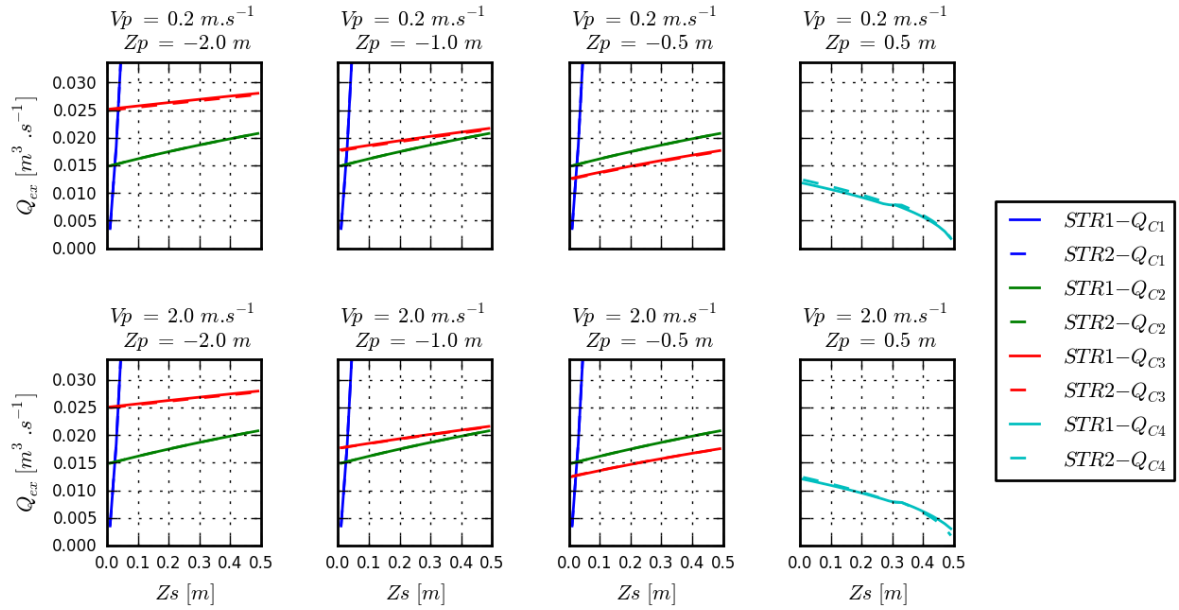

Figure 4.12 : Flow exchange discharges computed at each control element for the two real exchange structures (STR1 in plain lines, STR2 in dotted lines)

Variations of most of the head loss coefficients used in the exchange model are strongly reduced for Reynolds number larger than 10^5. For this reference set of parameters, this value is reached in the connecting pipe when exchange discharges exceed 0.0025 $m^3.s^{-1}$, which is almost always the case. In this case, for a given set of parameters, the only head loss coefficients that may significantly vary are the ones associated to the junction of the connecting pipe and the main pipe for STR1. Using the methodology proposed in 4.5.3, equivalent discharge coefficients to use for an orifice equation are derived for C3 and C4 (respectively μ_{C3} and μ_{C4}), considering the exchange model results of the different runs. Average values and standard deviation are given in Table 4.5. Note that these results are directly correlated to the range of hydraulic parameters tested, which has been chosen to match data of the experimental urban drainage model and field cases situations, but may not be statistically relevant. Several conclusions can still be deduced. First, for STR2, as expected, both coefficients have similar average values and show very low variations, as a result of very similar head losses terms and a low dependency on Reynolds number. For STR1, average coefficients differ from each other, which shows the impact of the head losses difference at the junction of the connecting pipe and the main pipe. Besides, variations of the associated head loss coefficient increase the range of the equivalent discharge coefficients (larger standard deviation). For both STR1 and STR2, variations are larger for μ_{C4} than for μ_{C3}, which is mainly due to the range of hydraulic parameters tested, with lower head differences and exchange discharges, and so lower Reynolds numbers.

	$\bar{\mu}_{C3}$	$\bar{\mu}_{C4}$	STD(μ_{C3})	STD(μ_{C4})
STR1	0.536	0.423	0.033	0.078
STR2	0.506	0.518	0.000	0.015

Table 4.5 : Average value and standard deviation of the equivalent orifice discharge coefficient for the real exchange structures

4.6.4 Sensitivity analysis

In order to characterize the importance of the exchange model parameters, a sensitivity analysis is carried out. For each parameter, the exchange model is run twice, each run with one of the parameter extreme values defined in Table 4.4 (other parameters value remaining set to the reference value), and an indicator is calculated to assess the effects of the selected parameter. The chosen indicator is the average value of the absolute difference between both run results, normalized by the reference results:

$$I_{EX(\Phi)} = \frac{1}{n}\sum_{k=1}^{n}\frac{\left|\Phi_{1,k} - \Phi_{2,k}\right|}{\Phi_{ref,k}} \qquad 4.15$$

With Φ an output variable of the exchange model, $\Phi_{1,k}$ and $\Phi_{2,k}$ the values of this variable computed for the extreme values of the studied parameter, and $\Phi_{ref,k}$ the value of this variable for the reference parameter, for the k^{th} flow condition (see Table 4.4). The variable on which this indicator is calculated are the discharge coefficients μ_{C3} and μ_{C4}, the effective exchange discharges for drainage Q_{dr} (minimum of Q_{C1}, Q_{C2} and Q_{C3}) and the overflow exchange discharge Q_{C4}. Additionally, to characterize the importance of the control C1, the maximum value among the two extreme model runs of the street water elevation for which the control passes from C1 to C2 or C3 is indicated ($Z_{s,C1}$).

Results are presented in Table 4.6, for STR1 only as STR2results yield to the same conclusions. The most influent parameter is the connecting pipe diameter d_t, which impacts strongly the exchange discharges, but also the discharge coefficients and the transition from control C1 to control C2 or C3. Typically, values of I_{ex} point out that the drainage discharges Q_{dr} can vary of more than 400% around the reference values (I_{ex}=4.38), which clearly shows that the connecting pipe diameter d_t should be precisely known. Other connecting pipe parameters (L_{t1}, L_{t2}, k_s) also have a significant impact, especially on the discharge coefficients, yet remain an order of magnitude smaller than the impact of d_t. Parameters related to the weir type flow around the street inlet grid (L_{si}, μ_w) slightly affect the transition from C1 to C2 or C3 but the effects remain even relatively low when compared to the ones of d_t. Effects of the

opening ratio f_{SI} are negligible. Height of the drainage box H_{db} and the orifice discharge coefficient μ_o have an effect on the drainage exchange discharges Q_{dr}, as they impact the discharge computed by the control C2.

Parameter	$I_{ex}(Q_{dr})$	$I_{ex}(\mu_{dr})$	$I_{ex}(Q_{ov})$	$I_{ex}(\mu_{ov})$	Z_{C1}
	-	-	-	-	m
L_{si}	0.05	0.05	0.01	0.01	0.03
H_{db}	0.22	0.00	0.00	0.00	0.01
f_{SI}	0.00	0.01	0.00	0.00	0.01
L_{t1}	0.06	0.16	0.13	0.13	0.01
L_{t2}	0.13	0.26	0.20	0.20	0.01
d_t	4.38	0.10	5.38	0.03	0.09
d_p	0.00	0.02	0.00	0.00	0.01
k_s	0.04	0.13	0.07	0.07	0.01
μ_w	0.02	0.00	0.00	0.00	0.03
μ_o	0.10	0.00	0.00	0.00	0.01

Table 4.6 : Results of the sensitivity analysis on the exchange model for the real structure STR1

These results point out that an accurate knowledge of the complete exchange structure geometry is required to accurately predict the exchange discharges. When this geometry is known, a sensitivity analysis may focus on residual parameters that are always uncertain (such as μ_w, μ_o or k_s). Oppositely, in the case of lack of precise knowledge of the geometrical parameters, the latter should be considered first to assess the model sensitivity.

Conclusion

Experiments on the DPRI urban drainage model have allowed a characterization of the flow interactions between a street and an underground drainage pipe through a specific experimental exchange structure. Analysis has been carried out essentially to describe the exchanges between the street flow and the pipe flow. As exchange flows were pressurized for all experiments, an exchange model has been developed by considering a head balance between both flow layers. Although the experimental exchange structure is somehow complex, its different parts can be modelled as standard pipe hydraulics elements, for which extensive research has been carried out (Miller 1978; Idelchik and Steinberg 1996) and can be used without calibration. The developed exchange model predicts the exchange discharges with fair accuracy (Figure 4.8) when the exchange flows are from the street to the pipe (drainage), but is less accurate in the opposite case (overflow). This higher discrepancy may

come from one or several inadequate head loss terms that form the base of the exchange model. In the absence of more detailed experimental data on the exchange flows, no attempt to improve the exchange model accuracy has been carried out. Detailed analysis of the results shows that the Reynolds number of the exchange flow has a significant impact on the exchange structure capacity, and this particularly prevents from using a unique equivalent orifice discharge coefficient. On a similar but more restricted way, the main pipe flow discharge is found to affect the exchanges, as a result of its direct connection to the drainage tube.

The exchange model has been validated by using measurements of street and pipe water flows as input data. This model being validated, it can be used within numerical simulations that include hydrodynamic models of the street flow and the pipe flow. Such simulations are carried out and results are presented in Chapter 5.

Now, results are highly related to the experimental exchange structure, and the chosen flow conditions (that is, pressurized exchange flows), so that they cannot be directly and fully extended to a field study. However the methodology presented in the experimental work can be extended for any real exchange structure that has a similar operation principle.

This last task has been carried out, by considering both assumptions done for the experimental model and the ones proposed by Leandro et al. (2007), which define several control elements for a given exchange structure. First, for hydraulic conditions typical of urban floods, the exchanges appear to be mainly controlled by the underground part of the exchange structure, and less affected by the street inlet capacity (Figure 4.12). Whereas the latter is an important and tricky point to consider for usual drainage cases (Gomez et al. 2011), it appears to be less influent for a flood event, so that in this case the use of a simple weir equation can be suitable.

Then, the scaling of the structure geometry imply that the exchange flow Reynolds number for most of the tested conditions is at least one or two order of magnitudes larger than the ones in the experimental structure. This leads to lower variations of the equivalent orifice discharge coefficient, and the increased possibility to consider one unique fitted value for the latter. Considering a structure with a manhole replacing the underground drainage pipe leads to similar exchange discharges, with smaller variations of the discharge coefficients. As these manhole configurations are more likely to be found on field cases and actually simplify the exchange models, they should be considered, rather than a direct connection to the main drainage pipe.

As expected, uncertainty on the actual parameters of a real exchange structure can have very important effects, in particular the ones defining the connecting pipe geometry. Studies that use similar exchange models or orifice equations (Djordjevic et al. 2005; Nasello and Tucciarelli 2005; Leandro et al. 2011) to model flow exchanges acknowledge the lack of accurate data on the exchange structure geometry and use arbitrary values. Therefore if such modelling aims at quantitative results, a sensitivity analysis may have to be carried out, depending on the uncertain parameters (e.g. Table 4.6). These results on real scale exchange structures highlight the key points to consider for a field study, and they will be used to model flow exchanges on the real case modelling presented in chapter 7.

Chapter 5.

Numerical simulations of the urban drainage model experimental flows

A set of data has been produced using the DPRI experimental urban drainage model, which includes a free surface flow in a street and a pressurized flow in a drainage pipe. Data include an extensive description of the model geometry and materials, and complete measurements describing both flow layers. This data is used for a detailed validation of a numerical model coupling a surface flow with a pipe flow in the present chapter.

This coupled model is based on the previously described 2D code Rubar20 (3.2.1) for the surface flow, along with the 1D code Rubar3 to model the pipe flow. The first step consists in validating the ability of the coupled model to simulate the experimental flows. This step appears to be required because of the lack of available data for field validation (Mark et al. 2004). Therefore, a first series of reference simulations are carried out to assess the coupled model stability and accuracy, especially regarding the pressurized flow computation and the exchange model implementation. Then a sensitivity analysis is carried out with a simplified representation of the urban drainage model surface topography, to assess the need of considering detailed topography when modelling urban floods.

5.1 Model set-up

5.1.1 Street flow model

5.1.1.1 Equations

The street flow is modelled using the Rubar20 code that solves the 2D shallow water equations, which has been presented in 3.2.1. To account for the flow exchanges, a source term corresponding to the local flow exchange is added on the right side of the continuity equation (Eq. 3.1), that becomes:

$$\frac{\partial h}{\partial t} + \frac{\partial (hu)}{\partial x} + \frac{\partial (hv)}{\partial y} = -q_{ex,2D} \qquad 5.1$$

Where $q_{ex,2D}$ is the source term associated to the exchange discharge with the underground pipe model (exchange discharge divided by the cell area). As a convention, the exchange discharge is considered positive when the exchange flow goes from the street to the pipe (drainage case), hence the minus in Eq. 5.1.

5.1.1.2 Mesh

The mesh of the street consists in a regular 5 by 5 cm grid for the whole channel, and an additional mesh for the upstream tank feeding the street. This tank is considered only for unsteady flows, in order to directly model its storage effects. The street and sidewalks elevation are set respectively to 0 and + 2 cm, so there is no consideration of the observed local topography variations (perfect geometry), as shown on Figure 4.4. The mesh is adapted to perfectly fit the street inlets locations. However this mesh requires choosing one bottom elevation for the nodes located on the interface sidewalks/street, which is actually vertical. In order to have the same bottom elevation all around the edges of the exchange structures, the interface nodes elevation is set to 0 (street level). For a given water elevation in the street, this implies an overestimation up to 10% for the street flow area and the volume stored in the street. A cross section of the experimental street topography and the present implementation in the numerical surface flow model is shown on Figure 5.6, along with other possible implementations that will be discussed in 5.3.

5.1.1.3 Parameters

The bottom roughness is modelled with a constant Strickler coefficient of K_s= 80 $m^{1/3}.s^{-1}$. This value corresponds to the lower bound of the range of typical Strickler coefficients for plastic materials. Given the low street flow Reynolds numbers (typically 10^3 – 10^4) the Manning-Strickler formulation is not adapted as it is only valid for fully turbulent flows. However, longitudinal variations of the street water elevation remain very low (less than 0.001 m/m) and have no significant impact on the flows interaction at the street scale, so errors arising from this bottom friction modelling remain low. Besides, at first, diffusion effects are not considered (K=0).

For steady flow simulations, the boundary conditions are taken from experimental measurements (inflow discharge, street water elevation). For unsteady flow simulations, the street downstream condition consists of a stage-discharge relationship derived from preliminary measurements for a free outlet of the street. Initial conditions are derived from the measurements to achieve faster convergence of the numerical model. The time step is fixed to 0.001 s.

5.1.2 Pipe flow model

5.1.2.1 Equations

The code Rubar3 is chosen to model the pipe flow (El Kadi Abderrezzak and Paquier 2011). It solves the 1D shallow water equations, written as:

$$\frac{\partial A}{\partial t} + \frac{\partial Q}{\partial x} = q_{ex,1d} \qquad 5.2$$

$$\frac{\partial Q}{\partial t} + \frac{\partial}{\partial x}\left(\frac{Q^2}{A}\right) = -gA\frac{\partial z}{\partial x} - f\frac{Q^2}{8AR_h^{2/3}} \qquad 5.3$$

in which Q is the flow discharge within the pipe, A the flow section area, f is the Darcy-Weisbach friction factor, z the pipe bottom elevation, and R_h the hydraulic radius. $q_{ex,1D}$ is the exchange discharge at an exchange point divided by the mesh length. Pressurized flow computation is made possible by the use of a Preissmann slot. The numerical scheme of this 1D code is similar to the one used by Rubar20, presented in 3.2.1.

5.1.2.2 Space step and section geometry

The longitudinal space step is fixed to 10 cm. As for the street model, the upstream tank feeding the pipe is explicitly modelled to account for its storage effects when simulating unsteady flows. The pipe section is a 5 cm diameter circle, modelled here with a 37 points section (29 for the global shape of the section, and 8 to model the Preissmann slot and the transition between these elements, see Figure 5.1). The Preissmann slot width is set to 0.1 mm, and the shape of the transition between the pipe top and the slot is taken from the geometry proposed by León et al. (2009). No transition from free surface to pressurized flow is observed in the experimental flows, but this should occur for the real case modelling in Chapter 7, so a smooth transition has been implemented in the model meshing tools and is tested here. With this geometry, the errors made on the computation of the pipe flow area and hydraulic radius are estimated to be lower than 0.5 %, which is acceptable for the present simulations.

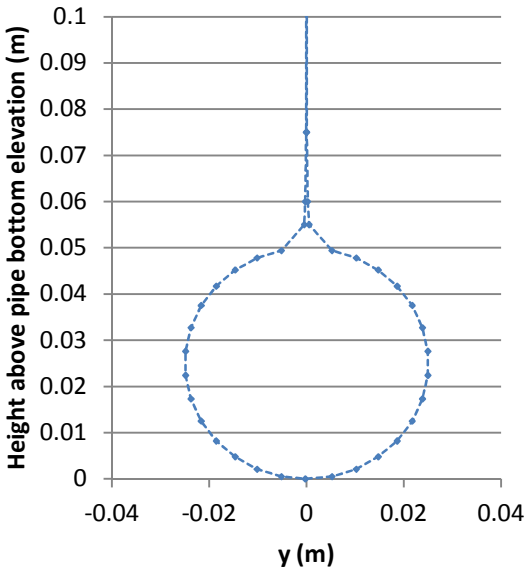

Figure 5.1 : Drainage pipe geometry with the Preissman slot

5.1.2.3 Parameters

The linear head losses are modelled with the use of a Darcy-Weisbach friction factor f (Equation 5.3). The empirical relationship linking this friction factor to the pipe flow Reynolds number is used (Eq.4.7), which allows *a priori* a good estimation of the linear head losses without additional calibration. This relationship is particularly useful as the pipe flow discharge (and so its Reynolds number) varies from the upstream to downstream parts, and even with time when considering unsteady flows. However, the empirical friction factor was

derived for pipe flows without any exchange, and the potential additional minor head losses arising from the flow exchanges are not considered.

Boundary conditions are directly taken from measurements for both steady and unsteady flows. The initial conditions are chosen considering the experimental measurements as for the street flow model. The time step is the same as in the street flow model (0.001 s).

5.1.3 Exchange model

The exchange model is the one developed in the previous chapter (4.5.1). Its implementation in the complete hydrodynamic model follows the following assumptions. The exchange structures are not explicitly considered, and only the exchange discharges are considered to link the 1D pipe and 2D street models (continuity equations 5.1 and 5.2). It implies the exchanges are done instantaneously, which does not affect steady flow simulations and is reasonable for unsteady flows, as the flowing time through the exchange structures are at least an order of magnitude lower than the ones through the street. Exchanges are represented with discharge exchanges between both flow models at specific locations. For each street inlet, the exchange discharge is distributed on the 4 edges of the street model cell located on the inlet location, assuming a uniform distribution (i.e. 1/4 of the exchange discharge through each edge). This choice is justified by the fact that the exchange flow in the experiments occurs on the whole street inlet area. The exchange discharge at one street inlet is distributed on 4 neighbouring cells in the pipe model around the actual (physical) exchange point, in order to smooth the discharge exchange in the pipe model.

The coupling method between the 1D and 2D codes is as follows (Paquier and Bazin 2014). 1D and 2D codes are embedded within the same Fortran program, along with the exchange model. The time step is the same for both flow models, and exchanges are computed at each time step. First, the 1D model is calculated up to the intermediate time $t_{n+1/2}$, i.e. steps 1 and 2 of the numerical scheme (similar to the one of the 2D model, explained in 3.2.2). Then the 2D model is fully calculated, exchanges being computed using the 1D predictions at the intermediate time. The flow variables used to compute the exchange discharge (use of the head difference between the street and the pipe at one exchange structure and of the upstream pipe discharge) are then:

- for the 2D model, predictions at the intermediate time of the water level and flow velocity at the middle of the chosen edge of the exchange cell

- for the 1D model, predictions at the intermediate time of the pipe water level and velocity 2 cells upstream of the actual pipe model exchange cell. This was chosen to avoid numerical oscillations (such oscillations occurred when using variables computed directly on the pipe model exchange cells).

Finally, once the 2D model time step is finished, the time step for the 1D model is finished (steps 3 and 4 of the numerical scheme).

5.2 Reference simulations

5.2.1 Steady flows

5.2.1.1 Street water depths, pipe pressures and exchange discharges

For a given flow, the longitudinal variations of the street water depths are low and simulated water depths discrepancies hardly impact the computed exchange discharges. On the contrary, there is a strong interdependence between the pipe pressure and the exchange discharges. On the one hand the pipe pressure can vary significantly from upstream to downstream, leading to strong variations of local exchange discharges. On the other hand, the cumulated exchange discharges lead to strong variations of the pipe flow discharge and so of the hydraulic head in the pipe. Therefore the pipe head and exchange discharge computations have to be analysed jointly.

Figure 5.2 presents longitudinal evolution of the street water elevation and pipe piezometric head for flows D6 and O4 (see Table 4.2). The simulations are in fair agreement with the experimental data, particularly when looking at the pipe piezometric head. Computation of the pressurized flows with the use of a Preissman slot is effective, and variations of the linear head losses are well predicted.

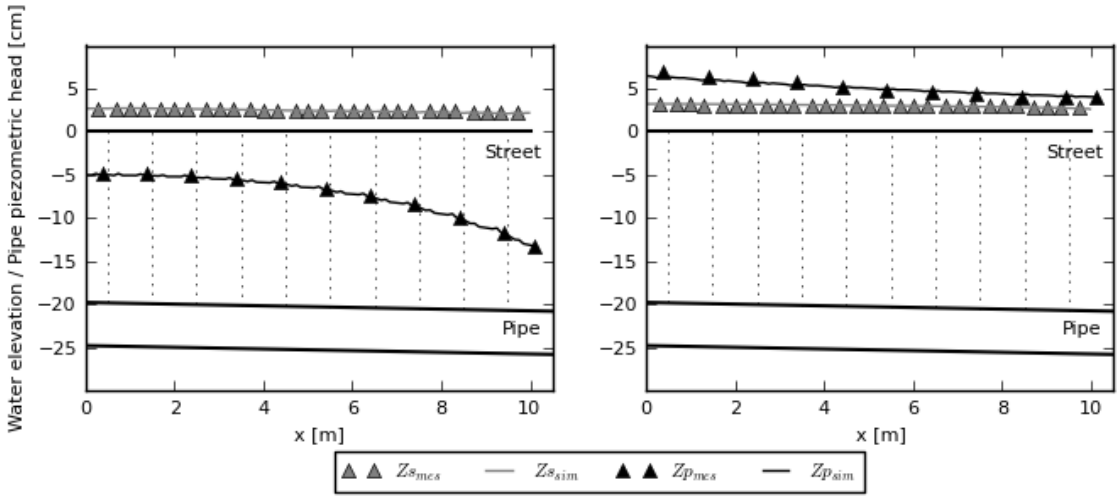

Figure 5.2: Measured (triangles) and simulated (lines) water elevation in the street and pipe piezometric head for flows D6 (left) and O4 (right). The pipe and the street geometry are indicated in bold lines, exchanges locations with dotted thin lines.

In order to characterize simulation errors for the whole series, 2 statistical indicators are introduced:

$$\Delta(\Phi) = \Phi_{sim} - \Phi_{mes} \qquad 5.4$$

$$\sigma(\Phi) = abs\left(\frac{\Phi_{sim} - \Phi_{mes}}{\Phi_{mes}}\right) \qquad 5.5$$

where Φ_{sim} and Φ_{mes} are the simulated and measured values of either Z_s, Z_p or Q_{ex} (respectively the street and pipe water levels, and total exchange discharge). To ease the comparison between drainage and overflow cases, Q_{ex} is considered in absolute value. Table 5.1 gives the average values of these 2 indicators for both drainage and overflow configurations. Globally, the experimental flows are simulated with a fair accuracy, relative errors remaining below a few per cent.

For the drainage cases, street water depths and pipe piezometric heads are slightly underestimated. The errors $\Delta(Z_s)$ and $\Delta(Z_p)$ are similar, so that the head differences between the street and the pipe at the exchange points are actually barely affected. The resulting simulated total exchange discharges Q_{ex} are thus in fair agreement with the measurements, and the remaining errors are consistent with the results of the exchange model (slight overestimation of the exchange discharges, see Figure 4.8).

For the overflow cases, the water depths in the street are simulated with almost no bias, whereas the pipe piezometric head is still slightly underestimated. This results in lower head differences ($\approx Z_s$-Z_p) at each exchange point, and so the computed exchange discharges Q_{ex} are lower than expected. As the exchange model tends to overestimate the flow exchange in

overflow configurations (Figure 4.8), this trend is finally reduced in the numerical simulations.

Flow configuration	Number of flows	$\Delta(Z_s)$ Cm	$\Delta(Z_p)$ cm	$\Delta(Q_{ex})$ $L.s^{-1}$	$\sigma(Z_s)$ %	$\sigma(Z_p)$ %	$\sigma(Q_{ex})$ %
Drainage	12	-0.27	-0.29	0.02	6.9	1.7	3.9
Overflow	4	-0.04	-0.22	-0.01	3.5	1.0	2.8

Table 5.1 : Comparison between measured and simulated water depths in the street (Z_s), pipe piezometric head (Z_p) and total exchange discharges (Q_{ex}) for the reference simulations

5.2.1.2 Street flow velocity

Comparison of LSPIV measurements and computed street velocity fields permits to assess the numerical model ability to predict the velocity field in the street for both drainage and overflow configurations. For flows D6 and O4, simulated and measured velocity profiles are compared at x=4 m in Figure 5.3. The comparison is carried out on the longitudinal velocity u normalized by its cross section averaged value u_{av}, as the measured velocities are surface velocities. A bias exists in the comparison, as the vertical velocity profiles are not the same along the cross section, thus the comparison is only qualitative. Besides the reference parameters, a second series of simulations is carried out by adding diffusion in the 2D surface model (k=1) and results are compared to the reference ones (k=0).

For the drainage case D6, the measured velocity profile is quite uniform but shows strong differences with numerical simulations. Errors arise from the exchange process in the numerical model, with important local water depths variations around the exchange cells. This results in computed high flow acceleration, always oriented in the streamwise direction downstream. By using a diffusion coefficient (k=1), this discrepancy is reduced, but still without any satisfying prediction of the velocity along the sidewalks. For the overflow case O4, the velocity distribution across the street is more heterogeneous and well predicted by the numerical model. However the low velocity near the street inlets axis (y=0.75 m and y=1.25 m) reveals discrepancies. Introducing diffusion tends to smooth the velocity profile but does not reduce these discrepancies. A refinement of the mesh with a 1cm regular grid was tested to allow a more accurate flow computation around the street inlets and along the sidewalks, without improving results (not shown here).

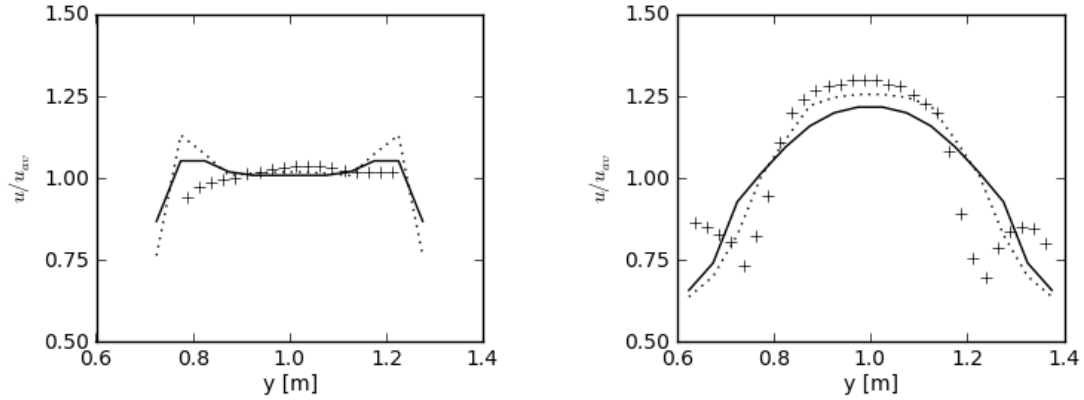

Figure 5.3 : Profile of the longitudinal velocity for flows D6 (left) and O4 (right) at the cross section x=4m measured (cross), and simulated with no diffusion (k=0, dotted line) and with diffusion (k=1, full line)

The whole simulation results for steady flows suggest that the numerical model is able to accurately predict the global characteristics of drainage or overflow experimental flows (street water depths, pipe piezometric heads, local flow discharges) in steady conditions. Simulations convergence is usually achieved for simulation times of around 100 s, which is the order of magnitude of the time required for the street flow to propagate between the upstream and the downstream boundaries. To complete the numerical model validation, its ability to model unsteady flows is studied in the next sub section.

5.2.2 Unsteady flows

Unsteady flows defined in Table 4.3 are modelled with the same parameters as in the steady flows simulations, with only a few modifications specific to unsteady flows:

- Initial conditions are simulated by running the model with the relevant boundary conditions until convergence is achieved.
- Both pipe and street models include the respective upstream feeding tank, to account for the storage effect of these tanks, as it was not possible to consider it in the boundary conditions.
- As the street volume-water depth relationship may impact unsteady flows, an adequate representation of the latter is required. No flow on the sidewalks was observed for unsteady flows, so the surface model here includes only the street so that the interface street/sidewalks are the model boundaries and there is no approximation of the surface topography (influence of the surface model geometry will be discussed in 5.3).

Finally, note that the validation data differ from the ones used in steady flows: here we use one local street water depth, three piezometer heads (at the 3rd, 5th and 8th exchange points) and the street outflow discharge.

5.2.2.1 Pipe overflow generated by a downstream pressurization (US1 and US2)

Note that the typical street flow and pipe flow velocities are significantly different, and so are the related propagation times. Figure 5.4 shows that as the downstream pipe pressure $Z_{p,dn}$ evolves, this impact rapidly propagates through the pipe on a typical time negligible compared to the typical duration of the unsteady condition. This propagation appears to be well simulated (see subplots for the pipe piezometric head on Figure 5.4). The impact on the street flow can be considered as slightly delayed, as the experiments show a time shift of around 25 s +/-3 s between the downstream pipe pressure $Z_{p,dn}$ and the street outflow discharge Q_{so} peak times for both unsteady flows. This delay is correctly predicted by the simulations for US1 (23 s) but overestimated for US2 (42 s).

The simulated initial and final pipe piezometric heads are in very good agreement with the measurements, but there is a small overestimation around the peak time. For the upstream piezometer P2, the maximal error at the peak time is of +0.3cm for US1 and +0.5 cm for US2, which is larger than the typical error observed for steady state flows (Table 5.1). This error leads to a less efficient drainage, and so to larger street flow discharges and water depths. The discrepancies are higher for US2, which has a slower time evolution than US1, and occur mainly as the head difference between the street and the pipe is low (between t=80 s and t=180 s), or when the pipe flow discharge and the exchange discharges reach minimum values. Discrepancies in this time interval can be partly explained by the exchange model, whose errors are larger for low exchange discharges (Figure 4.8), and by an overestimation of the head losses in the pipe for these flow conditions.

Finally, measured water depths in the street and piezometric heads in the pipe suggest that overflow should occur for both flows ($Z_{p2}>Z_s$ around the peak time), even if the measured street outflow discharges never exceed the street inflow discharge (Q_{si} = 1.5 L/s). Simulation results indicate local overflows from the pipe for both cases, but with a low exchange discharge and during a limited time. Because of the inertia of the street flow, the overflow coming from the upstream exchange points is drained downstream, and this phenomenon is

not directly reflected on the street outflow discharge. For both simulated flows, the transition from drainage to overflow is continuous and does not lead to instabilities.

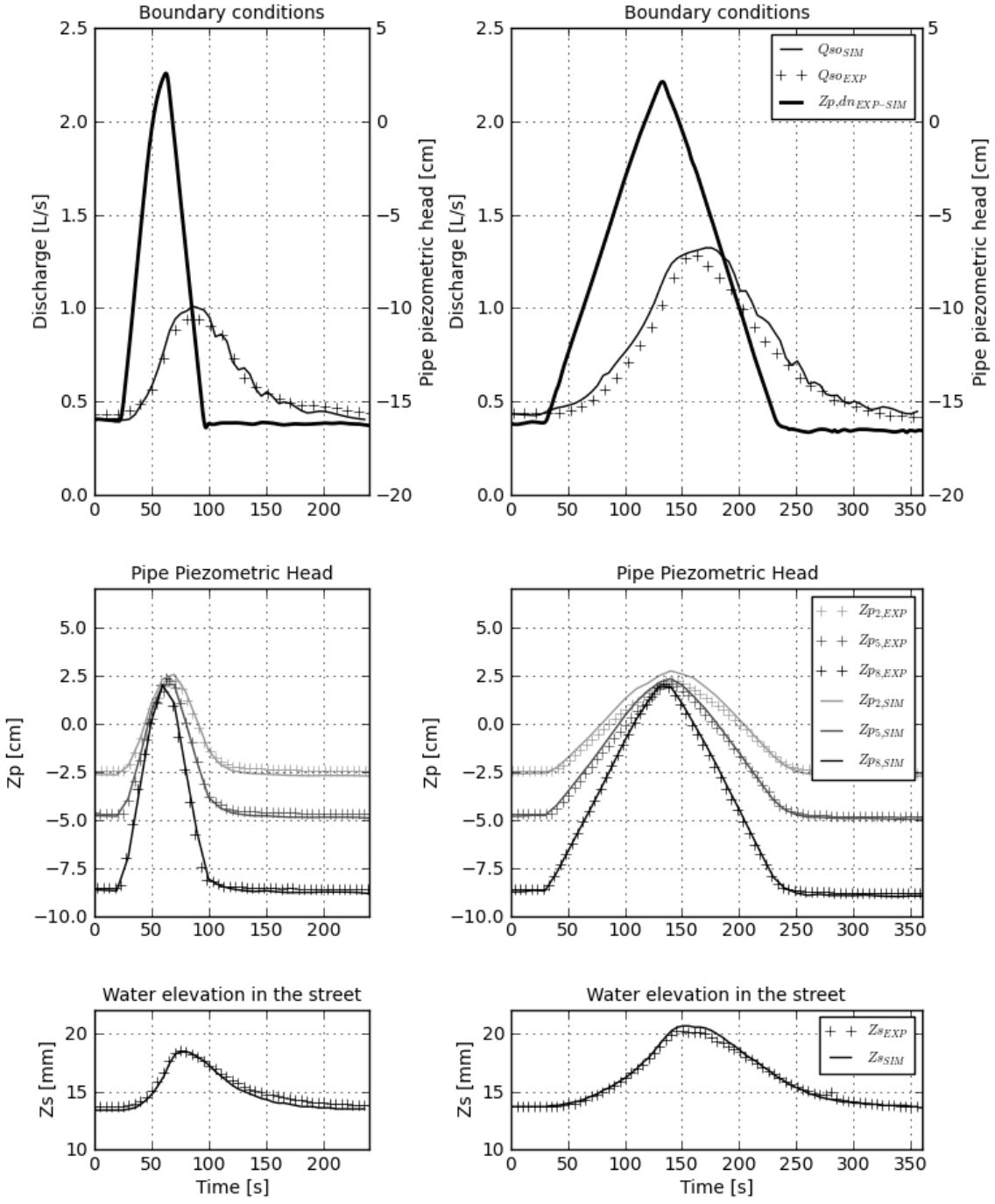

Figure 5.4: Comparison of experimental measurements (black crosses) and simulation results (plain lines) for the unsteady cases US1 (left) and US2 (right). The unsteady condition is indicated in bold on the top graph. Z_{p3}, Z_{p5} and Z_{p8} are the pipe piezometric heads just upstream of respectively the 3rd, 5th and 8th couples of street inlets, Zs is the water elevation in the centre of the street (x=5 m, y=1 m).

5.2.2.2 Flooding in a initially dry street (US3 and US4)

For flow US3, the experiment shows that the whole street inflow (Q_{si}) is drained before reaching the street outlet ($Q_{so,exp}$ = 0 in the left part of Figure 5.5). The numerical simulation is globally in fair agreement with experimental observations but fails in perfectly predicting the complete drainage, as the street remains flooded when reaching the downstream limit of the domain. Moreover, the simulated water depths are rather higher than the measurements, and the arrival time of the street flow at the measurement point (centre of the street, x=5 m) is predicted with a delay of +9 s in comparison with experimental measurements. Errors in the propagation of the street flow are explained by the flow shallowness, which is out of the 2D model assumptions (effects of the flow capillarity and viscosity, modelling of the bottom friction, etc.) and is sensitive to local topographical irregularities. The latter can influence the flow dynamics when the water depths are very low, although it can be neglected for higher water depths.

For flow US4, the street inflow hydrograph $Q_{si}(t)$ presents larger discharge and duration, and a significant part of the flow reaches the street outlet ($Q_{so,EXP}>0$). During the initial phase of the street flow propagation, drainage increases as well as the pipe piezometric head, until the whole system reaches a quasi-steady state where the drainage capacity is at its maximum (between t=170 s and t=300 s). This quasi steady state of the drainage process occurs just after the street flow reaches the downstream end of the street, leading to a full operation of all exchange structures. Then the street starts to empty and there is a quick drop of the pipe piezometric head. These different phases are globally well simulated, even though discrepancies are encountered: as for flow US3, the simulated street flow propagation is slower than the experimental observations (+15 s for the arrival time at the centre of the street). This generates a delay for the rise of the pipe piezometric head in the initial phase (around +10 s for the 3 piezometers). The street outflow discharge Q_{so} is well simulated until t=200 s, but then becomes much lower than the measurements, which means that the exchange discharges (drainage) are overestimated during the quasi steady state phase. The simulated water depths in the street are just slightly higher than the measurements until the hydrograph peak, but then become lower. This inversion comes from the balance between the too low simulated street flow discharges, and the trend of the model to compute too high street water depths during the wave propagation. As the drainage process is overestimated, the

emptying of the street occurs sooner in the simulations than in the experiment, finally leading to earlier fall of the pipe piezometric head, yet with similar evolution.

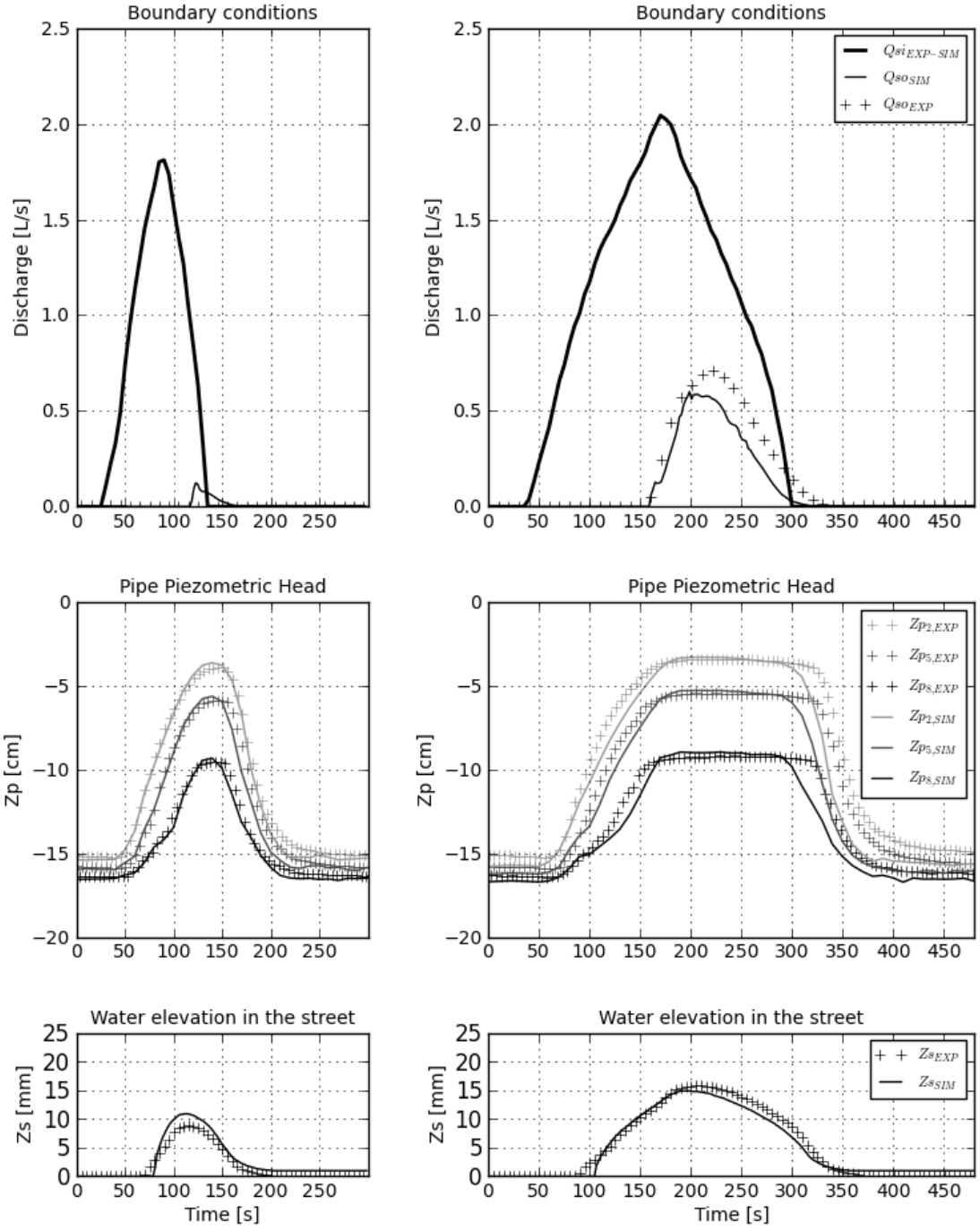

Figure 5.5 : Comparison of experimental measurements and simulation results for the unsteady cases US3 (left) and US4 (right). The unsteady condition is indicated in bold on the top graph. Z_{p3}, Z_{p5} and Z_{p8} are the pipe piezometric heads just upstream of respectively the 3rd, 5th and 8th couples of street inlets, Z_s is the water elevation in the centre of the street (x=5 m, y=1 m).

5.3 Influence of the surface topography

5.3.1 Definition of different surface model topographies

Numerical simulations have been carried out with a reference model that includes the best description of the experimental model and a set of parameters that can be considered as optimal. Under such modelling conditions, simulation results agree quite well with observations, so that the numerical model is validated and could be used for similar flows for a field case.

However when modelling a field case, many uncertainty sources require attention. In particular, defining the surface topography usually requires compromises between computational times and the model accuracy, which becomes a real problem in areas with steep changes in the topography. Other uncertainty sources exist and can generate larger errors for a field case (bottom friction, boundary conditions, exchange points and exchange laws), but they are not considered here. Indeed, analysing the impact of these uncertainty sources on the experimental model could not be extrapolated because of the similitude discrepancies (materials, scale, number of exchange structures and exchange laws…). Oppositely, the experimental surface channel cross section permits to study different ways of considering the topography and reflects quite accurately the issues raised for a field case study.

Note that in last subsection, depending on whether the simulated flow was steady or unsteady, the surface model was respectively a rough representation of all the surface channel with a coarse simplification of the street/sidewalks interface (*Ref* on Figure 5.6), and a restrained representation including only the street (*Street*). The latter allowed to assess the numerical model accuracy without influence of topographical approximations, but this representation works only for street water levels lower than sidewalks levels and therefore cannot be considered as a general technique to use for any urban flood modelling. Instead, as an alternative, we will consider here an average bottom elevation (*Avg*), as it was done to model sidewalks effects on bifurcation flows (3.5). Following this approach, the model *Avg* includes a constant bottom elevation for the surface layer of (2 x (2.0x15.0))/80.0 = 0.75 cm.

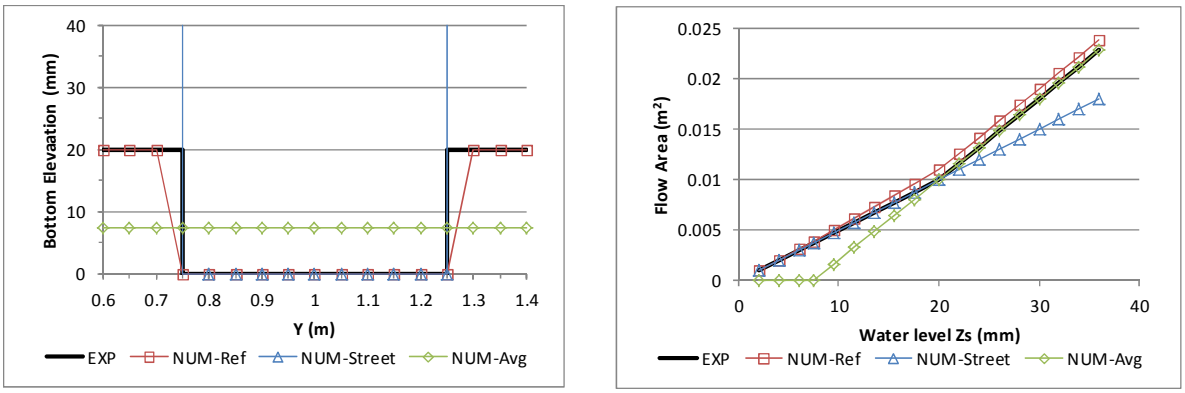

Figure 5.6 : Cross section of the experimental urban drainage model surface component and its approximations in the numerical models (left), and resulting flow area – street water level relationship (right)

5.3.2 Steady flow simulations

The numerical model is run with a surface model including an average bottom elevation ($Z_{b,NUM\text{-}Avg}$), all other reference parameters being kept equal to the reference ones (including the street downstream condition, that it the measured water level). As for the reference simulations, indicators are calculated for the street water elevation, the pipe piezometric head and the total exchange discharges (Table 5.2). Simulation results are still in fair agreement with experimental measurements and errors are very close to the ones of the reference simulations (see Table 5.1). The computed street water level globally increases (slightly higher values of $\Delta(Z_s)$), because of both the decrease of the flow area and the increase of the flow velocity. This impacts the relative errors on the computed street water depths (indicated by $\sigma(Z_s)$) as errors are mainly generated for flows with low street water depths. Pipe piezometric heads for the *Avg* model are very similar as the ones of the *Ref* model, yet slightly lower (lower values of $\Delta(Z_p)$). However the impact on the total exchange discharge is hardly visible, so that the impact of the representation of the topography for steady flows can be considered as negligible at the street scale.

Flow configuration	Number of flows	$\Delta(Z_s)$ cm	$\Delta(Z_p)$ cm	$\Delta(Q_{ext})$ L.s^{-1}	$\sigma(Z_s)$ %	$\sigma(Z_p)$ %	$\sigma(Q_{ex})$ %
Drainage	12	-0.11	-0.36	0.02	10.2	2.0	4.0
Overflow	4	0.12	-0.29	0.00	10.0	1.1	2.4

Table 5.2 : Comparison between measured and simulated water depths in the street (Z_s), pipe piezometric head (Z_p) and total exchange discharges ($Q_{ex,tot}$) for the average bottom elevation model (Avg) simulations

5.3.3 Unsteady flow simulations

To characterize the errors, indicators defined in Equations 5.4 and 5.5 are used, except that values averaged in time are used, instead of values averaged in space for steady flows. Moreover, these indicators are also estimated for the total exchange volume during unsteady conditions V_{ex}.

Results show that for all unsteady flows, there is no significant difference between the *Street* and the *Ref* models when looking at the indicators (Table 5.3). Both models fairly agree with experimental measurements. Figure 5.7 shows the evolution of the surface flow water elevation and streamwise velocity at the centre of the street for flows US2 and US4. Both models show very similar results for the street flow dynamics (hydrograph propagation for US4), and the only significant difference comes from the water elevation when this latter is high for flow US2. In this case, the topographical differences between both models reach a maximum (the flow area in the *Ref* model is 10% larger than the one in the *Street* model for a street water elevation reaching the sidewalks level), and so it has larger effects.

Flow	Model	$\Delta(Z_s)$ cm	$\sigma(Z_s)$ %	$\Delta(Z_{p5})$ cm	$\sigma(Z_{p5})$ %	$\Delta(Q_{so})$ $L.s^{-1}$	$\sigma(Q_{so})$ %	$\Delta(V_{ex})$ L	$\sigma(V_{ex})$ %
US1	Street	-0.04	3%	-0.09	1%	0.00	6%	-2.6	-2%
	Ref	-0.04	3%	0.05	1%	-0.03	8%	1.8	1%
	Avg	0.42	29%	0.14	1%	-0.02	14%	0.2	0%
US2	Street	0.01	1%	0.09	1%	0.05	8%	-17.3	-7%
	Ref	-0.01	2%	0.22	1%	0.03	6%	-10.5	-4%
	Avg	0.42	29%	0.29	2%	0.03	10%	-10.5	-4%
US3	Street	0.12	43%	-0.28	4%	0.01	-	-2.6	-2%
	Ref	0.11	44%	-0.27	4%	0.01	-	-2.4	-2%
	Avg	0.70	292%	-0.43	4%	0.00	-	-1.4	-1%
US4	Street	-0.09	27%	-0.79	9%	-0.13	46%	19.7	8%
	Ref	-0.08	26%	-0.72	9%	-0.16	47%	23.9	10%
	Avg	0.50	182%	-0.58	7%	-0.25	81%	38.4	16%

Table 5.3 : Indicators for the numerical simulations of unsteady flows

The model *Avg* strongly impacts the computed street water depths, with an average increase of around 4 to 6 mm depending on flow cases, when compared to the *Street* or *Ref* models. For US1 and US2, piezometric heads and exchange discharges also increase, yet with a very limited magnitude. For US3 and US4, the street flow is slower for *Avg* model (shown for US4 on Figure 5.4), which tends to delay the street drainage and the rise of the pipe piezometric head during the hydrograph propagation. For US3, the whole drainage process is

slowed down, and the pipe piezometric head is lower than in other models. The exchange volume is slightly larger, as a smaller fraction of the initial hydrograph reaches the street outlet. For the flow US4, the initial propagation represents only a part of the hydrograph duration (Figure 5.5), and the model *Avg* rather leads to the differences observed for US1 and US2 (global increase of the street water depth, pipe piezometric head and exchange discharge).

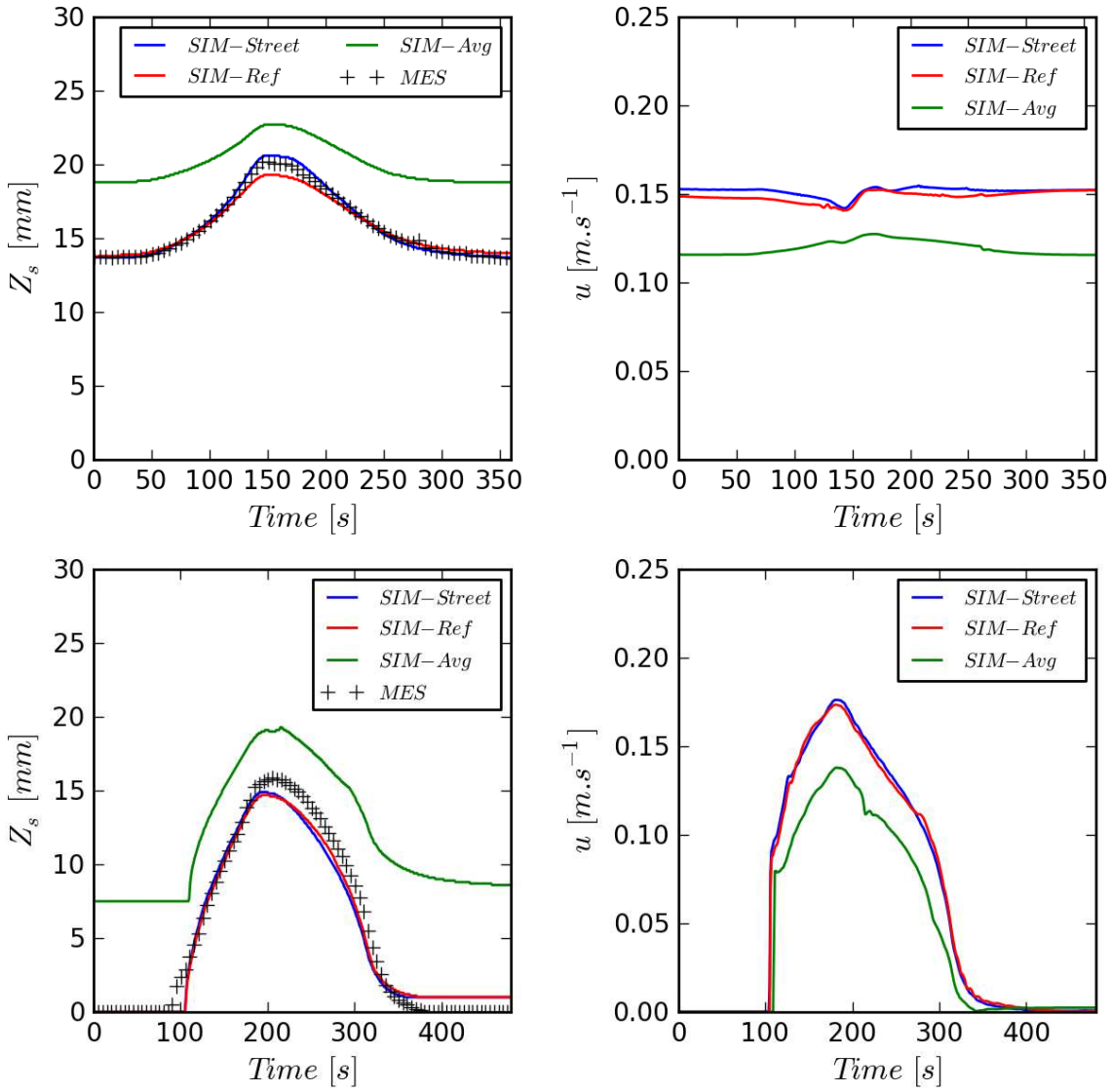

Figure 5.7 : Evolution of the simulated street water elevation and streamwise velocity for the case US2 (top) and US4 (bottom) at the centre of the street. Measurements of the street water elevation are indicated with black crosses.

The influence of the topography representation for the dual drainage modelling cases presented above can be summed up as follows:

1. The *Ref* model leads to satisfying results for both steady and unsteady flows.

2. For unsteady flows, using a more accurate representation (*Street*) does not lead to significant improvements, the only benefits observed being a better street water elevation computed at the peak time for flow US2.
3. The *Avg* model leads to strong overestimation of the street water elevation, and affects the street flow dynamics. However, effects on the exchanges at the street scale on the whole unsteady flow time remain limited. Indeed, whereas the instantaneous street outflow discharge Q_{so} is affected by the topography representation, the total exchange volume V_{ex} is less affected. Besides, note that the street flow water depths in the unsteady flows remain low (below the sidewalks height of 2 cm), which puts at a disadvantage the *Avg* model, when looking the corresponding errors on the street flow area (Figure 5.6).

Conclusion

Complete hydrodynamic numerical simulations have been carried out to simulate experimental flows observed on the DPRI urban drainage model (presented in Chapter 4), with a code coupling a surface flow model and a pipe model. The deep knowledge of the experimental device geometry, as well as preliminary calibration or validation steps (pipe linear head losses, exchange model) allowed to set up a numerical model with optimum parameters. Besides, the use of an experimental device permits to produce a complete set of validation data with both local and global measurements.

Simulation results fairly agree with experimental measurements for both steady and unsteady flows, when looking at the street water depths, the pipe piezometric heads and the exchange discharges. The numerical model appears to be stable, to simulate either drainage or overflow cases, with transitions from one case to the other (e.g. Figure 5.4 and Figure 5.5). Pressurized pipe flows are accurately simulated. However, the range of pipe flow conditions considered in this chapter are limited to pressurized flows, and modelling of more complex flows may require specific changes in the numerical approach (Djordjevic et al. 2004) or an additional validation step.

Analysis of computed street velocity field shows that the numerical model fails in representing local perturbations due to the drainage or overflow processes near street inlets. Such details could be obtained by using more advanced computational fluid dynamics models (Hilden 2005; Djordjevic et al. 2013; Lopes et al. 2013) but these models cannot be applied

for large areas due to computational limitations. In our configuration, this lack of representation has no global impact, but it could become a limiting factor if the exchange discharges were affected by the surface flow characteristics (e.g, Gomez et al. 2011). Note that for a field case, street roughness and cross section would yet reduce these discrepancies at least for drainage flows, by a faster homogenization of the velocity fields and a higher concentration of the street flow into drainage channels.

The sensitivity analysis carried out on the representation of the topography in the surface model shows that using an approximate representation of the street profile leads to reasonably accurate simulated water depths in the street (model *Ref* in Table 5.3), even if errors on the flow area can be as high as 10%. Errors generated by the spatial discretization at the interface street/sidewalks are negligible most of the time when considering the flow exchanges at the street scale. The use of an average street bottom elevation (model *Avg*) yields to larger errors on the computed street water elevations, mainly when the latter are low. However, impacts on the exchange discharges at the street scale remain low and both these representations show benefits for a real case modelling, where street water levels might be higher than the sidewalks level. Therefore, for a real case modelling, the choice of a ground level representation may rather be set by the need of precisely estimating the surface flow pathways (Ettrich et al. 2005), or of modelling drainage processes controlled by street inlets.

Part III.

Modelling of floods in Oullins

Laboratory experiments permitted to validate the ability of the two-dimensional model (Rubar20) to simulate detailed surface flows that can occur in urban floods, as well as the capacity of the 1D/2D model (Rubar3-Rubar20) to simulate interactions between surface and subsurface flows. Previous studies with Rubar20 have been carried out and showed the ability of the code to simulate extreme urban flood events (Mignot et al. 2006; El Kadi Abderrezzak et al. 2009), also pointing out the uncertainties corresponding to such modelling such as the input hydrographs or the bottom friction. However these simulations were limited to surface flows modelling as they neglected interactions with the underground drainage system.

In this part, both 2D and 1D-2D models are used to simulate the floods on a well-documented field case. The real case chosen is a part of the city centre of Oullins, located along the right bank of the Yzeron River. The latter flooded 4 times in Oullins in the past ten years, and the underground drainage network is also often overflowing in the streets of the town centre. Therefore, simulations presented in this part concern urban floods generated by a fluvial flooding, and their potential interactions with the urban drainage system. Chapter 6 presents the modelling of the surface flows, by neglecting the interactions with the underground drainage system (as performed in most studies in the literature). This allows a focus on several key points related to the modelling on the surface flow during urban floods. Modelling of the flows in the underground drainage system and its coupling with the surface flow model are separately presented in Chapter 7. Analysis is then reported on the exchanges between both flow layers, and their impact on flood hazard for major river flood events.

Chapter 6.
Surface flows modelling during floods in Oullins

6.1 Presentation of the study case and modelling objectives

6.1.1 The Yzeron River

The Yzeron River collects water from a small peri-urban catchment located at the south west of Lyon, and flows downstream into the Rhône River (Figure 6.3). This catchment is representative of small peri-urban catchments in France, and has been instrumented and studied by researchers for more than 10 years, especially with the set-up of the OTHU[1] (Field Observatory for Urban Water Management). Previous research has mainly focused on the hydrological processes of the catchment, both for water quality and water resources. Besides an accurate understanding of the catchment hydrological processes, the data gathered by the OTHU have been a precious way to validate hydrological models.

The growing urbanization in the second part of the 20th century has been proved to lead to increase of flood risks. Breil et al. (2010) report that urbanization rates on the Yzeron catchment has gone from 6 to 19 % between the 1970s and the 1990s. As a result, occurrence of frequent floods (typically, 1-year flood) has increased. Oppositely, larger floods (10-year flood) are not impacted, as they are mostly controlled by the saturation of the upstream rural

[1]http://www.graie.org/othu/

parts of the catchment (Braud et al. 2013). These studies also highlight the role of the sewer system in the hydrological regime, as infiltration into the sewer reaches 30% of its annual discharge. Integrating impact of these hydrological modifications due to urbanization growth is beyond the objectives of this thesis, but it shows the interest of modelling frequent floods for such catchments.

6.1.2 Recent flood events

Four floods of the river Yzeron recently occurred in the city centre of Oullins: in 2003, 2005, 2008 and 2009. Flow hydrographs (Figure 6.1) have been recorded at the hydrological station at Taffignon, 3 km upstream of the studied area (a map of the catchment is presented on Figure E.1, Appendix E). The 2009 flood has been associated to only very low river overflowing, so the capacity of the river main channel is evaluated to be around 50 $m^3.s^{-1}$. Hydrographs of 2003, 2008 and 2009 present a similar shape, with a typical duration of around 12hours. The 2005 flood duration is larger, especially regarding the falling limb of the hydrograph.

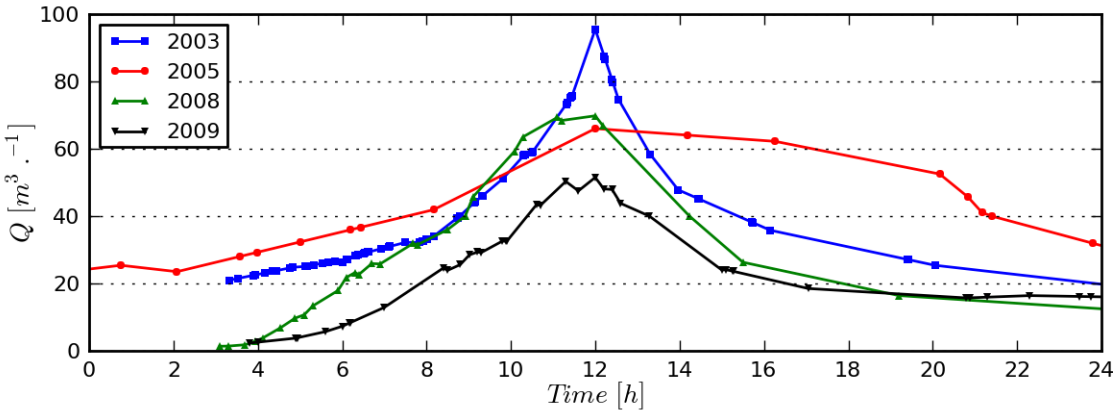

Figure 6.1 : Flow hydrographs of the Yzeron River recorded at the Taffignon station for events of 2003, 2005, 2008 and 2009

Yzeron overflowing concerns mainly areas located downstream of the Taffignon station, where the topography is flatter and the river starts meandering. Flooded areas consist of commercial areas upstream of the bridge Pont Blanc (bridge location shown on Figure 6.3), and residential areas located downstream from this bridge. Further downstream, as the Yzeron river flows in an artificial channel toward the confluence with the Rhône, the floodplain topography is relatively elevated compared to the main channel and potential floodplain flows go back to the latter. Flooding in the residential area implies several processes (Figure 6.2): a direct overflow of the river into the street *Boulevard de l'Yzeron* (street closely following the

river on its right bank, see $Yzeron_{Bank}$ on Figure 6.3), a deeper intrusion in the city centre with flows in the street network, and flow penetration into the built-up areas through different types of opening (low walls, barriers, hedges...).

Figure 6.2 : Photos taken during the 2003 flood in Oullins : flooding along the Yzeron (top) and in a near-by street (middle), filling up of a built-up area (bottom). Source : Irstea.

6.1.3 Analysis of recorded maximum water levels during past floods

Besides the available hydrological input data (rainfall on the catchment and flow discharge in the river), two types of data have been collected to better understand flooding processes and to validate surface flow modelling:

- 3 stage gauges (named L_1, L_2, L_3, see Figure 6.3) have recorded the Yzeron water level during the floods of 2008 and 2009. They are located respectively upstream from the flooded area, and in the upstream and downstream parts of the meander, where flows pass from the main channel to the urbanized floodplain and *vice versa*.
- A series of flood marks have been recorded for the floods of 2003 and 2008.

Other validation data exist but concern the underground drainage network, so they are presented in Chapter 7 and Appendix E.

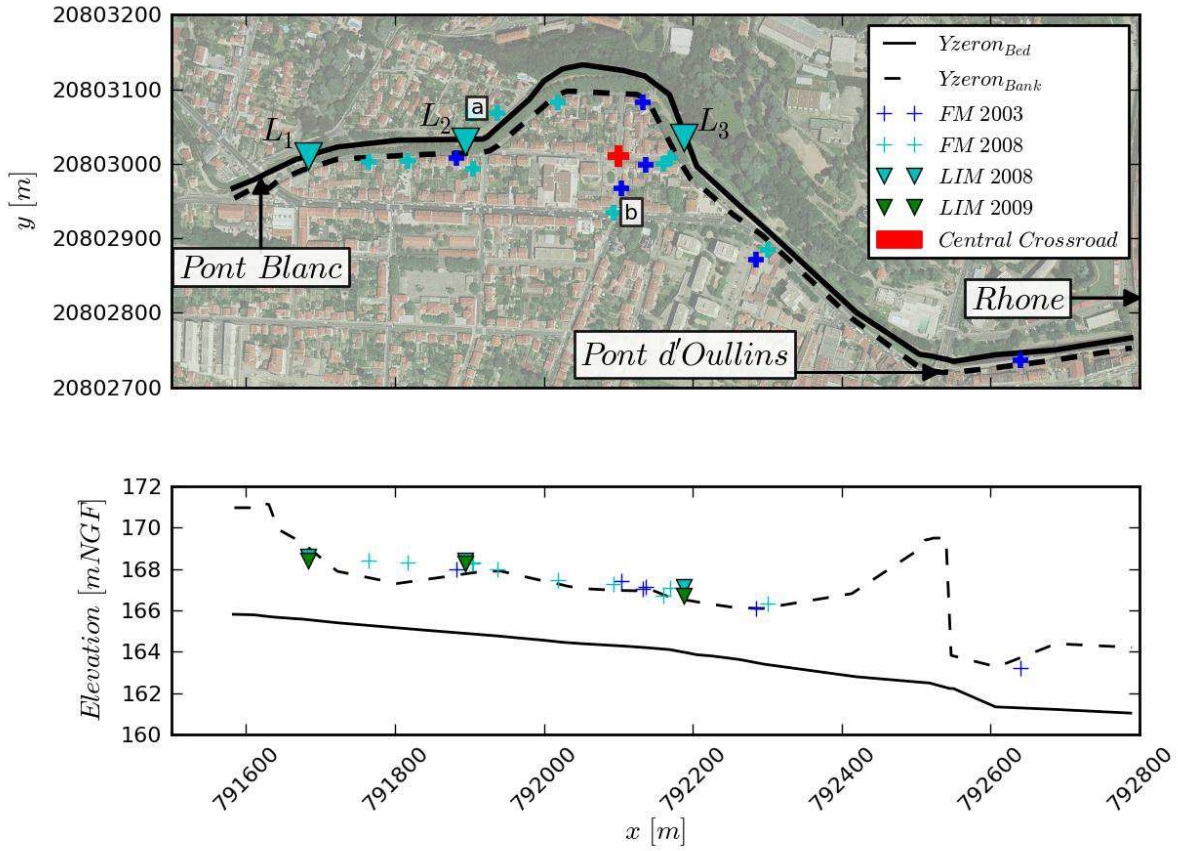

Figure 6.3 : Top view of the flooded area with recorded flood marks (FM) and stage gauges (LIM). View along x-axis of the river bed elevation ($\text{Yzeron}_{\text{Bed}}$*), right bank elevation (*$\text{Yzeron}_{\text{Bank}}$*), recorded flood marks and maximum water levels at the stage gauges.*

The spatial distribution of the flood marks for 2003 and 2008 floods shows an overview of the inundated area. The latter mainly consists of the area within the meander (Figure 6.3). Elevation of the right bank ($Yzeron_{bank}$ on Figure 6.3) shows that the inundation is limited by the presence of the bridges *Pont Blanc* and *Pont d'Oullins*. Finally, when looking at the evolution along x axis (west to east, roughly the river direction in the flooded area) of the recorded maximum water levels for floods of 2003, 2005 and 2009 (which have similar peak discharges, as shown in Figure 6.1), we can notice that:

- The maximum water levels in the floodplain (indicated by the flood marks *FM*) follow quite well the ones in the main channel (stage gauges L_i), yet with slightly lower values. This suggests that the floodplain is quickly filled up (compared to the river overflow durations) and that the flow spreading dynamics has only limited impact on flood extent or maximum water levels.
- There is a break of the maximum water elevation slope around the stage gauge L_2. The maximum water levels observed for the mentioned floods indicate an almost horizontal water elevation line upstream of L_2, whereas the water surface slope downstream rather tends to follow the main channel bed elevation slope ($Yzeron_{bed}$ on Figure 6.3)

Both these remarks on the maximum observed water levels show *a priori* the paramount importance of the river flow for the flooding processes in Oullins.

6.1.4 Modelling objectives

Recent inundations in Oullins show that the city is severely affected by floods caused by the Yzeron River. Understanding the corresponding processes requires *a priori* an adequate modelling of the river flow and of its penetration in the urbanized area. The floodplain topography (see Figure 6.7) implies that the flow extension is very limited, so that a precise modelling of a restrained area can be carried out. Following the thesis objectives and the state of the art in urban flood modelling, the present modelling should permit to assess the effects of:

- the topography (especially in the streets),
- the buildings and built-up areas representation,
- the mesh resolution, and
- the bottom roughness

Considering all these parameters, it is clear that the available validation data cannot accurately characterize pertinence of each modelling assumptions. Therefore, the proposed approach consists first in running simulations with different sets of parameters and comparing the results with available field data (i.e. water levels) in order to get a preliminary assessment of the model sensitivity, and second in comparing each run with any other one, using additional variables (inundation extents, street flow discharges...). As the 2008 flood is well documented, it is particularly studied, and the other floods are only used for model verification.

6.2 Numerical model set-up

6.2.1 Topographical data processing and mesh generation

The model mesh and topographical data are generated in a common step by interpolating available cross-sections of the river and the streets. As the number of available cross-section is not sufficient, a linear interpolation between couples of cross sections is carried out by considering structuring lines, which link specific points of the cross-sections (sidewalks, drain channels, river banks... etc.). A transverse linear interpolation is then performed within each cross-section. Result of this interpolation step leads to a Digital Elevation Model (DEM), including both measured and interpolated topographical points. The mesh is built-upon this data, using both triangular and quadrilateral cells. The mesh structure follows the initial topographical lines, as well as other structural lines such as built-up areas boundaries (this aspect is detailed in 6.2.2).

The model mesh set-up uses:

- 48 available street cross sections with 9 points each (Figure 6.4). The latter are measured at least on each extremity of the crossroads, and intermediary cross-sections are added.
- 18available river cross sections with 10 to 15 points, their location reflecting change in the main channel geometry or direction.
- A cloud of topographical points given by the Great Lyon administration, in order to derive bottom elevation where no other measurement is available (built-up areas) and to interpolate with higher accuracy several intermediary street cross-sections.

The area covered by the model is limited in the streamwise direction upstream by the bridge *Pont Blanc* (as flooding of the urban area mainly occurs downstream of this bridge), and downstream by the bridge *Pont d'Oullins*. Lateral expansion of floods is limited by the terrain topography that becomes steep away from the river (see Figure 6.7), so that the model boundaries can be conservatively fixed.

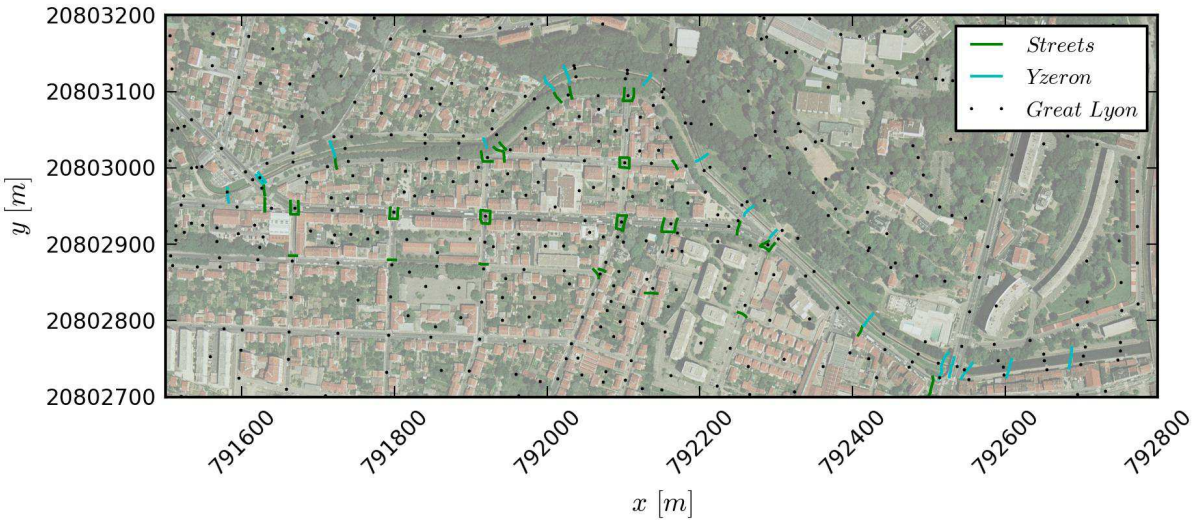

Figure 6.4: Original topographical data used to set-up the model mesh and topography (lines: cross-sections, points: topographical points)

Points spacing within a street cross-section can be as low as 10 cm (drain channels) and creating a mesh that strictly follows the original topography is forbidden for computational time reasons. The chosen solution (referred as *Ref*) consists in simplifying each drain channel / sidewalks interface, keeping only the lowest drain channel point (Figure 6.5). This allows to represent the drain channel (low elevation point), but tends to increase the street flow area, as sidewalks are not accurately modelled using this approach. Errors on the flow area are high for water depths in the drain channels lower than 20 cm (Figure 6.6), but are typically less than 10% for higher values, that is when sidewalks are flooded.

Beyond the *Ref* simplification, a second simplified topography representation is implemented in the surface model, by considering an average bottom elevation on the whole section (*Avg*), as it was done for laboratory experiments (see chapters Chapter 3 and Chapter 5). This representation leads, **in average**, to a decrease of the sidewalks elevation and a "filling" of the drain channels, with an average elevation very close to the street centre elevation (Figure 6.5). For low water elevation in the street, this model underestimates the flow area (with possibly no flow allowed), but errors are rapidly decreasing as the water level increases and the sidewalks become flooded, and become null once the street water elevation

exceeds the highest cross section point (Figure 6.6). Therefore the *Avg* model leads to negligible errors for high street water levels, whereas it cannot represent drain channels flows when water levels are low.

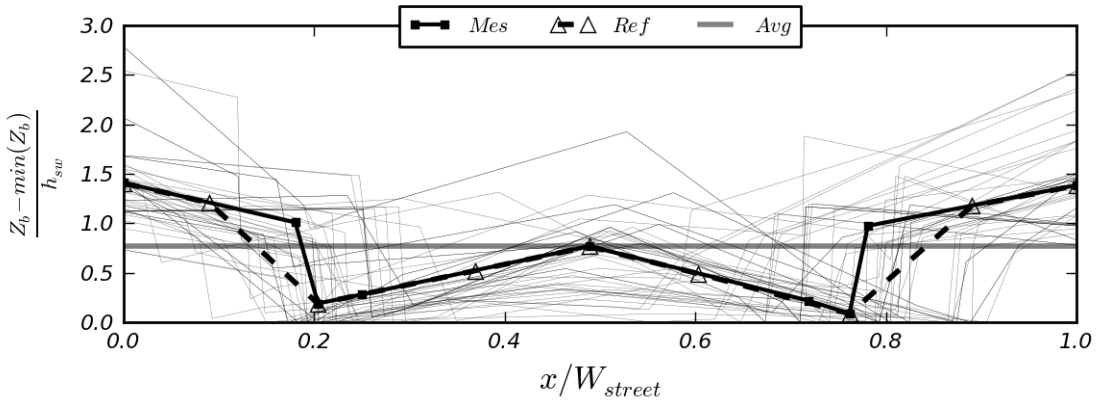

Figure 6.5 : Measured street cross sections (thin lines) normalized by the street width W_{street} *and the sidewalks height* h_{sw}*. Average cross section is plotted in bold (*Mes*), along with the typical integration in the surface numerical model (*Ref *and* Avg*).*

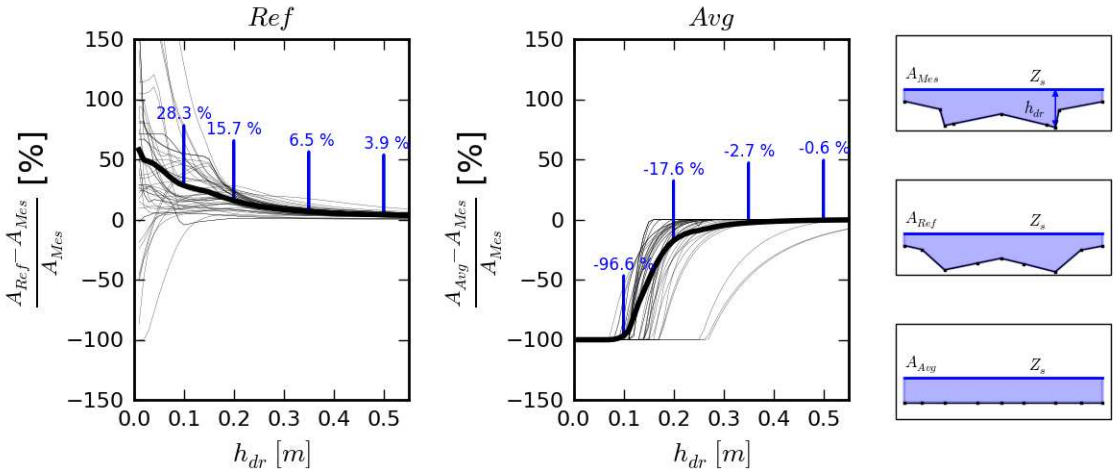

Figure 6.6 : Relative error on the flow area in the street cross sections for the models Ref *(left) and* Avg *(right), computed for a series of street water surface elevation* Zs *constant over the cross section (results given in respect of the maximum water depth on the section* h_{dr}*). Bold line represents the average error on all cross sections.*

Besides these two options in the street topography modelling, a sensitivity analysis is carried out on the built-up areas topography. Oppositely to the streets, the latter is actually rather uncertain, and can be derived either from the Great Lyon topographical points (*GL*), or from an interpolation of the neighbouring measured curbs elevation (*Curb*). **In the present modelling, "built-up areas" indicate urban areas formed by buildings, small gardens, walls, car parks... etc., that usually create blocks around the street network (that is all surface area apart from the streets and the river).** Three sets of topographical data are then considered in the sequel (Table 6.1).

Name	Street topography	Built-up areas topography
Topo1	*Ref*	*GL*
Topo2	*Ref*	*Curb*
Topo3	*Avg*	*GL*

Table 6.1 : Topographical data used for each Oullins surface model topography

Finally, two meshes are implemented. The first one (*m1*) aims at providing mesh cells with typical dimensions not larger than 2 m, whereas a second one (*m2*) is created with a 10 m limitation, yet with at least 2 cells across each street profile. Actual mesh elements size is given in Table 6.2, along with the number of cells. For the fine mesh *m1*, the number of cells across a street lies between 7 and 9, depending on the street width and the interpolation process. For such a resolution, implementation of the detailed topography *Ref* is possible, and the 3 topographical data from Table 6.1 are considered. Oppositely, for the coarse mesh*m2*, the small amount of cells across the street implies that only the topography *Avg* can be used (*Topo3*).

Mesh	Number of cells	Typical cells dimensions		
		River	Streets	Built-up areas
m1	135750	2.67 m^2(~1.64 m)	2.67 m^2(~1.64 m)	2.66 m^2(~1.63 m)
m2	6129	59.0 m^2(~7.68 m)	40.82 m^2(~6.39 m)	62.24 m^2(~7.89 m)

Table 6.2 : Number of cells and typical dimensions for the meshes m1 and m2 (average cell area, and square root of this area in parenthesis)

Result of the topographical interpolation for the fine mesh *m1*and topography *Topo1* is shown on Figure 6.7. Implementation of the detailed topography is effective, as footprint of the sidewalks is easily identified. As expected, the *Avg* topography (see Figure 6.7) tends to increase the streets elevation, with quite important local variations. Analysis of the bottom elevation difference (*Avg-Ref*) shows an average difference of +3.0 cm, with a standard deviation of 10.9 cm. Therefore, switching from a street topography representation to another can be seen as an uncertainty analysis, as it can be done by introducing noise in topographical data (Brown et al. 2007).

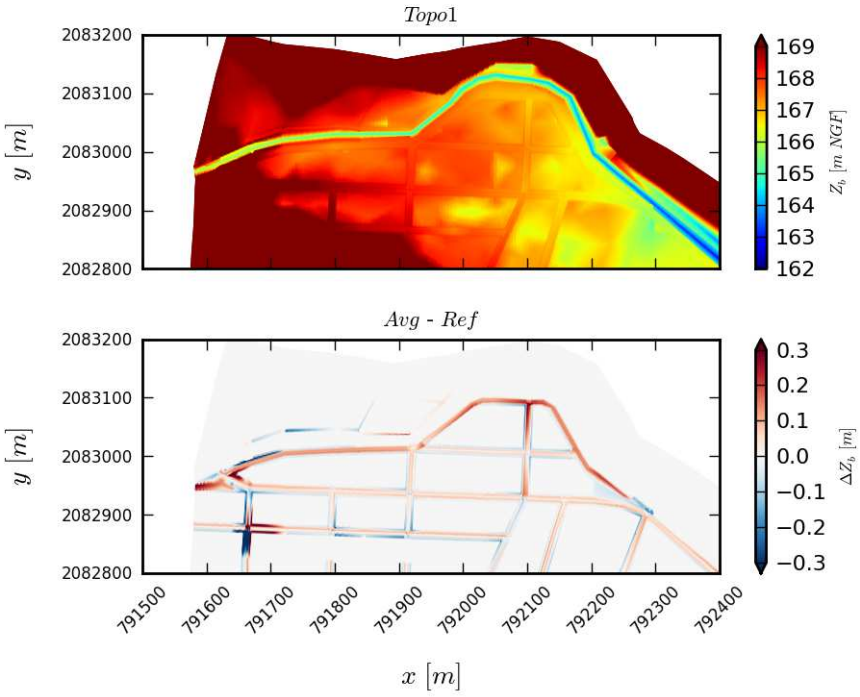

Figure 6.7 : Digital Elevation Model derived for the topography 1 (top), and comparison of street elevation between Ref *and* Avg *model (bottom), based on the fine mesh* m1

6.2.2 Structural elements

The floodplain in Oullins is characterized by the presence of built-up areas, which can be represented as groups of buildings, surrounded by different types of vertical openings or blockages (walls and barriers). A GIS layer provided by the Great Lyon gives the buildings footprint, and the latter are integrated in the numerical model as impervious areas (solid boundaries). Respecting strictly these footprints would require meshing tools that can generate an unstructured mesh based on this information (e.g., Schubert et al. 2008). This cannot be automatically achieved with the available tools, so a cell is considered here as impervious if more than 50% of its area is occupied by buildings. For the mesh *m1*, using this method leads to a global buildings area exceeding of +2.3% the area specified by the GIS layer, which is reasonable (the mesh *m2* is not used for such modelling, as explained below).

Location and type of boundaries separating the streets from the built-up areas have been obtained during a field survey. From a hydraulic perspective, these boundaries have been divided into 4 categories:

- Impervious boundaries *Imp* (high walls or buildings)
- Pervious boundaries *Per* (no physical boundary observed, or boundaries that do not prevent flows, such as wire fences)

- Semi-pervious boundaries *Bar* (typically barriers with small openings at the bottom)
- Boundaries *Low* where flow can pass depending on water elevation (low walls)

Boundaries *Bar* are modelled using an orifice equation to model the flow through the low elevation opening element (with a 5 cm high opening starting from the ground level, and a discharge coefficient of 0.5). This representation is rather simple but is closer to the actual hydraulic behaviour than a free opening. Boundaries *Low* are modelled with a weir equation, with weir crest elevation equals to the low wall elevation, and a discharge coefficient of 0.4.

Mesh structure has been carefully designed so that the interfaces streets/built-up areas are accurately covered by some cells edges, so that the recorded boundaries can be directly integrated in the numerical model (see Figure 6.8). Besides these streets/built-up areas interfaces, inner walls are added to separate individual gardens within a built-up block (with impervious wall *Imp*). As for buildings, some errors remain as the mesh nodes on the built-up areas boundaries do not necessarily fit with the measured changes of boundary type.

The integration in the numerical model is carried out by defining how flow exchanges between two cells are governed (that is: shallow water equations (*Per*), solid boundary (*Imp*) or a specific equation (*Bar* and *Low*)).

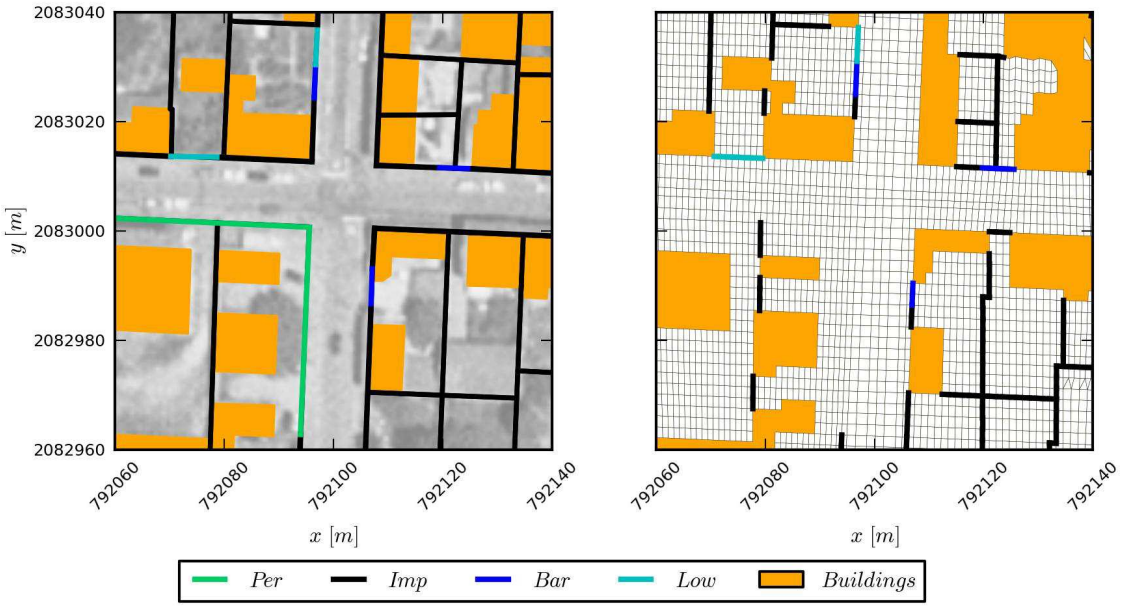

Figure 6.8 : Available data on structural elements (left) and integration in the numerical model with the mesh m1 *(right). Zoom on the crossroad located within the meander.*

In order to assess the influence of these structural elements, four models with various complexities are defined:

- Model *Walls*, including all buildings and boundaries

- Model *Bdg*, including all buildings, but with totally pervious boundaries (all boundaries set as *Per*)
- Model *Street*, excluding built-up areas, so that flow in the urbanized floodplain can only flow in the streets
- Model *Free*, without buildings and walls, with flow possible all over the floodplain

For mesh resolution reasons, integration of buildings and detailed boundaries is only done for the fine mesh (*m1*). Therefore, for the coarse mesh, only the model *Street* is used.

6.2.3 Friction

The bottom friction is modelled through the use of a Manning-Strickler coefficient (K_s=1/n). Strickler coefficients are lumped in the model (Figure 6.9) to reflect the different ground types. Choosing a value for this coefficient is always partly arbitrary and remains uncertain (actual bottom roughness, presence of debris and sediments, effects of small topographical details not represented in the model topography... etc.), so that a calibration step or a sensitivity analysis has to be carried out. The domain is divided into four ground types, for which a reference Strickler coefficient $K_{s,ref}$ and a lower one $K_{s,low}$ are assigned:

- The river bed, made of damaged concrete and bare earth ($K_{s,ref}$ = 50 $m^{1/3}.s^{-1}$, $K_{s,low}$ = 30 $m^{1/3}.s^{-1}$)
- The river banks and other areas with vegetation of variable density ($K_{s,ref}$ = 30 $m^{1/3}.s^{-1}$, $K_{s,low}$ = 20 $m^{1/3}.s^{-1}$)
- The streets, made of asphalt ($K_{s,ref}$ = 70 $m^{1/3}.s^{-1}$, $K_{s,low}$ = 30 $m^{1/3}.s^{-1}$)
- The built-up areas, for which low values are assigned to account for the different elements that block the flows ($K_{s,ref}$ = 10 $m^{1/3}.s^{-1}$, $K_{s,low}$ = 3 $m^{1/3}.s^{-1}$)

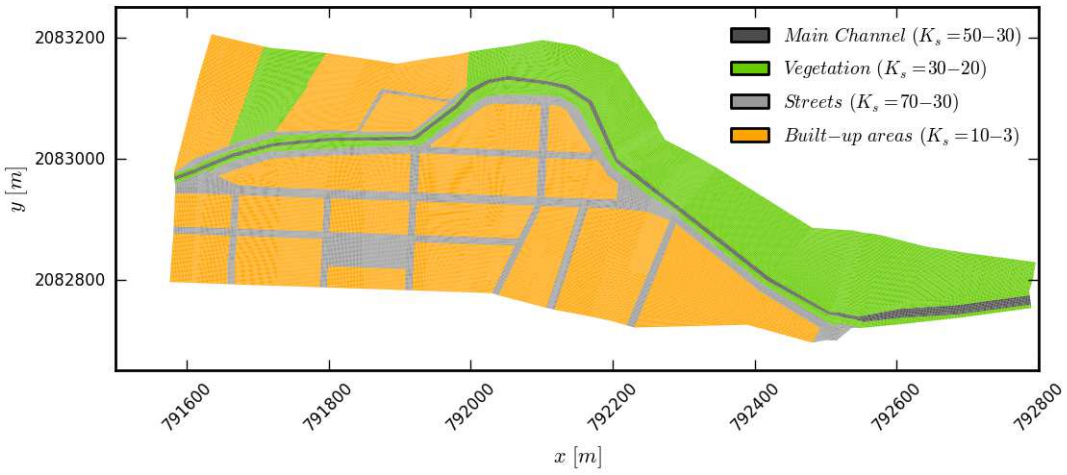

Figure 6.9 : Distribution of Strickler coefficients K_s *for Oullins surface model (*K_s *indicated in* $m^{1/3}.s^{-1}$*).*

6.2.4 Boundary conditions

The upstream flow discharge is recorded at the Taffignon station, 3 km upstream from the model upstream boundary. At this station, about 95% of the catchment has been drained into the Yzeron River, and the additional catchment area between the station and the model is strongly urbanized, so that part of the rainfall on this area is likely to be drained into the sewage network. To account for the additional inflow at the upstream boundary of the model, the measured discharge is multiplied by $(A_{model}/A_{Taffignon})^{0.8}$ = 1.04 (Ministère de l'agriculture 1980), where A_{model} and $A_{Taffignon}$ are the catchment area respectively at the model upstream boundary and at the hydrological station. This correction only leads to a 4% increase of the flow discharge, and uncertainty is then mostly due to the measurement uncertainties. Besides, as described in 6.1.2, flooding occurs upstream of the modelled area, so that the flow hydrograph may be significantly impacted.

A simplified Rubar20 2D model was set up from Taffignon station to the upstream boundary section to study effects of the flood propagation in this river reach. Available data were rather poor (streamwise evolution of the main channel lowest point, 4 main channel cross-sections and a 10 m resolution DEM for the floodplain) so that results must be carefully considered. Figure 6.10 shows for the 4 floods studied the simulated propagation of the hydrograph between the measurement point (*Taffignon*) and the upstream boundary of the surface model of Oullins (*Oullins*). For the floods of 2005, 2008 and 2009, measured (*Taffignon*) and propagated (*Oullins*) hydrographs are very similar. The propagation only smoothes the measurements, with a slight decrease of the peak discharge and a delay of a few

minutes. However, for the 2003 flood, the peak discharge is reduced by 23%, with a report of the discharge on the hydrograph falling limb. For this event, both hydrographs (*Taffignon* and *Oullins*) will be considered as upstream boundary condition as this may be a real source of uncertainty. For other events, we use only the hydrographs *Oullins*, as they are very close to the measurements, but with smoother and more realistic shapes around the peak time.

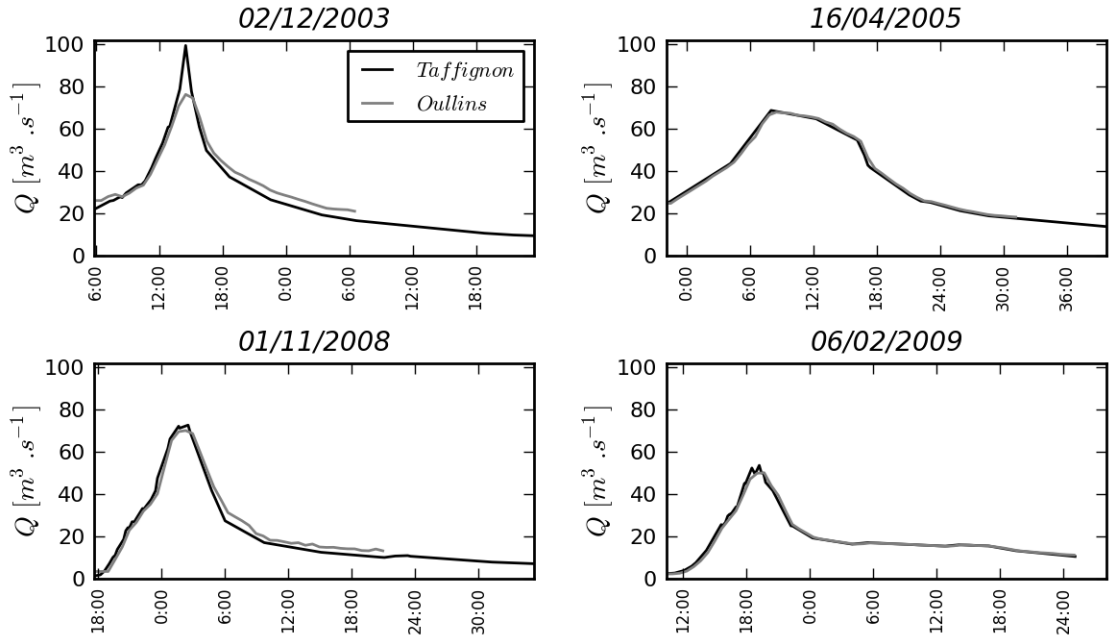

Figure 6.10 : Hydrographs propagation for the past floods between the hydrological station and the upstream boundary of the Oullins surface model

Alternatively, for the 2008 and 2009 floods, the upstream boundary condition can be set as a time series of the river water level, as the latter is measured at stage gauge L_1 near the boundary condition (bridge *Pont Blanc*, see Figure 6.3). As the difference of water level between these 2 points (model upstream boundary condition and L_1) varies with the river discharge, recorded water levels at L_1 cannot be easily transformed into a perfectly suitable upstream boundary condition. Preliminary simulations showed that specifying L_1 measurements at the model upstream boundary (without shifting the water levels) was the best way to simulate the adequate water level at the location of the stage gauge L_1 around the peak time (which means the water level is almost horizontal for large discharges in the upstream part of the model). This solution is adopted, as we are mainly interested in the simulation of flows around the peak time.

The flow downstream of the flooded area is controlled by the bridge *Pont d'Oullins*, with a contraction of the flow due to its two piers, an acceleration along the steep slope of the main channel across the bridge, and an expansion of the river main channel just downstream into a wider channel that continues to the confluence with the Rhône. For sake of simplicity,

the model downstream condition is set to a critical condition in a cross section further downstream. A sensitivity analysis has been carried out with another downstream condition, (uniform regime, which increases the downstream water depths up to 80%). Areas impacted by this change of downstream condition remain downstream from the bridge *Pont d'Oullins*, so that there is no impact on areas where flooding occurs.

6.3 Study of the 2008 flood

A series of 12 runs is carried out for the 2008 flood (Table 6.3). The run 1 is considered as the reference run, with the most accurate representation of the topography and structural elements. Other runs consist in lowering modelling details on the structural elements (runs 2-4) or the topography (runs 9 and 10), or in assessing sensitivity of the model to upstream conditions (run 8), bottom friction (runs 5-7), and mesh density (run 12). As the coarse mesh *m2* (run 12) could only be used with the simplified topography *Avg* (average bottom elevation across the streets) and without accurate consideration of structural elements (model *Streets*, with only a representation of the street network), the run 11 is introduced. This run has the same level of simplifications as run 12, except for the mesh density (use of the fine mesh *m1*), which permits an intermediary comparison with run 1.

Run	Mesh	$K_{s,banks}$	$K_{s,\ main\ channel}$	$K_{s,\ streets}$	$K_{s,\ built\text{-}up\ areas}$	Upstream condition	Structural elements	Topography
1	*m1*	30	50	70	10	$Q_{Oullins}$	*Walls*	*Topo1*
2	*m1*	30	50	70	10	$Q_{Oullins}$	***Buildings***	*Topo1*
3	*m1*	30	50	70	10	$Q_{Oullins}$	***Free***	*Topo1*
4	*m1*	30	50	70	10	$Q_{Oullins}$	***Streets***	*Topo1*
5	*m1*	30	50	**30**	10	$Q_{Oullins}$	*Walls*	*Topo1*
6	*m1*	**20**	**30**	70	10	$Q_{Oullins}$	*Walls*	*Topo1*
7	*m1*	30	50	70	**3**	$Q_{Oullins}$	***Free***	*Topo1*
8	*m1*	30	50	70	10	L_1	*Walls*	*Topo1*
9	*m1*	30	50	70	10	$Q_{Oullins}$	*Walls*	***Topo3***
10	*m1*	30	50	70	10	$Q_{Oullins}$	*Walls*	***Topo2***
11	*m1*	30	50	70	10	$Q_{Oullins}$	***Streets***	***Topo3***
12	***m2***	30	50	70	10	$Q_{Oullins}$	***Streets***	***Topo3***

Table 6.3 : Simulations parameters for the surface flow modelling in Oullins. Parameters that change from the reference ones (run 1) are indicated in bold. Strickler coefficients K_s *are in* $m^{1/3}.s^{-1}$.

6.3.1 Analysis of the reference simulation results

Results of the run1 provide a preliminary description of the flow during the 2008 flood. Figure 6.11 shows the evolution of water depths in the urbanized floodplain during the flood. Overflows first occur on the left side of the river, inundating the street following the river (at 23:36). Overflow on the right bank occurs later (at 0:36), and locally starts on both ends of the meander. At the peak time (2:36), floodplain flows are mainly along the street following the right bank of the river with important water depths (typically 50 cm). Further urban areas (i.e. south of the river) are also impacted, yet with shallower water depths (10-20 cm).

Importance of the street network to convey flows in the floodplain is evident. Water spreads within the street network right after the beginning of right bank overflows, with almost no inundation of the built-up areas (0:16). As the peak discharge approaches, the water penetrates the built-up areas. Inundation of the built-up areas still remains limited, as a consequence of the overall low water depths in the floodplain (even at the peak time), and of the integration of walls for this run.

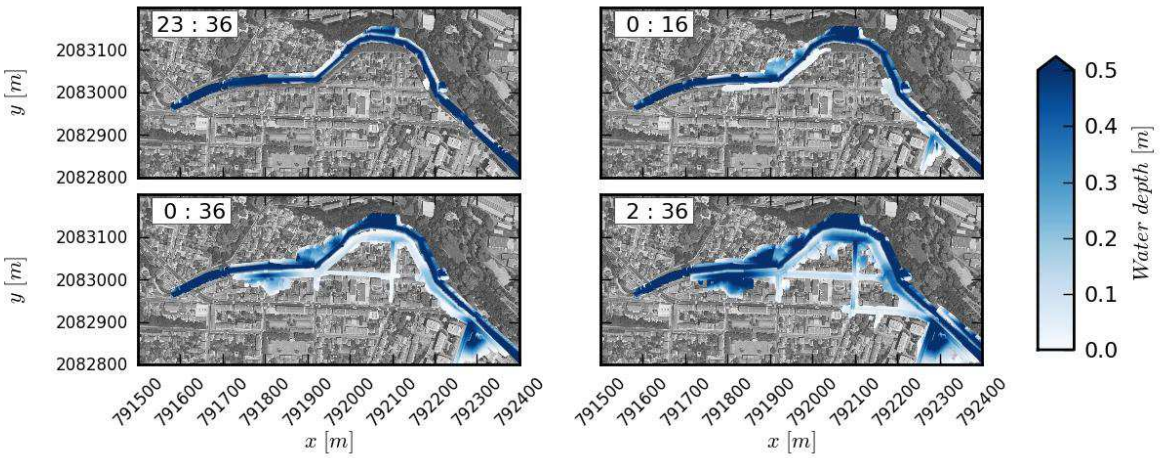

Figure 6.11 : Time evolution of the simulated water depths until the peak time of the 2008 flood for run 1

The corresponding water elevation (shown at the peak time on Figure 6.12) shows very smooth spatial evolutions at a given time. Evolution of the water level in the overflowing area (around the meander, between x=791900 m and x=792200 m) is mainly along the river direction, with almost no transverse variations (i.e. South-North). This supports the hypothesis done in 6.1.3, for which recorded flood marks and river water levels suggested that the water levels in the floodplain closely follow the ones of the river. Further downstream (x>792200 m), water levels in the main channel and in the floodplain are not coupled anymore as there is no more overflow from the river toward the urban area.

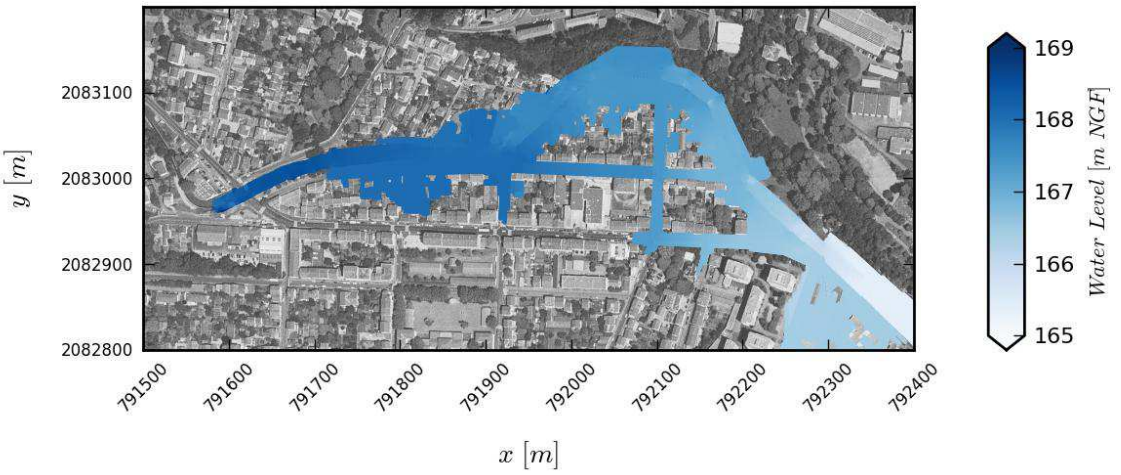

Figure 6.12 : Simulated water surface elevation in Oullins at the peak time for the 2008 flood (run1)

6.3.2 Comparison with the measured flood marks and river water levels

The simulated maximum water levels for each run are compared to the 10 recorded flood marks of the 2008 flood. Figure 6.13 shows average (δ) and root mean square (RMS, σ) of the difference between these simulated and measured maximum water levels. Note that results for runs 4/11/12 are given but the number of flood marks considered is rather low (4), as several of them are located within built-up areas. Therefore, results of these runs are not discussed for flood marks. Globally, typical errors are around 15-20 cm, and one can assume there is no optimum set of numerical parameters, as the number of flood marks is small (10), and variations of the RMS σ from one to another are low. Yet the average difference δ is more sensitive to numerical parameters. The reference run (run 1) tends to a global underestimation of the water level in the inundated area of about 10 cm. Several runs significantly modify the value of δ when compared to run 1, which gives a first assessment of the model sensitivity:

- Increasing friction in the streets (run 5) or in the main channel (run 6) increases the computed water levels (as expected). The model appears to be clearly more sensitive to the river friction than the streets, even if the street friction is increased to an extreme value (run 5).
- Changing of input hydrograph has a slight impact on the computed maximum water levels (run 8). Interest of this run is discussed further below.

- Considering an average street bottom elevation (run 9) also increases the simulated water levels. This is consistent with the fact that the topography *Avg* leads to globally higher street bottom elevation than the topography *Ref*.

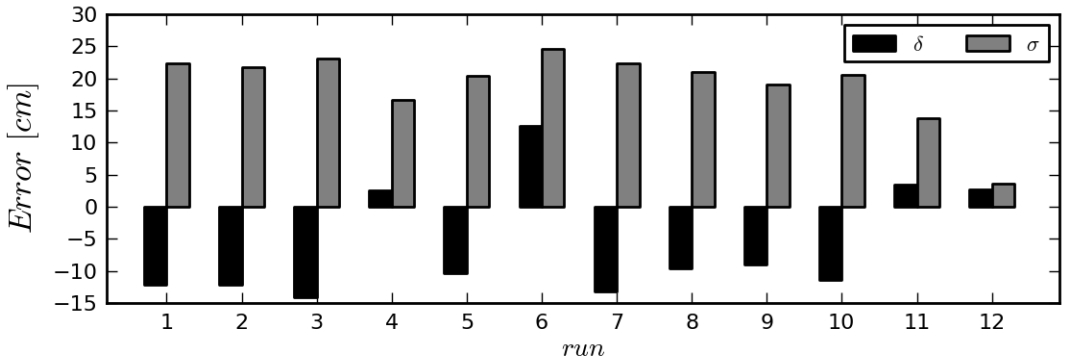

Figure 6.13 : Average error (δ) and root mean square error (σ) of the simulated water levels at the 2008 flood marks for each run (1 to 12, as defined in Table 6.3)

Analysis of the spatial distribution of these errors on the flood marks and comparison with the recorded maximum river water levels at the three stage gauges reveals a general bias in the model. Figure 6.14 shows errors on the maximum simulated water levels at the flood marks for runs 1 and 6. Run 1 underestimates (respectively overestimates) the water levels in the upstream area (respectively downstream area). Increasing friction in the river main channel and banks (run 6) leads to better agreement in the upstream area but also to larger overestimation in the downstream area (when compared to run 1). Therefore calibrating one single river bottom friction cannot lead to a better prediction of the water levels in the whole flooded area.

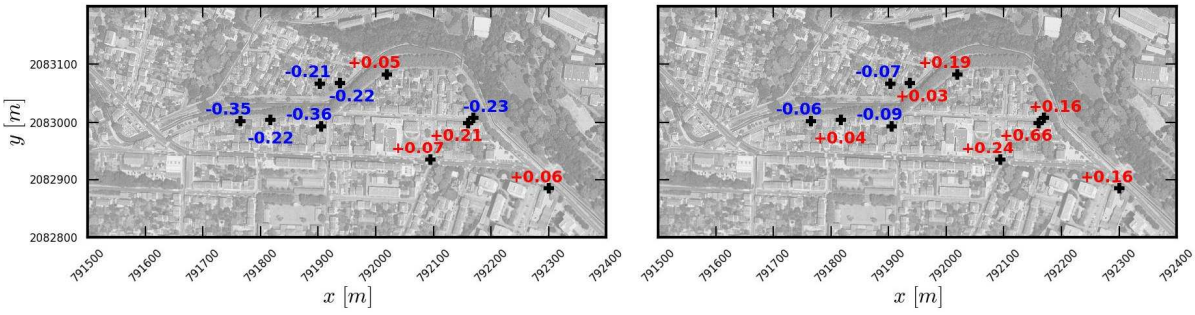

Figure 6.14 : Difference between simulated and measured maximum water levels at the 2008 flood marks for runs 1(left) and 6 (right), in meters.

Now, Figure 6.15 shows the measured and computed water levels in the river for these latter runs (stage gauges location is shown on Figure 6.3), along with run8, for which the upstream boundary condition consist in imposing the water level measured at the stage gauge L_1. For the reference run (run1), the rise of the water levels during the rising limb of the

hydrograph is underestimated. Considering the simulated water levels during the falling limb for this run (fairly well predicted), discrepancies before the peak discharge can be attributed to errors in the flow hydrograph. The intermediary catchment between the hydrological station and the model upstream boundary reacts faster than the main catchment (i.e., the one upstream of the hydrological station). Therefore additional inflows should be concentrated during the rising limb of the measured hydrograph, which is consistent with the discrepancies observed.

The water level at L_2 is underestimated of around 25 cm at the peak time. Given its location, this is consistent with the underestimation of the floodplain water levels in this area (see errors on the flood marks on Figure 6.14). This discrepancy is the highest one encountered in the present simulations; it is discussed further below.

The measured water level at L_3 shows a sudden rise around 4:00, which is not simulated by any of the present runs. Considering both other measurements, this abrupt change in water level is rather difficult to explain. It is likely to come from a measurement error or a phenomenon not accounted for in the simulations (temporal flow blockage, influence of the bridge near the stage gauge L_3, driftwoods…). Apart from this short event, water levels are fairly simulated at this stage gauge.

Imposing the time series of the water level L_1 at the upstream boundary (run 8) permits to simulate a more accurate water level for L_1 around the peak time (compared to the reference run 1). This implies the simulated water levels are almost horizontal in the upstream part of the model (first 100 meters). This boundary condition also improves the simulated water levels at L_2 during the rising limb of the hydrograph, but the peak water level is still underestimated. These results also support the assumption of an inaccurate shape of the flow hydrograph rising limb. Increasing the main channel and bank friction (run 6) only improves the maximum simulated water level at L_2, but deteriorates simulation adequacy for other measurements (L_1, L_3).

None of the other simulations leads to a better prediction of the river water level than these 3. These discrepancies were also observed for the 2009 flood simulations (which barely led to river overflows, see 6.4.3). Therefore, this systematic error should arise from the modelling of the river flow.

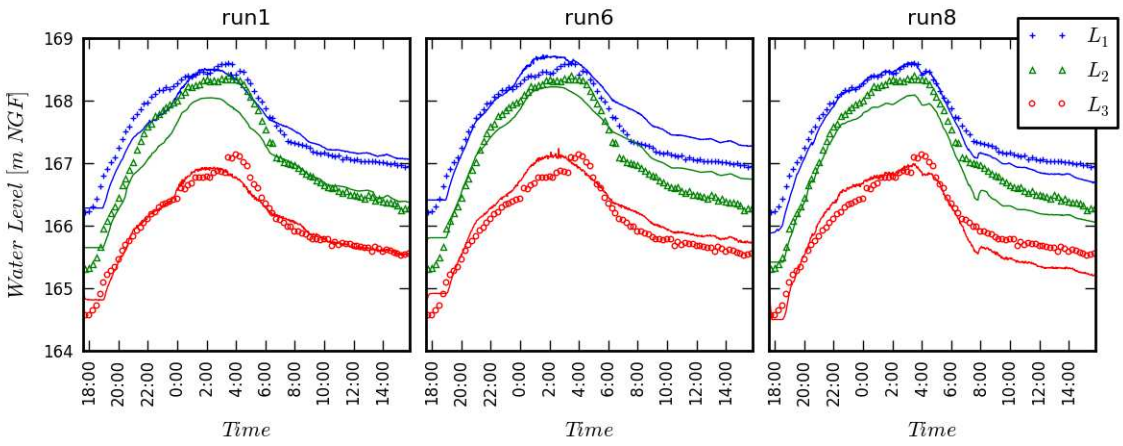

Figure 6.15 : Simulated (lines) and measured (symbols) water levels at the stage gauges L_1-L_3 *for runs1, 6 and 8*

Errors in the river flow modelling around L_2 may arise from several sources. First, the available topography includes a limited number of cross sections, and the linear interpolation carried out may miss some important change in the main channel geometry. In this case, results suggest that errors should mainly be located in the upper part of the main channel cross-sections, as low discharges are well simulated. Available cross-sections show that the left bank capacity changes in the meander, and that both right and left banks widen as they reach the bridge *Pont d'Oullins*. However, no other data is available to assess whether significant errors are done during the interpolation process.

Then, simulation discrepancies may arise from the friction modelling. Considering discrepancies shown on Figure 6.15, two attempts to calibrate the model by changing the river friction have been carried out:

- by increasing bed and banks friction between stage gauges L_2 and L_3 only
- by increasing only the bank friction (the river bed keeping its reference value).

Both attempts gave results somehow between run 1 and run 6, but in any case failed in achieving better agreement with the measured water levels than run 1 (not shown herein).

Another source of error is the presence of two small bridges located near L_2 and L_3, which may locally affect the main channel flow area and even limit the flows if the latter reaches the bridge level. This latter is likely to happen for the bridge located near the stage gauge L_2 (see Figure 6.16). An attempt to model effects of this bridge was carried out by defining impervious cells (roughly 2 m x 2 m cells on each bank of the river) in the model. This lead to a local increase of a few centimetres of the water level at the peak near L_2, which is not enough to explain observed discrepancies. **Errors are thus more likely to come from**

a wider topographical error (due either to a bad description of some of the river cross sections or to the interpolation process).

Figure 6.16 : Small bridge at stage gauge L_2 location photographed after the 2009 flood (Source: Google Map)

6.3.3 Comparison of simulations

The series of simulations presented in sections 6.3.1 and 6.3.2 show that the model can predict the water levels in the inundated area with typical errors around 15 – 20 cm, mainly arising from the modelling of the river flow. Field data alone cannot assess the pertinence of the different runs carried out, as variations from one run to another on the computed water levels are usually smaller or of the same order of magnitude as the differences observed with field data (see Figure 6.13). In this section, we compare simulations results with each other, considering the following variables:

- Maximum volume of water stored in the built-up areas $V_{built\text{-}up,max}$ during the event
- Maximum value of the global exchange discharge between built-up areas and streets $Q_{built\text{-}up,max}$, defined as the time derivative of the volume of water stored in built-up areas
- Inundation extent A_{in} (cumulated area of all flooded cells)

Besides, for runs 2-12, computed water levels in the streets are compared to the ones computed with run 1, using an average difference $\Delta Z_{s,street}$. All these indicators are given in Table 6.4 and discussed in the following sub sections.

run	$\Delta Z_{s,street}$	A_{in}		$V_{built\text{-}up,max}$		$Q_{built\text{-}up,max}$	
	cm	x10^4 m^2		x10^3 m^3		$m^3.s^{-1}$	
1	-	6.8		4.1		1.04	
2	0.2	8.4	+24%	7.4	+81%	1.28	+23%
3	-1.0	10.0	+50%	1.0	+154%	1.66	+60%
4	-0.2	5.5	-20%	-	-	-	-
5	3.5	7.0	+3%	4.6	+14%	1.11	+7%
6	16.8	8.3	+23%	8.9	+119%	1.46	+40%
7	-0.4	10.0	+48%	9.7	+139%	1.63	+57%
8	-2.6	7.0	+3%	4.5	+10%	0.54	-48%
9	2.4	7.2	+6%	4.8	+18%	1.15	+11%
10	-0.4	6.5	-4%	2.7	-34%	0.62	-40%
11	2.0	5.5	-19%	-	-	-	-
12	1.2	5.5	-19%	-	-	-	-

Table 6.4 : Simulation indicators on the 2008 flood: inundation extent Ain, maximum volume stored in built-up areas Vbuilt-up,max, maximum exchange discharge Qbuilt-up,max. Relative difference with run 1 results is reported in percents. ΔZs,street compares the computed street water levels between runs 2-12 and run 1

6.3.3.1 Influence of structural elements

Representation of walls and buildings has a strong impact on the inundation extent (Figure 6.17). In particular, omitting the walls obviously strongly increases the flow penetration in built-up areas (see runs 1, 2 and 3). Increase of the inundated areas can exceed 50% when compared with run 1 (Table 6.4). Simulated flows in built-up areas are slow and are mainly set by the water levels of the surrounding streets. As a result, increasing friction in built-up areas has very low impact (from run 3 to run7 in Table 6.4). This method is not efficient to represent flow blockage due to structural elements, and the latter have to be included in the model to predict the right inundation extent. Analysis of the maximum volume stored in the built-up areas leads to the same conclusions.

The maximum value of the exchange discharge ($Q_{built\text{-}up,max}$) between streets and built-up areas is obtained when walls and buildings are not represented (run3 in Table 6.4). This has a limited global impact on the computed water levels in the streets (-1.0 cm in average for the run 3), as the effective area available for floodplain flows increases. However, although variations of the exchange discharge $Q_{built\text{-}up,max}$ are significant from one run to another, the values are small when compared to the river peak discharge (around 70 $m^3.s^{-1}$) and the discharge overflowing from the river to the floodplain (at least 10 $m^3.s^{-1}$). This explains why

the precise representation of the structural elements of the urban area does not strongly impact the computed water levels in the river or in the floodplain.

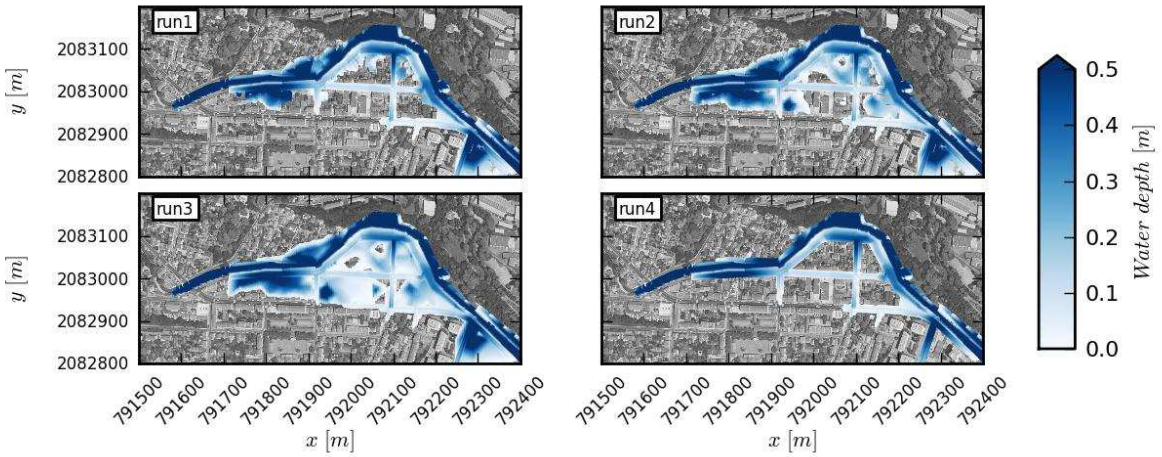

Figure 6.17 : Influence of the structural elements on the simulated water depths at the peak time (runs 1, 2, 3 and 4)

Locally, flow characteristics may vary depending on the structural elements representation. Figure 6.18 shows the time evolution of the computed water depths and velocities at points *a* and *b* (shown on Figure 6.3). For the point within the built-up area (point *a*), the velocity is almost null for the reference run (run 1). Omitting structural elements (runs 2 and 3) leads to a significant flow through this built-up area, and velocities become significant. This in turn impacts the simulated local water depth, which is lower for runs 2 and 3. For the point b, which is located within the street network, there is no significant difference amongst runs 1-4.

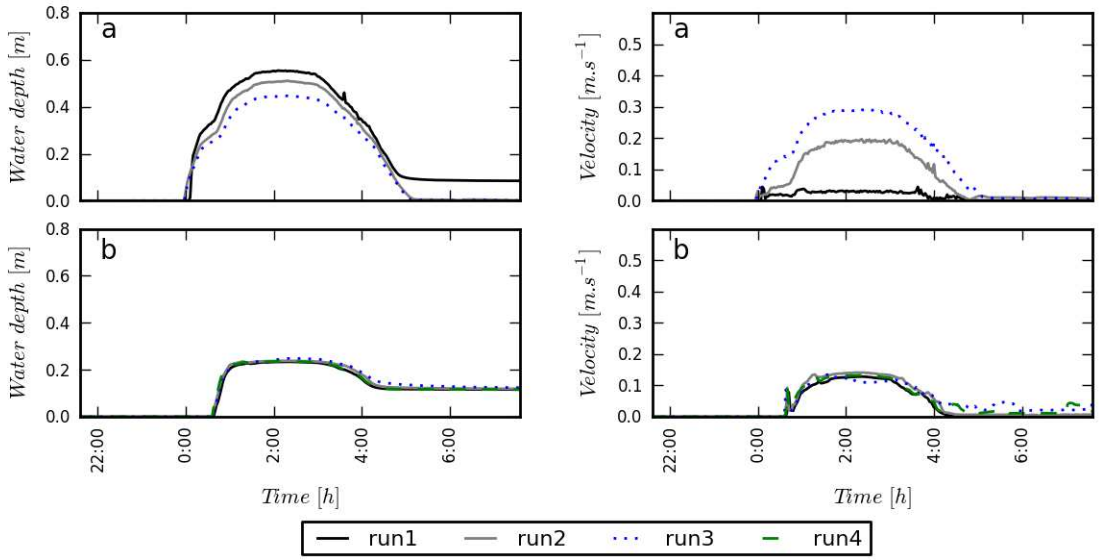

Figure 6.18 : Time evolution of local water depths and velocities computed at points a and b (defined on Figure 6.3) for runs 1, 2, 3 and 4

6.3.3.2 Influence of bottom friction

As seen in section 6.3.2, the model is highly sensitive to the river bottom roughness. The computed maximum water levels are increased by an average of 16.9 cm when increasing friction in the main channel and the banks (run 6, Table 6.4). This is substantial when compared to the water depths in the streets (typically 10 – 50 cm). As a consequence, a larger part of the urban area is inundated (+ 23%), and more water is stored in the built-up areas (+119 %). Increasing the friction in the streets (run 5) leads to the same type of effects, yet with much smaller amplitude.

6.3.3.3 Influence of topography and mesh density

Figure 6.19 shows the computed water depths at the peak time for runs 1, 9, 11 and 12. Comparing runs 1 (reference) and 9 (average bottom elevation in the streets), we can see that the inundated area is larger for run 9, as a consequence of a global increase of the streets water level (+2.4 cm). Moreover, for the latter run, flooding occurs on the whole streets width, as a direct consequence of the topography simplification.

Runs 11 and 12 represent further simplification of the model, with a representation of the street network only and an average street bottom elevation, respectively with a fine and a coarse mesh. Globally, both runs lead to similar results as the reference (run 1) when looking at the flood extent (Figure 6.19). The average increase of water level in the streets $\Delta Z_{s,street}$ for run 11 is very close to the one computed with run 9 (Table 6.4). Therefore the simulated water levels appear to be more influenced by the street topography than by the built-up areas representation. Use of the coarse mesh *m2* (run 12) barely alters the simulated water levels when compared to the equivalent run with the fine mesh (run11). These small changes may also come from the river modelling (as the river mesh differs too), so that influence of the mesh density can be overall considered to have no significant impact on the water levels.

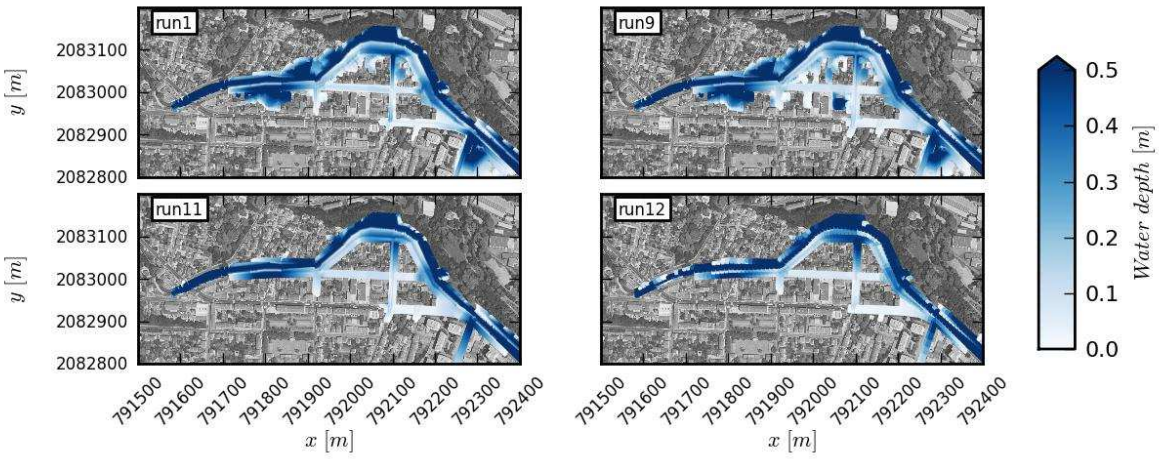

Figure 6.19 : Influence of the street topography and mesh resolution on the simulated water depths at the peak time (runs 1, 9, 11 and 12)

Local water depths and velocities simulated at the point *a* (located in the built-up area) do not vary between runs 1 and 9, as the structural elements are represented the same way. At the point *b* (southern flooded crossroad), the flooding is slightly delayed for the runs that do not integrate the drain channels topography (street topography *Avg*, runs 9, 11 and 12). The local water depth at the peak time is lower for these runs than for the run 1, though this partly comes from the difference of ground elevation. The computed velocities differ too, both at the arrival of the flood wave and around the peak time, which shows that the flow dynamics can be locally impacted by the mesh resolution and the topography.

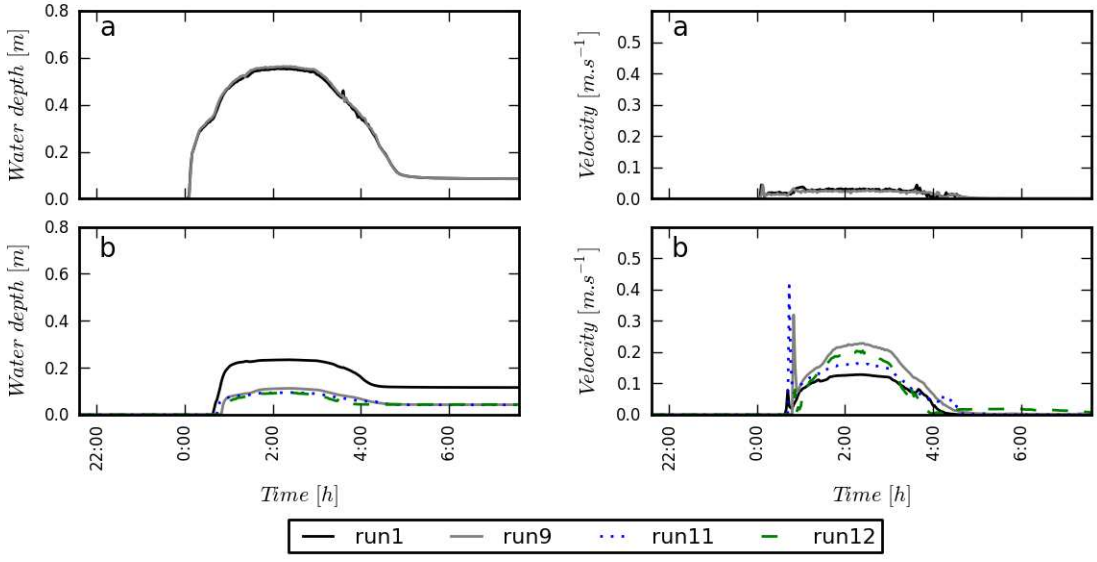

Figure 6.20 : Time evolution of local water depths and velocities computed at points a and b (defined on Figure 6.3) for runs 1, 9, 11 and 12

6.3.4 Analysis of the flow in the central crossroad

For the 3 runs including only the street network (runs 4, 11 and 12), the detailed velocity field and flow discharges across the central flooded crossroad (defined on Figure 6.3) is shown on Figure 6.21. Simplifying the street topography (from run 4 to run 11) generates flooding on the whole street width, and smoothes the velocity profiles. However, the flow distribution across the crossroad is quite well preserved. A direct comparison remains delicate as the flow conditions at each street ends differ. However, considering the ratio of the southern street to the western street discharges, similar values are computed for runs 4 and 11 (31% and 28%). This ratio increases to 37 % for the run 12, but the flow conditions clearly change (inflow in the western street is divided by 2, the northern street flows in the opposite direction) so that cause of this change cannot be easily assessed.

These observations on the flow discharge distribution confirm the conclusions brought up by the laboratory experiments and numerical simulations on flows through bifurcations with sidewalks (part I): a representation of the average ground elevation around a crossroad leads to a similar prediction of the discharge distribution as a detailed representation of the topography. The simplification of the velocity field is even higher in the present case study than in the bifurcation simulations, but the impact on the flow distribution remains low. However, comparison of the run 12 with more detailed runs (run 4, run 11) shows that for the present flooding, water levels may be accurately simulated with a coarse model, whereas local velocities and flow discharges may be significantly altered.

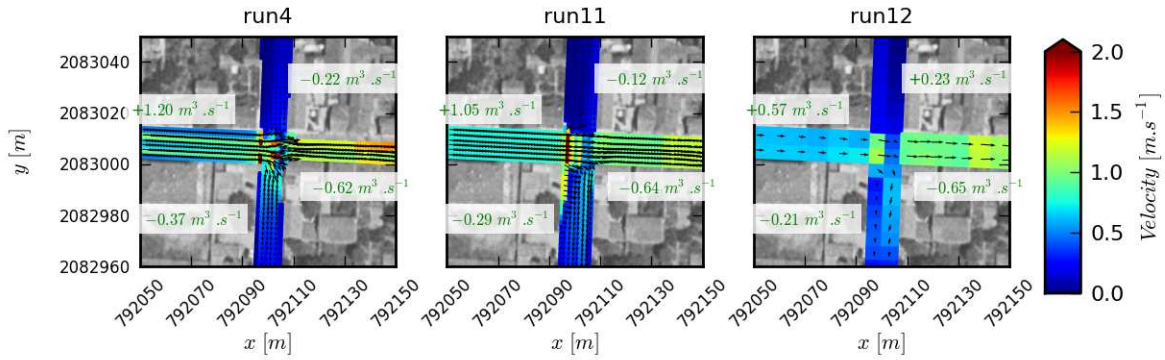

Figure 6.21 : Distribution of the flow velocities and discharges around the central crossroad for runs 4, 11 and 12. Discharges are indicated as negative when the flow goes out of the crossroad.

6.4 Validation on other past floods

Simulation results on the 2008 flood show that the present numerical model can predict fairly well the water levels in Oullins during floods of the Yzeron River, with discrepancies attributed to the modelling of the river main channel flow. Other past floods have a very similar hydrograph as the one of the 2008 flood (Figure 6.1), so that the flooding processes can be assumed to be similar. Therefore the analysis of the different numerical parameters and modelling techniques studied in the last section is not carried out here. Only parameters of the run 1 (reference) are used to model the floods of 2003, 2005 and 2009. Additionally, a run with an imposed water level time series as the upstream boundary condition is studied for the 2009 event (as run 8 in Table 6.3). Finally, the 2003 flood is simulated with both available hydrographs (due to uncertainty on the hydrograph propagation from the hydrological station to the present model, see Figure 6.10).

6.4.1 Simulation of the 2003 flood

Computed water depths for the 2003 flood are shown on Figure 6.22. Peak discharges for the hydrographs *Oullins* (propagated from the hydrological station) and *Taffignon* (measured at the hydrological station) are respectively of 76.5 $m^3.s^{-1}$ and 99.5 $m^3.s^{-1}$. Therefore the simulated water depths for the first simulation (*Oullins*) are close to the ones of the 2008 flood (Figure 6.11), which has a similar peak discharge (72 $m^3.s^{-1}$). Adequacy with recorded flood marks (Figure 6.22) for this hydrograph seems slightly better than with the hydrograph *Taffignon*. However there are only 4 flood marks, and their accuracy was questioned in the Rives project (Cemagref 2009).

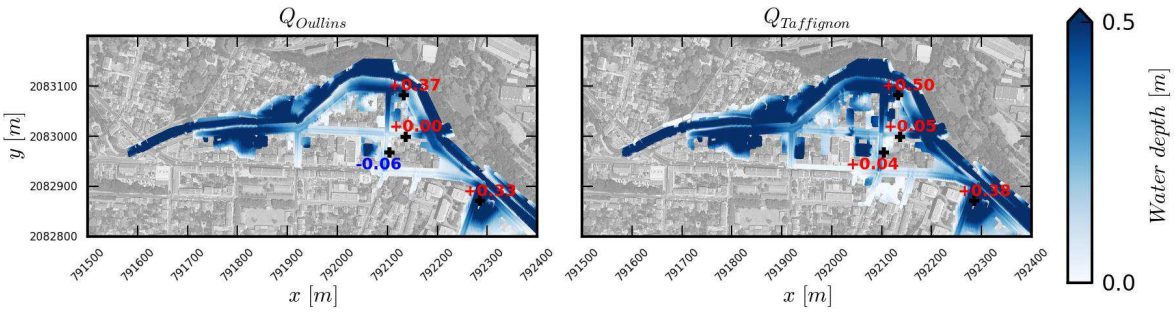

Figure 6.22: Simulated water depths at the peak time with hydrographs Oullins *and* Taffignon *for the 2003 flood, and errors on the flood marks*

6.4.2 Simulation of the 2005 flood

The 2005 flood has a peak discharge of 68 $m^3.s^{-1}$, which is close to the 2008 one (72 $m^3.s^{-1}$). Simulated water depths at the peak time are thus very similar (see Figure 6.11 and Figure 6.23). No validation data is available for this flood.

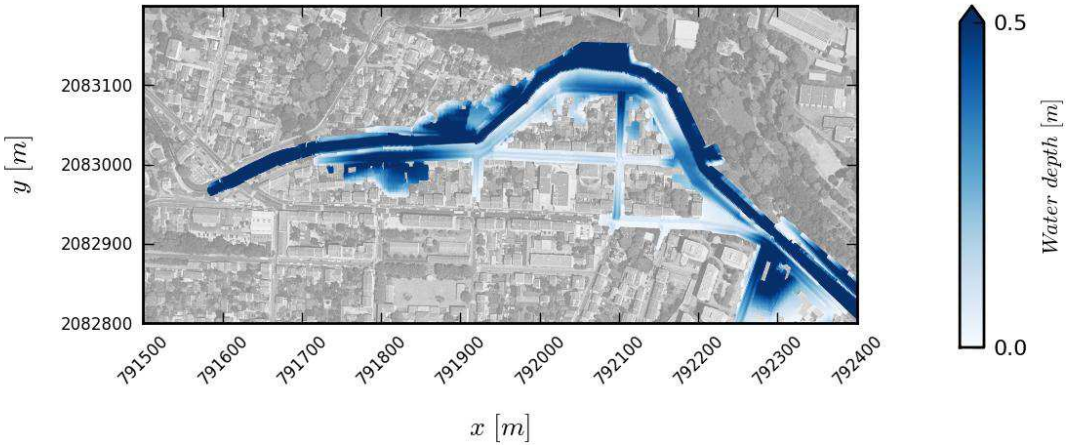

Figure 6.23 : Simulated water depths at the peak time for the 2005 flood

6.4.3 Simulation of the 2009 flood

The 2009 flood was reported to lead to only slight local overflows of the Yzeron River, so that this flood is not a real inundation event. As for the 2008 flood, water levels were recorded at 3 different points (shown on Figure 6.3). The reference simulation (run 1, with the propagated hydrograph) leads to a fair agreement with measurements (Figure 6.24), except for the computed water levels at the stage gauge L_2 around the peak time. As for the 2008 flood, water levels in this area appear to be underestimated for high discharges. This supports the remarks on the modelling of the river flow detailed in 6.3.2.

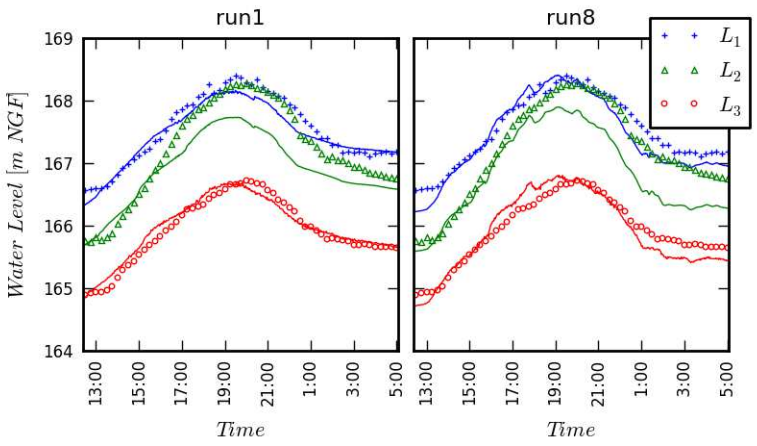

Figure 6.24 : Comparison of measured (symbols) and simulated (lines) water levels for the 2009 flood, with upstream boundary condition being either the time series of the flow discharge (run 1) or water level (run 8, as in Table 6.3)

The computed water depths at the flood peak are shown on Figure 6.25. The river overflowing appears to be very local, as it was reported after the real event. Moreover, some of the flow in the streets may have been quickly drained towards the underground drainage network, which is not considered in the present simulation.

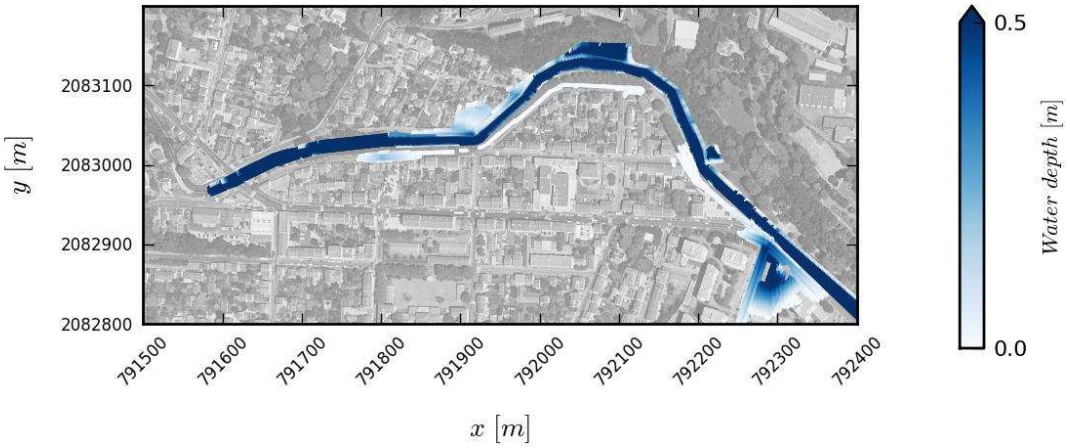

Figure 6.25 : Simulated water depths with run 1 parameters for the 2009 flood in Oullins at the peak time

Conclusion

A detailed modelling of the past flood events in Oullins has been carried out by using a 2D model to simulate the surface flows generated by floods of the Yzeron river, and neglecting interactions with the sewer network. The 2008 flood has been carefully studied, as it is a well-documented event and as it is found to be representative of other past events on the same site (see flood hydrographs on Figure 6.1). Different runs have been carried out to assess the model sensitivity to the representation of built-up areas, topography, bottom friction and mesh density. Simulation of other events partly confirms the observations made on the 2008 event, although validation data are scarce or non-existent.

Overall, inundation processes in Oullins appear to be largely dominated by the flows in the river main channel and the floodplain topography. Available topographical data permit to accurately simulate most of the water levels on the studied area, with typical errors around 15 cm (Figure 6.13). The main discrepancy lies in the estimation of local water levels upstream of the meander, where a significant part of the flooding occurs. This discrepancy is also found for the 2009 event, which barely led to flooding of the urban area. Therefore, model discrepancies are attributed to a large extent to the main channel flow modelling.

The flooding process being mainly controlled by the river water level, all representations of the urban area lead to very similar global flood extent. Storage effects of the built-up areas are negligible when compared to the floodplain flow discharge during floods of the Yzeron River. However, actual inundated areas in the urban area are extremely sensitive to the representation of structural elements defining these built-up areas (Figure 6.17). Moreover, whether walls are represented or not has a significant impact on the flow structure at the city scale, as the floodplain flows can flow or not through the built-up areas. This latter process may have significant impact when the dynamics of the flood spreading is important (which is not the case here). Presently, this type of data on vertical elements (walls, barriers…etc.) is not easy to gather, but advances in data acquisition such as terrestrial LiDAR (Sampson et al. 2012) or urban elements detection (Heo et al. 2013) may accelerate and simplify such data providing in future. The precise modelling of horizontal flow exchanges (streets / built-up areas) remains delicate (Hingray et al. 2000). However, the simple modelling used here proves to be efficient, as in our case study, water levels in built-up areas rapidly equals the ones in the surrounding streets.

The detailed representation of the streets topography is not evident, even though original topographical data used here are quite accurate (9 points cross sections, fairly describing the sharp changes in ground elevation across the street). Especially, the streets drain channels are too narrow to be correctly included in the mesh. The chosen reference solution leads to a simplification of these areas and in return to a slight overestimation of the streets capacity for low water depths. An alternative solution was tested, by specifying a unique averaged ground elevation (on the street width) at each street profile, as previously done for experimental flows (Chapter 3 and Chapter 5). This second solution increases in average the streets ground elevation of +3.0 cm, and the computed street water levels of +2.4 cm (Table 6.4). This is not negligible if compared to the effects of strongly increasing friction in the streets (+3.5cm). This solution obviously smoothes local transverse variations of flow depths and velocities across the streets. Yet, analysis of the main flooded crossroad shows that the global flow structure and distribution across the crossroad is preserved. This confirms results presented in Chapter 3, here with more complex streets profiles.

Use of a coarse mesh and a simplified topography has only a small incidence on the computed water levels. However, the velocity field may be excessively simplified (Figure 6.21). Street discharges are also impacted, though this may arise from changes in the river mesh.

Finally, this chapter has focused on the modelling of surface flows during Yzeron floods in Oullins, showing the paramount importance of the river flow. In the next chapter, exchanges between the surface flows and the sewer flows are included for the same events. Following this chapter conclusions, vertical exchanges are not expected to have significant impact on the global flooding processes. Therefore analysis will focus on the exchange modelling, based on the work presented in the part II.

Chapter 7.

Interactions between surface flows and underground pipe flows in Oullins

Inundations in Oullins arising from the Yzeron River overflows have been modelled and described in the previous chapter, by considering only the surface flows and neglecting the underground drainage system. In the present chapter, potential interactions between these surface flows and the flows in the sewer system are studied. The chapter aims at providing a description of the flows interactions that may occur on this site, with a special care towards the modelling of exchanges between the street and pipe flows, following the main results presented in the part II.

7.1 Description of the sewer system

7.1.1 Pipe network

The sewer system in Oullins is a combined sewer system, with underground drainage pipes receiving both rain and wastewaters. A large collector (roughly 2 m diameter) runs along the left bank of the Yzeron river and collects flows from a large part of the urbanized areas located upstream of the modelled area (synthetic map of the catchment is shown on Figure E.1 (Appendix E), and a local map of the detailed drainage system is shown on Figure 7.1). Therefore, this collector flows through Oullins with particularly important flow

discharges, which are generated far from the modelled area. A secondary collector is located on the right side of the river and passes through the flooded urban centre (Figure 7.1). Both collectors are linked through a connection pipe that runs beneath the bed of the Yzeron River (near the bridge at x=791600 m). The rest of the drainage system consists of smaller pipes that route urban runoff and wastewaters to the collectors.

The pipe invert levels follow fairly well the global ground topography in the area (the latter is shown on Figure 6.7), with steep slopes far from the river, and a relatively flat pipe network in the vicinity of the river. The network is densely interconnected in the south part of the city. Further downstream (eastward direction), both collectors continue to flow along the Yzeron river and then flow out in a near-by wastewater treatment plant.

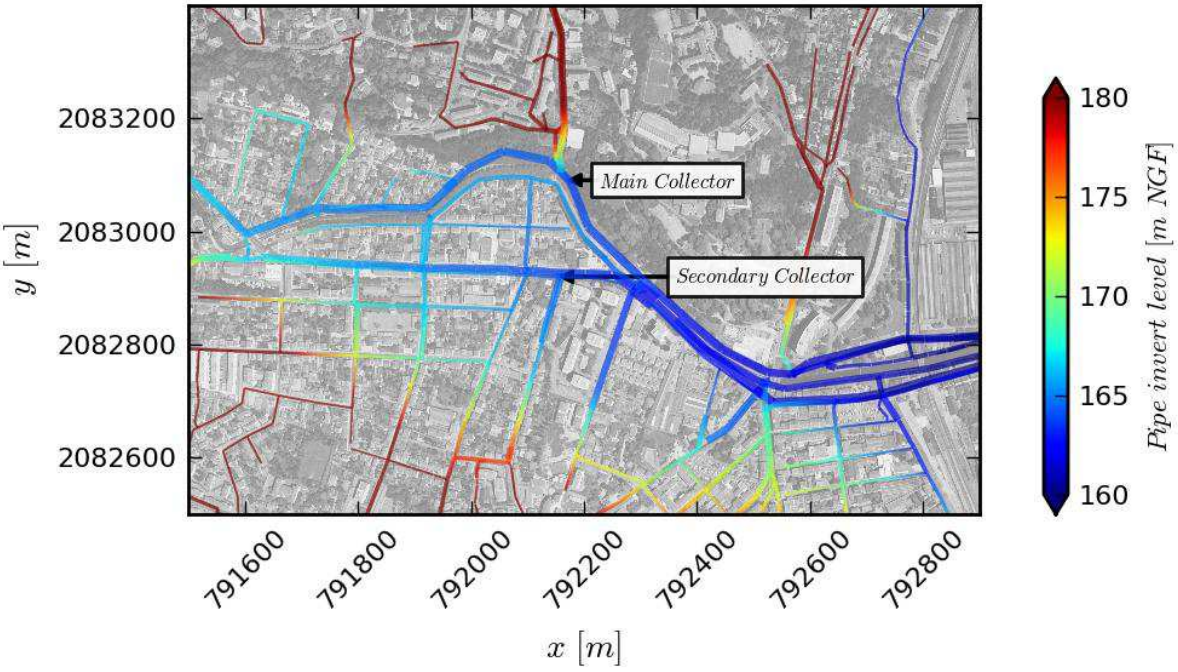

Figure 7.1 : Underground drainage network around the studied area in Oullins.

7.1.2 Exchange points with surface flows

Flow exchanges between the upper (surface) and lower (sewer) flow layers in Oullins can occur through street inlets (and associated underground exchange structures) and combined sewer overflows (CSO). These latter allow overflows from the sewer to the Yzeron River when the sewer system is surcharged. Manholes covers are all impervious in the area, so they are not considered as exchange points. This kind of structure can actually become an exchange point if the cover is removed (e.g. because of a manhole surcharge, as suggested by (Djordjevic et al. 2005)), but such a fine modelling assumption will not be considered here.

Streets inlets location and characteristics (equivalent weir width for the encountered rectangular grids and curb-opening inlets) were obtained during a field survey (Figure 7.2). From the original field survey data, 71 street inlets are included in the model, in order to cover the 2D model footprint. The spatial distribution shows that the left bank of the river (north side) has few street inlets, which indicates that the surface runoff during rainfalls is likely to flow directly into the river.

5 CSOs are located in the modelled area (Figure 7.2), on both sides of the river. Their characteristics have been provided by the Great Lyon and are reported on Table 7.1. Dimensions of these structures are relatively important, as they are connected to the main and secondary collectors.

N°	Bank	Z_{CSO} m NGF	L_{CSO} m
1	Left	166.15	0.6
2	Right	166.48	2
3	Left	166.76	1.5
4	Right	165.16	1.17
5	Right	164.46	0.5

Table 7.1 : Combined sewer overflow characteristics in Oullins: elevation Z_{CSO} and length L_{CSO} of the weir and location regarding the Yzeron River

7.2 Numerical model set-up

7.2.1 Underground drainage pipes and exchange points

The underground drainage system in Oullins is dense, highly interconnected and it has a large extent (it is actually connected to almost all urban areas in the catchment through the main collector). Modelling of the whole drainage system would be fastidious, so a simplified modelling is carried out here. We consider only the pipe network included in the 2D surface model footprint (Figure 7.2). Further simplifications are carried out, mainly by grouping adjacent pipes flowing in the same direction (for instance two parallel pipes located on both sides of a street). Grouping of pipes is carried out by considering a unique circular pipe with an equivalent flow area. This permits to eliminate complex pipe connections, for which the hydraulic behaviour is difficult to model and can lead to numerical instabilities. The left bank / right bank connection pipe is not explicitly modelled, as it includes pipes with very high slopes. Flow through this structure is modelled as a flow through an orifice, considering the

pipe diameter and length, and a threshold weir elevation governing the exchanges (formulation from Chanson 2004).

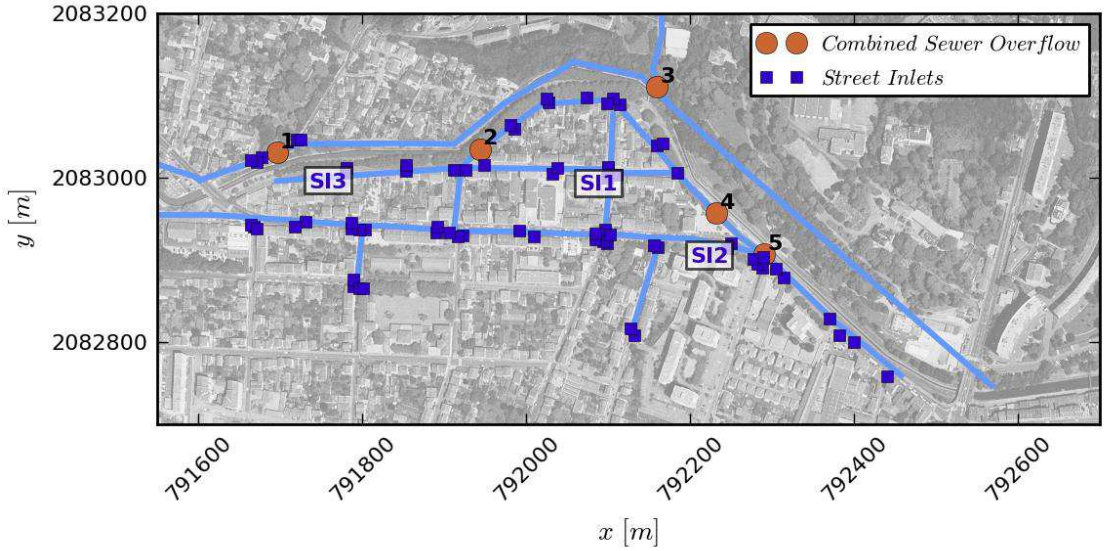

Figure 7.2 : Simplified model of the Oullins drainage system with location of exchange points with the surface flows. SI_1, SI_2 *and* SI_3 *are street inlets selected to analyze simulation results.*

7.2.2 Street/Sewer exchange modelling

An exchange structure between the streets and the underground drainage pipes is shown on Figure 7.3 (the scheme is taken from a document on CSO_2 provided by the Great Lyon). The connection between the street and the manhole is very close to the structure STR2 of section 4.6 (Figure 4.11), except for the slope of the connecting pipe. No other documents could be gathered on other exchange structures in Oullins drainage system, so it is assumed that all structures connecting street inlets to underground pipes are of the same type as the one shown here.

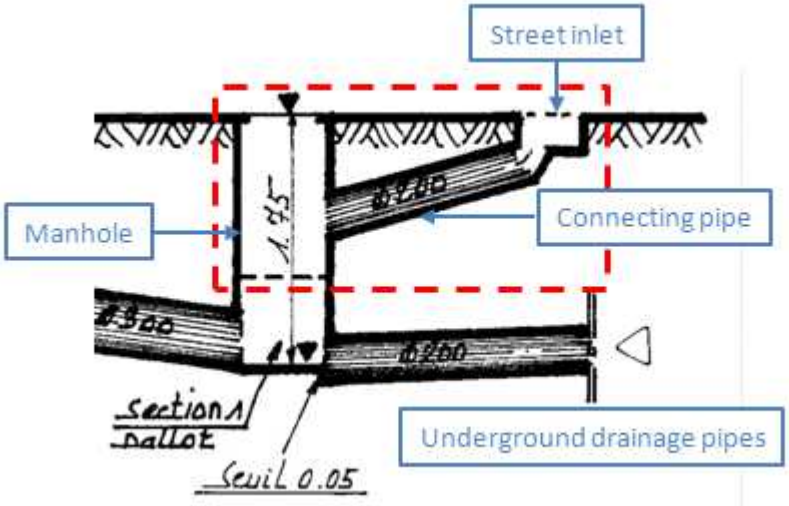

Figure 7.3 : Connection of one street inlet to the underground drainage system. The exchange structure is indicated with the dashed red line.

The exchange model developed in Chapter 4 and extrapolated to real scale exchange structures (§4.6) is used here to model flow exchanges between surface and pipe flows. The set of parameters required to define exchanges (see Figure 4.11 for a precise description) are chosen as follows:

- The drainage box area and inlet perimeter are based on field measurements (in §4.6, these parameters were conjointly defined considering a *square* drainage box of length L_{SI})
- The height of the drainage box H_{db} is set to 0.5 m. This is not an exact measurement but reflects observations on the field.
- The inlets opening ratio f_{SI} is arbitrarily fixed to 0.5 (i.e. the effective flow area through the street inlet is 50 % of the total street inlet area)
- The horizontal distance from the street inlets to the closest manhole L_{t2} is evaluated through GIS (ranging from 0.5 m to 5 m). The vertical distance L_{t1}between the drainage box bottom and the junction point with the manhole is arbitrarily fixed to 0.5 m.
- The connecting pipe diameter is fixed to 0.2 m, as described on Figure 7.3, and its roughness height equals 0.5 mm (concrete pipe)
- Weir and orifice discharge coefficients respectively equal μ_w=0.4 and μ_o=0.6. As recalled in §4.6.2, these values are standard ones for usual weirs and orifice configurations (Lencastre 1986), and remain consistent for the present application.

Actually, the main uncertainty may arise from clogging effects or other operating issues, but this will not be considered here.

When the flow is pressurized in the exchange structure, the exchange model assumes a control by the whole structure and requires an implicit computation. This method is computationally expensive, so an equivalent orifice discharge coefficient is preliminary computed (as explained in sections 4.5.3 and 4.6.3), using the following flow conditions:

- The street water level is 0.2 m above the street inlet level, and the pipe water level 2 m underneath for the computation of the drainage coefficient μ_{C3}
- The street water level is 0.2 m above the street inlet level, and the pipe water level 0.5 m above the street inlet level for the computation of the overflow coefficient μ_{C4}

This preliminary computation leads to average values of 0.51 for μ_{C3} (ranging from 0.42 to 0.57 for the different structures), and of 0.49 for μ_{C4} (ranging from 0.48 to 0.51). Variations of μ_{C3} and μ_{C4} are limited, as the only varying parameters from one exchange structure to another consist of the horizontal length of the connecting pipe and the area of the drainage box.

7.2.3 Definition of flow hydrographs

As in Chapter 6, we model here the floods of 2003, 2005, 2008 and 2009. Integration of the sewer system requires flow hydrographs for the upstream pipes (upstream boundary conditions). These flow hydrographs have not been measured and a rainfall-runoff model has been set-up to estimate them. The model transforms a rainfall measured at the centre of the Yzeron catchment into flow hydrographs at several locations in the sewer network, using a reservoir model applied to the corresponding sub-catchments. Model details are presented in Appendix E; we sum-up the main results here.

Overall, given the complexity of the hydrological processes on the catchment, an accurate estimation of the hydrographs remains delicate. The rainfall-runoff model has been calibrated against field measurements for the main and secondary collectors (discharges within the collectors have been measured with flow-meters during several months in the period 2007-2009). For both collectors, the peak time can be fairly represented. However computation of the peak discharge remains less accurate and accuracy strongly depends on the measured rainfall consistency. Indeed, a single time series of rainfall is used and the rainfall variability on the catchment is not considered.

Moreover, field measurements (see Figure E.3 in Appendix E) show that the main collector often reaches its full capacity[1],so some CSOs are likely to operate upstream of the studied area (even for common rainfall). A detailed integration of these CSOs cannot be achieved with the present rainfall-runoff model. For simplicity, we consider here that the main collector cannot accept flow discharges larger than 4 $m^3.s^{-1}$ (estimated capacity based on field data analysis). This can lead to "truncated" flow hydrographs, but should provide better estimations of the peak discharges.

Figure 7.4 presents a comparison of this rainfall-runoff model for the main collector together with the river flow hydrographs for the 4 studied recent floods (propagated hydrograph from the one measured at the hydrological station, as defined and used in §6.2.4), and recorded rainfall on the catchment. Rainfall intensities significantly differ from one event to another, with a long and not intense rainfall for the 2005 flood, shorter and more intense rainfall for 2008 and 2009 events, and a "double rainfall" event for the 2003 flood. The main collector flow hydrographs vary accordingly, with relatively short response times (typically one hour for the main collector, against 6 hours for the river). Yet, the main collector and the river main channel can simultaneously reach or exceed their capacity (respectively 4 and 50 $m^3.s^{-1}$), so that interactions between both flows may occur in both directions.

Clearly, this hydrological modelling is uncertain, and no field data are available to validate the flow hydrographs during the studied floods. Therefore, numerical simulations presented in the following section will partly be carried out to discuss effects of the surface model accuracy on the computations of exchange discharges (through comparisons of different numerical simulations). Depending on the results, analysis of the flow exchanges will be nuanced by the uncertainties on the underground drainage system flow hydrographs.

[1] This operating discrepancy has already been identified by the Great Lyon, and as a result the main collector capacity is being doubled by setting up a near-by new collector of the same size (2013)

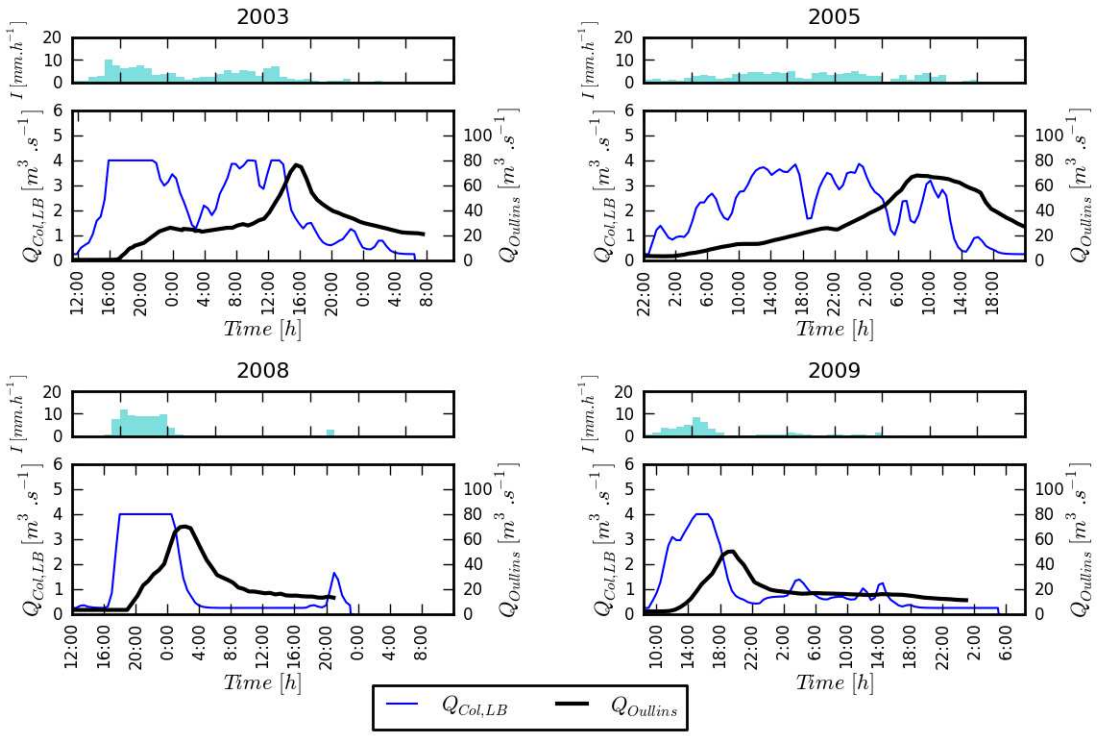

Figure 7.4 : Rainfall intensity I, *Yzeron flow discharge at Oullins* $Q_{Oullins}$ *and main collector flow hydrograph* $Q_{Col,LB}$ *just upstream of the modelled area (computed with the rainfall-runoff model) for the 4 studied flood events*

7.3 Numerical simulations

Due to computational time constraints, the coupled model (1D for the pipe network, 2D for the surface) can only be run with the coarse mesh of the surface model (mesh *m2* in §6.2.1). This comes from the need of running the coupled model with a fixed time step, which strongly penalizes the fine mesh when simulating a whole flood event. A preliminary series of simulations is carried out with the 2D model alone (§7.3.1), integrating the street inlets (simulation of the drainage process without influence of the underground pipes). This allows us to assess effects of mesh density and topography simplifications on the exchange discharges computation. For this preliminary step, only the 2008 flood is simulated, as surface flows for other floods are similar. Coupled modelling of surface and pipe flows is presented in a second step (§7.3.2), with simulations carried out for all floods.

7.3.1 Integration of street inlets in the surface flows simulations

7.3.1.1 Description of the simulations

4 runs are carried out to model exchanges from the streets to the underground drainage system, with different simplifications in the street representation (the built-up areas are not represented here : we use the model *Streets* from Chapter 6). The streets inlets elevation Z_{SI} has not been directly measured but can be derived from the measured (or interpolated) streets cross sections. Z_{SI} can be taken either as the actual street drain channel elevation ($Z_{SI,Ref}$) or as the average elevation on the street cross section ($Z_{SI,Avg}$). Parameters of the 4 runs are summed up in Table 7.2. The run *Surf1* is considered as a reference, and others runs are used to assess influence of the mesh resolution and of the topography. **Note that for runs *Surf1* and *Surf2*, the street inlets elevations are equal to the local ground elevations, which is not the case for runs *Surf3* and *Surf4* as they are based on *Avg* topography and $Z_{SI,Ref}$ street inlet elevation.** Therefore, the exchanges in the numerical simulations are computed considering water levels over the specified street inlets elevation (which corresponds to the actual street water depth for runs *Surf1* and *Surf2*, and to a fictive one for runs*Surf3* and *Surf4*). Aim of runs *Surf2* and *Surf3* is to assess which street inlet elevation should be used when the model topography is simplified. Aim of the run *Surf4* is to assess influence of the mesh resolution.

Other parameters (bottom friction and boundary conditions) equal the ones of the reference surface run of the Chapter 6 (run 1 in Table 6.3). All runs are carried out for the 2008 flood only.

Run	Mesh	Street topography	Street inlet elevation
Surf1	m1	*Ref*	$Z_{SI,Ref}$
Surf2	m1	*Avg*	$Z_{SI,Avg}$
Surf3	m1	*Avg*	$Z_{SI,Ref}$
Surf4	m2	*Avg*	$Z_{SI,Ref}$

Table 7.2 : Description of the runs carried out with the surface model only including drainage through streets inlets

7.3.1.2 Analysis of the exchanges

In this series of simulations, streets inlets can drain flows out of the 2D surface model, without interaction with the pipes underneath. Therefore, “exchange discharges” always correspond to drained discharges, and the latter are taken as the minimum allowed between

the street inlet capacity and the upper part of the connecting pipe underneath (respectively control sections C1 and C2 of the exchange model, see set-up of the latter in §4.6).

Figure 7.5 shows the time evolution of the surface water level Z_s, water depth h_s and exchange discharge Q_{ex} for 3 selected street inlets (SI_1, SI_2 and SI_3 on Figure 7.2). The water depths significantly vary from one inlet to another, and this has a strong impact on the agreement between the different runs (defined in Table 7.2). For low water depths (street inlet SI_1), the exchange discharge is controlled by C1 (weir equation applied to the *water level* over the specified street inlet elevation). The computed exchange discharge is then extremely sensitive to the local water depth, which relative variations are important from one run to another (because of changes in both the local topography and surrounding flow characteristics). For the street inlet SI_2, the water level in the street around the peak time is quite similar for the 4 runs. In this case, the local water depth *used for the exchange discharge computation* (actual or fictive) is similar for runs *Surf1*, *Surf3* and *Surf4*, hence very similar computed exchange discharges. The computed exchange discharge for run *Surf2*is smaller, as in this run the street elevation differs ($Z_{SI,Avg}$). Yet, for these water depths (slightly larger than the ones ofSI_1), the exchange discharge is controlled by C2 (orifice equation applied to the *water level over the drainage box bottom elevation*, located at H_{db}=0.5 m below the street inlet elevation). This formulation is less sensitive to the water depth variations, which explains why the computed exchange discharge for run *Surf2* is only slightly overestimated. This analysis is globally verified for the street inlet SI_3. However, the water depths for SI_3 being quite large, differences in the computed exchange discharge between run *Surf2* and other runs become very small.

Switch from C1 to C2 control sections will depend on the size of the street inlets. Comparing results of the three presented street inlets SI_1, SI_2 and SI_3, the transition seems to occur for local street water depths around 10 cm. This value is consistent with results of the sensitivity analysis carried out on the exchange model parameters in §4.6.4 (a transition at Z_{C1}=9 cm was found for a connecting pipe diameter of 25 cm, see Table 4.6).

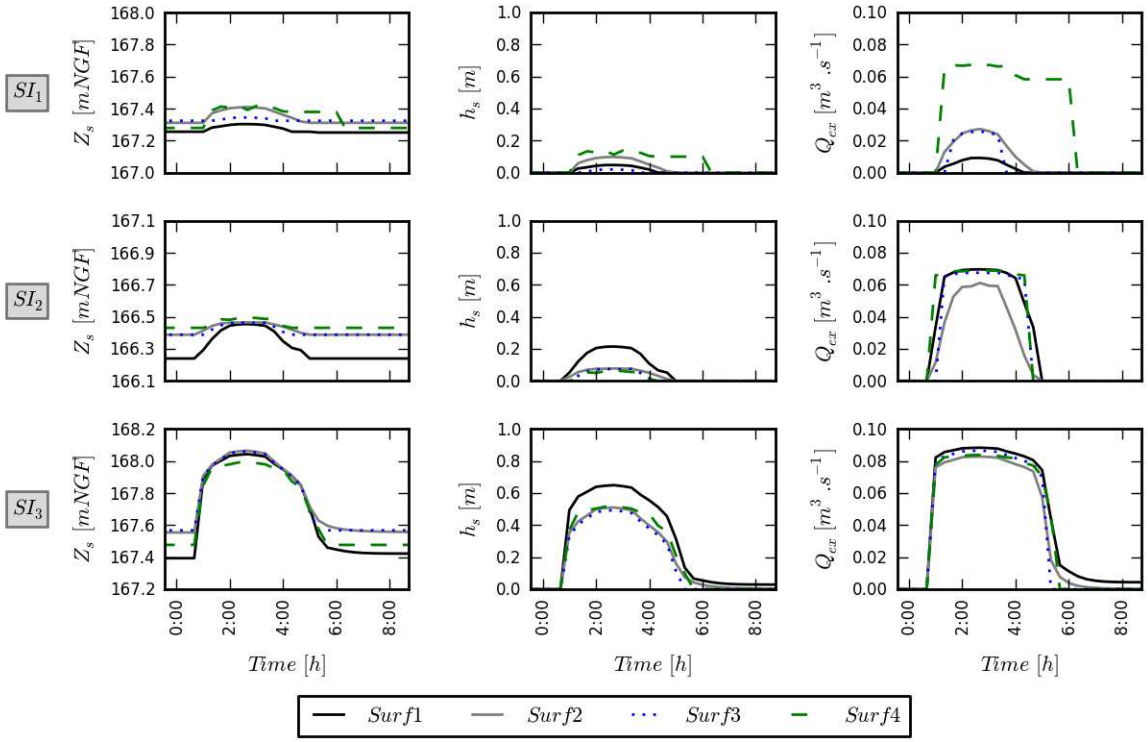

Figure 7.5 : Time-evolution of the water levels Z_s*, water depths* h_s *and drained discharges* Q_{ex} *at the streets inlets* SI_1*,* SI_2 *and* SI_3 *(defined on Figure 7.2), for runs* Surf1 *to* Surf4 *(2008 flood)*

At the scale of the flooded area, the global exchange discharge $Q_{ex,total}$ (sum of all local exchange discharges) simulated with the 4 runs shows similar differences as for the street inlets SI_2 and SI_3 (Figure 7.6). We can observe that, globally:

- Specifying the real street inlet elevation $Z_{SI,Ref}$ while using a simplified street topography *Avg* (run *Surf3*) leads to very similar global results as the detailed run (*Surf1*).
- For the same topography and inlet elevation but using the coarse mesh (run *Surf4*), the total exchange discharge is slightly overestimated (+ 10% at the peak when compared to run *Surf1*). As the water levels computed with the coarse mesh are globally close to the ones computed with the fine mesh (as seen in Chapter 6, see results of run 12 in Table 6.4), this bias can be attributed to discrepancies when computing local low water depths (as for the street inlet SI_1 in Figure 7.5).
- The run *Surf2* globally underestimates the exchange discharge (- 11% at the peak time), due to the systematically too large street inlet elevations.

These results point out the difficulty to model fine exchange discharges (such as SI_1 on Figure 7.5) with the accuracy of an operational surface flow model. Now, for this specific case study, the typical street water depths are high enough to globally reduce errors and even

allow simplifications in the surface representation. It then appears reasonable to use the coarse mesh surface model (*Surf4*) within the 1D/2D model.

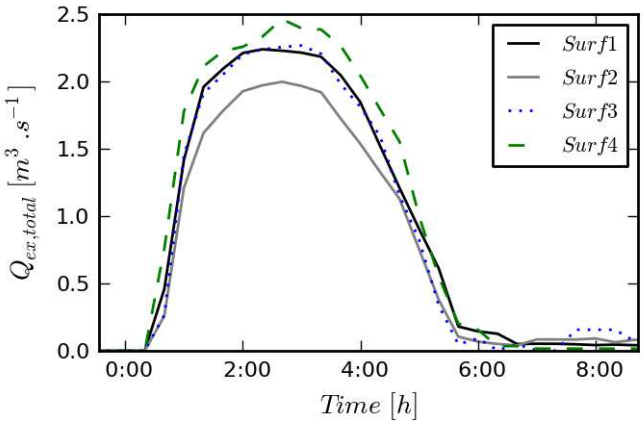

Figure 7.6 : Total exchange discharge computed with runs Surf1 *to* Surf4

7.3.1.3 Influence of exchanges on surface flows

On Figure 7.7, maximum water levels simulated with run *Surf1* are compared to the ones simulated with an equivalent run without street inlets (run 12 in Table 6.3). Effects are globally limited, the average decrease of water level in the street network being 1.7 cm (and 1.9 cm when including the river). However, the water level can locally be lowered by more than 5 cm, especially in the streets relatively far from the river. The water level in the river is only slightly affected in the upstream part, whereas it decreases of more than 5 cm downstream, as a part of the floodplain flow does not flow back towards the main channel (as it reaches the underground pipe network). This impact is of the same order of magnitude as the one observed for simulations without street inlets but with different assumptions in the surface model (Chapter 6, see values of $\Delta Z_{s,street}$ in Table 6.4). This simulated impact of the drainage process on the surface flows can be considered as a maximum, as no limitation by the underground pipes is considered.

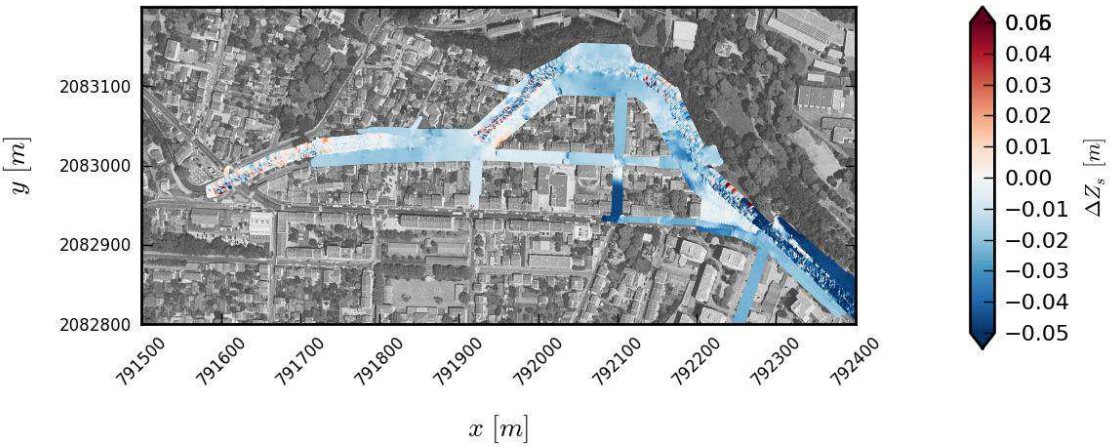

Figure 7.7 : Evolution of the simulated maximum water levels when introducing street inlets in the surface model (difference between Surf1 *of Table 7.2 and run 4 of Table 6.3)*

7.3.2 Coupled modelling of interactions between surface and pipe flows

Excepted for low water depths, the use of the coarse mesh surface model appears to predict similar exchange discharges as the model with the fine mesh and accurate topography. Results of a coupled model 1D/2D are presented below, considering the run *Surf4* for the surface flow, the underground drainage system model presented in §7.2 (pipes network, flow hydrographs and exchanges modelling). The pipes friction is modelled using a Strickler coefficient of 60 $m^{1/3}.s^{-1}$, and the downstream condition for both collectors is set to a uniform regime (considering the average downstream slopes of the collectors invert levels, collectors geometry and the assigned Strickler coefficient).

7.3.2.1 Detailed analysis of the 2008 flood

Integration of the underground drainage system within the numerical simulations permits to study both its impact on the exchanges through the street inlets and its interactions with the river through the CSOs. Simulation results show that the CSO_1 operates from the sewer to the river during the 2008 flood, whereas pipes water levels at the other CSOs do not threshold overflows. Note that flows from the river to the sewer through the CSOs are not allowed in the simulations, to account for the presence of check valves on the field. The Figure 7.8 shows the exchanges at CSO_1 and their impact on the exchanges between the left and right bank collectors (respectively referred as *Col,LB* and *Col,RB*). As the flow propagates in the left bank collector, the water level $Z_{Col,LB}$ rises and reaches the CSO_1 weir

crest elevation. A part of the collector flow discharge is diverted into the river (Q_{CSO1}), without influence of the water level in the latter. The collector hydrograph shape (see Figure 7.4) and the low water level in the river imply a stabilization of the flows (i.e. $Z_{Col,LB}$ and Q_{CSO1}) during 2 hours. Then, as the flood propagates in the river, the river water level Z_{Yzeron} rises and starts limiting overflows at CSO_1, leading to a sudden rise of the left bank collector water level. This rise thresholds overflows from the left bank collector to the right bank collector upstream of CSO_1 ($Q_{LB\text{-}RB}$ on the left part of Figure 7.8). Finally, as the input discharges in the drainage system decrease, collectors' water levels $Z_{Col,LB}$ and $Z_{Col,RB}$ rapidly decrease, and flow exchanges stop. The surface flood keeps flowing in the river, without impacting the pipe flows at these particular points.

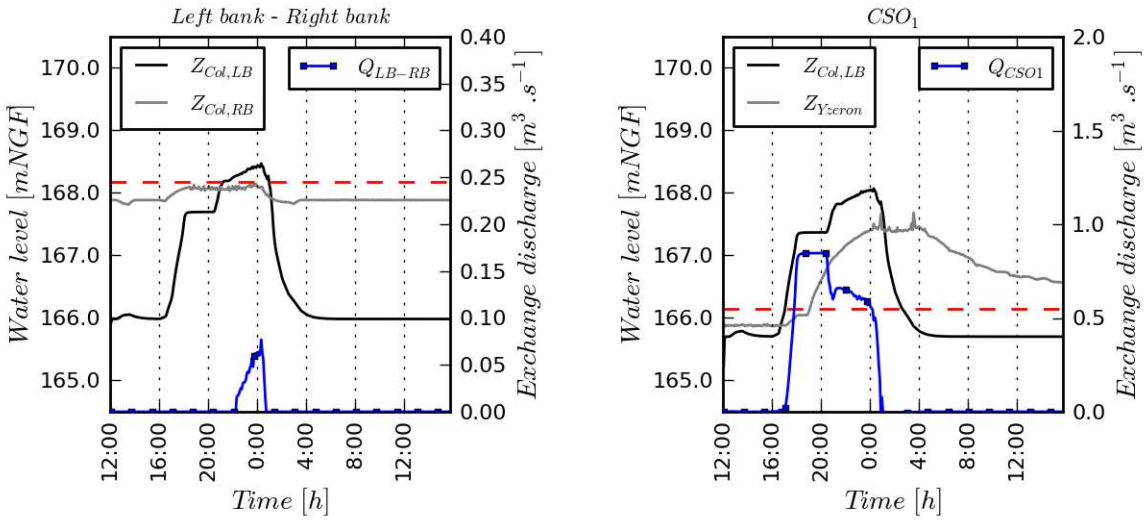

Figure 7.8 : Flow exchanges between the left and right bank collectors (left) and between the left bank collector and the Yzeron River at CSO_1 *(right). Water levels simulated on each side of the exchange structures are indicated in plain lines (*$Z_{Col,LB}$*,* $Z_{Col,RB}$ *and* Z_{Yzeron}*), and the exchange structure weir crest elevation is plotted in dash. Exchanges discharges* $Q_{LB\text{-}RB}$ *and* Q_{CSO1} *are defined positive from the left bank collector to respectively the right bank collector and the river.*

This analysis actually shows the discrepancies of the underground drainage system. The rainfall that generates the 2008 flood is rather long but non intense (around 70 mm in 6 hours, quite uniformly distributed in time, as shown on Figure 7.4). This rainfall generates low water levels in the right bank collector but totally surcharges the left bank collector, with important overflow towards the river (at CSO_1), and even flow exchanges from the left bank to the right bank collector (whereas the corresponding exchange structure is designed to operate in the opposite way). The exchange discharges remain limited (when compared to the river discharge or the right bank collector capacity), so that this drainage system discrepancy has

overall no significant impact. Yet, this type of interactions clearly shows the benefits of a 1D/2D model for such a complex urban drainage system.

Now, simulations results show that integration of the sewer system has an impact on the flow exchanges in the flooded area. Figure 7.9 shows the total exchange discharge $Q_{ex,total}$ from the street network to the underground drainage pipes for simulations with (present simulation, named *Surf4-Pipe*) and without (run *Surf4* of §7.3.1) integration of the underground drainage pipes. Integration of the underground pipes leads to a decrease of 26 % of the maximum total exchange discharge. Part of exchange discharges computed with the C2 control in the run *Surf4* (exchange flow controlled at the connecting pipe top) passes to C3 exchange discharges (pressurized exchange flow through the whole exchange structure, with a "downstream control" by the pipe water level) in the run *Surf4-Pipe*, which clearly explains the decrease of the total exchange discharge (Figure 7.9). The control C1 is mainly effective at the beginning and the end of the street flooding, when some local water depths are low (i.e. at both ends of the $Q_{ex,total}$ hydrograph).

Overflows (control C4, with negative discharges on Figure 7.9) are computed by the run *Surf4-Pipe*, but analysis of simulation results suggests that this is not realistic. Indeed, the overflows occur from a unique small straight pipe draining a flat area in the right bank (see Figure 7.10). This pipe has a small conveyance capacity, but the upstream flow hydrograph (upstream boundary condition) may not be adapted, as flows exceeding the pipe capacity should not actually enter the pipe. This discrepancy comes from the simplifications in the hydrological inputs (delineation of urban catchments is rather raw, see Appendix E.3.3), and from the separation of the runoff generation from the hydraulic modelling. Except for that particular drainage pipe, no overflow is computed in the coupled simulation *Surf4-Pipe*. This suggests that adding flows drained from the flooded streets to initial pipe flows (hydrological inputs) does not surcharge the underground drainage system.

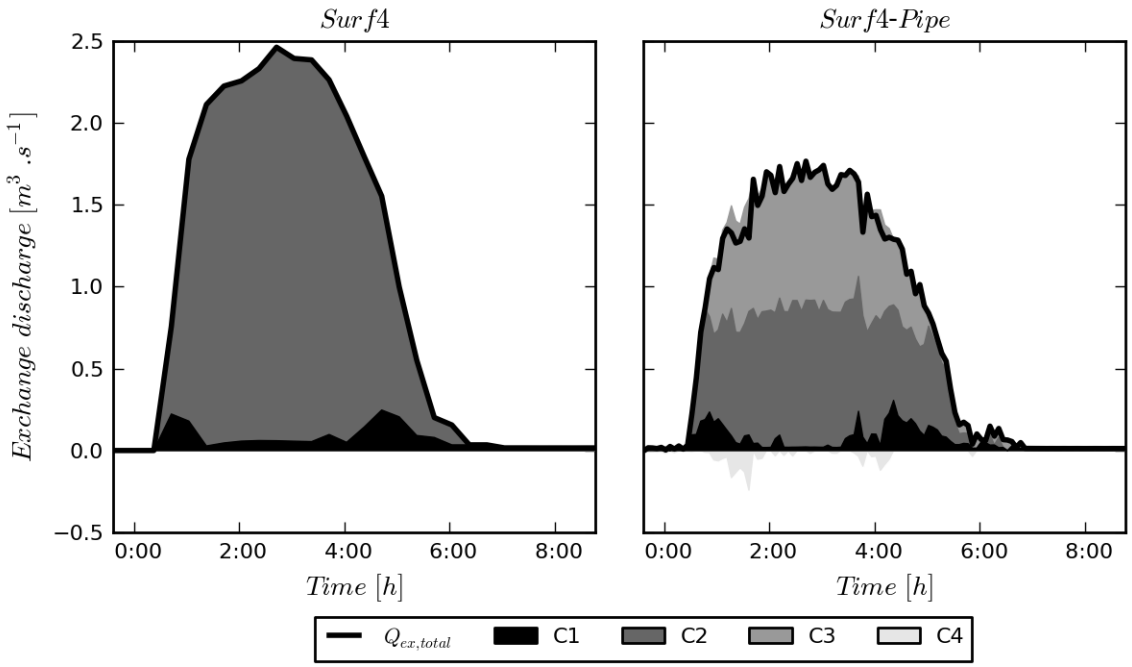

Figure 7.9 : Total exchange discharge $Q_{ex,total}$ *and part of the drainage (C1, C2 and C3) and overflow (C4) discharges computed by the different control sections for the simulations of the 2008 flood, with the surface model only (*Surf4*), and with integration of the underground pipes (run* Surf4-Pipe*)*

The spatial distribution of the control sections defining local exchange discharges is quite well correlated with local pipe pressurizations (see Figure 7.10). A pattern of the exchanges can be identified at the scale of the flooded area (extent of the latter can be seen for *run12* on Figure 6.19). The drainage process is controlled by the underground pipes capacity in the centre of the right bank flooded area (y>2083000 m in Figure 7.10), the street water depths being quite large, and the drainage pipes having relatively small capacities. This leads to a global pressurization of the underground pipe flows and a limitation of the exchanges (control C3). Oppositely, exchanges discharges along the right bank collector are controlled by the exchange structures capacity themselves (controls C1 and C2), the street water depths beings lower, and the collector capacity much larger. No exchanges with the streets occur on the left bank, the few street inlets (shown on Figure 7.2) being not flooded.

Therefore, all the water drained from the streets reaches the secondary collector (right bank). Although this additional discharge can be important (maximum value of 1.77 $m^3.s^{-1}$), the right bank collector is never surcharged, so that incoming flows from the southern urban catchments do not lead to local overflows when reaching this collector. As a conclusion, for the 2008 flood, interactions between the flows in the river and in the underground drainage system truly exist, but they do not increase flood hazard.

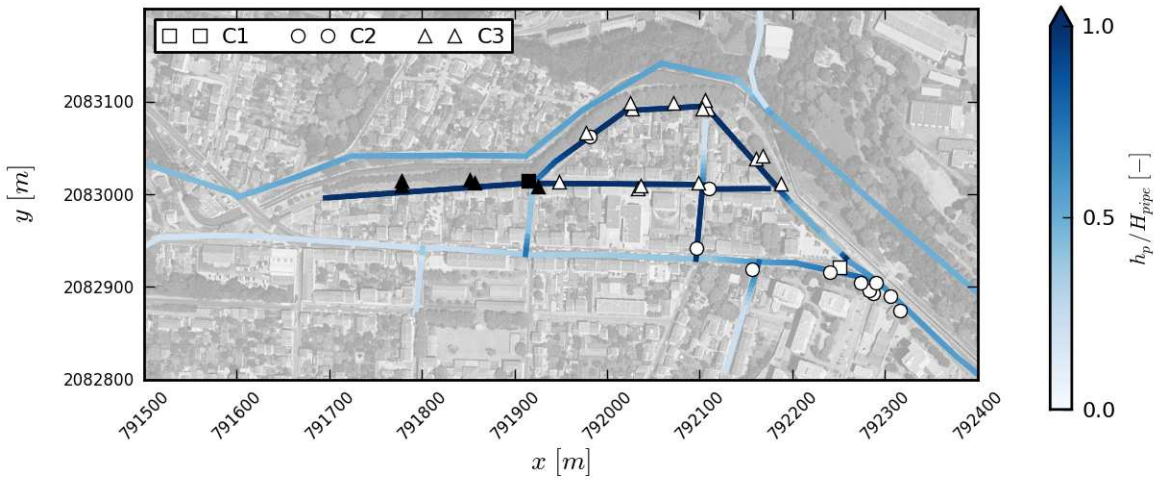

Figure 7.10 : Pipe water depths (or equivalent relative pressure) normalized by the pipe height h_p/H_{pipe}*, and control section at the operating exchange structure at the river flood peak time for run* Surf4-Pipe*. Black-filled symbols indicate that overflow occured at the corresponding exchange structures during the simulation time*

7.3.2.2 Recapitulation on the 4 recent floods

The 3 other recent floods (2003, 2005 and 2009) have been simulated with the same 1D/2D model and numerical parameters as the 2008 flood, and the corresponding inflow sewer hydrographs presented on Figure 7.4. For these 3 floods, the nature of exchanges between the underground drainage pipes, the river and the streets is the same as for the 2008 flood, only the timing and the importance of the exchanges vary. In particular, the following processes previously described for the 2008 flood occur (not shown in details herein, as it does not change qualitatively):

- the sewer overflow device CSO_1 operates, as the discharges in the left bank collector remain important for all floods
- flow exchanges between the left bank collector and the right bank collector remain low (2003), or become even null (2005,2009)
- there is no overflow from the underground pipes to the streets, except for the already mentioned (§7.3.2.1)) low-capacity pipe for which hydrological inputs may not be relevant

To summarize the exchange processes for the 4 recent floods, the flow discharge at the downstream end of the right bank collector $Q_{Col,RB}$ is analysed (Figure 7.11), by computing the respective parts of the 3 potential discharge sources:

- hydrological inputs Q_{input} (sum of all right bank pipes upstream flow hydrographs)

- flow discharge arriving from the left bank collector $Q_{LB\text{-}RB}$
- total exchange discharge with the streets $Q_{ex,total}$

No time shift is considered between these 3 sources. Yet, under this assumption, analysis of the downstream right bank collector flow hydrograph is consistent (i.e. $Q_{Col,RB}(t) \approx Q_{input}(t) + Q_{LB\text{-}RB}(t) + Q_{ex,total}(t)$), and several observations can be made concerning the operation of this collector during recent river floods.

First, the final shape of the outflow hydrograph $Q_{Col,RB}$ significantly differs from one event to another, reflecting the various initial hydrological events that generate these floods (see rainfall on Figure 7.4). The relatively shorter and more intense rainfall for 2008 and the "double rainfall" of 2003 lead to flooding in the streets (indicated by non-null values of $Q_{ex,total}$ on Figure 7.11) while the underground drainage pipe flows are still important. This timing also means that for these two floods, the river and the main collector (left bank) can simultaneously reach high water levels/pressure, leading to flow exchanges from the left bank to the right bank collectors ($Q_{LB\text{-}RB}>0$). Oppositely, floods of 2005 and 2009 lead to street flooding while input discharges in the drainage pipes are relatively low, so that the former interaction is not simulated ($Q_{LB\text{-}RB}=0$). However, note that for the 4 floods the "worst-case" scenario is always avoided, as the underground and surface flows peak times are always separated by a few hours.

Then, we have seen the similarity of the street flooding for the floods of 2003, 2005 and 2008 (Chapter 6). As a result, the total exchange discharges $Q_{ex,total}$ between the streets and the underground pipes are quite similar for these 3 events. Although the upstream pipe flow hydrographs slightly differ (Q_{input}), this has no strong impact on the exchanges with the street, which indicate that the saturated parts of the underground drainage network are rather saturated by the on-going exchanges with the street than by the initial input hydrograph. During the 2009 flood, the river only slightly overflows in the city centre, so that flows drained from the streets to the underground pipes are limited.

Finally, as it was described for the 2008 flood, the maximum flow discharge in the right bank collector is severely impacted by the exchanges with the street, yet without reaching its capacity (estimated to 4 $m^3.s^{-1}$). This implies that *i)* the exchange discharges with the streets are locally controlled, by the corresponding exchange structure capacity or the local underground drainage pipe capacity (with only little influence of the right bank collector water level) and *ii)* the runoff collected by the southern urban catchments can be routed into

the right bank collector as in usual operating conditions (no surcharge of this collector at the junction points with the southern drainage pipes).

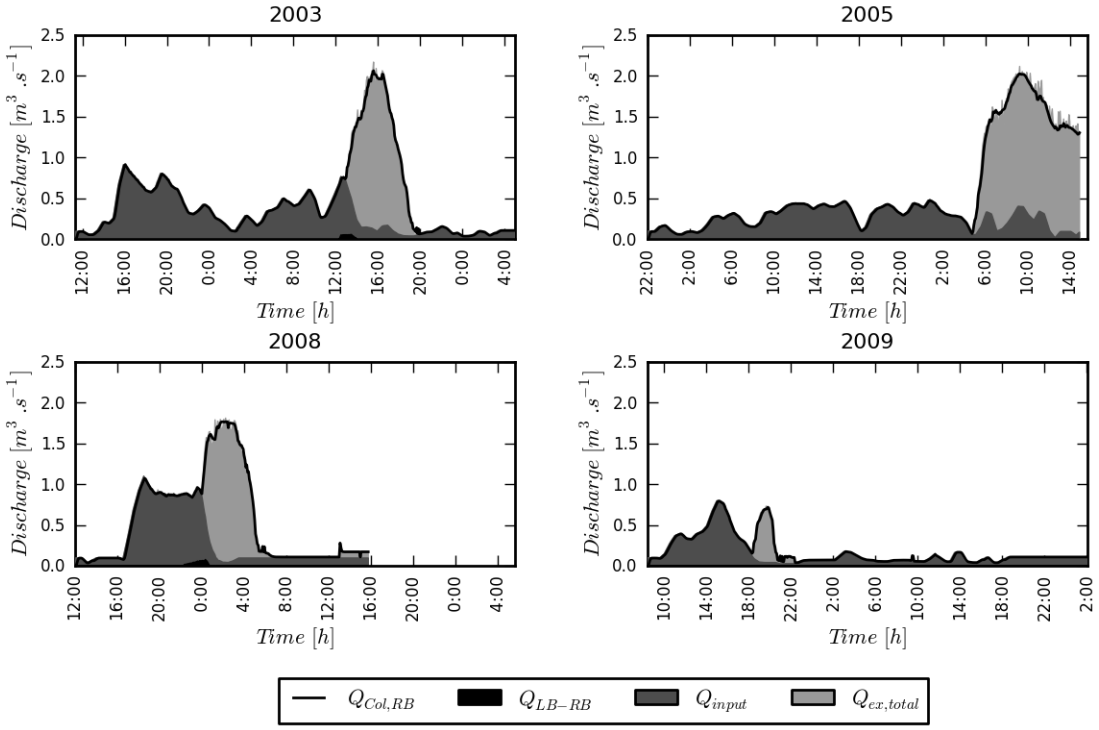

Figure 7.11 : Simulated flow discharge $Q_{Col,RB}$ *at the downstream end of the right bank collector during the recent floods in Oullins, and proportion of hydrological inputs* Q_{input}*, exchanges with the left bank collector* Q_{LB-RB} *and with the streets* $Q_{ex,total}$

Conclusion

In this chapter, interactions between surface flows in the streets or the Yzeron River and the pipe flows in the underground drainage system in Oullins have been studied through numerical simulations. Simulation methodology presented here is based on the exchange model developed in Chapter 4, and the 1D/2D model validated in Chapter 5. Results of this chapter point out some general difficulties about these two key points inherent to the modelling of real flood cases. In parallel, they allow a more accurate description of the flows during floods in Oullins.

In a first step, simulations of the 2008 flood surface flows alone have been carried out to define the best way to implement the exchange model when using a coarse mesh and a rough topography in the surface, by comparing with a reference run with fine mesh and accurate topography. It appears that for our case specifying the actual street inlet elevation in models

with simplified topographies lead to similar results as the reference ones (Figure 7.6), provided that exchange discharges are not computed with the actual street water depth, but with a fictive water depth taken as the water level over the specified street inlet elevation. This result was expected, as Chapter 6 proved that computed street water levels exhibit low relative variations amongst runs with different meshes and street topographies. However, for low water depths (case of the street inlet SI_1 on Figure 7.5), these variations can strongly impact the computed exchange discharges. Indeed, the exchange model is very sensitive for low water depths (use of a weir equation applied on the street inlet contour). In this case, none of the simplified runs is in agreement with the reference one, pointing out the necessity of using such modelling details for usual urban drainage studies. Such exchange conditions (low street water depths) are yet not strongly encountered for the studied flood, so that even the most simplified simulation is globally in fair agreement with the detailed one.

The second step consisted in setting-up an underground pipe network model and coupling it to a simplified surface model (coarse mesh, simplified streets topography), to fully investigate flow interactions in Oullins. The 4 studied floods lead to the same qualitative conclusions, so we quote here the results of the 2008 flood simulation, as it was more accurately described.

The main consequence of including the drainage pipes for this flood is that the drainage process in the streets can be locally reduced due to the conveyance capacity of some underground drainage pipes (occurrence of the exchange model control section C3 in Figure 7.9). This limitation itself is important, as the maximum total drained discharge is then lowered by 26%. More qualitatively, simulation results show the existence of 3 different areas regarding these exchange processes in the flooded areas: i) a left bank with actually no interaction between the streets and the main collector (as no exchange structure is located in the flooded area), ii) a network of small drainage pipes which capacities limit the local drainage processes from the flooded streets above, and iii) two streets directly drained into the right bank collector, without influence of the water levels in the latter, as its capacity is not reached.

The simulated impact of the underground drainage system on the surface flows remains overall limited. First, the partial saturation of the right bank drainage system does not extend to the right bank collector, its capacity being much larger than the ones of the surrounding pipes. As a result, incoming flows from the southern urban catchments are not blocked when reaching this collector, so there is no overflow from the underground pipes to the surface. From a flood risk perspective, the only impact observed in the simulations is the decrease of

the water depths in the street network and in the river downstream from the flooded area, as a result of the global drainage effect. This does not change conclusions brought up in Chapter 6 on the paramount importance of the river main channel flow on the flooding processes in Oullins. Yet it is worth noticing that effect of the drainage process on the street water depths is of similar order of magnitude as the one due to the uncertainties on the street bottom friction or the modelling assumptions on the urban area structural elements.

Besides these results on the exchanges with the street, the detailed analysis of the 2008 flood shows an interesting example of river / urban drainage system interactions. Simulations suggest that the river water level during floods can limit the operation of a sewer overflow device and lead to unusual flow exchanges from the main collector to the secondary collector (left bank to right bank exchanges, shown on Figure 7.8). This phenomenon is also simulated for the 2003 flood but it does not occur for other floods (2005, 2009), pointing out the importance of the initial hydrological event characteristics (and corresponding shapes of the river and pipe flow hydrographs).

Finally, simulations presented in this chapter require many hydrological inputs and numerical parameters, which could not always be validated. Modelling of the surface flows can be considered as validated, considering results of the previous chapter. Similarly, the exchange model used to compute exchange discharges between the streets and the underground pipes has been developed and at least partly validated for exchange structures similar as the ones found in Oullins. The main uncertainty lies in the estimation of the upstream flow hydrographs (hydrological modelling) and in the parameterization (friction, downstream conditions) of the underground drainage system model. We can assume that this uncertainty hardly affects the results on the right bank pipes (the input discharges for the studied events being overall low when compared to the drained discharges in the flooded streets). However, the uncertainty regarding the main collector hydrograph may have higher impact. For instance, larger inflow peak discharges would lead to larger discharges diverted into the secondary collector or the operation of other sewer overflow devices. Therefore, we conclude that the 1D/2D model used here can simulate several types of flow interactions and gives an order of magnitude of the importance of exchange flows during floods in Oullins. A finer analysis should be supported by a more accurate modelling of the hydrological processes upstream of the modelled area. Such a detailed modelling would also permit to simulate scenarios of intense rainfall events and eventually assess the risk of combined pluvial and fluvial flooding on this site.

General conclusion and perspectives

This thesis aimed at studying the detailed modelling of flows during urban floods. Especially, impacts of topographical singularities and of exchanges with the sewer system on surface flows were addressed.

The first part of the thesis focused on the experimental characterization of small-scale obstacles impacts on flows through urban crossroads (Chapter 2), and on the possibility of using a 2D hydrodynamic flow model to simulate such flows (Chapter 3). In the second part, interactions between a flooded street and an underground drainage pipe were experimentally studied, notably leading to the development of an exchange model (Chapter 4). This exchange model was integrated in a 1D/2D hydrodynamic model, in order to achieve complete simulations of these experimental flows (Chapter 5). The third part was dedicated to the numerical modelling of an urban flood field case, detailing effects of the surface representation (Chapter 6), then analysing flows interactions based on the developed exchange model and the 1D/2D model (Chapter 7). Finally, the problem of street topography representation into numerical models was addressed through the entire thesis, in order to develop different points of view about this modelling question.

In the following, main results of these different parts are synthesized. Then some perspectives are proposed, considering the present conclusions and recent literature results.

General conclusion

Integration of structural elements in urban flood models

Three types of urban structural elements affecting surface flows have been studied in this thesis: generic small obstacles in Chapter 2 and Chapter 3 (representing pieces of urban furniture), as well as buildings and fine vertical elements (walls, barriers) in Chapter 6. Let us consider results of chapters Chapter 2 and Chapter 3. Even with a relatively small size (1/6 of a street width, which is about 1-2 m), an obstacle located in the street network can have a significant impact on the surface flow: local acceleration, additional head loss, and above all a potential change in the discharge distribution if the obstacle is located near a crossroad. **In the range of the studied flow configurations, effects of these small-scale obstacles are judged important enough to be included within urban flood models.** Further analysis shows the importance of the flow characteristics and of the obstacles location on these effects, so that modelling the latter implies an explicit modelling with a hydrodynamic model.

Numerical modelling of these experimental flows with obstacles using a code solving the two-dimensional shallow water equations exhibits accurate results (Chapter 3). Looking at the discharge distribution and upstream channel water depth, **most of the obstacles effects can be fairly simulated using a relatively coarse mesh, specifying the obstacle as an impervious area and neglecting turbulence effects. Such modelling in a real case would reduce uncertainties related to the streets bottom friction** (implicit consideration of the head losses generated by the obstacle), **and improve the flood hazard estimation** (local velocities and global street discharges). In our case, a finer modelling (using a 10 times denser mesh) did not significantly improve simulations. Actually, such fine modelling should be associated to a more adequate modelling of the turbulence effects, and even finer meshes. Now, **the potential gain of using finer meshes and more accurate turbulence models cannot justify the corresponding increased computational efforts**, so that for now, such approach remains out of the operational urban flood models framework. Finally, accurate simulations of flows with obstacles can be attributed to the subcritical regime of the flows considered in Chapter 3. The presence of fully or transitional supercritical regime would lead to higher errors (Mignot et al. 2008; El Kadi Abderrezzak et al. 2011). In parallel, experimental results have shown that for all obstacles, effects were enhanced for flows with higher inertia (high Froude numbers). Therefore, we must keep in mind that **these results and recommendations are limited to subcritical flows. The case of supercritical flows seems**

both promising and delicate to study. This would require a better modelling of supercritical and transcritical flow divisions through bifurcations.

Integration of large-scale structural elements (buildings, walls) in an urban flood model has been studied during the modelling of floods in Oullins (Chapter 7). Overall, these elements have no impact on the global flood extent, as the built-up areas storage capacity is negligible when compared to the flow discharge passing through the floodplain. This conclusion should stand for any similar field case (river flooding in a narrow floodplain). Now, walls have a paramount importance when defining actual inundated areas, which is the base of flood risk estimation. Actually, **for such type of urban area** (individual houses and gardens grouped into built-up areas blocks, and separated by many walls), **the walls have a stronger impact than the buildings**. Indeed, the latter are mostly in high-friction areas and surrounded by "independent" walls, so that their impact on the surface flows is limited.

Moreover, **the flow structure at the scale of the street network can change depending on whether or not flows through the built-up areas blocks are computed.** This can indeed modify the flow discharge in the streets, which is a key variable for flood risk estimation. Similarly, this could impact the flood extent if the surface flow dynamics in the urban area controls at least partly the flooding process.

Integrating buildings in urban flood models has become a standard practice, notably leading to the development of automatic methods for mesh generation (e.g. Schubert et al. 2008; Tsubaki and Fujita 2010). Buildings are generally the most important feature of urban areas regarding flood propagation, and for extremely large events they indeed control dynamics of the surface flows. For smaller flood events, the results presented here show that **urban flood models should benefit from a more systematic integration of other types of flow-blocking elements.** Such integration contributes to exploit the potential of 2D models running on unstructured grids, without significantly increasing computational efforts. Yet this integration requires important data acquisition and pre-processing, and should be associated to the development of adapted tools.

Exchange models between streets and drainage pipes

Exchange flow between a street and an underground drainage pipe necessarily involves some important tri-dimensional flow patterns. Hydrodynamic simulation of the latter (Fang et al. 2010; Djordjevic et al. 2013) would be too complicated to integrate in an operational urban flood model. Therefore, **consideration of exchange flows is reduced to the computation of**

exchange discharges using analytical exchange model. Such a model was developed for the cases where the flow in the exchange structure is pressurized, which often happens during urban floods (Chapter 4). The basic idea is to link the local exchange discharge to the available head difference through the vertical exchange structure, detailing each of the head losses impacting the exchange flow. Comparison with experimental data shows the benefits of the method, with reasonably well predicted exchange discharges, while all model parameters are geometrical or physical ones. Both experiments and model results indicate that an orifice type equation (widely used within 1D/2D urban flood models) cannot be calibrated, as the usual calibration parameter (discharge coefficient) varies from one flow to another. This is attributed to the effects of the exchange flow regime (laminar/turbulent) and the exchange flow direction (i.e. drainage or overflow), both impacting local head losses through the exchange structure. Extrapolation of this model to a real-scale exchange structure was performed. **It then appears that an orifice equation is usable for a real scale modelling, provided that the equivalent discharge coefficients are preliminary computed by analysing exchange structures geometry.**

The exchange model was completed by following the approach proposed by Leandro et al. (2007), which suggests to integrate the potentially limiting capacity of the street inlet, and of the top part of the connecting pipe located underneath for drainage cases. This completed exchange model could not be directly validated with field data, but its use in the real case modelling (Chapter 7) shows two significant trends that set its potential and limitation.

First, for street water depths larger than a few dozens of cm (usual for an urban flood), local exchange discharges are likely to be high enough to saturate the underground drainage system. In this case, the exchange discharge can be computed with the specifically developed model (considering pressurized exchange flows, Chapter 4). This computation is only slightly sensitive to the detailed representation of the street topography, potential errors due to the street water depths computation being low when compared to the head differences used in the exchange model. **For such flooding condition, estimation of the exchange discharge appears to be suitable for simplified surface models (coarse mesh and low topographical data resolution).**

Now, for lower water depths (typically less than 10 cm), the exchange discharge is mainly governed by the street inlet capacity and constitutes a challenging modelling task. Available exchange equations are complex (see some relevant parameters in Despotovic et al. 2005), because they can require the use of local flow depths and velocities, or the

consideration of the surface flow at the street scale. Their implementation in a surface flow model is not trivial. Besides, even when using a simplified equation (weir equation in our case), computed exchange discharges are very sensitive to local flow characteristics (Chapter 7), and an adequate modelling requires both an accurate description of the street topography and an accurate simulation of the street flow. **Successful implementation of such fine exchanges within an operational hydrodynamic model remains uncertain and may require a further quantitative validation on experimental cases.** One way of reducing computation uncertainties can be the use of global exchange equations (which give for instance the exchange discharge considering the approaching street flow discharge and street geometry), provided they are applicable and can be implemented.

On the need of considering detailed streets topography into numerical models

Integration of streets topography in numerical models was studied through generic street profiles in laboratory experiments (i.e. presence of sidewalks), and more realistic profiles for the field case. In each case, detailed and simplified topographies were used in numerical simulations, the latter consisting in using a constant ground elevation across the transverse street profiles, taken as the average ground elevation on the profile. **Aim of using a simplified streets topography is to free the mesh structure from the streets main topographical lines** (drain channels, sidewalks), which reduces global modelling errors when working with coarse meshes.

Numerical simulations on bifurcation flows (Chapter 3) clearly show that both detailed and simplified street topographies lead to correct estimations of the discharge distribution through the downstream channels. Now, these results also point out that **at a crossroad scale with subcritical flow regime, a bias in the average ground elevation specified in a numerical model leads to errors when estimating discharge distribution in the surrounding streets.** Considering simulation results in Oullins (Chapter 6), we can see that using a simplified street topography necessarily impacts computed local flow water depths and velocities. Yet this has a negligible impact on the flood extent as the latter is mostly imposed by the global floodplain topography. **Therefore, for the modelling of such surface flows (water levels set by a downstream control), use of cross-section averaged street ground elevations appears to be an efficient option for urban flood models.**

The case of low water depths flows remains problematic. Simulation of small flood waves propagation in a street (Chapter 5, unsteady flows) shows that the averaged topography model leads to important relative errors on the flow water depths and velocities. This has only local impact for the simulation of this experimental flow, but similar flows simulated in the field case modelling show that the evaluation of the exchange process with the underground drainage system can then be biased by topographical approximations. **For this type of flows (water levels typically lower than the curb level), numerical models should include a detailed topography of the streets, despite the potentially finer meshes required and larger computational efforts.**

A few lessons from the modelling of floods in Oullins

Present results show that the flooding process in the city of Oullins is mainly controlled by the Yzeron River main channel flow, and that the latter is barely affected by the detail level in the floodplain flow modelling (built-up areas representation, exchanges with the underground drainage system, detailed streets topography). **In this case, the optimum numerical model strongly depends on the modelling aim.** If the modelling aims only at computing maximum water levels in the floodplain, simplified approach should be a better compromise, such as full 1D models or 1D/2D models (main channel/floodplain) models with coarse representation of floodplain flows (e.g. Yu and Lane 2006; McMillan and Brasington 2007). If the floodplain flow dynamics has to be known in details (e.g. local velocities, discharges in the streets), the approach used here should be retained.

Oullins is one particular case of river flooding, and some key elements may change for other sites. In particular, **the case of a large floodplain with significant flow discharges may be interesting to study.** This type of large-scale flooding may show a stronger influence of the floodplain flows and the different urban areas representations used here may then have a more global impact.

Finally, surface modelling in Oullins has been globally validated, using recorded maximum water levels during the recent flood events. Oppositely, modelling of flows in the sewer system clearly lacks validation data, whereas some input data remain uncertain (e.g. input hydrographs or pipe frictions). Coupling several types of flow models to describe flows interactions in urban areas forms a powerful tool, but its use should be validated with additional field data. Obviously, this type of data remains hard to produce (Mark et al. 2004) and should focus on some key points. Following the results of flood modelling in Oullins,

measuring flow discharges in a collector downstream of a recurrently flooded area may help to characterize flow exchanges and improve this modelling.

Perspectives

Additional physical processes

Part of this thesis is based on experimental models, which proved to be useful to study flows that are not easily observable during real flood events. Such approach (or advanced CFD models) should be used to continue describing flows occurring during urban floods. At the scale of a crossroad or a street, effects of friction (including bottom and wall friction, as well as macro roughness arising from very small obstacles) could be assessed, in order to improve numerical model parameterization. Aim here would be to both set rules to guide the choice of a street friction, and assess the impact of friction on discharge distribution in a street network. Considering the present results on detailed topography and small obstacles along with previous results on crossroad flows, this additional work could lead to an extensive description of flows in a flooded street network.

The proposed exchange model would be interesting to validate or extend, using observations on a real-scale exchange structure. This kind of study has been recently carried out (Djordjevic et al. 2013), but results generalization requires complementary work. Measuring flow characteristics within real scale structures avoids scaling effects (low Reynolds numbers) and allows fine measurements, which were somehow missed to validate some hypotheses in our experiment.

An experimental study of drainage processes in a street network with low water depths should be carried out, with street inlets operation impacted by the surface flow inertia. The gathered data would be an efficient way to validate the ability of a hydrodynamic numerical model to compute exchange discharges from simulated local flows characteristics.

Data acquisition and pre-processing

Present results point out the benefits of integrating fine details into surface flow models (small-scale obstacles, walls and barriers, detailed street topography for urban drainage applications) when simulating urban flood events. However, all methods used in the thesis are

entirely operational. It is worth keeping in mind that overall, a model applicability also depends on its operation and set-up easiness.

Topographical data acquisition is an active research topic (e.g. Mason et al. 2007; Sampson et al. 2012) and urban data base become more and more precise. Therefore part of the work required for our real case modelling could have been readily reduced (namely the field surveys to gather topographical data or street inlets location), provided new methods of data acquisition are somehow cost-effective. However, location of streets small-scale obstacles (not studied in Oullins for schedule reasons) or type of built-up areas boundaries ("manual" field survey in our case) remain difficult to gather and may benefit from an advanced use of recent technologies (like terrestrial LiDAR).

Now, should all these data be easily available, their integration in numerical models requires a compromise between pre-processing efforts and the final accuracy. For the surface flow model of Oullins (Chapter 6), the method used is based on a manual definition of the global mesh structure and a semi-automatic mesh generation. This leads to a quite accurate description of the river and streets topography, and of the built-up areas/streets boundaries. Besides, this allows a systematic simplification of the street topography (by analysing cross-sections), as well as a fine positioning of the walls/barriers. However, such technique requires simplifications of buildings footprint and is not fitted for integration of small-scale obstacles, the mesh being not easily adaptable to these details. An attempt to overcome this has been carried out by using the unstructured mesh generator Gmsh (Geuzaine and Remacle 2009). The latter can be easily adapted to generate meshes respecting buildings footprint, but the re-interpolation of the topographical data requires specific care. Indeed, the few carried out attempts lead to a mistaken river main channel topography (which is of paramount importance to evaluate flood risk in Oullins). Therefore, adapting these tools to allow an automatic generation of surface flow model including several types of urban structural elements would lead to an optimum use of 2D models running on unstructured meshes.

Use of simplified numerical models

The governing equations and the numerical scheme of the code used for the surface flow modelling (Rubar20) can be considered as quite accurate, when compared to other urban flood models. There has been recently a growing interest about simplified flood models, which notably include simplifications of the governing equations. Some model benchmarks have been carried out (Fewtrell et al. ; Hunter et al. 2008), but the comparisons remain rather

global and do not necessarily involve field or laboratory validation data. Therefore, an interesting task would be to use one or several different models (ideally, two-dimensional models requiring smaller computational efforts) to simulate flows from this thesis or other past experiments. In particular, flows presented in Chapter 2 may help to further characterize the ability of simplified models to simulate flows at a street or a crossroad scale.

References

Aberle, J. and J. Järvelä (2013). "Flow resistance of emergent rigid and flexible floodplain vegetation." *Journal of Hydraulic Research* **51**(1): 33-45.

Apel, H., G. T. Aronica, H. Kreibich and A. H. Thieken (2009). "Flood risk analyses-how detailed do we need to be?" *Natural Hazards* **49**(1): 79-98.

Aronica, G., G. Freni and E. Oliveri (2005). "Uncertainty analysis of the influence of rainfall time resolution in the modelling of urban drainage systems." *Hydrological Processes* **19**(5): 1055-1071.

Aronica, G. T., F. Franza, P. D. Bates and J. C. Neal (2012). "Probabilistic evaluation of flood hazard in urban areas using Monte Carlo simulation." *Hydrological Processes* **26**(26): 3962-3972.

Aronica, G. T. and L. G. Lanza (2005). "Drainage efficiency in urban areas: a case study." *Hydrological Processes* **19**(5): 1105-1119.

Bazin, H. E. (1898). *Expériences nouvelles sur l'écoulement en déversoir exécutées a Dijon de 1886-1895*. Paris, V. C. Dunod.

Bazin, P. H., A. Bessette, E. Mignot, A. Paquier and N. Riviére (2012). "Influence of detailed topography when modeling flows in street junction during urban flood." *Journal of Disaster Research* **7**(5): 560-566.

Bertrand-Krajewski, J. L. (2006). Cours d'Hydrologie Urbaine - Le ruissellement, Insa Lyon - URGC Hydrologie urbaine**:** 21.

Braud, I., P. Breil, F. Thollet, M. Lagouy, F. Branger, C. Jacqueminet, . . . K. Michel (2013). "Evidence of the impact of urbanization on the hydrological regime of a medium-sized periurban catchment in France." *Journal of Hydrology* **485**: 5-23.

Bravo, H. R. and F. M. Holly (1996). "Turbulence model for depth-averaged flows in navigation installations." *Journal of Hydraulic Engineering-Asce* **122**(12): 718-727.

Breil, P., B. Radojevic and B. Chocat (2010). Urban development and extreme flow regime changes. *6th World FRIEND Conference "Global Change: Facing Risks and Threats to Water Resources"*, Fez, Morocco.

Breusers, H. N. C., G. Nicollet and H. W. Shen (1977). "Local scour around cylindrical piers." *Journal of Hydraulic Research* **15**(3): 211-252.

Brown, J. D., T. Spencer and I. Moeller (2007). "Modeling storm surge flooding of an urban area with particular reference to modeling uncertainties: A case study of Canvey Island, United Kingdom." *Water Resources Research* **43**(6).

Cea, L. and M. E. Vazquez-Cendon (2010). "Unstructured finite volume discretization of two-dimensional depth-averaged shallow water equations with porosity." *International Journal for Numerical Methods in Fluids* **63**(8): 903-930.

Cemagref (2009). Projet RIVES Risques d'inondation en ville et Etude de Scenarios. Rapport scientifique final.

Chanson, H. (2004). *The hydraulics of open channel flow: an introduction*. Oxford, Elsevier.

Chen, A. S., B. Evans, S. Djordjević and D. A. Savić (2012). "Multi-layered coarse grid modelling in 2D urban flood simulations." *Journal of Hydrology* **470-471**: 1-11.

Chen, A. S., M. H. Hsu, T. S. Chen and T. J. Chang (2005). "An integrated inundation model for highly developed urban areas." *Water Science and Technology* **51**(2): 221-229.

Chen, D. Y. and G. H. Jirka (1995). "Experimental study of plane turbulent wakes in a shallow-water layer." *Fluid Dynamics Research* **16**(1): 11-41.

Desbordes, M. (1974). Réflexions sur les méthodes de calcul des réseaux urbains d'assainissement pluvial. Montpellier. **PhD:** 224.

Despotovic, J., J. Plavsic, N. Stefanovic and D. Pavlovic (2005). "Inefficiency of storm water inlets as a source of urban floods." *Water Science and Technology* **51**(2): 139-145.

Djordjevic, S., D. Prodanovic and C. Maksimovic (1999). "An approach to stimulation of dual drainage." *Water Science and Technology* **39**(9): 95-103.

Djordjevic, S., D. Prodanovic, C. Maksimovic, M. Ivetic and D. Savic (2005). "SIPSON - Simulation of interaction between pipe flow and surface overland flow in networks." *Water Science and Technology* **52**(5): 275-283.

Djordjevic, S., D. Prodanovic and G. A. Walters (2004). "Simulation of transcritical flow in pipe/channel networks." *Journal of Hydraulic Engineering-Asce* **130**(12): 1167-1178.

Djordjevic, S., A. J. Saul, G. R. Tabor, J. Blanksby, I. Galambos, N. Sabtu and G. Sailor (2013). "Experimental and numerical investigation of interactions between above and below ground drainage systems." *Water Science and Technology* **67**(3): 535-542.

Dottori, F. and E. Todini (2013). "Testing a simple 2D hydraulic model in an urban flood experiment." *Hydrological Processes* **27**(9): 1301-1320.

EEA (2010). Mapping the impacts of natural hazards and technological accidents in Europe

An overview of the last decade. Copenhagen, Denmark, European Environment Agency (EEA)**:** 146.

El Kadi Abderrezzak, K., L. Lewicki, A. Paquier, N. Riviere and G. Travin (2011). "Division of critical flow at three-branch open-channel intersection." *Journal of Hydraulic Research* **49**(2): 231-238.

El Kadi Abderrezzak, K. and A. Paquier (2009). "Discussion of “Numerical and Experimental Study of Dividing Open-Channel Flows” by A. S. Ramamurthy, Junying Qu, and Diep Vo." *Journal of Hydraulic Engineering* **135**(12): 1111-1112.

El Kadi Abderrezzak, K. and A. Paquier (2011). "Applicability of Sediment Transport Capacity Formulas to Dam-Break Flows over Movable Beds." *Journal of Hydraulic Engineering-Asce* **137**(2): 209-221.

El Kadi Abderrezzak, K., A. Paquier and E. Mignot (2009). "Modelling flash flood propagation in urban areas using a two-dimensional numerical model." *Natural Hazards* **50**(3): 433-460.

Ettrich, N., K. Steiner, M. Thomas and R. Rothe (2005). "Surface models for coupled modelling of runoff and sewer flow in urban areas." *Water Science and Technology* **52**(5): 25-33.

Fang, X., S. Jiang and S. R. Alam (2010). "Numerical simulations of efficiency of curb-opening inlets." *Journal of Hydraulic Engineering* **136**(1): 62-66.

Fang, X. and D. H. Su (2006). "An integrated one-dimensional and two-dimensional urban stormwater flood simulation model." *Journal of the American Water Resources Association* **42**(3): 713-724.

Fewtrell, T. J., A. Duncan, C. C. Sampson, J. C. Neal and P. D. Bates (2011). "Benchmarking urban flood models of varying complexity and scale using high resolution terrestrial LiDAR data." *Physics and Chemistry of the Earth* **36**(7-8): 281-291.

Freni, G., G. La Loggia and V. Notaro (2010). "Uncertainty in urban flood damage assessment due to urban drainage modelling and depth-damage curve estimation." *Water Science and Technology* **61**(12): 2979-2993.

Gallegos, H. A., J. E. Schubert and B. F. Sanders (2009). "Two-dimensional, high-resolution modeling of urban dam-break flooding: A case study of Baldwin Hills, California." *Advances in Water Resources* **32**(8): 1323-1335.

Gallegos, H. A., J. E. Schubert and B. F. Sanders (2012). "Structural Damage Prediction in a High-Velocity Urban Dam-Break Flood: Field-Scale Assessment of Predictive Skill." *Journal of Engineering Mechanics-Asce* **138**(10): 1249-1262.

Geuzaine, C. and J. F. Remacle (2009). "Gmsh: A 3-D finite element mesh generator with built-in pre- and post-processing facilities." *International Journal for Numerical Methods in Engineering* **79**(11): 1309-1331.

Ghostine, R., G. Kesserwani, J. Vazquez, N. Riviere, A. Ghenaim and R. Mose (2009). "Simulation of supercritical flow in crossroads: Confrontation of a 2D and 3D numerical approaches to experimental results." *Computers & Fluids* **38**(2): 425-432.

Ghostine, R., E. Mignot, M. Abdallah, F. Lawniczak, J. Vazquez, R. Mose and C. Gregoire (2010). "Discontinuous Galerkin Finite-Element Method for Simulation of Flood in Crossroads." *Journal of Hydraulic Engineering-Asce* **136**(8): 474-482.

Ghostine, R., R. Mose, J. Vazquez, A. Ghenaim and C. Gregoire (2010). "Two-Dimensional Simulation of Subcritical Flow at a Combining Junction: Luxury or Necessity?" *Journal of Hydraulic Engineering-Asce* **136**(10): 799-805.

Ghostine, R., J. Vazquez, A. Terfous, R. Mose and A. Ghenaim (2012). "Comparative study of 1D and 2D flow simulations at open-channel junctions." *Journal of Hydraulic Research* **50**(2): 164-170.

Golding, B. W. (2009). "Uncertainty propagation in a London flood simulation." *Journal of Flood Risk Management* **2**(1): 2-15.

Gomez, M., F. Macchione and B. Russo (2011). "Methodologies to study the surface hydraulic behaviour of urban catchments during storm events." *Water Science and Technology* **63**(11): 2666-2673.

Gomez, M. and B. Russo (2009). "Hydraulic Efficiency of Continuous Transverse Grates for Paved Areas." *Journal of Irrigation and Drainage Engineering-Asce* **135**(2): 225-230.

Graf, W. H. and B. Yulistiyanto (1998). "Experiments on flow around a cylinder; the velocity and vorticity fields." *Journal of Hydraulic Research* **36**(4): 637-653.

Guinot, V. and S. Soares-Frazao (2006). "Flux and source term discretization in two-dimensional shallow water models with porosity on unstructured grids." *International Journal for Numerical Methods in Fluids* **50**(3): 309-345.

Guo, J., K. MacKenzie and A. Mommandi (2009). "Design of Street Sump Inlet." *Journal of Hydraulic Engineering* **135**(11): 1000-1004.

Heo, J., S. Jeong, H.-K. Park, J. Jung, S. Han, S. Hong and H.-G. Sohn (2013). "Productive high-complexity 3D city modeling with point clouds collected from terrestrial LiDAR." *Computers, Environment and Urban Systems* **41**(0): 26-38.

Hilden, M. (2005). "Simulation of floods caused by overloaded sewer systems: extensions of shallow-water equations." *Hydrological Processes* **19**(5): 1037-1053.

Hingray, B., B. Cappelaere, C. Bouvier and M. Desbordes (2000). "Hydraulic Vulnerability of Elementary Urban Cell." *Journal of Hydrologic Engineering* **5**(4): 402-410.

Hsu, C. C., C. J. Tang, W. J. Lee and M. Y. Shieh (2002). "Subcritical 90 degrees equal-width open-channel dividing flow." *Journal of Hydraulic Engineering-Asce* **128**(7): 716-720.

Hunter, N. M., P. D. Bates, S. Neelz, G. Pender, I. Villanueva, N. G. Wright, . . . D. C. Mason (2008). "Benchmarking 2D hydraulic models for urban flooding." *Proceedings of the Institution of Civil Engineers-Water Management* **161**(1): 13-30.

Idelchik, I. E. and O. Steinberg (1996). *Handbook of Hydraulic Resistance*, Begell House.

Inoue, K., K. Kawaike and H. Hayashi (2000). "Numerical simulation models on inundation flow in urban area." *Journal of Hydroscience and Hydraulic Engineering* **18**(1): 8.

Ishigaki, T., Y. Asai, Y. Nakahata, H. Shimada, Y. Baba and K. Toda (2010). "Evacuation of aged persons from inundated underground space." *Water Science and Technology* **62**(8): 1807-1812.

Jamieson, S. R., J. Lhomme, G. Wright and B. Gouldby (2012). "A highly efficient 2D flood model with sub-element topography." *Proceedings of the Institution of Civil Engineers-Water Management* **165**(10): 581-595.

Jamison, D. K. and J. R. Villemonte (1971). "Junction losses in laminar and transitional flows." *Journal of the Hydraulics Division* **97**(7): 1045-1063.

Jiang, C. B., C. Yang and D. F. Liang (2009). "Computation of shallow wakes with the fractional step finite element method." *Journal of Hydraulic Research* **47**(1): 127-136.

Jonkman, S. N., J. K. Vrijling and A. C. W. M. Vrouwenvelder (2008). "Methods for the estimation of loss of life due to floods: a literature review and a proposal for a new method." *Natural Hazards* **46**(3): 353-389.

Kasthuri, B. and N. V. Pundarikanthan (1987). "Separation zone at open-channel junctions - Discussion." *Journal of Hydraulic Engineering-Asce* **113**(4): 543-544.

Kawaike, K., K. Inoue, K. Toda and M. Noguchi (2004). "Inundation flow analysis due to heavy rainfall in low-lying river basin." *Journal of Hydroscience and Hydraulic Engineering* **22**(1): 14.

Kawaike, K., H. Nakagawa, Y. Baba and A. Shimizu (2011). Experimental Study on Validation of Stormwater Interaction Model between the Ground Surface and Sewerage System. Conference on Hydraulics in Water Engineering (10th : 2011 : Brisbane, Qld.). Barton, A.C.T., Engineers Australia**:** 1889-1896.

Khan, A. A., R. Cadavid and S. S. Y. Wang (2000). "Simulation of channel confluence and bifurcation using the CCHE2D model." *Proceedings of the Institution of Civil Engineers-Water Maritime and Energy* **142**(2): 97-102.

Kouyi, G. L., N. Riviere, V. Vidalat, A. Becquet, B. Chocat and V. Guinot (2010). "Urban flooding: one-dimensional modelling of the distribution of the discharges through cross-road intersections accounting for energy losses." *Water Science and Technology* **61**(8): 2021-2026.

Law, S. W. and A. J. Reynolds (1966). "Dividing flow in an open channel." *Journal of the Hydraulics Division - Proceedings of the ASCE* **92**(HY2): 207-231.

Leandro, J., A. S. Chen, S. Djordjevic and D. A. Savic (2009). "Comparison of 1D/1D and 1D/2D Coupled (Sewer/Surface) Hydraulic Models for Urban Flood Simulation." *Journal of Hydraulic Engineering-Asce* **135**(6): 495-504.

Leandro, J., S. Djordjevic, A. Chen and D. Savic (2007). The use of Multiple-linking-element for connecting sewer and surface drainage networks. *32nd Congress of IAHR-Harmonizing the Demands of Art and Nature in Hydraulics*, Venice, Italy.

Leandro, J., S. Djordjevic, A. S. Chen, D. A. Savic and M. Stanic (2011). "Calibration of a 1D/1D urban flood model using 1D/2D model results in the absence of field data." *Water Science and Technology* **64**(5): 1016-1024.

Lencastre, A. (1986). *Manuel d'hydraulique générale*. Paris, Eyrolles.

León, A. S., M. S. Ghidaoui, A. R. Schmidt and M. H. García (2009). "Application of Godunov-type schemes to transient mixed flows." *Journal of Hydraulic Research* **47**(2): 147-156.

Lhomme, J., C. Bouvier, E. Mignot and A. Paquier (2006). One-dimensional GIS-based model compared with a two-dimensional model in urban floods simulation. P. S. Mikkelsen, A. Ledin and T. Hvitved-Jacobsen. **54:** 83-91.

Li, C. W. and C. Zeng (2010). "Flow division at a channel crossing with subcritical or supercritical flow." *International Journal for Numerical Methods in Fluids* **62**(1): 56-73.

Lipeme Kouyi, G., D. Fraisse, N. Rivière, V. Guinot and B. Chocat (2009). "One-dimensional modelling of the interactions between heavy rainfall-runoff in an urban area and flooding flows from sewer networks and rivers." *Water Science and Technology* **60**(4): 927-934.

Lloyd, P. M. and P. K. Stansby (1997). "Shallow-water flow around model conical islands of small side slope .1. Surface piercing." *Journal of Hydraulic Engineering-Asce* **123**(12): 1057-1067.

Lopes, P., J. Leandro, R. F. Carvalho, P. Páscoa and R. Martins (2013). "Numerical and experimental investigation of a gully under surcharge conditions." *Urban Water Journal*.

MacKenzie, K. and J. Guo (2011). Hydraulic efficiency of street inlets common to UDFCD region. Denver, CO, Urban Drainage and Flood Control District**:** 27.

Mark, O., S. Weesakul, C. Apirumanekul, S. B. Aroonnet and S. Djordjevic (2004). "Potential and limitations of 1D modelling of urban flooding." *Journal of Hydrology* **299**(3-4): 284-299.

Marsalek, J. (1984). "Head losses at sewer junction manholes." *Journal of Hydraulic Engineering* **110**(8): 1150-1154.

Mason, D. C., M. S. Horritt, N. M. Hunter and P. D. Bates (2007). "Use of fused airborne scanning laser altimetry and digital map data for urban flood modelling." *Hydrological Processes* **21**(11): 1436-1447.

McMillan, H. K. and J. Brasington (2007). "Reduced complexity strategies for modelling urban floodplain inundation." *Geomorphology* **90**(3-4): 226-243.

Mignot, E., A. Paquier and S. Haider (2006). "Modeling floods in a dense urban area using 2D shallow water equations." *Journal of Hydrology* **327**(1-2): 186-199.

Mignot, E., A. Paquier and T. Ishigaki (2006). "Comparison of numerical and experimental simulations of a flood in a dense urban area." *Water Science and Technology* **54**(6-7): 65-73.

Mignot, E., A. Paquier and N. Riviere (2008). "Experimental and numerical modeling of symmetrical four-branch supercritical cross junction flow." *Journal of Hydraulic Research* **46**(6): 723-738.

Mignot, E., N. Riviere, R. Perkins and A. Paquier (2008). "Flow patterns in a four-branch junction with supercritical flow." *Journal of Hydraulic Engineering-Asce* **134**(6): 701-713.

Mignot, E., C. Zeng, G. Dominguez, C.-W. Li, N. Rivière and P.-H. Bazin (2013). "Impact of topographic obstacles on the discharge distribution in open-channel bifurcations." *Journal of Hydrology* **494**(0): 10-19.

Miller, D. S. (1978). *Internal flow systems*, BHRA Fluid Engineering.

Ministère de l'agriculture, S. (1980). Synthèse nationale sur les crues des petits bassins versants. Fascicule 3 : la méthode CRUPEDIX.

Nasello, C. and T. Tucciarelli (2005). "Dual Multilevel Urban Drainage Model." *Journal of Hydraulic Engineering-Asce* **131**(9): 748-754.

Neary, V. S. and A. J. Odgaard (1993). "3-Dimensional flow structure at open-channel diversions." *Journal of Hydraulic Engineering-Asce* **119**(11): 1223-1230.

Neary, V. S., F. Sotiropoulos and A. J. Odgaard (1999). "Three-dimensional numerical model of lateral-intake inflows." *Journal of Hydraulic Engineering-Asce* **125**(2): 126-140.

Nougaro, J., P. Boyer and J. Claria (1975). "Comportement d'une dérivation de canaux lorsque les biefs aval sont pourvus de retenues." *La Houille Blanche*(4): 267-273.

Papanicolaou, A. N., M. Elhakeem and B. Wardman (2011). "Calibration and Verification of a 2D Hydrodynamic Model for Simulating Flow around Emergent Bendway Weir Structures." *Journal of Hydraulic Engineering-Asce* **137**(1): 75-89.

Paquier, A. (1995). Modelisation et simulation de la propagation de l'onde de rupture de barrage. Lyon, Jean Monnet. **PhD:** 193.

Paquier, A. (2013). Logiciel Rubar20 - Notice d'emploi. Lyon, France, Irstea, Departement Eaux, Unité de recherche Hydrologie Hydraulique**:** 65.

Paquier, A. and P.-H. Bazin (2014). Coupling 1-D and 2-D Models for Simulating Floods: Definition of the Exchange Terms. *Advances in Hydroinformatics*. P. Gourbesville, J. Cunge and G. Caignaert, Springer Singapore**:** 129-140.

Pedersen, F. B. and O. Mark (1990). "Head losses in storm sewer manholes: submerged jet theory." *Journal of Hydraulic Engineering* **116**(11): 1317-1328.

Ramamurthy, A. S., J. Qu and D. Vo (2007). "Numerical and experimental study of dividing open-channel flows." *Journal of Hydraulic Engineering* **133**(10): 1135-1144.

Ramamurthy, A. S. and M. G. Satish (1988). "Division of flow in short open channel branches." *Journal of Hydraulic Engineering-Asce* **114**(4): 428-438.

Ramamurthy, A. S., D. M. Tran and L. B. Carballada (1990). "Dividing flow in open channels." *Journal of Hydraulic Engineering-Asce* **116**(3): 449-455.

Richardson, J. E. and V. G. Panchang (1998). "Three-dimensional simulation of scour-inducing flow at bridge piers." *Journal of Hydraulic Engineering-Asce* **124**(5): 530-540.

Riviere, N., G. Travin and R. J. Perkins (2007). Transcritical flows in open channel intersections. *32nd IAHR Congress*, Venice, Italy.

Sampson, C. C., T. J. Fewtrell, A. Duncan, K. Shaad, M. S. Horritt and P. D. Bates (2012). "Use of terrestrial laser scanning data to drive decimetric resolution urban inundation models." *Advances in Water Resources* **41**(0): 1-17.

Schmitt, T. G., M. Thomas and N. Ettrich (2004). "Analysis and modeling of flooding in urban drainage systems." *Journal of Hydrology* **299**(3-4): 300-311.

Schubert, J. E., B. F. Sanders, M. J. Smith and N. G. Wright (2008). "Unstructured mesh generation and landcover-based resistance for hydrodynamic modeling of urban flooding." *Advances in Water Resources* **31**(12): 1603-1621.

Schumann, G. J. P., J. C. Neal, D. C. Mason and P. D. Bates (2011). "The accuracy of sequential aerial photography and SAR data for observing urban flood dynamics, a case study of the UK summer 2007 floods." *Remote Sensing of Environment* **115**(10): 2536-2546.

Serre, M., A. J. Odgaard and R. A. Elder (1994). "Energy Loss at Combining Pipe Junction." *Journal of Hydraulic Engineering-Asce* **120**(7): 808-830.

Sharp, Z. B., M. C. Johnson, S. L. Barfuss and W. J. Rahmeyer (2010). "Energy losses in cross junctions." *Journal of Hydraulic Engineering* **136**(1): 50-55.

Shettar, A. S. and K. K. Murthy (1996). "A numerical study of division of flow in open channels." *Journal of Hydraulic Research* **34**(5): 651-675.

Smith, M. B. (2006). "Comment on [`]Analysis and modeling of flooding in urban drainage systems'." *Journal of Hydrology* **317**(3-4): 355-363.

Soares-Frazao, S., J. Lhomme, V. Guinot and Y. Zech (2008). "Two-dimensional shallow-water model with porosity for urban flood modelling." *Journal of Hydraulic Research* **46**(1): 45-64.

Soares-Frazão, S. and Y. Zech (2008). "Dam-break flow through an idealised city." *Journal of Hydraulic Research* **46**(5): 648-658.

Stansby, P. K. (2006). "Limitations of depth-averaged modeling for shallow wakes." *Journal of Hydraulic Engineering-Asce* **132**(7): 737-740.

Struve, J., R. A. Falconer and Y. Wu (2003). "Influence of model mangrove trees on the hydrodynamics in a flume." *Estuarine, Coastal and Shelf Science* **58**(1): 163-171.

Taylor, E. (1944). "Flow characteristics at rectangular open-channel junctions." *Transactions of the American Society of Civil Engineers* **109**: 893-912.

Toda, K., K. Inoue, K. Kuriyama and O. Maeda (2001). *Inundation flow analysis in urban areas considering streets and underground space effects*.

Tsubaki, R. and I. Fujita (2010). "Unstructured grid generation using LiDAR data for urban flood inundation modelling." *Hydrological Processes* **24**(11): 1404-1420.

Van Emelen, S., S. Soares-Frazao, C. K. Riahi-Nezhad, M. H. Chaudhry, J. Imran and Y. Zech (2012). "Simulations of the New Orleans 17th Street Canal breach flood." *Journal of Hydraulic Research* **50**(1): 70-81.

Vanleer, B. (1979). "Towards the ultimate conservative difference scheme .5. 2nd-order sequel to Godunovs method." *Journal of Computational Physics* **32**(1): 101-136.

Vojinovic, Z. and D. Tutulic (2009). "On the use of 1D and coupled 1D-2D modelling approaches for assessment of flood damage in urban areas." *Urban Water Journal* **6**(3): 183-199.

Wilkerson, G. V. (2007). "Flow through trapezoidal and rectangular channels with rigid cylinders." *Journal of Hydraulic Engineering-Asce* **133**(5): 521-533.

Xia, J., F. Teo, B. Lin and R. Falconer (2011). "Formula of incipient velocity for flooded vehicles." *Natural Hazards* **58**(1): 1-14.

Xia, J. Q., R. A. Falconer, B. L. Lin and G. M. Tan (2011). "Numerical assessment of flood hazard risk to people and vehicles in flash floods." *Environmental Modelling & Software* **26**(8): 987-998.

Yen, B. C. (2002). "Open Channel Flow Resistance." *Journal of Hydraulic Engineering* **128**(1): 20-39.

Yu, D. and S. N. Lane (2006). "Urban fluvial flood modelling using a two-dimensional diffusion-wave treatment, part 1: mesh resolution effects." *Hydrological Processes* **20**(7): 1541-1565.

Yu, D. and S. N. Lane (2006). "Urban fluvial flood modelling using a two-dimensional diffusion-wave treatment, part 2: development of a sub-grid-scale treatment." *Hydrological Processes* **20**(7): 1567-1583.

Yu, D. and S. N. Lane (2011). "Interactions between subgrid-scale resolution, feature representation and grid-scale resolution in flood inundation modelling." *Hydrological Processes* **25**(1): 36-53.

Yulistiyanto, B., Y. Zech and W. H. Graf (1998). "Flow around a cylinder: Shallow-water modeling with diffusion-dispersion." *Journal of Hydraulic Engineering-Asce* **124**(4): 419-429.

Appendix

Appendix A
Additional results for bifurcation flows

A.1 Initial flows simulation results for the run 4

Figure A.1 shows for each experimental flow simulation results of the run 4 (Table 3.1) around the junction, including the following characteristics:

- velocity magnitude normalized by the bulk velocity in the upstream channel V/V_{u0},
- streamlines,
- water depths normalized by the upstream channel water depth h/h_{u0},
- areas where flow is supercritical (indicated with hashed areas on the right part of figures)
- dividing stream line and recirculation area (red lines on the right part of figures)

Besides, single obstacles locations are indicated with white squares.

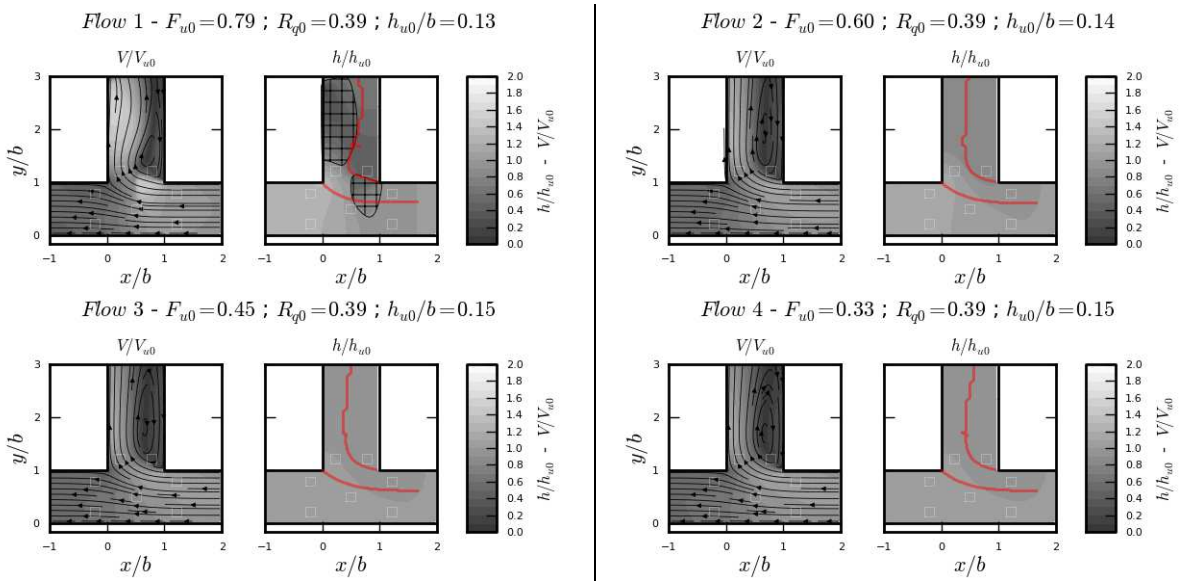

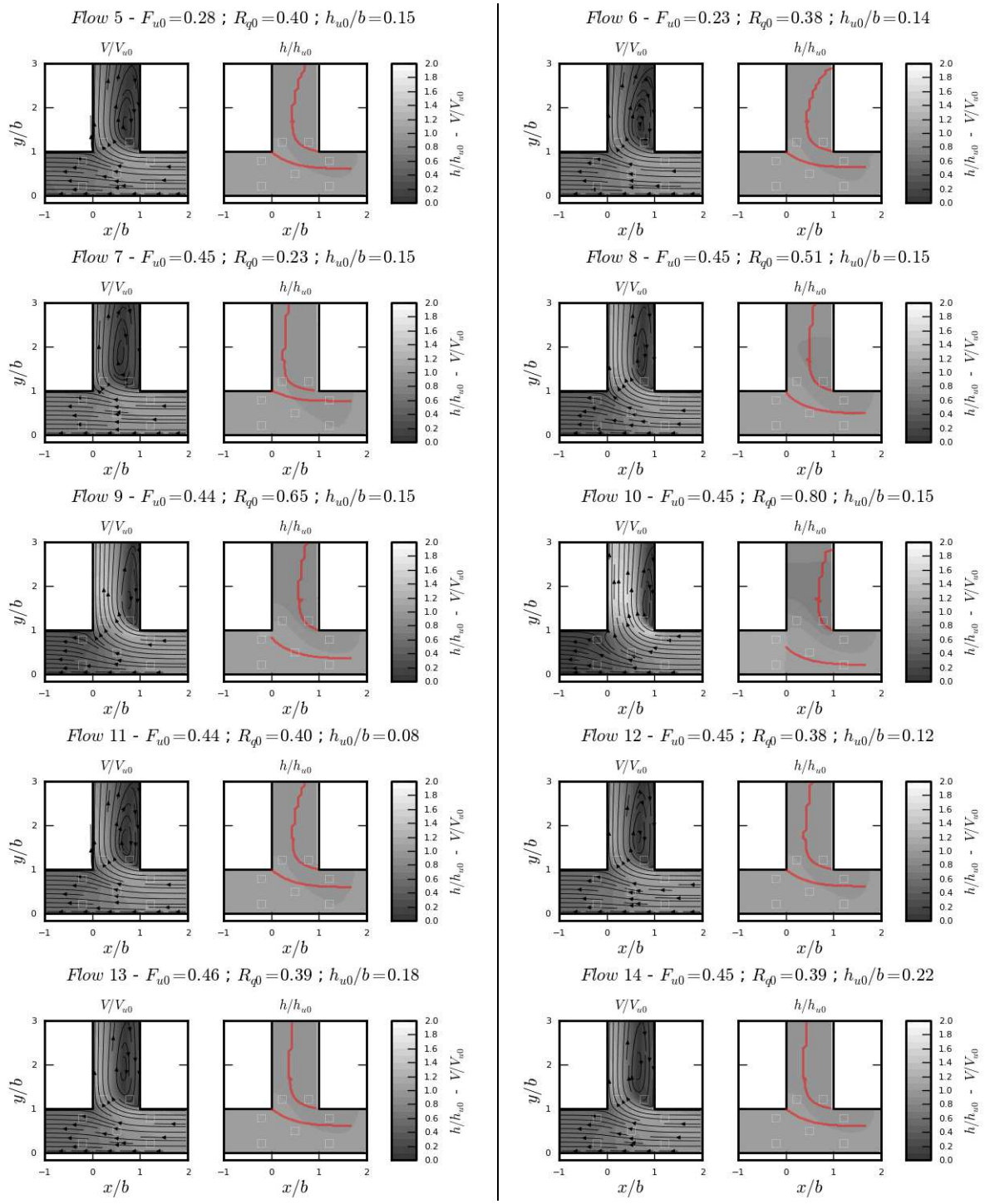

Figure A.1 : Computed initial dividing flow characteristics near the junction with run 4

A.2 Comparison of simulation results and experimental measurements

Simulation results are compared to all available experimental measurements. For obstacles, for scarcity, only results from the run 4 (fine mesh, with the eddy viscosity coefficient set to K=1x10^{-3} m^2.s^{-1}, see Table 3.3) are used for the water depths, as it is the

optimum set of parameters to simulate the branch channel water depths. For the velocity fields, the run 10 is also used to show the influence of a coarse mesh. Note that the arrow plot densities may be reduced for visibility.

Water depths measurements include for each flow (except flows 5 and 6, which are very close to flow 4) the initial flow and a flow with one obstacle. LSPIV measurements are available for flow 3, for each obstacle configuration. PIV measurements are available for flow 6, for the initial flow, and for obstacles (1, 2, 4, 5 and 6).

A.2.1 Water depths

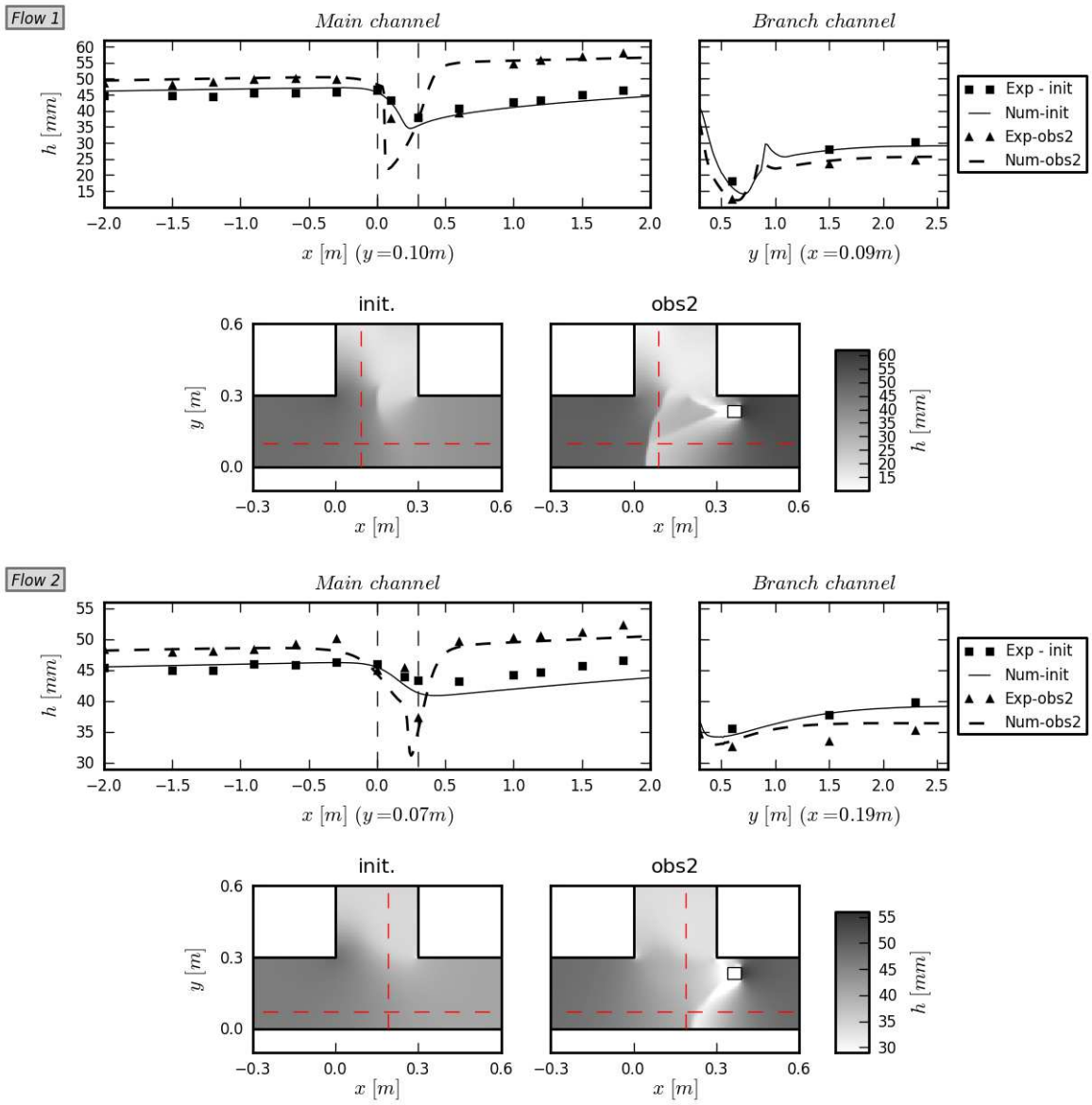

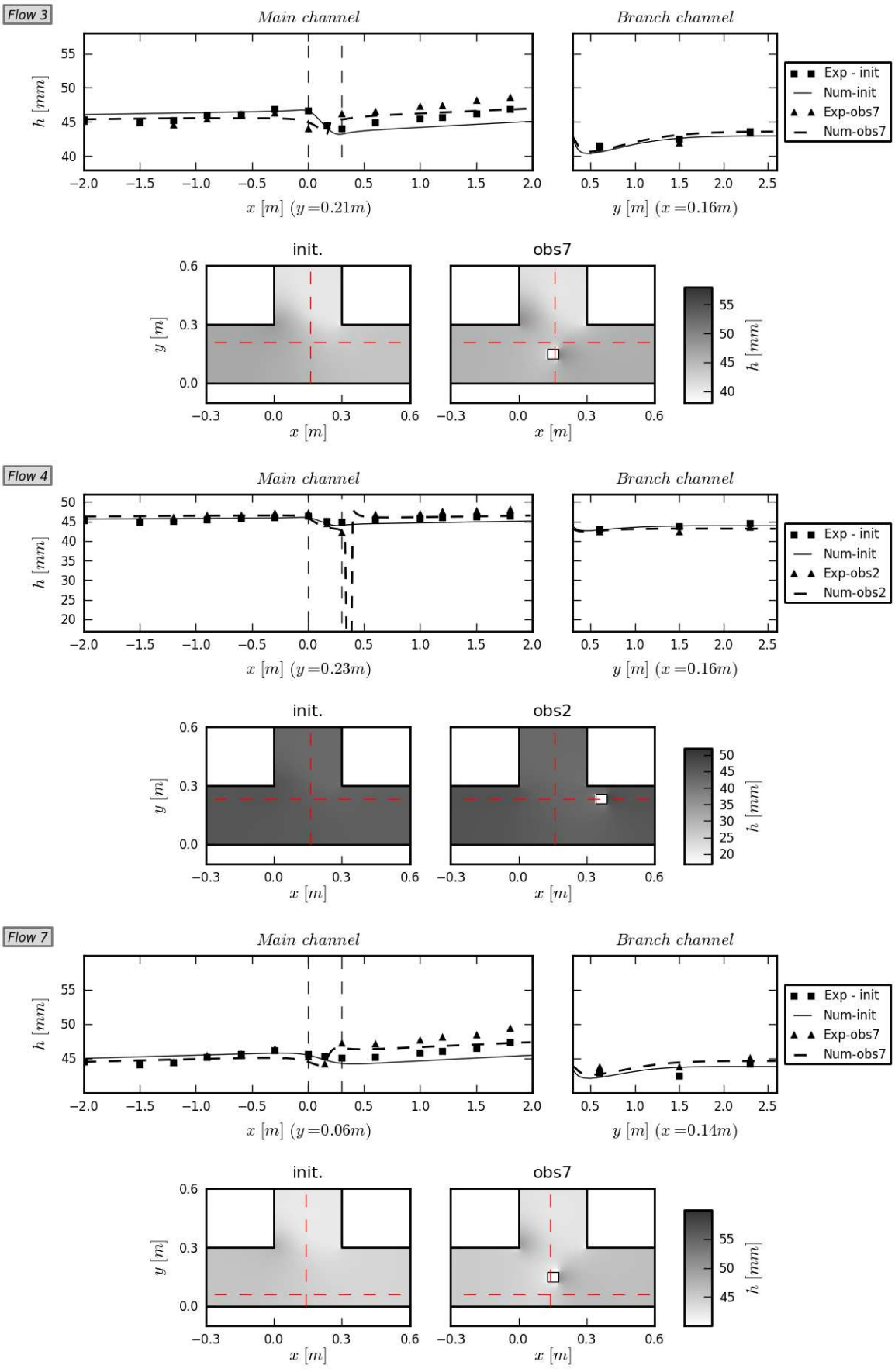
Flow 3
Main channel
Branch channel
h [mm]
x [m] (y=0.21m)
y [m] (x=0.16m)
Exp - init
Num-init
Exp-obs7
Num-obs7
init.
obs7
y [m]
x [m]
h [mm]
Flow 4
Main channel
Branch channel
h [mm]
x [m] (y=0.23m)
y [m] (x=0.16m)
Exp - init
Num-init
Exp-obs2
Num-obs2
init.
obs2
y [m]
x [m]
h [mm]
Flow 7
Main channel
Branch channel
h [mm]
x [m] (y=0.06m)
y [m] (x=0.14m)
Exp - init
Num-init
Exp-obs7
Num-obs7
init.
obs7
y [m]
x [m]
h [mm]

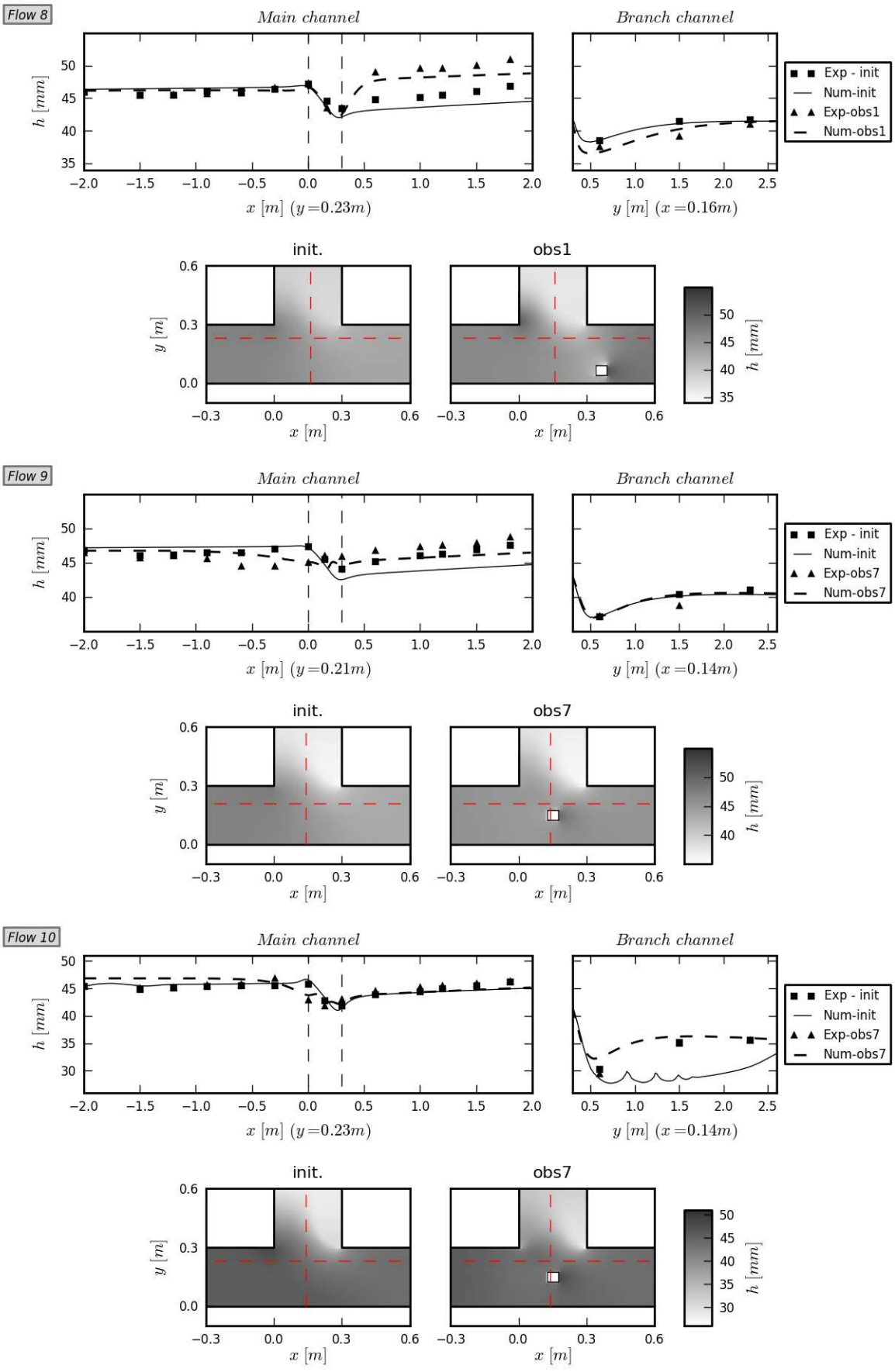
Flow 8
Main channel
Branch channel
h [mm]
x [m] (y=0.23m)
y [m] (x=0.16m)
Exp - init
Num-init
Exp-obs1
Num-obs1
init.
obs1
y [m]
x [m]
h [mm]
Flow 9
Main channel
Branch channel
x [m] (y=0.21m)
y [m] (x=0.14m)
Exp - init
Num-init
Exp-obs7
Num-obs7
init.
obs7
Flow 10
Main channel
Branch channel
x [m] (y=0.23m)
y [m] (x=0.14m)
Exp - init
Num-init
Exp-obs7
Num-obs7
init.
obs7

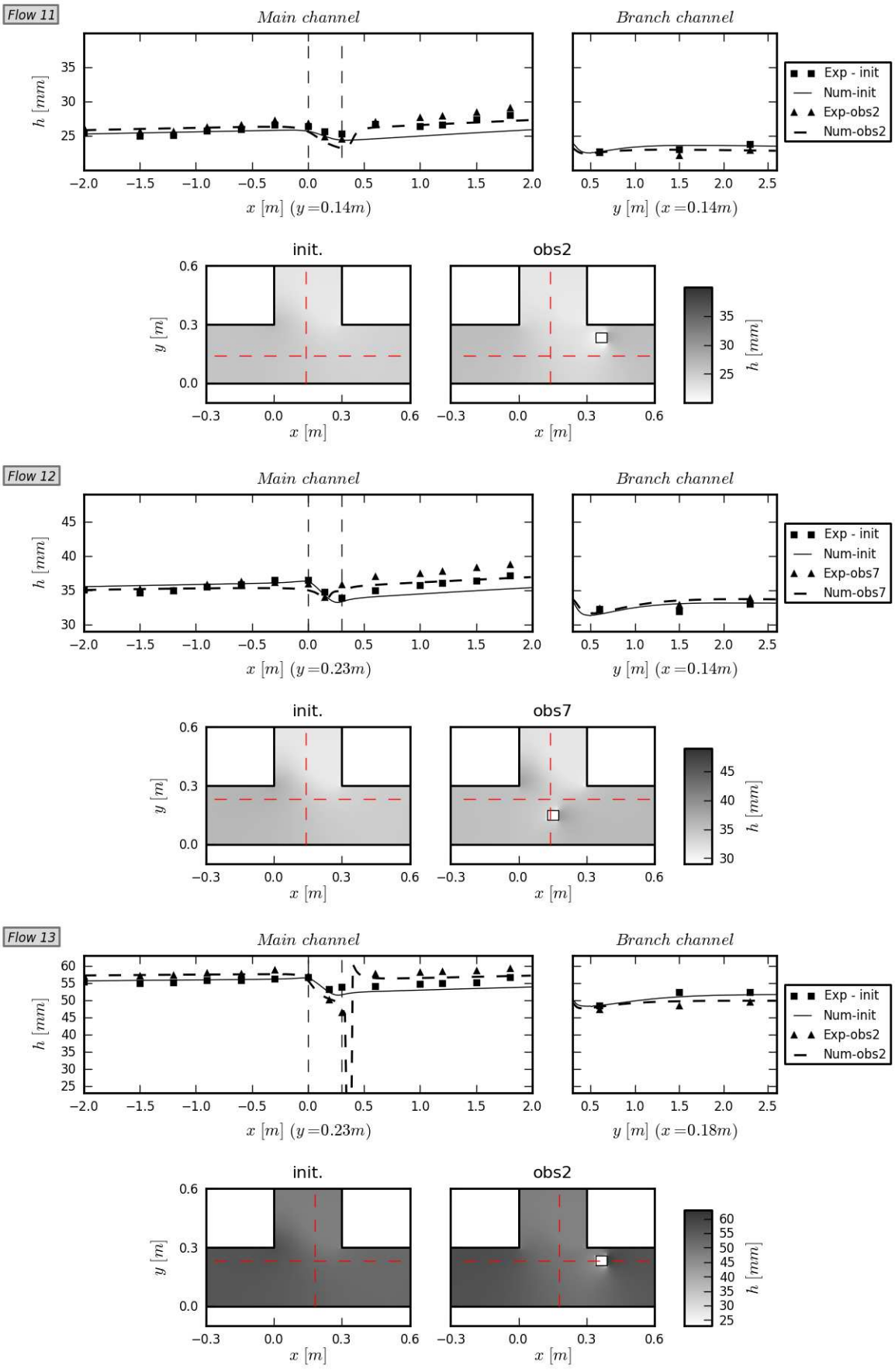
Flow 11
Main channel
Branch channel
h [mm]
x [m] (y=0.14m)
y [m] (x=0.14m)
Exp - init
Num-init
Exp-obs2
Num-obs2
init.
obs2
y [m]
x [m]
h [mm]
Flow 12
Main channel
Branch channel
x [m] (y=0.23m)
y [m] (x=0.14m)
Exp - init
Num-init
Exp-obs7
Num-obs7
init.
obs7
Flow 13
Main channel
Branch channel
x [m] (y=0.23m)
y [m] (x=0.18m)
Exp - init
Num-init
Exp-obs2
Num-obs2
init.
obs2

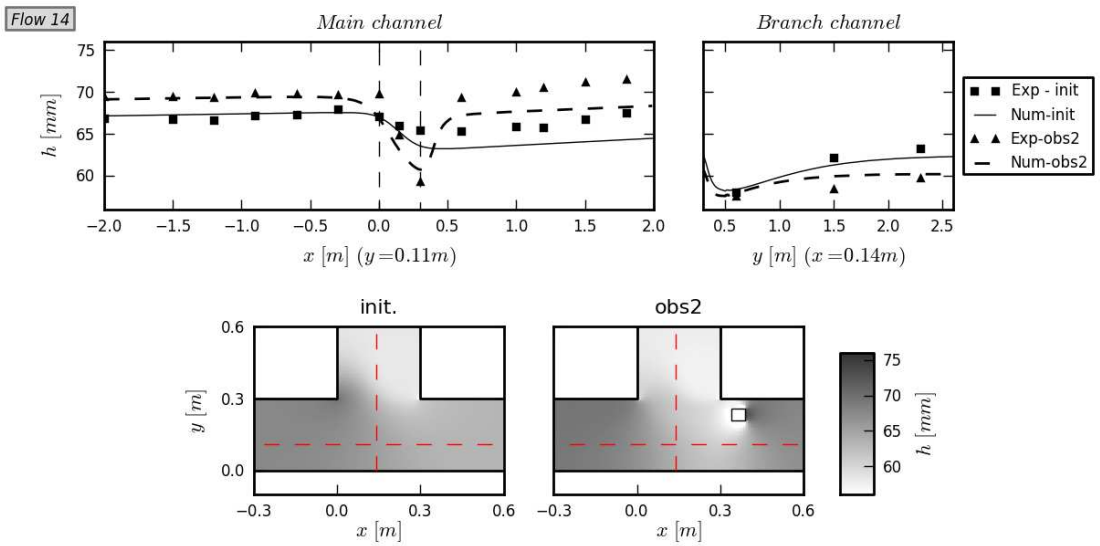

Figure A.2 : Top: comparison of measured and simulated (run 4) water depths along one line in both the main and branch channel, without obstacle (init.) and with one selected obstacle (obsi). Bottom : computed water depths around the junction without obstacle and with one obsatcle; red dash lines indicate measurements lines.

A.2.2 Velocity fields

A.2.2.1 LSPIV

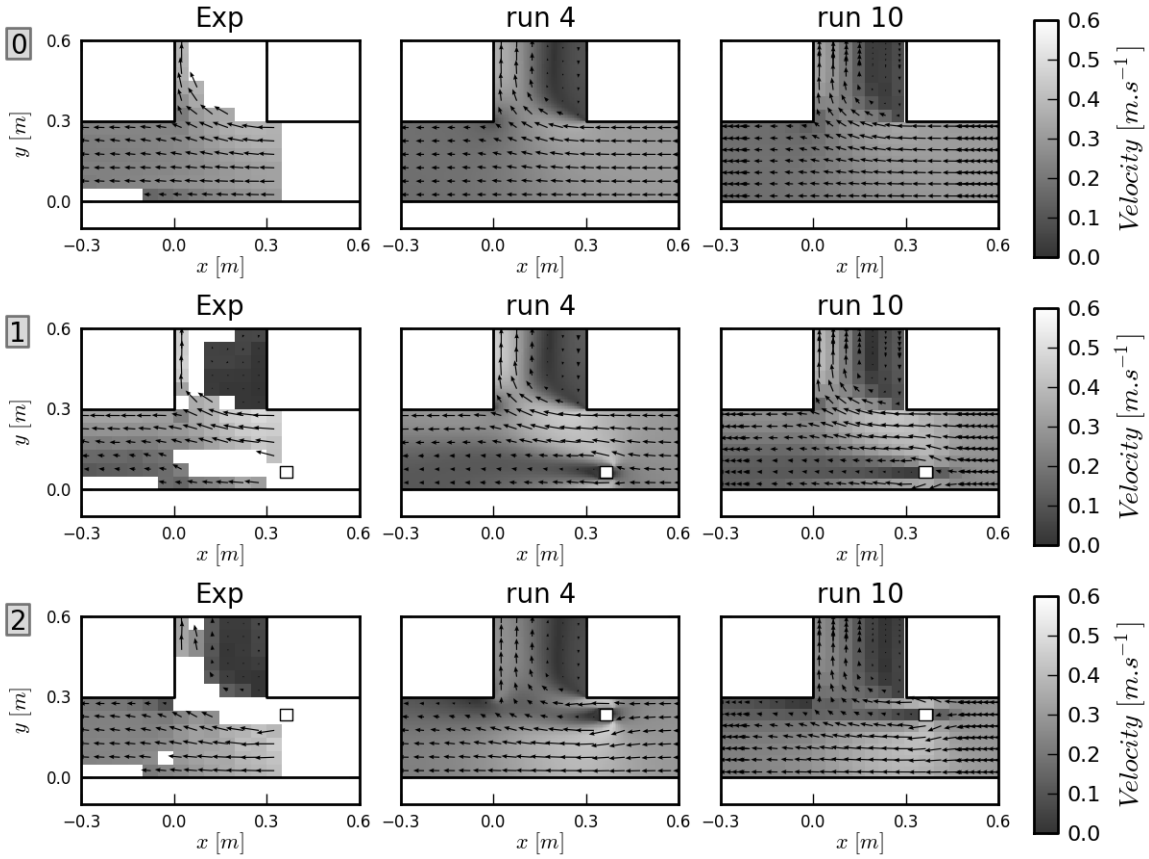

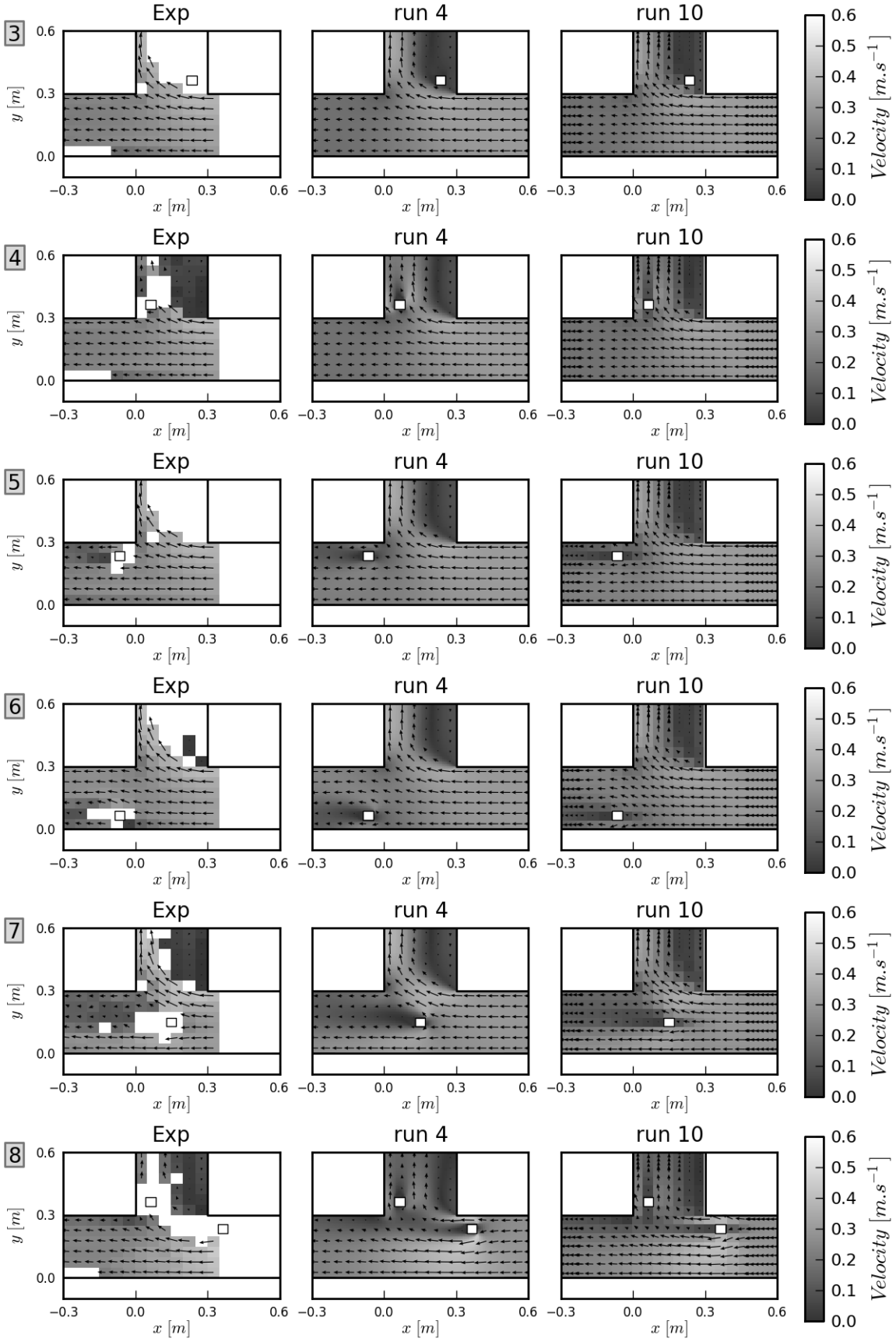
3
4
5
6
7
8
Exp
run 4
run 10
y [m]
x [m]
Velocity [m.s⁻¹]
0.0
0.1
0.2
0.3
0.4
0.5
0.6
−0.3
0.0
0.3
0.6

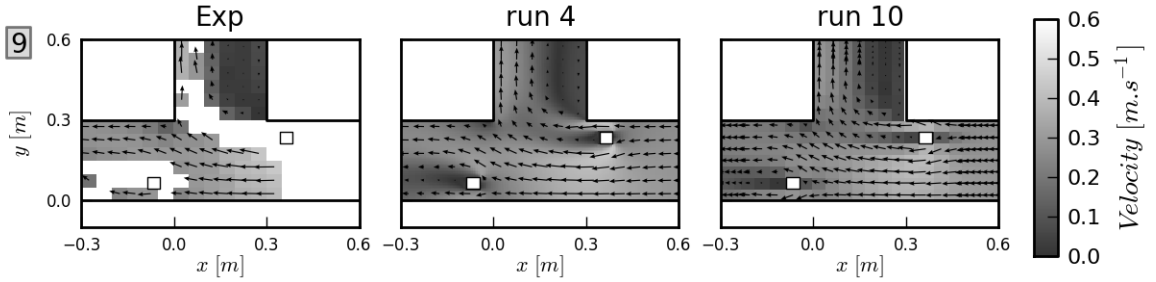

Figure A.3 : Measured surface velocities with LSPIV (Exp) and simulated depth averaged velocities with runs 4 and 10 for the reference flow 3

A.2.2.2 PIV

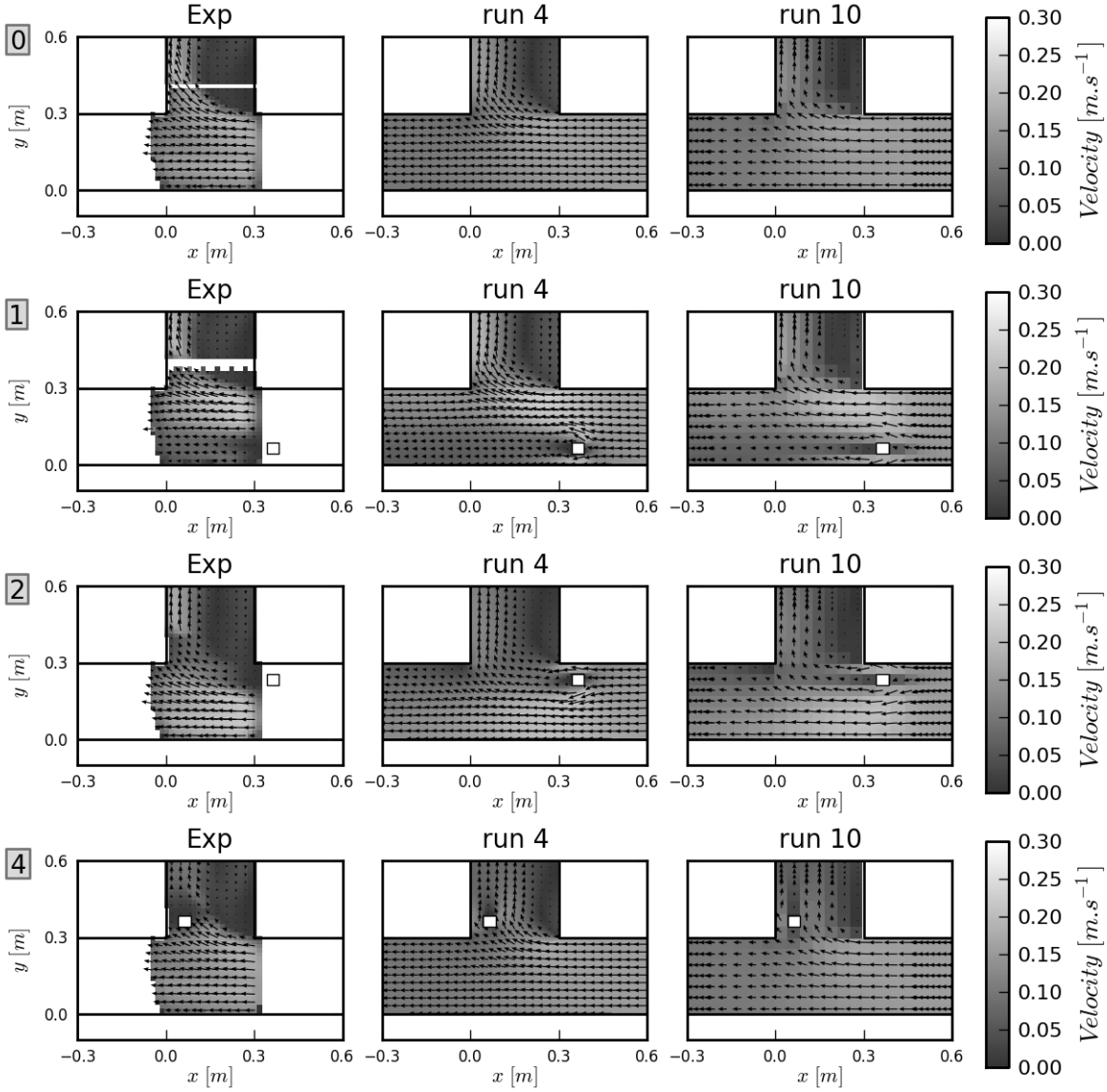

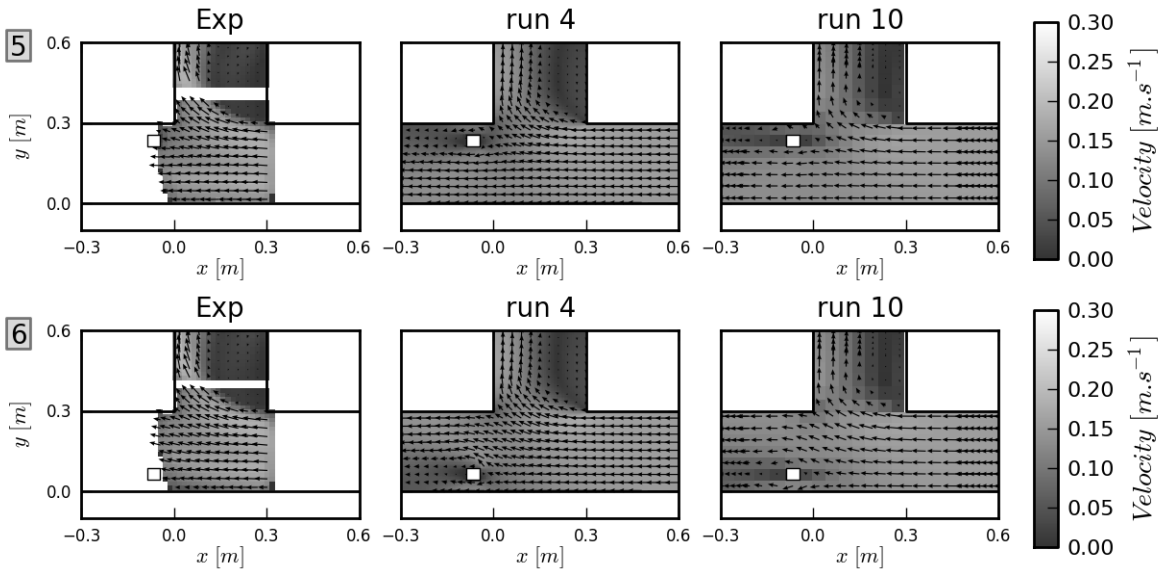

Figure A.4 : Measured velocities at z=3 cm with PIV (Exp) and simulated depth-averaged velocities with runs 4 and 10 for the flow 6

Appendix B
Detailed measurements carried out on the DPRI urban drainage model

B.3 Street and sidewalks elevation measurements

B.3.2 Measurements

The original design of the surface channel consists of a horizontal street (10 m long, 50cm wide) with 2cm high sidewalks. Temperatures in the laboratory as well as the different experimental facility modifications carried during the experiments may alter the actual topography of the street and the sidewalks. The model bottom topography has been measured 4 times during the 2 stays at the DPRI. One reference measurement was carried out at the beginning of each stay (Bathy1 and Bathy4), and 2 coarser additional measurements were carried out on the same day during the first stay, to check the influence of a model operation on the topography (Bathy 2 and Bathy3).

Name	Date	Number of points	Measurement of sidewalks	Comment
Bathy1	04/23/12	235	Yes	Initial measurement prior experiments including street flow
Bathy2	05/16/12	95	No	Measurement after a 24h pause in the experiments
Bathy3	05/16/12	95	No	Measurement just after a street flow generation and a quick drying
Bathy4	10/01/12	235	Yes	Control measurement of the second stay, after a street flow generation and a 6h drying

Table B.1 : Urban drainage model topography measurements carried out during the 2 stays at DPRI

B.3.3 Analysis of the street bottom elevation

The street bottom elevation is shown on Figure B.1 for the 4 measurements, the zero being the average measured elevation. There is a general pattern showing that a small pond exists in the centre of the street (x=4.5 m), and that the upstream (x~0 m) and downstream

(x~10 m) ends of the latter are higher than the average. Generating flows in the street slightly affects its topography, globally decreasing the bottom elevation, with more significant changes upstream (comparison of Bathy2 and Bathy3 measurements). Bathy4 shows that the topography still remains constant with time, except in the first 50 cm upstream. However this difference is likely to come from an error in the sensor positioning, which can be large in the very upstream and downstream parts.

Local average value $\overline{Z_b}$ and maximum deviation $Z_{b,max}$-$Z_{b,min}$ are considered respectively as the reference value and an uncertainty range to carry out experimental data analysis. These values are used through the thesis and are shown in the relevant chapter (Figure 4.4 p.76).

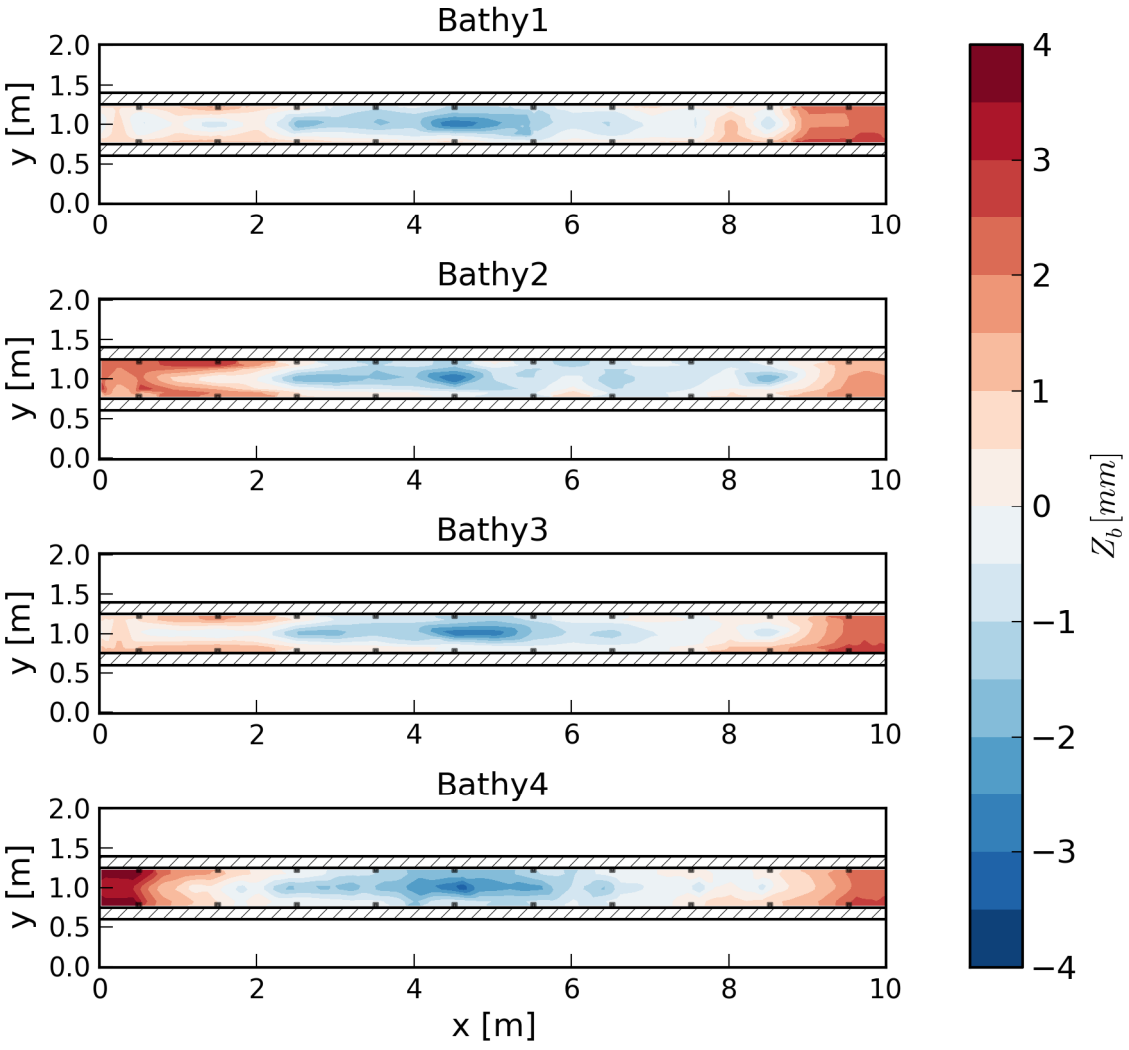

Figure B.1 : Measurements of the street bottom elevation. Street inlets location are indicated in gray squares and sidewalks with hashed rectangles

B.3.4 Analysis of the sidewalks elevation

The sidewalks elevation Z_{sw} has been measured for the series Bathy1 and Bathy4, along the axis x=0.675 (right side sidewalk) and x=1.325 m (left side sidewalk). Longitudinal variations are related to those observed for the street bottom. The average sidewalks elevation is around 20.2 and 19.3 mm respectively for the right and left sidewalks, which remains close to the original design (20 mm). As for the street bottom elevation, an average value and an error are defined based on these 2 series of measurements, and are used through the experimental analysis.

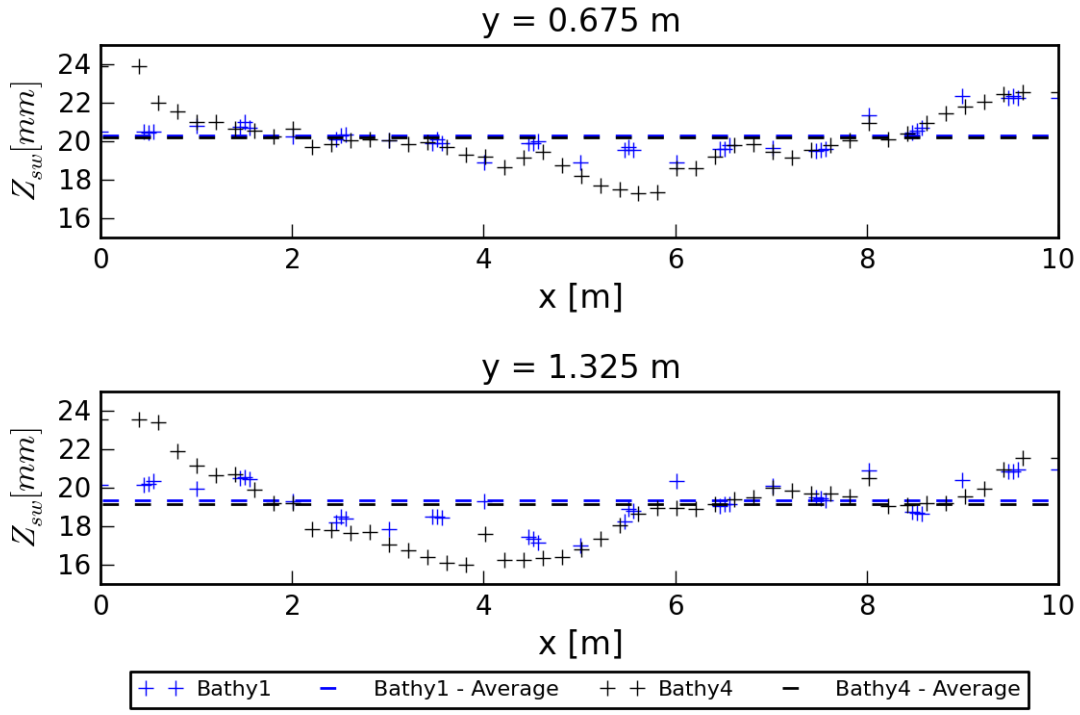

Figure B.2 : Longitudinal evolution of the right (top) and left (bottom) sidewalks elevation. Averaged values are indicated in dashed lines.

B.4 Flow Measurements

The following table sums up all steady flows measured, with:

- Q_{si} : upstream street flow discharge
- Q_{pi} : upstream pipe flow discharge
- $h_{p,dn}$: water level above the downstream end pipe bottom
- Q_{so} : downstream street flow discharge
- Q_{po} : downstream pipe flow discharge

- Q_{ex} : total exchange discharge between the street and the pipe
- $Q_{ex,err}$: mass balance error
- $\overline{h_s}$: average water depth in the street

LSPIV indicates whether Large Scale Particle Image Velocimetry was carried out or not.

		Q_{si} L.s^{-1}	Q_{pi} L.s^{-1}	$h_{p,dn}$ cm	Q_{so} L.s^{-1}	Q_{po} L.s^{-1}	Q_{ex} L.s^{-1}	$Q_{ex,err}$ L.s^{-1}	$\overline{h_s}$ cm	LSPIV
Street flow	S1	1.30	0.00	-	1.30	0.00	0.00	0.00	2.0	✓
	S2	0.52	0.00	-	0.52	0.00	0.00	0.00	1.3	✓
	S3	1.95	0.00	-	1.88	0.00	0.00	-0.07	3.0	✓
Pipe flow	P1	-	0.73	9.7	-	-	-	-	-	-
	P2	-	1.00	10.1	-	-	-	-	-	-
	P3	-	1.27	10.5	-	-	-	-	-	-
	P4	-	1.50	11.0	-	-	-	-	-	-
	P5	-	1.25	15.6	-	-	-	-	-	-
	P6	-	0.74	14.9	-	-	-	-	-	-
	P7	-	0.50	9.3	-	-	-	-	-	-
	P8	-	0.15	9.3	-	-	-	-	-	-
	P9	-	0.23	9.5	-	-	-	-	-	-
	P10	-	1.66	3.5	-	-	-	-	-	-
	P11	-	1.85	3.5	-	-	-	-	-	-
	P12	-	0.30	9.8	-	-	-	-	-	-
	P13	-	0.42	10.0	-	-	-	-	-	-
	P14	-	0.59	10.3	-	-	-	-	-	-
Drainage	D1	1.99	0.00	11.5	0.73	1.29	1.29	0.03	1.8	-
	D2	1.99	0.00	15.4	0.88	1.12	1.12	0.01	1.7	-
	D3	1.98	0.00	20.9	1.17	0.81	0.81	0.00	1.9	-
	D4	1.98	0.00	26.5	1.60	0.34	0.34	-0.03	2.2	-
	D5	1.99	0.00	12.7	0.70	1.30	1.30	0.01	2.8	✓
	D6	3.34	0.00	12.6	2.04	1.28	1.28	-0.02	2.5	✓
	D7	1.30	0.00	12.6	0.00	1.32	1.32	0.02	3.4	✓
	D8	2.02	0.00	12.6	0.63	1.40	1.40	0.02	5.1	✓
	D9	2.03	0.00	11.4	0.58	1.44	1.44	-0.01	5.0	-
	D10	2.03	0.00	15.6	0.73	1.28	1.28	-0.03	5.1	-
	D11	2.02	0.00	21.1	0.94	1.02	1.02	-0.06	5.3	-
	D12	2.01	0.00	26.6	1.25	0.68	0.68	-0.08	5.6	-
Overflow	O1	0.49	1.00	28.8	0.94	0.56	-0.44	0.00	1.8	✓
	O2	0.00	1.02	29.0	0.50	0.51	-0.51	-0.01	1.4	✓
	O3	0.49	0.99	29.9	0.93	0.56	-0.44	0.00	3.0	✓
	O4	2.50	1.00	29.9	2.92	0.56	-0.44	-0.03	3.0	✓
Drainage with one couple of	SI1	0.225	0.199	11.0	0.061	0.365	0.166	0.002	1.7	-
	SI1	0.225	0.199	11.9	0.066	0.360	0.161	0.001	1.7	-
	SI1	0.225	0.199	13.0	0.070	0.352	0.153	-0.001	1.7	-

		Q_{si} L.s^{-1}	Q_{pi} L.s^{-1}	$h_{p,dn}$ cm	Q_{so} L.s^{-1}	Q_{po} L.s^{-1}	Q_{ex} L.s^{-1}	$Q_{ex,err}$ L.s^{-1}	$\bar{h_s}$ cm	LSPIV
street inlets	SI1	0.225	0.198	14.0	0.075	0.346	0.148	-0.002	1.7	-
	SI1	0.224	0.198	14.8	0.080	0.342	0.144	0.000	1.7	-
	SI1	0.224	0.197	15.8	0.085	0.337	0.140	0.001	1.7	-
	SI1	0.224	0.198	16.8	0.090	0.329	0.131	-0.003	1.8	-
	SI1	0.224	0.198	17.7	0.094	0.322	0.124	-0.006	1.8	-
	SI1	0.223	0.198	18.7	0.101	0.317	0.119	-0.003	1.8	-
	SI1	0.224	0.198	19.8	0.109	0.309	0.111	-0.004	1.8	-
	SI1	0.222	0.198	20.8	0.114	0.300	0.102	-0.006	1.8	-
	SI1	0.223	0.197	21.9	0.122	0.292	0.095	-0.006	1.9	-
	SI1	0.222	0.198	22.6	0.129	0.284	0.086	-0.007	1.9	-
	SI1	0.222	0.197	23.7	0.140	0.270	0.073	-0.009	1.9	-
	SI1	0.223	0.198	24.6	0.147	0.259	0.061	-0.015	1.9	-
	SI1	0.221	0.197	25.5	0.158	0.243	0.046	-0.016	2.0	-
	SI1	0.222	0.197	26.2	0.173	0.222	0.025	-0.025	2.0	-
	SI2	1.084	0.199	10.3	0.907	0.374	0.175	-0.002	1.8	-
	SI2	1.085	0.200	11.9	0.916	0.365	0.165	-0.005	1.8	-
	SI2	1.085	0.199	12.8	0.922	0.360	0.161	-0.003	1.8	-
	SI2	1.086	0.200	13.7	0.930	0.353	0.153	-0.002	1.8	-
	SI2	1.085	0.200	14.9	0.941	0.347	0.147	0.003	1.8	-
	SI2	1.085	0.199	16.0	0.945	0.341	0.142	0.002	1.8	-
	SI2	1.085	0.198	17.1	0.947	0.333	0.135	-0.004	1.9	-
	SI2	1.087	0.198	17.9	0.957	0.328	0.130	0.000	1.8	-
	SI2	1.087	0.198	18.7	0.966	0.322	0.124	0.003	1.9	-
	SI2	1.087	0.198	19.8	0.972	0.315	0.117	0.002	1.9	-
	SI2	1.087	0.198	20.8	0.983	0.306	0.108	0.004	1.9	-
	SI2	1.086	0.198	21.7	0.991	0.299	0.101	0.006	1.9	-
	SI2	1.087	0.198	22.8	0.998	0.285	0.087	-0.002	1.9	-
	SI2	1.087	0.198	23.8	1.013	0.273	0.075	0.002	1.9	-
	SI2	1.084	0.198	24.7	1.024	0.259	0.061	0.001	1.9	-
	SI2	1.087	0.198	25.5	1.033	0.245	0.047	-0.007	2.0	-
	SI2	1.084	0.197	26.3	1.053	0.216	0.019	-0.012	2.0	-
	SI3	1.760	0.198	10.3	1.566	0.375	0.177	-0.017	1.9	-
	SI3	1.759	0.199	12.0	1.584	0.367	0.168	-0.006	1.9	-
	SI3	1.759	0.198	12.9	1.581	0.359	0.161	-0.017	1.9	-
	SI3	1.758	0.197	13.9	1.587	0.356	0.159	-0.012	2.0	-
	SI3	1.758	0.198	14.8	1.593	0.351	0.153	-0.012	2.0	-
	SI3	1.759	0.198	15.8	1.593	0.345	0.147	-0.019	2.0	-
	SI3	1.758	0.198	16.9	1.606	0.339	0.141	-0.012	2.0	-
	SI3	1.758	0.197	17.8	1.609	0.331	0.134	-0.015	2.0	-
	SI3	1.758	0.197	18.7	1.624	0.322	0.125	-0.009	2.0	-
	SI3	1.758	0.197	19.8	1.624	0.318	0.121	-0.012	2.1	-
	SI3	1.759	0.197	20.7	1.637	0.310	0.113	-0.009	2.1	-
	SI3	1.759	0.197	21.7	1.637	0.300	0.103	-0.020	2.1	-
	SI3	1.757	0.197	22.9	1.649	0.288	0.091	-0.017	2.1	-

	Q_{si} L.s^{-1}	Q_{pi} L.s^{-1}	$h_{p,dn}$ cm	Q_{so} L.s^{-1}	Q_{po} L.s^{-1}	Q_{ex} L.s^{-1}	$Q_{ex,err}$ L.s^{-1}	$\overline{h_s}$ cm	LSPIV
SI3	1.759	0.197	23.7	1.655	0.276	0.079	-0.025	2.1	-
SI3	1.758	0.197	24.7	1.674	0.262	0.065	-0.019	2.2	-
SI3	1.757	0.196	25.4	1.680	0.253	0.057	-0.019	2.2	-
SI3	1.757	0.197	26.1	1.699	0.235	0.038	-0.019	2.2	-
SI4	0.216	1.001	22.8	0.155	1.107	0.061	0.044	2.0	-
SI4	0.215	1.001	21.9	0.143	1.121	0.072	0.048	2.0	-
SI4	0.216	1.001	21.0	0.130	1.126	0.086	0.039	1.9	-
SI4	0.216	1.002	20.0	0.122	1.141	0.094	0.045	1.9	-
SI4	0.215	1.002	18.9	0.114	1.146	0.101	0.043	1.9	-
SI4	0.216	1.002	17.6	0.096	1.155	0.120	0.033	1.8	-
SI4	0.215	1.013	15.9	0.079	1.165	0.136	0.017	1.8	-
SI4	0.216	1.014	14.8	0.071	1.190	0.145	0.031	1.8	-
SI4	0.217	1.014	14.0	0.067	1.200	0.150	0.036	1.8	-
SI4	0.216	1.014	12.6	0.060	1.205	0.156	0.035	1.8	-
SI4	0.216	1.011	11.4	0.055	1.210	0.161	0.038	1.7	-
SI4	0.216	1.010	10.6	0.052	1.215	0.164	0.041	1.7	-
SI4	0.217	1.010	9.4	0.045	1.215	0.172	0.033	1.7	-
SI4	0.216	1.013	8.7	0.042	1.220	0.174	0.034	1.7	-

Table B.2 : List of the steady flows measured on the experimental urban drainage model

Appendix C
Processing of the DPRI urban drainage model experimental data

C.1 Street flow discharge computation

Flow discharges in the experimental model are only known at both ends of the street and the pipe (Q_{si}, Q_{pi}, Q_{so} and Q_{po}), and there is no measurement of the exchange discharge through the exchange structures. The latter would be an interesting improvement to analyse the exchanges. Experimental measurements have been used to compute the street flow discharge evolution and to derive the corresponding flow exchanges. To compute flow discharges along the street, the following data are available:

- Water elevation and bathymetry along the street, with an overall accuracy of +/- 0.3 mm
- Surface velocity measured with LSPIV, with errors estimated to be less than 0.5 cm/s, except near the street inlets.

For all flows, out of the street inlet influence area, the water elevation is almost constant along y axis, and so at a specific cross section, variations of the water depth are mainly due to the bathymetry variations. However, surface velocities vary along y axis, depending on the importance of the drainage or overflow processes.

C.1.1 Computation method

The velocity field is interpolated on a regular 5 cm grid which eases the discharge computation and is justified by the fact that LSPIV data are available on a roughly 5cm grid. For the water depths, the density of point varies with the experimental flows, but the longitudinal evolution remains very low, so that a linear interpolation on such a fine grid is reasonable. The *raw* street flow discharge is then computed by integrating the linear discharge along y axis:

$$Q_{s,LSPIV0}(x) = \int_{0.6}^{1.4} \left(Z_s(x) - Z_b(x,y)\right) \cdot u_{LSPIV}(x,y) \cdot dy \qquad C.1$$

where Z_s is the street water elevation, Z_b the street bottom elevation, and u_{LSPIV} is the surface velocity along x axis measured with LSPIV. To account for the vertical velocity distribution, a velocity correction factor C_v is introduced to derive the actual street flow discharge:

$$Q_{s,LSPIV}(x) = C_v(x) \cdot Q_{s,LSPIV0}(x) \qquad C.2$$

C_v should actually vary with both x and y and be included directly in Eq. C.2, but regarding the available experimental data and the restricted aim of the present computation, we assume a constant coefficient over a cross section. For the water depths, the errors due to the sensor positioning (vertically) are strongly reduced when subtracting bed elevations to water elevations, and the main error source lies in the street bottom elevation. For the velocity, the error associated to the LSPIV computation is very low and is thus not considered : ortho-rectification effects are strongly limited by the camera position, particle seeding ensure that no areas are filmed without particles except near the street inlets and along the walls/sidewalks, and time convergence of velocities is always respected. However the uncertainty on the vertical velocity distribution may be important for the following reasons:

- There is no direct measurement of this distribution, and the actual flow discharge is only known at the upstream and downstream ends of the street.
- The vertical velocity distribution can be affected by the exchange process, the local variations of the street bottom elevation, and the interface street/sidewalks

Particularly, because of these local variations of the vertical velocity profile, it is impossible to predict a velocity correction factor by using a log-law or other theoretical equations. Therefore, street flow discharge computations are carried out first on constant street flows (without exchanges, so that the street flow discharge is known at each section) to compute empirical values of the velocity correction factor, and assess the accuracy of the method.

C.1.2 Application to street flows without interaction with the pipe

For the three street flows S1, S2 and S3 (defined in Table B.2), the street flow discharge is constant and can be used to estimate the velocity correction factor C_v. The latter is shown on Figure C.1, with an uncertainty range derived from the street bottom elevation uncertainty. Clearly, C_v cannot be assumed to be constant, even for a given flow. This coefficient is strongly impacted by the feeding system for x<3 m, and variations also occur for x>7 m, because of the downstream condition or of the bathymetry variations in this area. Otherwise, in the centre part of the channel, variations of the coefficient are smaller and more continuous (except, of course, at the location of the street inlets at x=0.5m, x=1.5m …etc.). For the flow S2, C_v values are particularly high and may be related to the very shallowness of the flow and its low velocities.

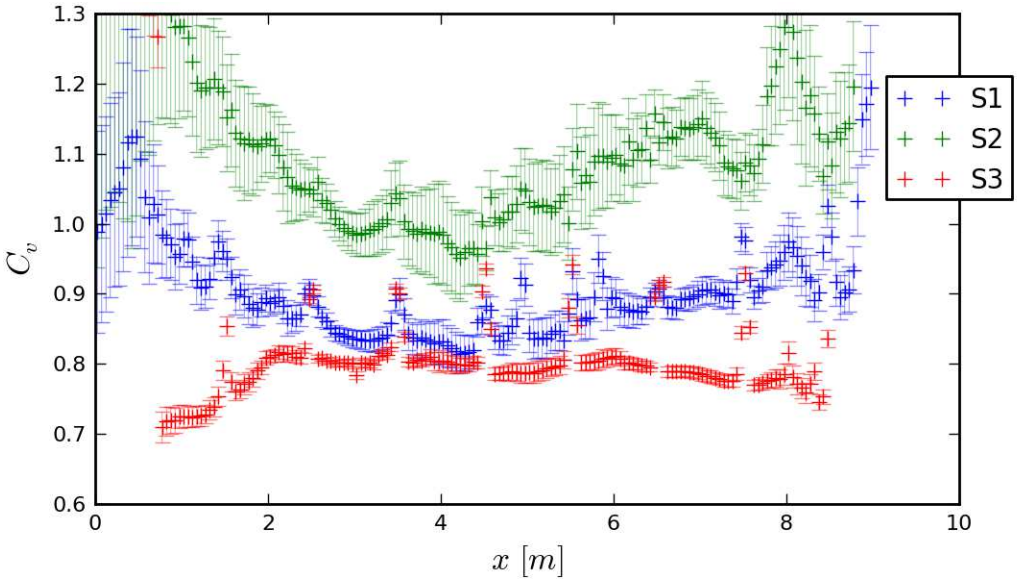

Figure C.1: Velocity correction factor estimated for the street flows S1, S2 and S3

Given these results, the accuracy of a street flow discharge computation for a flow with exchanges with the pipe is very low. The raw street flow discharge ($Q_{s,LSPIV0}$) can be computed, but estimating local velocity correction factors remains too uncertain to derive the actual street flow discharge, because:

- Exchanges with the pipe will generate local additional 3D effects and variations of the coefficient C_v.

- The coefficient C_v strongly vary in the upstream and downstream ends of the street, and therefore cannot be locally calibrated using the upstream and downstream street flow discharge measurements.

Considering uncertainties due to the coefficient C_v and to the street bottom elevation, the computation of the street flow discharge based on the experimental data would lead to typical uncertainties of 10%. Keeping in mind that the exchange discharge at a given couple of street inlets is only a few per cent of the local street flow discharge, deriving exchange discharges with the present computation would lead to very large errors (more than 100%). Therefore, this computation method is not applied to steady flows with exchanges and we conclude that with the present experimental data, the local exchange discharges cannot be derived.

C.2 Unsteady flow measurements

A series of unsteady flows have been measured, for which a specific instrumentation of the experimental model has been required, as well as a specific experimental data post-processing, which are detailed here after. As the unsteady conditions were manually controlled and could not be accurately repeated, each unsteady flow was generated and recorded once. 10 flows were generated in a row (total experiment duration of slightly more than one hour) and four were selected for the thesis.

C.2.1 Instrumentation

To record the time evolution of the street and pipe flow characteristics, the following instrumentation has been set up (Figure C.2):

- 4 video cameras to record :
  - The water level at piezometer P2 (x=2m)
  - The water level at piezometer P5 (x=5m) and the water depth at the centre of the street (x=5 m, y=5m)
  - The water level at piezometer P8 (x=8m)
  - The pipe and street flow meter display (inlet flows)
- 3 water gauges (resistive probes linked to a data logger) to record the water elevation in :

- The street downstream measurement tank
- The pipe downstream measurement tank
- The pipe downstream control tank

This instrumentation choice permits to record time evolution of the street water depth at one location, and pipe piezometric head at 3 points, which is consistent with the spatial evolution observed for steady flows (greater variations of the pipe piezometer head than the street water depth). The inlet and outlet pipe and street flow discharge recordings (through upstream flow meters and downstream measurement tanks) permits to have a global description of the exchange processes. The time evolution of the pipe downstream piezometric head (approximately equal to the pipe control tank water level) completes the boundary conditions recording and so is useful for numerical simulations. The feeding tanks water level could not be instrumented, so the storage effects of these tanks cannot be directly accounted for in the post processing of experimental data.

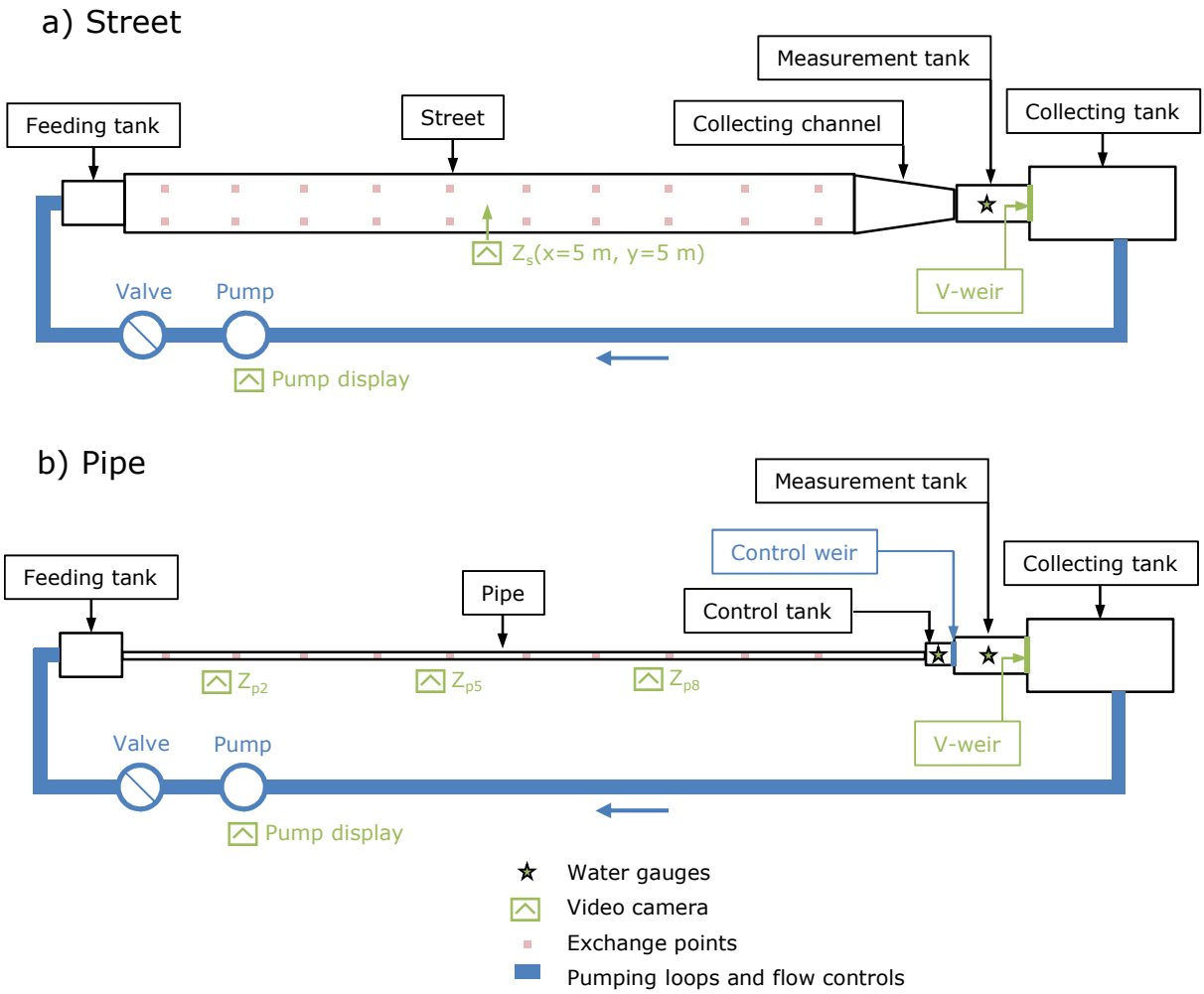

Figure C.2: Scheme of the urban drainage model pumping loops and instrumentation for unsteady flows (top view)

C.2.2 Video camera data processing

Videos were recorded at 30Hz, from which images were extracted at specific time steps. Image analysis is manually done. Table C.1 sums up the time step and the number of data points extracted.

	Q_{si}	Q_{pi}	Z_s	Z_{p2}	Z_{p5}	Z_{p8}
Time step (s)	1.0	1.0	5.0	5.0	5.0	5.0
Number of points	4565	4565	795	806	797	736

Table C.1 : Video data extraction parameters for unsteady flows

C.2.3 Water gauges data processing

Calibration of water gauges consisted in doing linear regressions on reference measurements, with regression coefficients all greater than 0.999, so that the water level for

each water gauge is assumed to be measured with negligible errors. During experiments, the acquisition frequency is set to 10 Hz; then data are filtered using a low pass filter to reduce the noise. The water elevation in the pipe control tank can be directly used, but the water elevations upstream of the V-notch weirs in the downstream measurement tanks need to be transformed into an equivalent flow discharge. The stage-discharge relationship of each V-notch weir has been previously calibrated, but the storage effects of the intermediary tanks separating the street and pipe outlets and the V-notch weirs have to be considered. We consider that the V-notch weirs stage-discharge relationships (previously established for steady flows) still lead to the right measurement tanks outflow discharges, and that the storage effects of the intermediary tanks can be directly calculated without considering time shifts. For the street, this leads to the following equation:

$$Q_{so}(t) = Q_{so,mes}(t) + A_{s,mes}\frac{dZ_{so,mes}}{dt}(t) \qquad C.3$$

with $Q_{so,mes}$, $A_{s,mes}$ and $Z_{so,mes}$ respectively the street measurement tank outflow discharge, horizontal area and water elevation, and Q_{so} the street outflow discharge. A similar equation is derived for the pipe discharge, with two intermediary tanks:

$$Q_{po}(t) = Q_{po,mes}(t) + A_{p,mes}\frac{dZ_{po,mes}}{dt}(t) + A_{p,ctrl}\frac{dZ_{po,ctrl}}{dt}(t) \qquad C.4$$

with $Q_{po,mes}$, $A_{p,mes}$ and $Z_{po,mes}$ respectively the pipe measurement tank outflow discharge, horizontal area and water elevation, $A_{p,ctrl}$ and $Z_{po,ctrl}$ respectively the pipe control tank horizontal area and water elevation, and Q_{po} the pipe outflow discharge. Use of these equations requires computing time derivatives of the 3 water elevations recorded with the water gauges. This is done by using a spline function and a smoothing over 20 points (equivalent to a 2 seconds period smoothing). An example of this treatment is shown on Figure C.3 for the case US1. The tanks storage effects appear to be significant, for both amplitude and timing of the pipe and street outflow hydrographs (e.g. time shift of 30s between the street measurement tank outflow peak time and the actual street outflow peak time). The derived pipe outflow discharge seems less well corrected, as there are still important fluctuations, which have not any physical meaning considering the continuous evolution of the exchange processes in this unsteady flow. This is due to the presence of two intermediary tanks, with combined effects that may not be properly modelled under the previous assumptions, especially the fact that we omit the flow delays between each measurement points. As a result, only the measurement of unsteady street outflow discharge

is used in the thesis, as it is considered more reliable and should contain almost all information on the exchange process at the street scale.

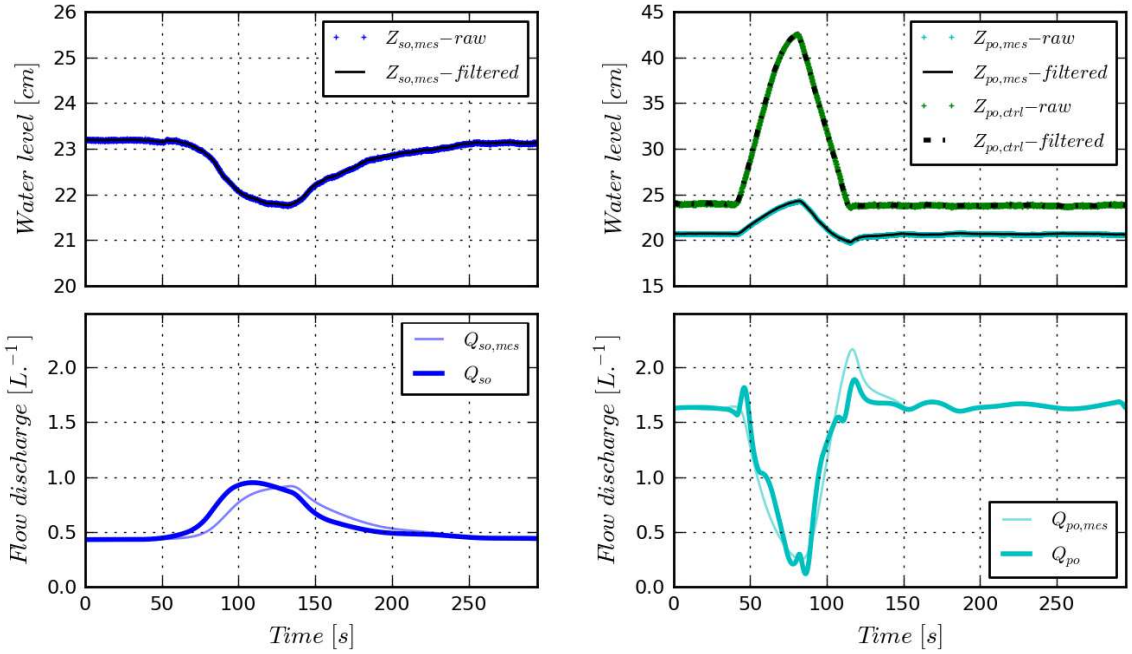

Figure C.3: Post-processing of the street and pipe outflow discharges for the case US1. Top: raw conversion of water gauges signal into water levels and data filtering. Bottom: derivation of street and pipe flow discharges from tanks water level measurements.

Appendix D
Development of an exchange model for the DPRI urban drainage model

D.1 Exchange structure

The street inlet grid is made of plastic grid of 5 cm by 5 cm, of a thickness w of around 0.5mm, with circular holes of diameter d_g 2.8 mm located every l_g = 3.8 mm (Figure D.1). The horizontal dimensions given here only consider the effective area of the grid, as the edges are used to fix the grid on the street. The ratio of void over total surface is f_g = 0.44. The drainage box under the street inlet grid has the same horizontal dimensions, and its height is 5 cm (H_{db}). The drainage tube is made of flexible plastic, with an inner diameter d_t of 1cm. Its length l_t from the bottom of the drainage box to the main pipe is 30 cm. The drainage pipe has an inner diameter d_p of 5 cm and is in plastic.

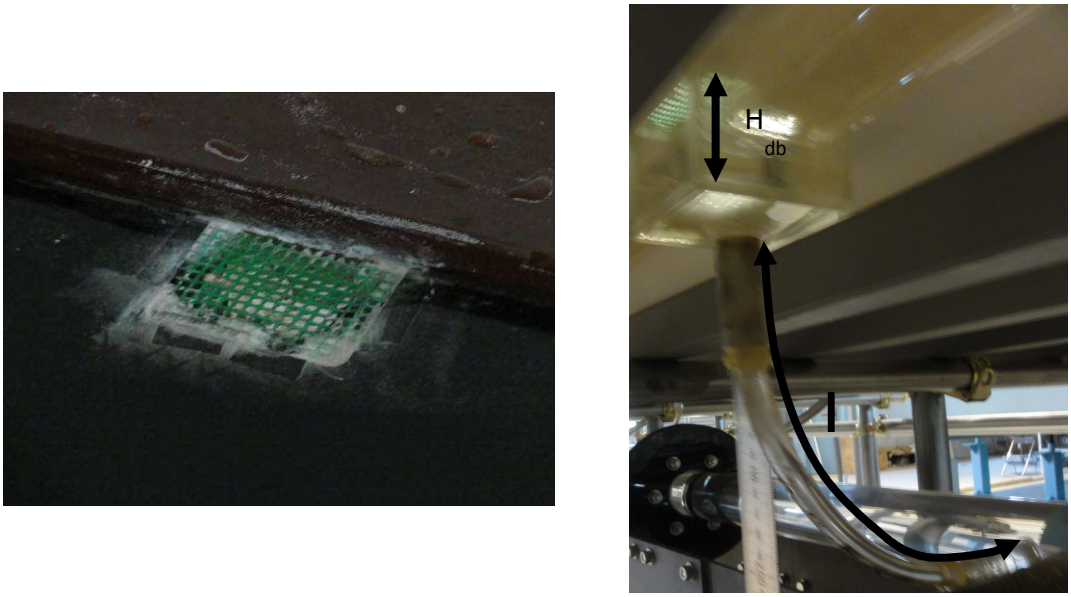

Figure D.1 : Photos of a street inlet grid (left) and of a connecting structure (right)

D.2 Modelling principle

The flow through the drainage box and the drainage tube is always pressurized, so that the exchange discharge can be computed using the Bernoulli principle. The latter is written between a section just above the street inlet grid (section 1 on the figure below) and a section in the main drainage pipe (section 5), so at both ends of the exchange structure.

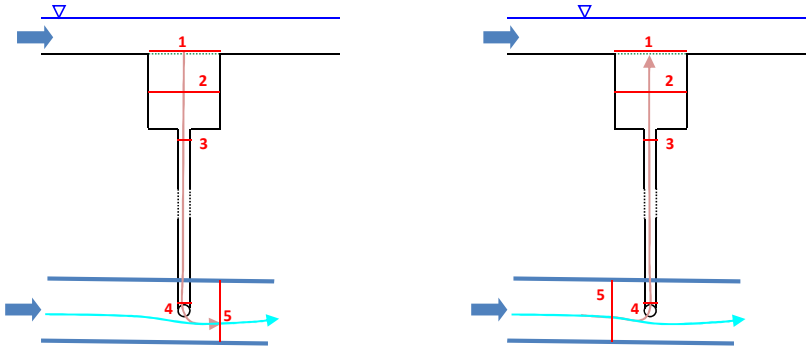

Figure D.2 : Sections for Bernoulli principle (left: drainage, right: overflow)

The mean head H on the section is:

$$H = \gamma \frac{V^2}{2g} + z + \frac{p}{\rho g} \qquad D.1$$

With V the mean velocity on the section, z the elevation and p the pressure at a chosen point of the section, g the acceleration due to the gravity, and γ the kinetic energy correction coefficient (or Coriolis coefficient). The latter accounts for the non-uniform velocity distribution across the section and is always larger than 1. However in the following, for simplicity, we will neglect its effect and assume it equals unity (γ=1).

Applying the Bernoulli principle then yields to the following equations for respectively drainage (D.2) and overflow (D.3) configurations:

$$\Delta H_{1-5} = \Delta H_{1-2} + \Delta H_{2-3} + \Delta H_{3-4} + \Delta H_{4-5} \qquad D.2$$

$$\Delta H_{1-5} = -(\Delta H_{2-1} + \Delta H_{3-2} + \Delta H_{4-3} + \Delta H_{5-4}) \qquad D.3$$

with $\Delta H_{1\text{-}5}$ the total head losses between upper and lower ends of the exchange flow, decomposed into the following head losses for drainage:

- the street inlet grid ($\Delta H_{1\text{-}2}$)
- the inlet of the tube ($\Delta H_{2\text{-}3}$)
- the tube ($\Delta H_{3\text{-}4}$)
- the combining flows at the junction between the tube and the pipe ($\Delta H_{4\text{-}5}$)

and for overflow:

- the dividing flows at the junction between the tube and the pipe ($\Delta H_{5\text{-}4}$)
- the tube ($\Delta H_{4\text{-}3}$)
- the outlet of the tube ($\Delta H_{3\text{-}2}$)
- the street inlet grid ($\Delta H_{2\text{-}1}$)

Note that to ensure continuity the total head losses are always expressed from point 1 to point 5 and can therefore be negative, whereas particular head losses are formulated according to the direction of the flow, hence the minus in Eq. D.3. These different head losses terms can be expressed with common hydraulic equations and abacuses. The following section details the various formulations found in the literature.

D.3 Head losses formulation

D.3.1 General consideration

Head losses are commonly expressed as a part of the flow kinetic energy:

$$\Delta H = K \cdot \frac{V^2}{2g} \qquad D.4$$

With K a coefficient derived from experimental or analytical work, and V the bulk velocity of flow at a specific location around the hydraulic structure that generates the head losses. For a given head loss formulation, K usually varies with the Reynolds number Re, and with the geometry of the hydraulic structure. Even if extensive studies deal with head losses, one must be careful on the validity range of the various formulations. In particular, in our experimental model, the Reynolds numbers are around $5\text{x}10^2 – 1\text{x}10^4$ and $2.5\text{x}10^3 – 4\text{x}10^4$ for respectively the exchange and the pipe flows. Depending on the head loss types, the dependence to the Reynolds number for the head loss coefficients is found to occur for Reynolds numbers lower than 10^4 - 10^6, which clearly shows that in our cases all coefficients will have dependencies on Re. Moreover, the transition between laminar and turbulent flows

(usually considered as 2000 < Re < 4000) is associated to important variations of the head losses coefficients, and may not be precisely known.

Idelchik and Steinberg (1996) and Miller (1978) summarized extensive set of experimental data and analytical work on head losses for pressurized flows. These books are used as references here, and formulations taken from them will be quoted with detailed section numbers. Additional formulations and considerations are taken from journal papers.

D.3.2 Formulation for each hydraulic structure

D.3.2.1 Street inlet grid

The head losses through a grid can be expressed as the head losses of a diaphragm of the equivalent free flow area (Idelchik and Steinberg 1996, §8.2.2), and the head loss coefficient is related to the averaged velocity through the grid/diaphragm. Formulas found apply for grids located across a pipe or a channel and directly perpendicular to the flow.

Here, for a drainage case the surface flow is parallel to the grid plane upstream of the street inlet then it becomes almost perpendicular when approaching the grid. For an overflow, the flow exiting the drainage tube arrives perpendicular to the grid (vertical jet) but becomes horizontal when interacting with the shallow street flow (Figure D.2). We assume that the equations still apply. The head loss coefficient is expressed as follows (Idelchik and Steinberg 1996, §4.16, Eq. 4.19):

$$K_{1-2} = \xi_\varphi + \varepsilon_0 \cdot \left(1 + 0.707\sqrt{1 - f_g} - f_g\right)^2 \qquad D.5$$

where ξ_φ and ε_0 are two empirical coefficients depending on the Reynolds number, f_g is the ratio of equivalent flow area of the grid to the drainage box area (equals to 0.44 in the experiment). The empirical coefficients and the resulting flow coefficient are given on Figure D.3. The head loss coefficient varies from 0.8 to 1.8 depending on the flow velocity. When using this formula, the Reynolds number is calculated for the flow through a grid hole:

$$Re_{12} = \frac{v_g d_g}{\nu} \qquad D.6$$

where v_g is the average flow velocity through the street inlet grid, d_g is the diameter of a grid hole and ν the kinematic viscosity of water.

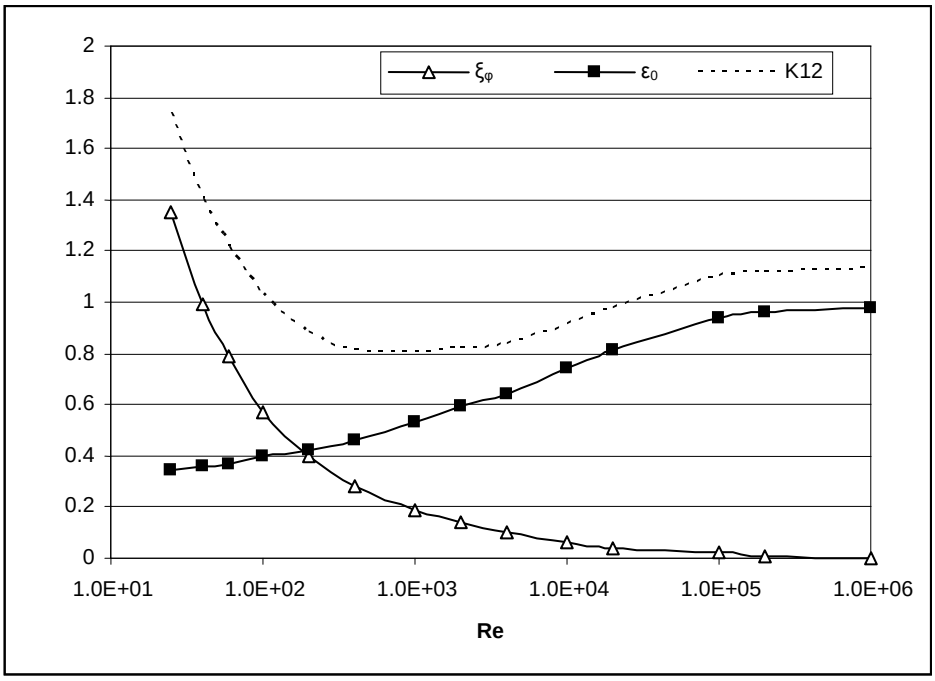

Figure D.3 : Empirical coefficients used to compute the grid head loss coefficient and resulting head loss coefficient

For drainage flows, the flow velocity to use can be assumed to be equal to the average flow velocity through the drainage box because i) the velocities in the street are usually an order of magnitude smaller than the velocities in the drainage tube, and ii) the contraction of the flow entering the drainage tube occurs near the inlet and should not affect the flow through the grid. Then we introduce a velocity factor to pass from the drainage tube to the drainage box velocity: $\alpha_{1\text{-}2}=A_t/A_{db}$. However, for overflow, the jet at the outlet of the drainage tube is certainly not spread on the whole drainage box section when it arrives at the street inlet grid, so the velocity profile just upstream of the grid is subject to uncertainties. The solution proposed is to use elements of free round jet theory to have an evaluation of the flow velocity profile (see end of the next sub section D.3.2.2).

D.3.2.2 Junction drainage tube/drainage box

Here two cases have to be distinguished according to the direction of the exchange flow. In both cases, the velocity to consider for the computation of the head losses is the flow velocity in the drainage tube V_3. The Reynolds number to consider is also relative to the drainage tube flow.

Drainage:

The head loss coefficient is expressed with the following equation (Idelchik and Steinberg 1996, §3.9 and abacus 3.10):

$$K_{2-3} = K' \cdot \left(1 - \frac{A_t}{A_{db}}\right) \qquad D.7$$

With A_t the flow section of the drainage tube, A_{db} the flow section of the drainage box and K' an empirical coefficient depending on the Reynolds number and the ratio $w=A_t/A_{db}$. In the facility, $w\approx0.04$, but the abacus only gives values for $w=0.1$ or more. An extrapolation is done for the experimental configuration, by considering that the increase of K_{2-3} between $w=0.1$ and $w=0.04$ is the same as the one between $w=0.2$ and $w=0.1$:

$$K_{2-3,chosen} = K_{2-3}(w = 0.1) + \left(K_{2-3}(w = 0.1) - K_{2-3}(w = 0.2)\right) \qquad D.8$$

This extrapolation is subjective (although variations observed between $w=0.3$, $w=0.2$ and $w=0.1$ support this approach) but should be closer to the reality than the coefficient given for $w=0.1$. The coefficients are reported on Figure D.4 for three values of A_t/A_{db}. (Idelchik and Steinberg 1996) formulation suggests that there is a peak in the coefficient for the transition laminar/turbulent.

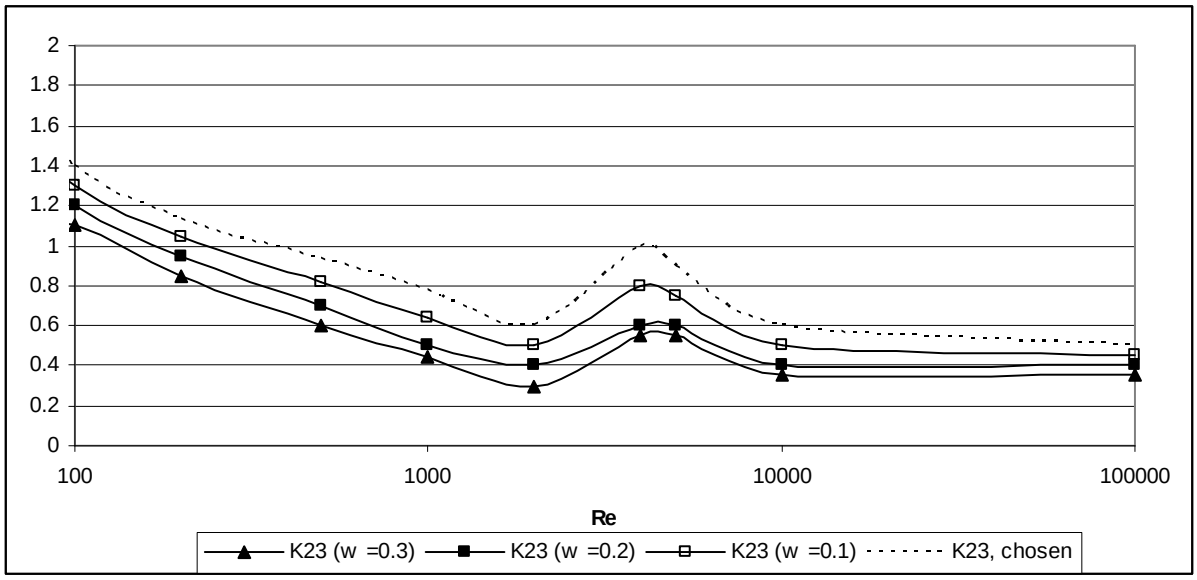

Figure D.4 : Values of K_{2-3} for different opening ratio and Reynolds number and extrapolation for the experimental facility

Overflow:

The head losses at the outlet of the drainage pipe are difficult to model as the jet flowing out of the tube will flow through the grid and reach the surface of the street flow before the energy dissipation is completed. The interaction of the jet with the street inlet grid and the free surface flow cannot be directly related to any simple configurations found in the literature.

Considering an abrupt opening from the drainage pipe to the drainage box may not be adapted. The length to recover static pressure is evaluated to be at least 5 times the large diameter (width of the drainage box in our case) in (Miller 1978, Fig. 5.67) and between 8 and 12 diameters in (Idelchik and Steinberg 1996), whereas the street level is located only one equivalent diameter above the outlet of the drainage tube. Miller (1978) also suggests that 50% of the head losses occur within a length of 2 diameters after the tube outlet.

We choose to model the head losses of the tube outlet as the total loss of the kinetic energy of the jet:

$$\Delta H_{3-2} = \frac{V_3^2}{2g} \qquad D.9$$

Head losses due to the grid are modelled as for drainage flows:

$$\Delta H_{2-1} = K_{2-1} \cdot \frac{(\alpha_{2-1} V_3)^2}{2g} \qquad D.10$$

where $K_{2\text{-}1}$ is the same coefficient as the one computed in D.3.2.1 ($K_{1\text{-}2}$) and $\alpha_{2\text{-}1}$ a correction factor for the velocity. Using theory on axisymmetric round jet presented in (Idelchik and Steinberg 1996), the quadratic average velocity is around 0.6 times the velocity in the drainage tube when the flow reaches the grid (so that $\alpha_{2\text{-}1}$=0.6). This value remains uncertain because of the lack of knowledge on the jet turbulence or on the combined effects of the grid and the tube outlet but seems consistent with the fact that in the experiments, jets caused by overflow perturb the street flow surface (so the jet velocity is significant when reaching the grid).

D.3.2.3 Drainage tube

Head losses through the drainage tube are due to the usual friction on the tube walls, but also to the tube curvature. If considering only the linear head losses for a straight pipe, the general formulation gives (for the drainage case head loss term here, but it is identical for overflow):

$$\Delta H_{3-4} = f_{3-4} \cdot \frac{l_t}{d_t} \cdot \frac{V_3^2}{2g} \qquad D.11$$

Where $f_{3\text{-}4}$ is the tube friction factor, l_t and d_t the length and diameter of the drainage tube, and V_3 the drainage tube velocity.

Reynolds numbers are around 10^3 - 10^4 and the drainage tube roughness height k_s is estimated to be 0.01 mm (which gives a relative roughness height of 0.001). In this case, the friction factor depends on both the Reynolds number and the relative roughness height k_s/d_t. Colebrook formula is usually adopted for Reynolds number greater than 10^4 but this equation is implicit so we use the following approximation for full pipe flows (Miller 1978) :

$$f_{3-4} = \frac{0.25}{log_{10}\left(\frac{k_s}{3.7d_t} + \frac{5.74}{Re^{0.9}}\right)^2} \qquad D.12$$

The tube curvature radius is significantly larger than the tube diameter: in this case Idelchik and Steinberg (1996) recommends to use higher friction coefficients (instead of an elbow or turning flow consideration). This is quite subjective, and the author also proposes a formula for large ratio of curvature radius to diameter for smooth pipes, that account for both wall friction and additional losses due to the pipe curvature:

$$f_{3-4,curv} = \frac{a_0}{Re^{a_1}} \cdot \left(\frac{d_t}{2R_0}\right)^{a_2} \qquad D.13$$

where R_0 is the curvature radius of the pipe. a_0, a_1 and a_2 are empirical coefficients depending on the Reynolds number and defined in the following table.

	a_0	a_1	a_2
$50 < Re \cdot \sqrt{\frac{d_t}{2R_0}} < 600$	20	0.65	0.175
$600 < Re \cdot \sqrt{\frac{d_t}{2R_0}} < 1400$	10.4	0.55	0.225
$1400 < Re \cdot \sqrt{\frac{d_t}{2R_0}} < 5000$	5	0.45	0.275

Table D.1 : Empirical coefficients for the total linear head losses in curved pipe with high ratio of curvature radius to pipe diameter

Results of these 2 models are given on the next figure, along with the Blasius equation for smooth pipes. The curved pipe model predicts higher friction than the Colebrook approximation for Reynolds numbers up to 5000, which is the upper bound of validity of the curved pipe model. We will use the latter for Re<5000 and the Colebrook approximation for Re>5000, as it is supposed to cover a wider range. The surface roughness height chosen for the drainage pipe (0.01 mm) is considered as a representative value for plastic pipes, but according to Miller (1978) actual values will depend on the manufacturing process. Although

this might be considered as a calibration parameter or for sensitivity analysis, effects of roughness for such Reynolds number is very limited and is not of prime concern.

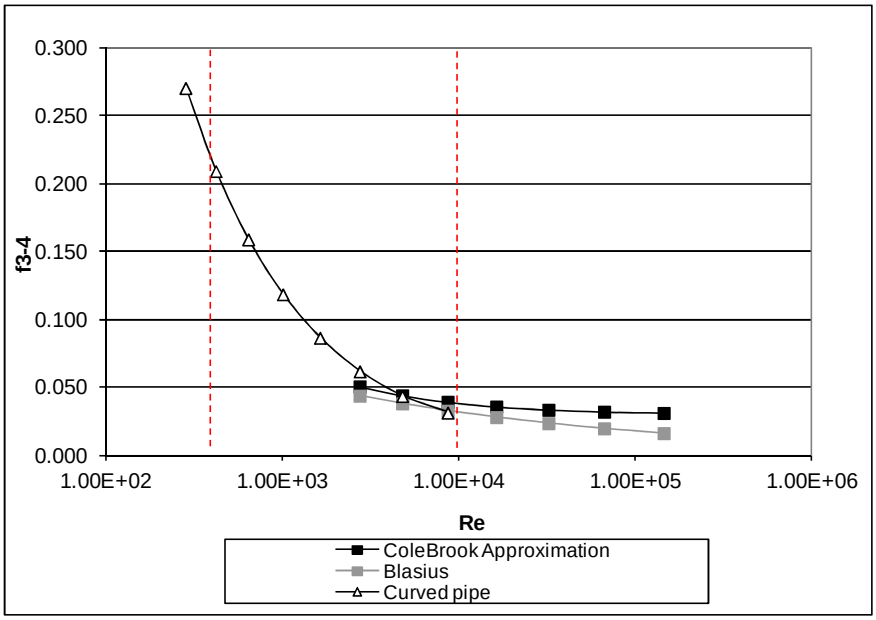

Figure D.5 : Friction factor in the drainage tube. The range of drainage tube flow typical Reynolds numberis within the dash red lines.

D.3.2.4 Junction between the drainage tube and the drainage pipe

Equation sources:

The experimental junction is characterized by a junction angle of 90° with sharp edges, which is a well-documented configuration. However, the head loss coefficients depend on other geometrical and flow parameters:

- ratio of lateral branch flow section to main branch flow section
- ratio of lateral branch flow velocity to main branch flow velocity (or discharge)
- Reynolds numbers in the different branches

Idelchik and Steinberg (1996) provides general formulations of the head losses for both combining and dividing flows. The head loss coefficient for a combining flow is expressed with the following equation and related to the drainage pipe velocity downstream of the junction:

$$K_{4-5,Idelchik} = 1.15 + \left(\frac{Q_t}{Q_p}\right)^2 \left[\left(\frac{A_p}{A_t}\right)^2 - \frac{4 \cdot \left(\frac{Q_p}{Q_t} - 2\right)^2}{2 - \frac{Q_t}{Q_p}}\right] \qquad D.14$$

where Q_p is the flow discharge in the pipe downstream of the junction and Q_t is the exchange flow discharge in one of the drainage tube (it is supposed here that a couple of

drainage tubes linked to the same junction have the same exchange flow, which seems accurate in the present symmetrical configuration). For dividing flows, the author suggests that the coefficient for a 3 branch junction can be used. This latter in our configuration depends only on the ratio of the tube flow velocity V_t to the pipe flow velocity V_p upstream of the junction:

$$K_{5-4,Idelchik} = 0.9 \cdot \left(1 + \left(\frac{V_t}{V_p}\right)^2\right) \qquad D.15$$

For the two latest equations, the author does not provide any validity range. Other sources can be found in the scientific literature, with specific focus points but also narrower validity ranges. Sharp et al. (2010) provides head loss coefficient for a cross junction under an extensive set of flow distribution, but the diameter of the 4 pipes are equal and no extrapolation can be easily done based on their data, as they provide only raw results with abacuses.

Jamison and Villemonte (1971) studied the influence of the Reynolds number on the head losses coefficients for both combining and dividing flow for a three branch junction with equal diameters and different velocity ratios. They show that for Re<1000, the head loss coefficients for a combining flow vary with the Reynolds number in the branch, independently of the ratio of the branch pipe flow velocity to the main branch pipe velocity :

$$K_{4-5,Jamison} = \frac{7300}{Re_{branch}} \qquad D.16$$

In the transition zone, the influence of the velocity ratio is important and no formulation is derived. For a dividing flow, they derive a similar formulation for ratios of lateral branch velocity to upstream branch velocity greater than 0.5:

$$K_{5-4,Jamison} = \frac{7000}{Re_{branch}} \qquad D.17$$

The authors point out that in the transition zone, there is no adequate relation derivable for the head loss coefficient.

Serre et al. (1994) studied combining flows for a right angle junction with a specific focus on the influence of the velocity ratios and flow section ratios between the lateral branch

and the main branch. They derive the following equation for the head loss coefficient, which is related to the velocity in the pipe upstream of the junction V_p:

$$K_{4-5,Serre} = \left(1 - 1.8\frac{A_t}{A_p}\right)\left(\left(\frac{V_t}{V_p}\right)^2 - 1\right) \qquad D.18$$

Comparison and choice of a formulation:

The following table sums up the different formulations presented above, with their range of applicability. Results from (Jamison and Villemonte 1971; Sharp et al. 2010) are not actually usable for our model because they do not consider low ratios of lateral branch flow section to main branch flow section. For combining flows, (Idelchik and Steinberg 1996) equation is applicable for 4 branch junction, whereas (Serre et al. 1994) equation is derived for a 3 branch junction. However, in this article, the authors did consider the equations proposed by Idelchik and Steinberg (1996) but rather developed new equations for very low pipe diameter ratios. As equation from Serre et al. (1994) is more documented with a validity range covering our experimental setup, we choose this formulation (D.18). A comparison of the 2 equations is shown on Figure D.6 for a low and a high pipe discharge, where we can see that (Serre et al. 1994) equation gives smaller head losses for drainage cases, even if the results are quite close.

For dividing flows (which corresponds to an overflow in our experiment) we use the only equations (apart from Jamison and Villemonte (1971), restricted to laminar flows) found in the literature (Idelchik and Steinberg 1996).

Source	Type of junction	Validity			Results
		$A_{lateral}/A_{main}$	$Q_{lateral}/Q_{main}$	Reynolds number	
Idelchik	3 branch dividing junction	-	-	-	Equation
Idelchik	4 branch combining junction	-	-	-	Equation
Jamison	3 branch combining and dividing junction	1	0 to 1	Re<1000	Equation
Serre	3 branch combining junction	0.02 to 0.2	0 to 1	10^5-10^6	Equation
Sharp	4 branch dividing and combining junction	1	0 to 1	10^4-10^5	Abacus

Table D.2 : Equations found in the literature for combining and dividing pipe flows

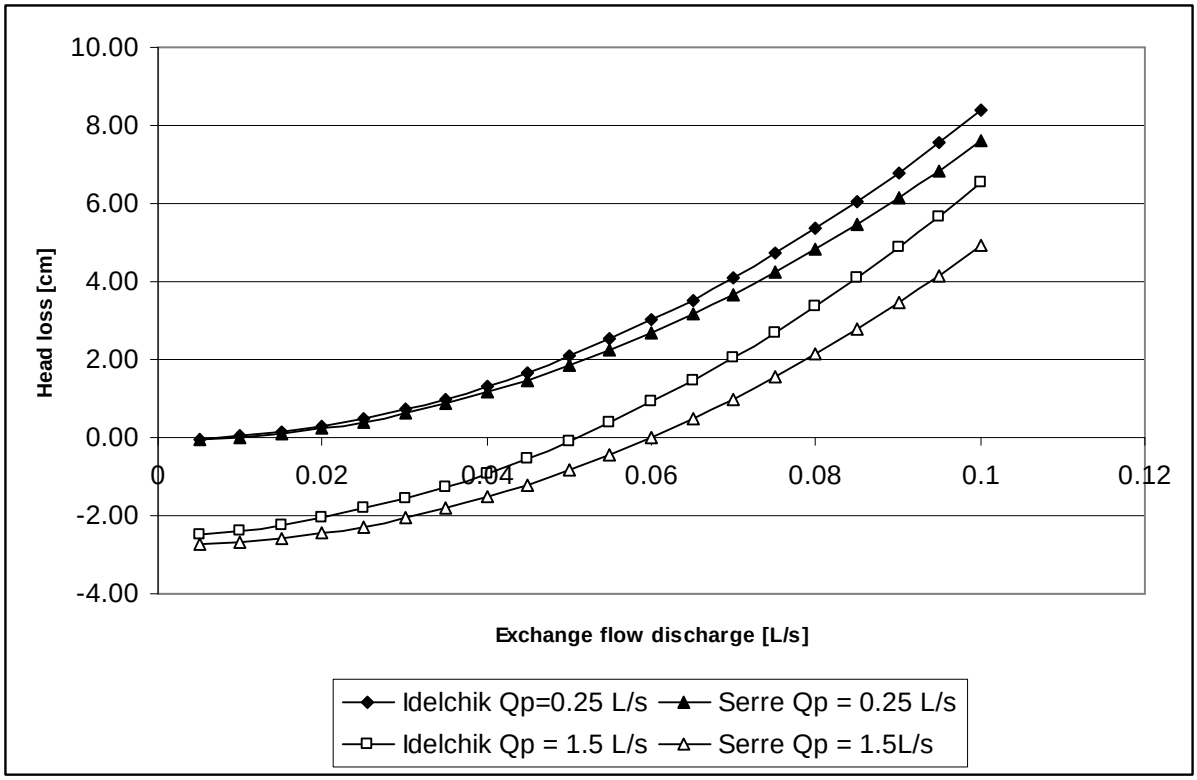

Figure D.6 : Head losses due to the combining flow at the junction pipe/tubes. Computation is done for 2 different pipe upstream discharges (Q_p)

Comments on the negative head losses :

For combining flows, the use of the chosen equation (D.18) implies that the head loss coefficient can be negative, leading in the end to "negative head losses" (as shown on Figure D.6). Noting *u*, *b* and *d* the 3 pipes of a combing flow (upstream, branch and downstream, as on), the energy loss per unit time ΔE in the junction is defined by:

$$Q_u H_u + Q_b H_b = Q_d H_d + \frac{\Delta E}{\rho g} \qquad D.19$$

Where Q and H are the discharge and mean total head in the sections around the junction. Noting that ΔE is always positive, we can write the following inequality :

$$\frac{Q_u}{Q_d} H_u + \frac{Q_b}{Q_d} H_b > H_d \qquad D.20$$

The negative head loss coefficients means that we can have $H_b<H_d$, which is not incompatible with the previous equation, depending on the discharge ratio Q_u/Q_d and Q_b/Q_d. When the branch discharge Q_b is low compared to upstream discharge Q_u (and thus downstream discharge Q_d), H_b can be smaller than H_d so that the branch flow can gain energy through the junction (Idelchik and Steinberg 1996).

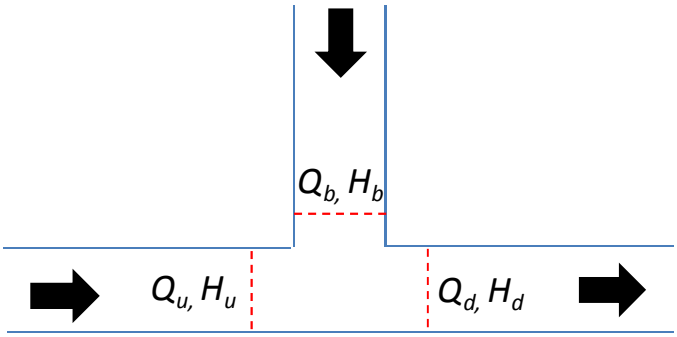

Figure D.7 : Notation for a 3 branch combining flow

Appendix E
Set up of a rainfall-runoff model for urban catchments near Oullins

The flow discharges in the underground pipe network draining Oullins have not been measured during the flood events studied in this thesis. Therefore it is necessary to set up a rainfall-runoff model to generate hydrographs for the simulations of the flows in the underground drainage network. The aim here is not to precisely describe the hydrological processes on the Yzeron catchment but to be able to predict with a right order of magnitude (amplitude and timing) the pipes flow hydrographs during major rainfall events. The methodology here relies on the analysis of available field data and the calibration of a simple rainfall-runoff model.

E.1 Overview of the drainage system and available data

The underground drainage system in Oullins has three main components:

1. A main collector that runs through the peri-urban areas on the Yzeron catchment, and flows along the left bank of the Yzeron river
2. A secondary collector that drains an intermediary catchment south-west of Oullins city centre, and runs on the right bank of the Yzeron river
3. A network of smaller pipes draining Oullins city centre and other surrounding urban areas, connected downstream to one of the collectors

The sewer system is mainly a combined one on the catchment, that is both wastewater and stormwater are collected in the same pipes. The left bank collector is supposed to have a relatively large reaction time, and large flow discharges during rainfall events, whereas the reaction time of the right bank pipe network is supposed to be short, with smaller flow discharges. The main and secondary collectors can exchange flows with each other through a connection pipe that is set up underneath the Yzeron river bed in Oullins centre.

Figure E.1 presents an overview of the Yzeron catchment, along with the measurements points for rainfalls and pipe flow discharges used in this appendix. The main pipes on the catchment are also plotted: they indicate areas drained by the main collector and location of

the latter. A zoom on Oullins city centre is provided on Figure E.6, with the catchment 1 being the one of the secondary collector. Areas drained by the main collector and the secondary collector are estimated to respectively 2300 ha and 128 ha.

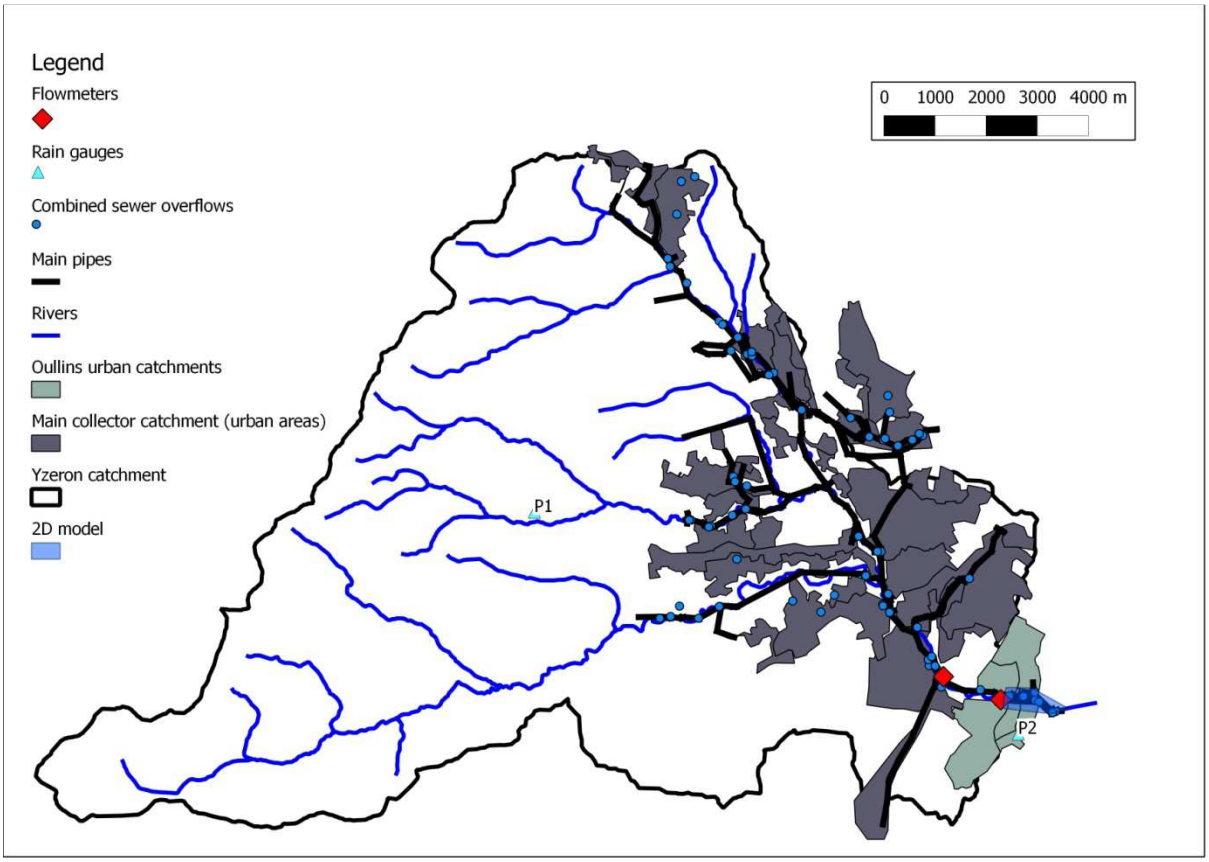

Figure E.1 : Overview of the Yzeron catchment, with urban areas, main elements of the drainage system and location of available measurements

Available rainfall data is measured at two locations (Figure E.1):

- At the centre of the Yzeron catchment, upstream of the urbanized areas that feed the sewer systems (rain gauge P1).
- South of Oullins centre, in the dense urban areas of the catchment (rain gauge P2)

Whereas the second rain gauge (P2) is supposed to be more representative of the rain falling on the dense urban area in the south of Oullins, it is not clear whether P1 or P2 is more suitable to simulate flow hydrographs of the left bank collector. For the latter only, both rain gauges will be considered, as a sensitivity analysis.

The flow discharge in the main collector has been measured between 2007 and 2009 during the Rives project (Cemagref 2009), just upstream of the modelled area (Figure E.1). The flow discharge in the secondary collector has been also measured, just upstream of its connection with the main collector. Due to measuring devices discrepancies, the gathered data are not continuous, but several hydrological events have been recorded (Figure E.2).

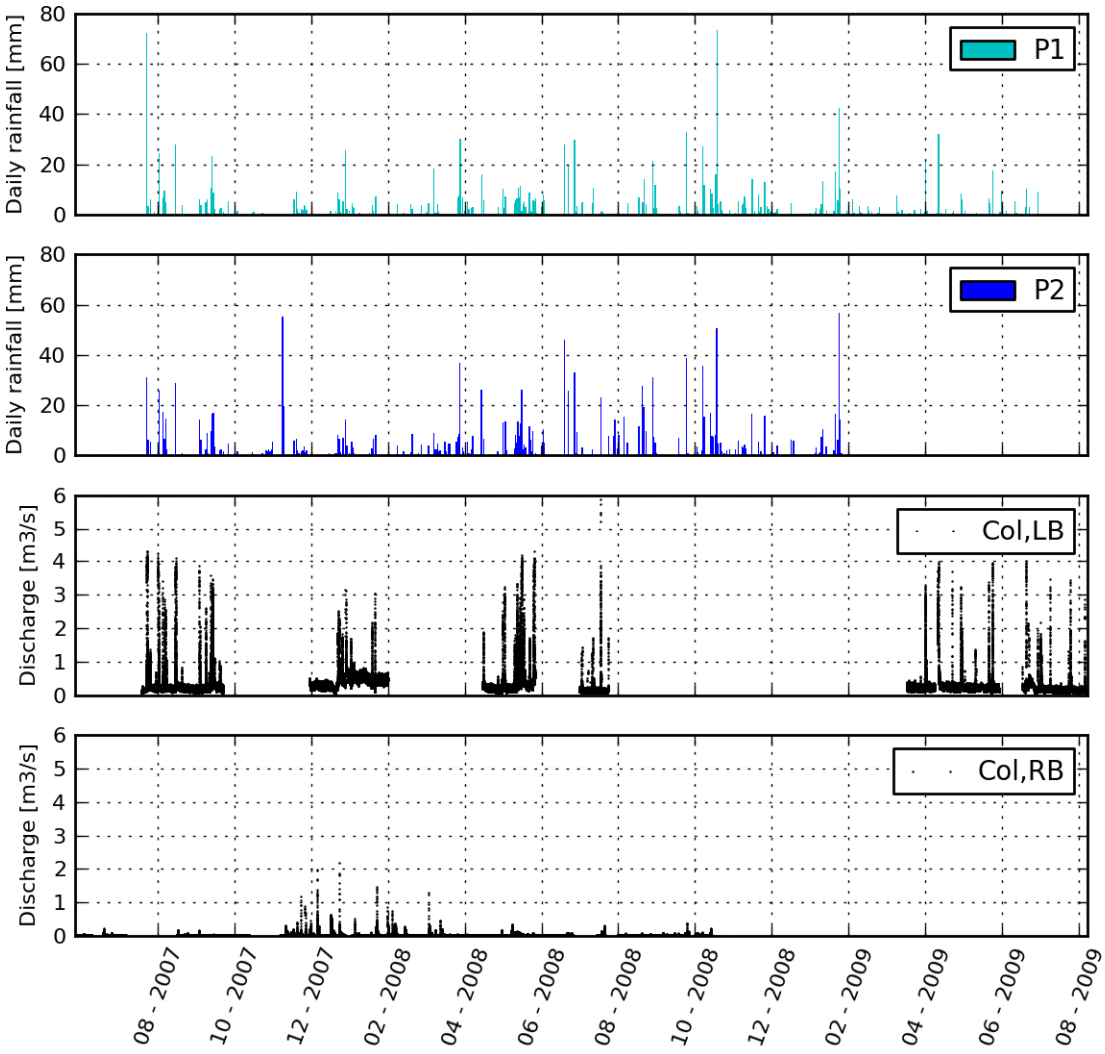

Figure E.2 : Rainfall measurements on the Yzeron catchment (P1 and P2) and discharge measurements in the left bank main collector (Col,LB) and right bank secondary collector (Col,RB) during the period 2007-2009

Finally, the Yzeron catchment is part of OTHU (Field Observatory for Urban Water Management) and other data have been produced or acquired in the past ten years. Among them, topographical data and sewer system data are used to delineate sub catchments. Footprints of built areas and roads are used to determine the imperviousness of these sub catchments.

E.2 Analysis of field data for both collectors

E.2.1 Collectors capacity

Available measurements for both collectors include the flow discharges ($Q_{Col,LB}$ and $Q_{Col,RB}$) and the water pressure at the collectors bottom ($P_{Col,LB}$ and $P_{Col,RB}$). The pressure will be here expressed and referred as the equivalent water depth (e.g., $h_{Col,LB} = \frac{P_{Col,LB} - P_{atm}}{\rho g}$). Figure E.3 shows the relationship between the measured collectors flow discharges and water depths.

The main collector flow discharge $Q_{Col,LB}$ increases strongly with the water depth until the flow becomes pressurized (for $h_{Col,LB}$=1.8m), and then becomes limited. On the whole measurement period, it seems that the flow discharges reached at the collector pressurization are between 2.5 and 3 $m^3.s^{-1}$ and that the maximum observed flow discharges are around 4 $m^3.s^{-1}$. There are higher observed values (almost 6 $m^3.s^{-1}$), but considering the corresponding flow hydrographs they are not assumed to be relevant, as such discharges occur twice in the measurement campaign, and only for a few minutes (the recording time step is 2 minutes). The important dispersion of the scatter plot in Figure E.3 for high water depths comes from the potentially different hydraulic configurations downstream (e.g. a surcharge of the drainage pipes in Oullins) and the operations of the many combined sewer overflows (CSO) located upstream of the measurement point (see Figure E.1). Therefore, we will consider that due to the CSOs, the maximum left bank collector flow discharge at this measurement point is 4.0 $m^3.s^{-1}$, even if a rainfall event generates higher runoff discharges. Note that the upstream CSOs should start to operate for lower discharges (typically as soon as the collector flow starts to be pressurized), but considering such effects would require to explicitly model the whole drainage network on the catchment, which is out of the scope of the present modelling.

Available measurements for the right bank collector cover mainly the winter 2007/2008 (see Figure E.2). On this period, this collector barely reached its full capacity, as shown on Figure E.3 ($Q_{Col,RB}$). Therefore, no discharge limitation is considered for this collector.

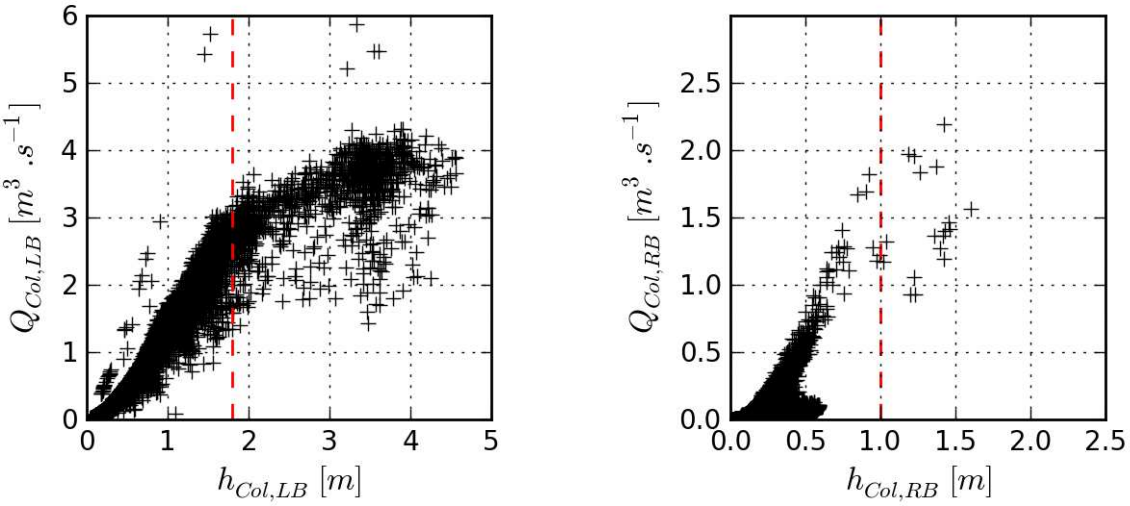

Figure E.3 : Discharge - water depth relationship for the main (left) and secondary collectors (right). The red dashed line indicates the height of the collectors.

E.2.2 Main hydrological events

A series of hydrological events are selected to analyse the urban runoff generation on the catchments of the main and secondary collectors. The selection is done on events that generate flow discharges higher than 3.0 $m^3.s^{-1}$and 0.5 $m^3.s^{-1}$ in respectively the main and the secondary collectors, and for which rainfall data are available. For each event selected for one of the collectors, the delay K_{Col} between the rainfall intensity peak time and the collector flow discharge peak time is manually evaluated. Then volumes of the water flowing in the collector V_{Col} and of the rain falling on the catchment V_{rain} are calculated for each event, considering the corresponding catchment areas. The ratio of these two volumes is calculated and gives an order of magnitude of the coefficient of imperviousness of the catchment C_{IMP}. Both K_{Col} and C_{IMP} are parameters required to run the chosen rainfall-runoff model (described in E.3).

Measurements details of these events for the main and secondary collectors are shown respectively on Figure E.4 and Figure E.5. Results of the analysis are respectively in Table E.1 and Table E.2 (subscripts *1* and *2* referring to rain gauges P1 and P2, *LB* and *RB* referring to the main left bank collector and secondary right bank collector).

For the main collector, $K_{Col,LB}$ and $C_{IMP,Col,LB}$ vary from one event to another, on the one hand because of the hydrological conditions specific to each event, but on the other hand because of the uncertainty on the rainfall. The latter can be clearly seen when comparing both rainfall measurements for a specific event (Figure E.4). For simplicity, for the rainfall-runoff

modelling we adopt a single value of 50 min for K_{col} and 12% for $C_{IMP,col}$, which are representative of the observed values.

Event	Date	$Q_{Col,LBmax}$ $m^3.s^{-1}$	$K_{Col,LB1}$ min	$K_{Col,LB2}$ min	$V_{Col,LB}$ m^3	V_{rain1} m^3	V_{rain2} m^3	$C_{IMP,Col,LB1}$ %	$C_{IMP,Col,LB2}$ %
1	16/08/2007	3.8	70	50	$4.1x10^4$	$5.6x10^5$	$5.6x10^5$	7.3	7.2
2	19/08/2007	3.1	50	20	$9.1x10^3$	$1.5x10^5$	$4.0x10^5$	6.0	2.3
3	30/08/2007	3.6	90	120	$6.1x10^4$	$4.9x10^5$	$4.1x10^5$	12.4	14.7
4	17/09/2007	3.6	50	40	$1.8x10^4$	$1.4x10^5$	$3.5x10^5$	12.7	5.0
5	22/12/2007	3.0	40	30	$3.4x10^4$	$6.2x10^5$	$3.7x10^5$	5.4	9.1
6	14/01/2008	3.0	60	30	$1.5x10^4$	$1.5x10^5$	$1.8x10^5$	10.3	8.3
7	11/02/2008	3.0	40	60	$2.4x10^4$	$1.6x10^5$	$3.1x10^5$	15.5	7.8
8	06/05/2008	3.1	30	50	$4.1x10^4$	$2.2x10^5$	$2.6x10^5$	18.8	15.8
9	21/05/2008	3.9	40	-	$4.2x10^4$	$1.3x10^5$	-	32.6	-
10	31/07/2008	3.0	50	-	$4.1x10^4$	$3.8x10^5$	-	10.8	-
11	16/04/2009	3.0	60	-	$2.4x10^4$	$2.0x10^5$	-	11.7	-
12	09/05/2009	3.7	60	-	$4.4x10^4$	$4.0x10^5$	-	11.1	-
13	15/05/2009	3.5	60	-	$2.6x10^4$	$2.3x10^5$	-	11.2	-

Table E.1 : Analysis of selected rainfall events for the main collector. $Q_{Col,LBmax}$ is the peak flow discharge measured in the collector. Subscripts 1 and 2 refers to calculation carried out for respectively rain gauges P1 and P2

For the secondary collector, only the rain gauge P2 is used, at it is located close to the corresponding catchment. The typical delay $K_{Col,RD}$ could not be evaluated, as its order of magnitude is the same as the time step of rainfall (6 minutes). Table E.2 shows that the computed values of the imperviousness coefficient $C_{IMP,Col,RB2}$ vary between 5 and 14%. We chose a representative value of 0.1 for the rainfall-runoff model.

Event	Date	$Q_{Col,RBmax}$ $m^3.s^{-1}$	$V_{Col,RB}$ m^3	V_{rain2} m^3	$C_{IMP,Col,RB2}$ %
1	07/06/2007	1.2	$1.64x10^3$	$3.00x10^4$	5
2	11/06/2007	0.8	$2.21x10^3$	$2.53x10^4$	9
3	20/06/2007	1.9	$4.07x10^3$	$6.96x10^4$	6
4	21/06/2007	1.7	$3.25x10^3$	$2.30x10^4$	14
5	08/07/2007	2.0	$3.71x10^3$	$5.27x10^4$	7
6	16/08/2007	0.8	$2.24x10^3$	$3.12x10^4$	7
7	19/08/2007	0.8	$1.14x10^3$	$2.20x10^4$	5
8	17/09/2007	1.2	$1.41x10^3$	$1.95x10^4$	7

Table E.2: Analysis of selected rainfall events (with rain gauge P2) for the secondary collector. $Q_{Col,RBmax}$ is the peak flow discharge measured in the collector.

E.3 Set up of a rainfall-runoff model

E.3.1 Reservoir model

The reservoir model is chosen to simulate the flow hydrographs, as it is a simple model, that can be easily set-up (few parameters and input data). Application of this model to the present urban catchments follows the guidelines provided by the engineering master course from Bertrand-Krajewski (2006). The different formulations presented below are taken from this source.

The model principle is to describe the catchment as a reservoir, with an inflow (rainfall) and an outflow (downstream pipe flow discharge). A reservoir model is based on a system of a continuity equation:

$$\frac{dV_s(t)}{dt} = Q_e(t) - Q_s(t) \qquad E.1$$

and a storage equation:

$$V_s(t) = f\big(Q_e(t), Q_s(t)\big) \qquad E.2$$

Where t is the time, V_s is the volume stored in the reservoir, Q_e and Q_s are respectively the fluxes coming into and out of the reservoir, and f a storage function.

The incoming flux can be written as follows:

$$Q_e(t) = A \cdot C_{IMP} \cdot I(t) \qquad E.3$$

Where A is the catchment area, C_{IMP} is the imperviousness coefficient of the catchment and I the rainfall intensity.

The Muskingum model proposes to write the storage function as follows:

$$V_s(t) = K\big(\alpha Q_e(t) + (1-\alpha) Q_s(t)\big) \qquad E.4$$

with K and α coefficients to determine (α lying between 0 and 1). K is homogenous to a time and represents the delay between the rainfall peak time and the catchment outlet discharge peak time. Deriving Equation E.4 and substituting in E.1, the following equation can be derived:

$$Q_e(t) - Q_s(t) = K\left(\alpha\frac{dQ_e(t)}{dt} + (1-\alpha)\frac{dQ_s(t)}{dt}\right) \qquad E.5$$

This equation can be solved numerically by a direct discretization in time. This is done here by using a Python script specifically written to numerically solve the final equation, considering measurements of rainfall and sets of numerical parameters (K, $C_{IMP,}$ A,α).

E.3.2 Application to both collectors

The presented reservoir model is used to model the runoff generation on both collectors' catchments. We use the previously determined values for K (50 min) and C_{IMP} (12%) for the main collector. For the secondary collector, we use also the previously estimated value for C_{IMP} (10%). The parameter K is evaluated to 6 minutes, following the approach presented in E.3.3. After a trial and error step, the time step for the calculation is fixed to 30 min for the main collector, 6 min for the secondary collector, and the value of α is set to 0.5. As mentioned in E.2.1, a discharge limitation is imposed for the main collector in order to account for the potential CSO effects upstream of the measurement point (fixed to 4.0 $m^3.s^{-1}$). Moreover, a constant base discharge is added to account for the wastewater flows and infiltration. From available measurements, this base discharge is evaluated to 0.25 and 0.01 $m^3.s^{-1}$ for respectively the main and secondary collectors (average discharge during dry weather periods).

For the main collector, the model is run for the 13 selected events and the 2 rainfall measurements (when available), and the comparison of the simulated and measured discharges is shown on Figure E.4. For most of the events, the simulated hydrographs are reasonably close to the measurements, and the highest discrepancies can be related to the uncertainties on the rainfall. The latter is obvious for event 7 for instance. The peak flow times are reasonably well reproduced, which was expected as the value of $K_{col,LB}$ was evaluated from available measurements. The limitation imposed on the collector discharge is effective for several events and leads to better results (e.g. events 1 and 4), but this assumption may not be sufficient for other events with intense rainfall (such as event 5).

For the secondary collector, the model is run for the 8 selected events, for the rainfall P2, and comparison with measurements is shown on Figure E.5. Again, peak discharges and hydrographs shapes are globally rather well simulated, although important errors are found.

Note that recorded rainfall and collector discharge do not always seem consistent with each other, which can explain a part of the discrepancies (see for instance events 4 and 7).

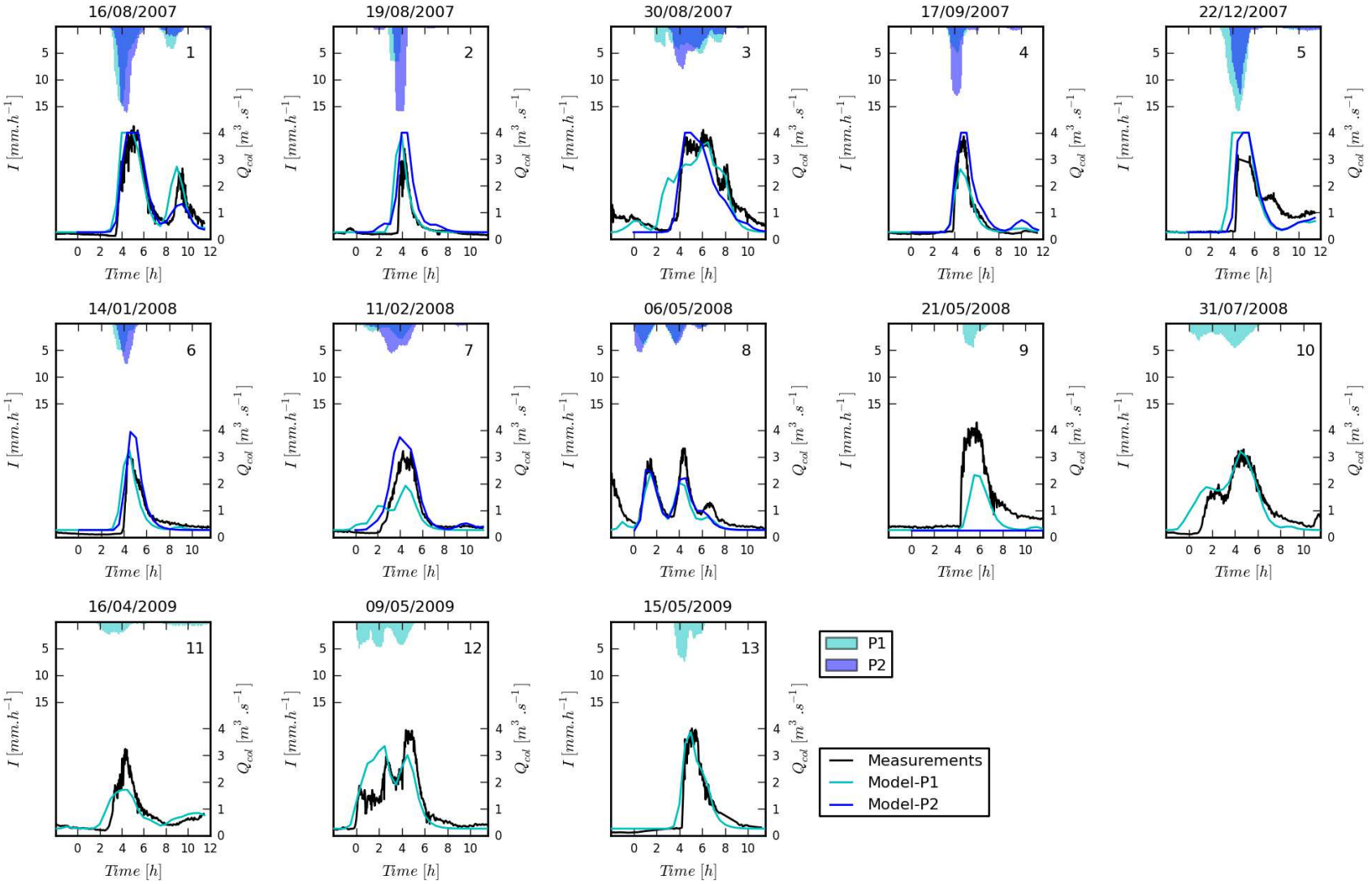

Figure E.4: Comparison of simulated and measured main collector flow discharges for the 13 selected events

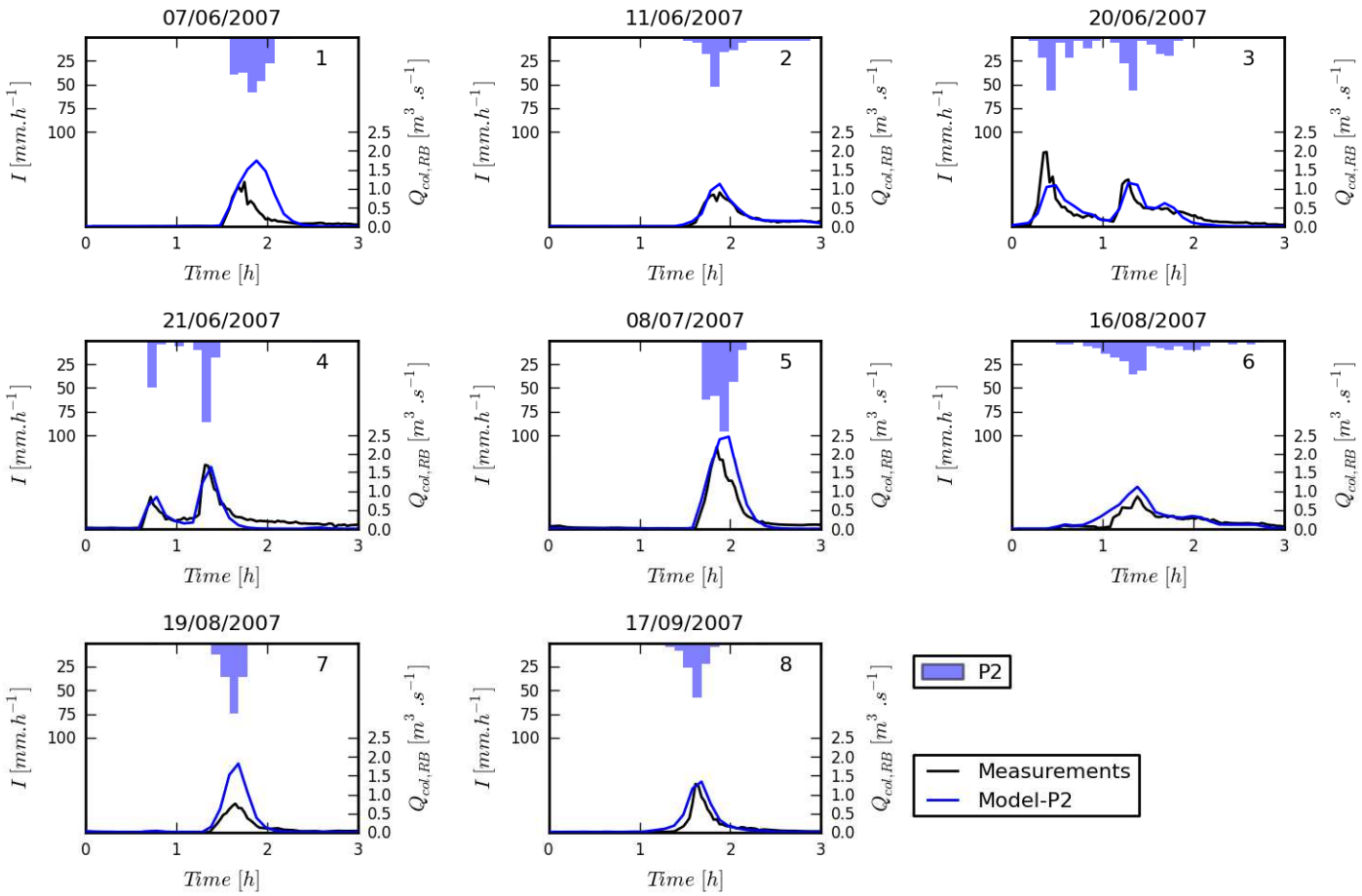

Figure E.5 : Comparison of simulated and measured secondary collector flow discharges for the 8 selected events

E.3.3 Application to other catchments

There is no hydrological data to validate the rainfall-runoff model on the sub-catchments feeding the small drainage pipes network in Oullins. The reservoir model can still be applied, but the values of K and C_{IMP} have to be determined without direct measurement. To estimate C_{IMP} for each catchment, we assume that the impervious areas consist of the road network and the buildings. These catchments have been delineated in GIS (Figure E.6), so that C_{IMP} can be calculated.

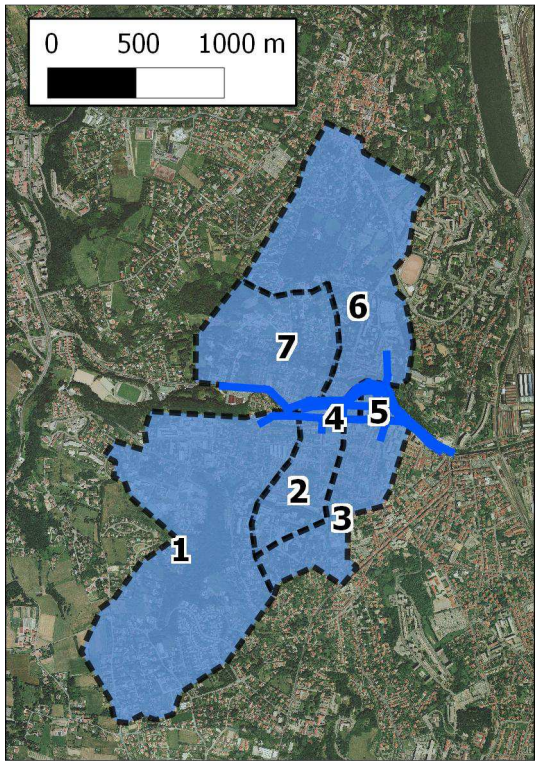

Figure E.6 : Urban catchments feeding the drainage pipes in Oullins. Catchment n°1 corresponds to the secondary collector.

Bertrand-Krajewski (2006) reports a formulation from Desbordes (1974), which proposed the following empirical relationship to estimate K from the catchment physical characteristics:

$$K = 0.494A^{-0.0076} \cdot C_{IMP}^{-0.512} \cdot S_0^{-0.401} \cdot L_p^{0.608} \qquad E.6$$

with A the catchment area, S_0 the average catchment slope and L_p the length of the longest drainage pipe on the catchment. Results for the previously delineated sub catchments are given in Table E.3. The imperviousness coefficients can reach high values, since some catchments are in dense urban areas. The computed values of K are around a few minutes,

which means these catchments rapidly react during rainfall events, especially when compared to the main collector.

Catchment	A	C_{IMP}	L_p	S_0	K
	ha	-	m	%	min
1	127.7	0.18	2278	3.51	6
2	22.1	0.34	800	7.00	2
3	31.6	0.34	890	5.06	3
4	3.0	0.57	250	0.32	3
5	2.7	0.53	130	0.62	2
6	83.8	0.14	1451	0.90	11
7	42.8	0.15	680	9.26	3

Table E.3 : Estimated parameters for the rainfall-runoff model of the small urban catchments in Oullins

From these results we conclude that the rainfall-runoff model can predict the right order of magnitude of the maximal flow discharges for the main and secondary collectors, and quite accurate peak times. The main error lies in the precise estimation of the peak discharge for some events (rather than the hydrograph shape). If required, a convenient way to consider this uncertainty when simulating floods in Oullins (Chapter 7) can consist in multiplying the whole simulated hydrographs by an arbitrary value (e.g. +25%, -25%).

ECOULEMENTS LORS D'INONDATIONS EN MILIEU URBAIN : INFLUENCE DE LA TOPOGRAPHIE DETAILLEE ET DES ECHANGES AVEC LE RESEAU D'ASSAINISSEMENT

Le but de cette thèse est d'étudier la modélisation détaillée des écoulements qui ont lieu lors des inondations urbaines. Dans une première partie, des écoulements en bifurcation incluant des petits obstacles génériques ou des profils de canaux avec trottoirs sont étudiés sur une maquette expérimentale, puis simulés numériquement avec le modèle bidimensionnel Rubar20. Les résultats expérimentaux et numériques montrent l'avantage d'inclure des obstacles de petite taille dans un modèle d'inondation urbaine, alors qu'il n'y a qu'un intérêt limité à utiliser une topographie détaillée des rues. Dans une deuxième partie, les interactions entre écoulements de surface et écoulements en conduites souterraines sont étudiées. Un modèle physique de système de drainage urbain permet de valider un modèle analytique prédisant les débits d'échange entre les deux couches d'écoulement. Une modélisation 1D/2D (conduite/rue) est mise en place avec les modèles Rubar3/Rubar20 et validée sur des écoulements expérimentaux observés sur le modèle physique. Dans une troisième partie, les inondations dans la ville d'Oullins (près de Lyon, France) sont étudiées. La modélisation des écoulements de surface est validée avec des données de terrain, et nous discutons l'intérêt de plusieurs représentations du milieu urbain. L'intégration du réseau d'assainissement dans un modèle 1D/2D reste affectée par plusieurs incertitudes, mais cette étape montre l'intérêt de la modélisation couplée pour décrire les interactions complexes des écoulements lors d'inondations urbaines, ainsi que les limites de l'approche développée pour les écoulements à faible profondeur.

Mots clés: inondation urbaine, modèle physique, simulation numérique, obstacle, topographie détaillée, modélisation couplée du drainage, Oullins

---

FLOWS DURING FLOODS IN URBAN AREAS: INFLUENCE OF THE DETAILED TOPOGRAPHY AND EXCHANGES WITH THE SEWER SYSTEM

Aim of this thesis is to study the detailed modelling of flows that occur during urban floods. In a first part, bifurcation flows including small obstacles or channel profiles with sidewalks are studied on an experimental facility, and then numerically simulated with the two-dimensional model Rubar20. Experimental and numerical results show the benefits of including small obstacles in an urban flood model, whereas there is only little benefit of using a detailed representation of the streets topography. In a second part, interactions between surface and underground pipe flows are studied. A physical model of an urban drainage system allows the validation of an analytical model predicting exchange discharges between both flow layers. A 1D/2D modelling (pipe/street) is set up with the models Rubar3/Rubar20 and validated on experimental flows observed on the physical model. In a third part, floods in the city of Oullins (near Lyon, France) are studied. Surface flows modelling is validated with field data, and we discuss the interest of several representations of the urban area. Integration of the sewer system in a 1D/2D model remains impacted by several uncertainties, yet this step shows the interest of the coupled modelling to describe complex flows interactions during urban floods, as well as limitations of the developed approach for shallow flows.

Keywords: urban flood, physical model, numerical simulation, obstacle, detailed topography, dual drainage modelling, Oullins